Doctoral Dissertation
Doctoral Program in Metrology (38th Cycle)

Electrochemical measurements to support energy transition: water electrolysers characterization

Valentina Maria Volanti

* * * * * *

Supervisors
Prof. Sabrina Grassini
Prof. Monica Santamaria

Doctoral examination committe:
Prof. Giulio Malucelli, Politecnico di Torino, Italy
Prof. Santoro Carlo, Università degli Studi di Milano-Bicocca
Prof. Lavacchi Alessandro, ICCOM-CNR

Politecnico di Torino
28th January 2026

I hereby declare that, the contents and organisation of this dissertation constitute my own original work and does not compromise in any way the rights of third parties, including those relating to the security of personal data.

…….....

Valentina Maria Volanti

Turin, January 28, 2026

Summary

Water electrolysis represents a key technology for energy transition, and among the different technologies, alkaline water electrolysis is the most developed, thanks to relatively low cost, compared to others, and the possibility of working without critical raw materials or noble electrodes. A crucial aspect of water electrolysis is the anodic process: oxygen evolution reaction (OER) is characterized by a sluggish kinetics, high overpotential, and severe stability issues in alkaline environments. For this reason, the design of active and stable catalysts is essential. However, despite the extensive research efforts in recent years, the lack of standardized protocols for catalyst testing make it difficult to compare results among different laboratories.

To address this gap, this research proposes to develop and apply standardized measurement methodologies for the characterization of electrodes used in water electrolysis, combining electrochemical techniques, to extract key performance indicators, with physicochemical characterization methods to correlate morphological and structural properties with electrochemical performance.

In particular, I defined two complementary experimental protocols, tailored to the specific nature of the investigated materials and integrating both DC and AC electrochemical techniques. In particular, DC methods provide quantitative insights on electrocatalytic activity and stability, while AC techniques, such as electrochemical impedance spectroscopy, represent a powerful diagnostic tool for resolving the individual contributions of charge transfer, double-layer capacitance, diffusion, and interfacial phenomena over a wide frequency range, by the usage of an electrical circuit, modeling the electrochemical behaviour of the system. The combination of both types of measurements allows to obtain a more comprehensive evaluation of electrocatalysts performance, enabling the identification of degradation pathways and enhancing the comparability of results. Experimental activity focused on functionalized Porous Transport Layers (PTLs) in stainless

steel, which can be used in new generation anion exchange membrane water electrolyzers (AEMWEs), and on perovskite-based electrodes, explored for their catalytic activity and stability toward the OER. These materials were selected to represent both technologically relevant and scientifically challenging systems, where surface modification, microstructural control, and compositional tuning play decisive roles in determining electrochemical behaviour.

A *Protocol for functionalized PTLs* was applied to Ni-based and NiFe-based metal–organic framework (MOF) nanostructures. NiFe MOF-based electrodes, in particular, have been integrated as anodes in anion-exchange membrane electrolyzers (AEMWE). In both cases, the measurement approach allowed a reliable correlation between structural features, electrocatalytic activity, and degradation mechanisms, highlighting the advantages of a reproducible measurement framework.

A *Thin-Film Electrode Protocol* was instead applied to perovskite catalysts, i.e. Ti-doped $SrCoO_{3-\delta}$. The application of a specific protocol, integrating electrochemical and spectroscopic techniques, confirmed the role of structural doping in achieving durable performance.

Overall, this dissertation demonstrates how measurement science can play a central role in electrocatalysis research providing a metrological framework for electrochemical measurements in hydrogen-related energy research, aiming to enhance the reliability and comparability of electrochemical testing across research institutions and industrial laboratories.

Acknowledgments

And I would like to acknowledge all the institutions and people who contributed to this work.

I am grateful to the University of Palermo (Unipa) and in particular to the *Laboratorio di Elettrochimica Applicata* for hosting me, for the scientific and technical support, and for providing a collaborative and stimulating research environment.

I also wish to thank RWTH Aachen University, specifically the Institut für Werkstoffe der Elektrotechnik 2, IWE 2, for hosting me offering and inspiring research environment that greatly supported the development of my research.

My thanks go also to the CNR of Messina for performing the experiments with the real electrolyzer, and to the ATeN Center (University of Palermo) and ZEA-3, Forschungszentrum Jülich, for their valuable support with the XPS analyses.

I would also like to thank the Società Chimica Italiana, and in particular the *Division of Applied Electrochemistry*, for awarding me the *Premio della Divisione di Elettrochimica "Metrohm Italiana" – Premio di Laurea 2023*.

My sincere thanks also go to the organizers of the International Ph.D. School "Italo Gorini" 2023, for recognizing my work with the *Best Sustainable Project (UN Agenda 2030) Award*.

Finally, I would like to acknowledge the contribution of my supervisors, Professor Sabrina Grassini and Professor Monica Santamaria for their guidance and collaboration throughout this research. I also wish to extend my thanks to Professor Andrea Zaffora, Professor Leonardo Iannucci, Professor Francesco Di Franco and all my colleagues, for their continuous encouragement and guidance over the years.

I would like to dedicate this thesis

To my family,
for their constant love, patience, and faith in me the quiet strength behind every step of this journey.

To my friends of a lifetime,
for always being there, no matter the distance or time, and for reminding me of where I come from.

To the friends I met along the way,
for sharing this experience with generosity, laughter, and understanding , you made the hard days lighter and the good ones brighter.

And to my partner,
for his patience, support, and unwavering belief in me.

But overall to myself, for never give up.

Contents

List of Tables

List of Figures

Chapter 1

Introduction

1.1 Green hydrogen

In the past few decades, the growth of global energy demand, driven by both economic and demographic increase, has resulted in a strong dependence on fossil fuels, such as oil, coal, and natural gas. At the same time, technological innovation has further increased the demand for energy, needed to power our vehicles, factories, and computers. While fossil fuels have supported the industrial development of the 20th century, their widespread usage is today recognized as one of the main drivers of climate change, due to the large amounts of Greenhouse gas emissions (GHG) that are released during their combustion [1–4]. It is documented by the International Energy Agency that, in 2010, around 69% of global greenhouse gas emissions were the result of fossil fuel combustion [5]. They are considered the primary agent of climate change, with nearly 90% carbon dioxide emissions, attributed to combustion [6]. The environmental and social consequences, including the rise in global temperature, extreme weather events, and biodiversity loss, make a transition to a more sustainable energy model a real and urgent necessity [7,8]. To address this challenge, at the 2015 UN Climate Change Conference, Parties to the United Nations Framework Convention on Climate Change (UNFCCC) adopted The Paris Agreement, which states the following goals: ‘’Hold the increase in the global average temperature to well below 2 °C above pre-industrial levels and pursue efforts to limit the temperature increase to 1.5 °C above pre-industrial levels, recognizing that this would significantly reduce the risks and impacts of climate change...’’ [9]. To achieve 1.5 °C target, as required, it is necessary to reduce CO_2 emission by about 37 Gigatons compared to 2022 levels, and reach zero-net emission in energy sector by 2050 [10].

Beyond their environmental impact, fossil fuels are also non-renewable resources, originated millions of years ago from buried organic matter. Although large deposits still exist worldwide, they have been widely exploited and are

gradually being depleted. It is estimated by the scientific community that crude oil reserves will be exhausted in 2042, natural gas in 2044, and coal in 2112, as shown in Figure 1.1 [11–13].

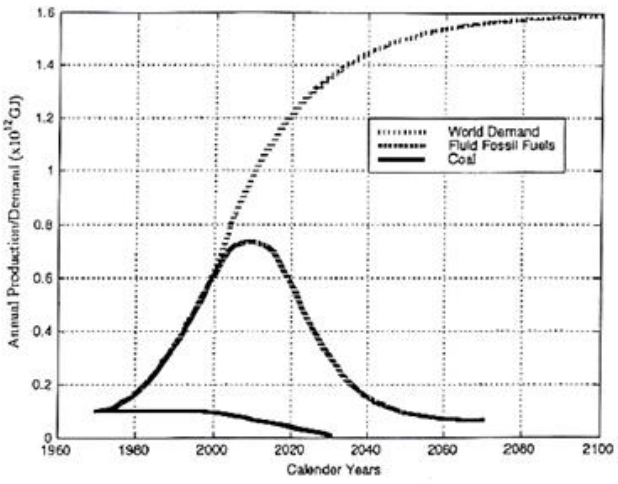

Figure 1.1 World Energy consumption, fossil fuel and coal depletion. Image taken from [13].

Thus make a transition to a sustainable energy paradigm essential. Electricity is expected to become the main energy carrier, accounting for over 50% of total final energy consumption by 2050 in the 1.5°C scenario [14]. However, to achieve full decarbonization, attention must also be paid to that sector where direct electrification is challenging, such as heavy industry, aviation, and international shipping. In these hard-to-abate sectors, bioenergy could represent a promising solution, for example as biofuel for transport with limited alternatives (such as aviation), or as carbon sources for synthetic fuel production. Additionally, technologies such as carbon capture and storage (CCS) can help to reduce residual emissions, especially in industrial plants already in operation or in processes that are difficult to decarbonize, such as cement production [15].

However, where it is possible, direct electrification remains the most efficient and simplest pathway, and it has already been successfully adopted in areas such as buildings, heating, and passenger transportation.

It is fundamental to invest in clean technology and renewable sources like solar, wind, and hydropower energy [16]. The percentage of renewable energy in the global energy mix is expected to increase from 16% in 2020 to 77% by 2050 [10]. However, their intermittent nature introduces significant challenges to the stability and reliability of energy grid. Consequently, it is necessary to find complementary solutions to store and transport energy more efficiently.

In this context, hydrogen is emerging as a key energy vector in a transition towards a low carbon emission system. One of the UN's sustainable development goals (SDGs) is the SDG7, i. e. "ensure access to affordable, reliable, sustainable and modern energy for all" [17]. Green hydrogen, produced using surplus renewable energy, could be a sustainable and climate-safe solution, especially for those hard to abate sectors [12,18–20] and, more broadly, for the decarbonization

of chemical processes [21–23], as it is shown in Figure 1.2. Hydrogen is mainly used today in crude oil refining and the synthesis of ammonia and methanol, together representing about 75% of the total demand for pure and hydrogen [8,24]. Moreover, green hydrogen can be used to generate clean energy, for instance through fuel cell, an electrochemical system that converts hydrogen's chemical energy into electrical energy producing only water and heat as by-products, without harmful emissions [25].

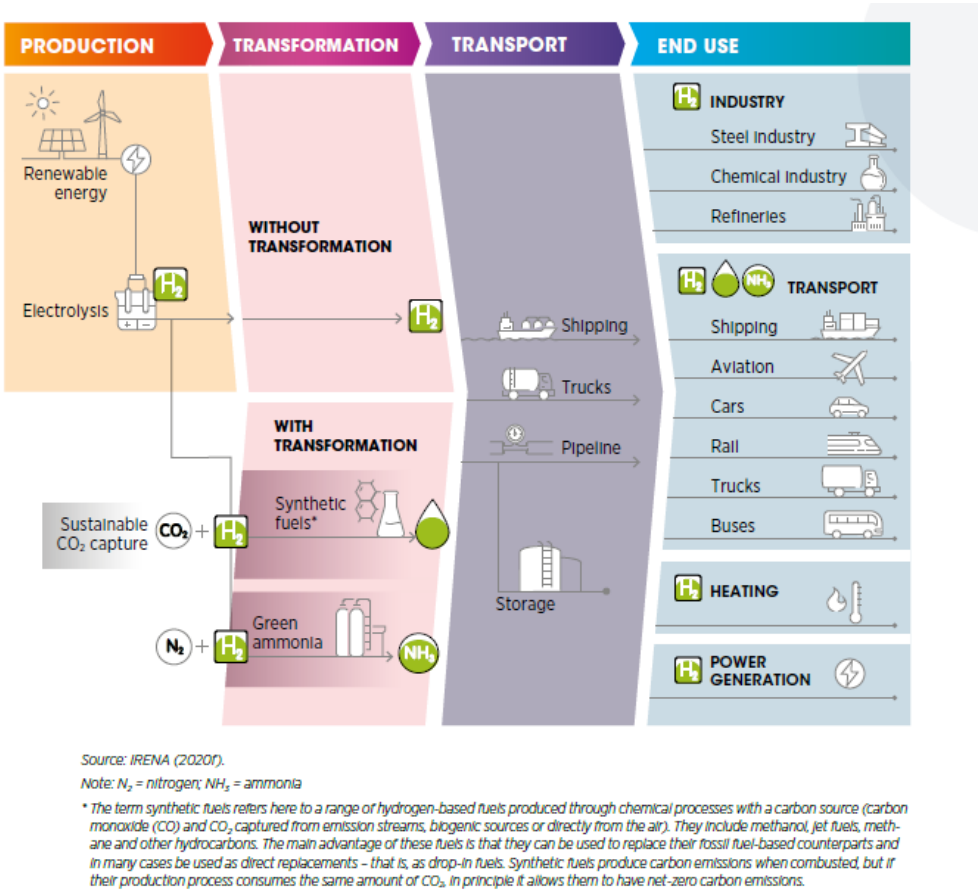

Source: IRENA (2020f).

Note: N_2 = nitrogen; NH_3 = ammonia

** The term synthetic fuels refers here to a range of hydrogen-based fuels produced through chemical processes with a carbon source (carbon monoxide (CO) and CO_2 captured from emission streams, biogenic sources or directly from the air). They include methanol, jet fuels, methane and other hydrocarbons. The main advantage of these fuels is that they can be used to replace their fossil fuel-based counterparts and in many cases be used as direct replacements – that is, as drop-in fuels. Synthetic fuels produce carbon emissions when combusted, but if their production process consumes the same amount of CO_2, in principle it allows them to have net-zero carbon emissions.*

Figure 1.2 Green hydrogen production, conversion and end uses across the energy system. Image taken from [26].

To better understand the potential of hydrogen in the energy transition, it is useful to recall some of its fundamental properties and how it is currently produced.

Hydrogen is the most abundant element in the universe; on earth it exists in composite forms with other elements. It can be combined with oxygen as water, or with carbon resulting in hydrocarbons present in natural gas, coal, or oil. Therefore, it must be extracted from its composites. 1 kg of hydrogen contains 33 KWh of energy, 3 times higher than gasoline, but when stored at atmospheric pressure, its volumetric energy content is 4 times lower [18,27]. Today 95% of global hydrogen production comes from fossil fuel, using technology such as methane steam reforming or coal gasification. However, these processes result in very high CO_2 emission, further contributing to global warming. The remaining 5% is a byproduct of chlorine production. Electrolysis, when coupled with renewable sources, represents the only way to produce hydrogen without any emission [27–30]. Global

Hydrogen consumption in 2020 was about 87 million tons (10440 PJ), with almost all of it produced by fossil fuels [31].

Hydrogen cleaning levels, are often described using a colour code, which is related to the technology used to its production, the resources from which it is extracted and the amount of polluting emission generated [29,30,32], Figure 1.3.

Grey, brown, and black hydrogen are produced using fossil fuels, such as coal and natural gas, releasing a huge amount of GHG emissions [30]. Grey hydrogen is obtained through natural gas reforming: to produce 1 ton of grey hydrogen, about 10 tons of CO_2 are emitted into the atmosphere [23]. Brown hydrogen is derived from lignite, while black hydrogen comes from hard coal. Coal gasification is the most polluting pathway, releasing both CO_2 and CO. Although the share of black and brown hydrogen is reducing, grey technology remains the primary source [27].

Turquoise hydrogen is produced by natural gas pyrolysis, where methane is thermally decomposed at temperatures between 600 °C and 1400 °C, splitting methane into hydrogen and carbon. Unlike grey hydrogen, this process doesn't emit CO_2, since the by-product is solid carbon (black carbon). However, carbon stability at this elevated temperature is critical, and also the use of renewable energy to make the process sustainable [23].

Blue hydrogen is also produced from fossil fuels, but with the addition of Carbon Capture and storage technology to reduce emissions.

Yellow, pink, and green hydrogen are produced by water electrolysis, differing only in the source of electricity. For pink hydrogen is nuclear energy, for yellow is grid electricity (with GHG emissions varying according to the sources used to power the grid) [30]. Although nuclear energy usage to produce hydrogen is not widespread around Europe, it could be relevant in countries like Russia and China. Green hydrogen is the only one produced using 100% renewable electricity [27].

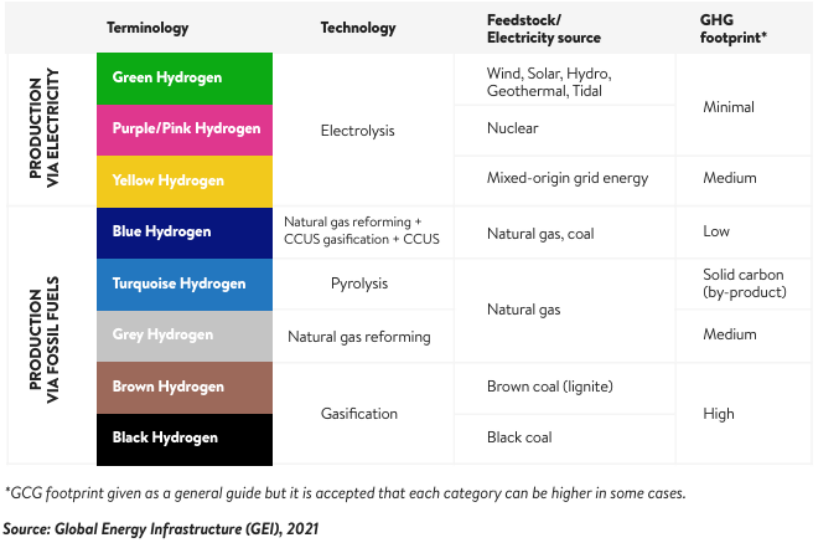

Figure 1.3 Hydrogen colour coding for various manufacturing processes. Image taken from [32].

In recent energy scenarios, green hydrogen is considered as one of the most promising solutions for a new low-emission economy [33,34]. This energy vector

represents a crucial link between sustainable energy production and various application sectors, like transportation or industry. Unlike fossil fuels, the unlimited availability of solar and renewable energy sources gives green hydrogen, a superior development potential, both in quantitative and environmental terms [35,36].

It is important to underline that, nowadays, green hydrogen represents the only truly carbon-free option for hydrogen production. Alternative technologies, such as carbon capture and storage (CCS), still face technical and infrastructural limitations. They reduce CO_2 emissions only partially, ideally by 85-95%, and are often economically and socially unsustainable [37–39]. Furthermore, CCS requires complex infrastructure for CO_2 transport and storage, is sensitive to fossil fuel prices fluctuation and may encounter social acceptance barrier. Moreover, methane leakage, linked to gas production and transportation creates an additional environmental concern, since methane has a global warming potential 86 times higher than CO_2 considering a 20-year period [30,40].

Despite its potential, large-scale development of green hydrogen technology still faces several obstacles. The most critical are prohibitive costs along the entire value chain, ranging from electrolysis to fuel cell, together with the lack of adequate infrastructure for storage and distribution, and significant-energy losses. Addressing these challenges requires a rapid expansion of renewable energy generation capacity, better management of the intermittency of these sources, and the development of advanced energy management systems to ensure continuous and reliable production. In addition, the market does not yet fully recognize the environmental benefit of reducing greenhouse gas emissions, limiting the economic incentive for green hydrogen adoption [14,39].

For these reasons, large-scale deployment of green hydrogen technologies remains both a challenge and a necessity, and understanding their cost dynamics is essential to assess their competitiveness.

The main cost driver of hydrogen production is electricity. However, the global trend of reduction of renewable electricity cost, is improving the competitiveness of green hydrogen. This dynamic opens the opportunity for a global market, where the regions reach of renewable sources could export to areas with less potential.

Trade could take place through transporting liquid hydrogen, using energy-dense chemical carriers, or the conversion of hydrogen into useful chemicals that can be easily integrated into existing industrial supply chains [41–43].

The technology used to convert water into green hydrogen is the electrolyzer.

An electrolyzer consists of two compartments, cathodic and anodic respectively, separated by a membrane or a diaphragm. Depending on the configuration, they are classified as Alkaline water electrolysis (AWE), Polymer electrolyte membrane electrolysis (PEM), and solid oxide electrolysis (SOEC). The main differences between these different technologies will be analysed in Section 1.2 [27,44].

Although this technology is well established in the chemical industry, its costs are still extremely high, compared to steam reforming, whose plants are often already operational and amortized.

Green hydrogen costs are influenced by many factors: first electrolysis' costs (assembly, operation, technology employed, capacity, and plant lifetime) [45]. In addition, the cost of electricity, which depending on location, represents the largest part of operating expenses.

Figure 1.4 compares the costs of hydrogen produced by steam methane reforming with CCS and by green hydrogen in Europe. Currently the cost of green hydrogen is about 2-3 times higher than blue hydrogen. In America it ranges between $2.18 and $6.67/kg of hydrogen, depending on plant efficiency, electrolyzer technology, and electricity source. In Europe, the cost rises, ranging between 4.13 and 9.30 €/kg of hydrogen. Grey hydrogen, from steam methane reforming, is the cheapest option, its cost is around $1/kg of hydrogen in America, and 3.76 €/kg of hydrogen in Europe, but as discussed earlier, this technology is the most impactful considering an environmental point of view. With Carbon Capture installation the cost increases, on average 4.41€/kg of hydrogen in Europe, and around $ 3.24/kg of hydrogen in America [28,46,47].

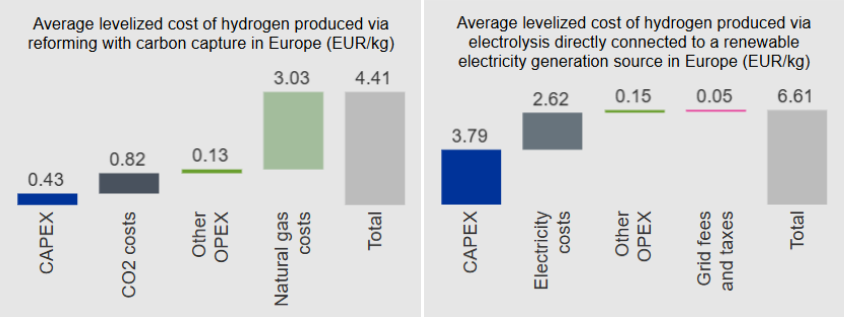

Figure 1.4 Average levelized cost in Europe for blue and green hydrogen production. Image taken from [46].

In some regions with particularly favourable conditions, the cost of production of green hydrogen is about $ 2.5/kg, like that of blue hydrogen. The final cost, as shown in Figure 1.5 depends on the operating hours of the electrolyzer plant, OPEX and CAPEX costs, and electricity prices [48,49].

When operating hours are low, for example when a plant is coupled with photovoltaic (PV) generation without storage or backup, or when curtailed electricity is used, the investment cost must be spread on a smaller output of hydrogen, so it dominates the overall cost. As the operating hours increase, however the operating costs become more relevant.

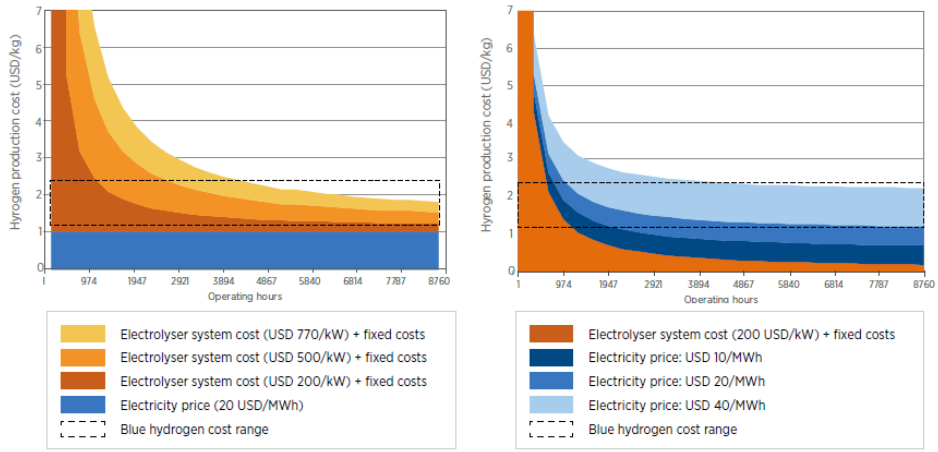

Note: Efficiency at nominal capacity is 65% (with an LHV of 51.2 kWh/kg H_2), the discount rate 8% and the stack lifetime 80 000 hours.

Based on IRENA analysis.

Figure 1.5 Hydrogen production cost as a function of investment, electricity price. Image taken from [25].

Supportive policies for solar projects, designed to reduce investment risks and guarantee stable payment, have already been implemented in countries like Brazil, Portugal, the United Arab Emirates, and the USA, achieving an electricity cost as low as USD 13.5-20/MWh [50].

The efficiency of the electrolyzer translates electricity cost to a final production cost of about 1.5 times higher. For instance, if the electricity cost is 20 USD/MWh, the corresponding hydrogen production costs would be about 31 USD/MWh, so about 1 USD/kg of H_2 [51,52].

Under ideal conditions of low-cost renewable electricity, small investment costs, and many operating hours, green hydrogen can compete with blue hydrogen. A reduction of the capital cost could be achieved considering an operating time of 3000-4000 hours, for example in that location of the world where electrolysis plants are coupled with PV or Wind power that could achieve a capacity factor of 5000 hours.

Right now, less than 0.02% of pure green hydrogen is produced by water electrolysis. Most of the projects are in the single-digit MW range, with the largest installations being a 10 MW alkaline electrolyzer in Japan and a 20 MW PEM electrolyzer in Bécancour, in Canada, operated by Air Liquide [50]. This technology is ready to be scaled up, with numerous projects to be powered by 2025 [36,53].

To make green hydrogen competitive, a significant scale-up is required, together with improvements in efficiency and lifetime, and further reductions in electricity prices [54]. To achieve these goals, it is also necessary to develop new catalysts and configurations, standardize the design of the equipment and mass production.

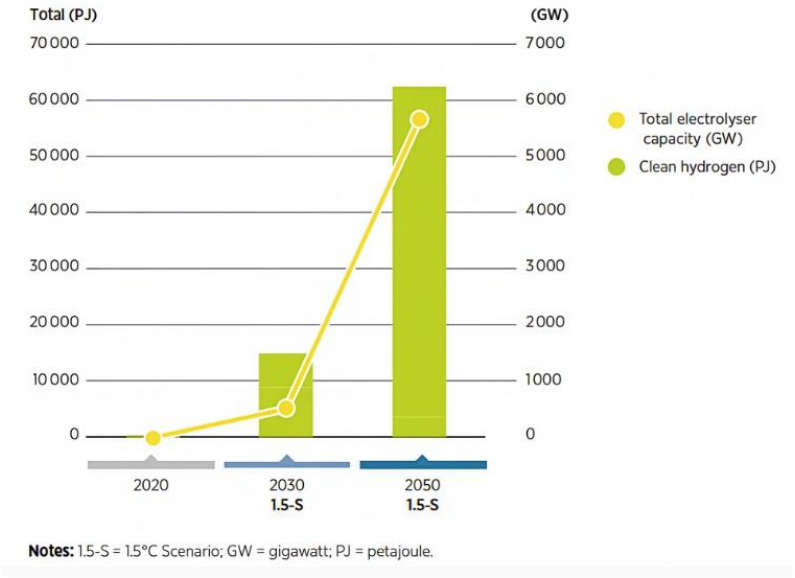

Figure 1.6 Global clean hydrogen supply in 2020, 2030 and 2050. Image taken from [10].

Looking ahead, scenarios consistent with limiting global warming to 1.5 °C assign a central role to hydrogen and its derivatives. In particular, products such as methanol and ammonia (more adapted for some applications and easier to be transported for long distances) would represent together 14% of energy consumption by 2050, while their contribution is negligible in the global actual energy mix.

According to IRENA's 1.5 °C scenarios, green and blue hydrogen production must grow from today's negligible levels to about 15 EJ (125 Mt) by 2030 and 63 EJ (523 Mt) by 2050, as shown in Figure 1.6. In the long term period green hydrogen is expected to become dominant, from 40% of total hydrogen production in 2030 to 94% in 2050. To achieve this goal electrolyzer capacity for green hydrogen must grow from 428 GW by 2030 to 5722 GW by 2050 [31].

In the earlier decades, hydrogen was primarily seen as a means to diversify energy supply and improve energy security, especially during oil supply disruption. In recent years, the interest has shifted to other sectors, driven by the objective of achieving net-zero emissions. As a result, a lot of hydrogen policies to support fuel cell vehicles and the development of refueling stations were born [55]. A change is expected in the next years, because greater attention is given to sectors where hydrogen is already used, using green hydrogen instead of fossil-based hydrogen [56,57].

This shift in focus highlights the need for coherent and integrated policy support to ensure that hydrogen can expand across different end-use sectors. Key elements of this approach are: the development of national hydrogen strategies that integrate relevant elements together, establishing a long-term vision shared with industry, the identification of policy priorities for sectors where hydrogen could add the most

value according to national conditions, and the implementation of governance systems and enabling policies that remove barriers and facilitate market expansion. [10,58].

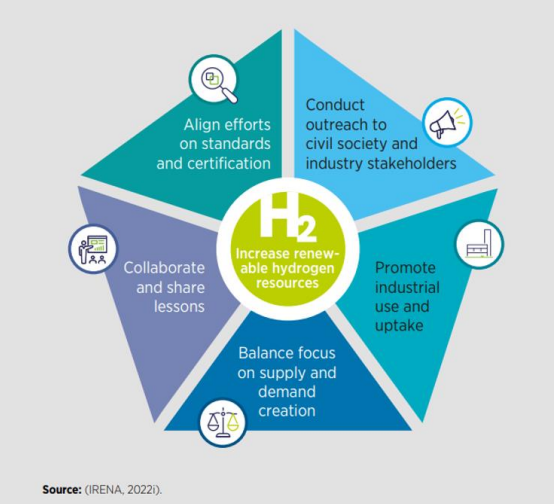

Figure 1.7 Recommendations for G7 members. Image taken from [10].

So, to respect the achievement of the Paris Agreement to get net zero emissions, in the last years numerous countries have adopted hydrogen policies and strategies aimed at both production and utilization. Among these strategies is crucial to talk about hydrogen colour, some of them are focused on green hydrogen, others in blue or grey, while more in a mixture of them.

In the long term there is widespread support on green hydrogen strategies, as it is considered as the only truly sustainable solution. In the short-term, however, blue hydrogen is seen as transitional solution, enabling faster decarbonization through established technologies [59,60].

The scale of these policies is also different, ranging from the absence of national targets to extremely ambitious strategies with electrolyzer and hydrogen production goals.

Several countries around the world announced their strategy, which in many cases represent the outcome of decades of investment in research and development and energy application since the 1970s, (Figure 1.8).

These results have been obtained through collaborations, which produced vision documents and roadmaps, setting the next steps of concrete policies in a long-term perspective. To be effective, these strategies must be followed by impact assessments, policy design, financial feasibility, and implementation. In the last few years, many countries have made lots of efforts to achieve these goals, but most of them are still under development rather than fully implemented. In Europe, for example, it is common to set capacity targets for electrolysis, while the policy instruments still need to be developed.

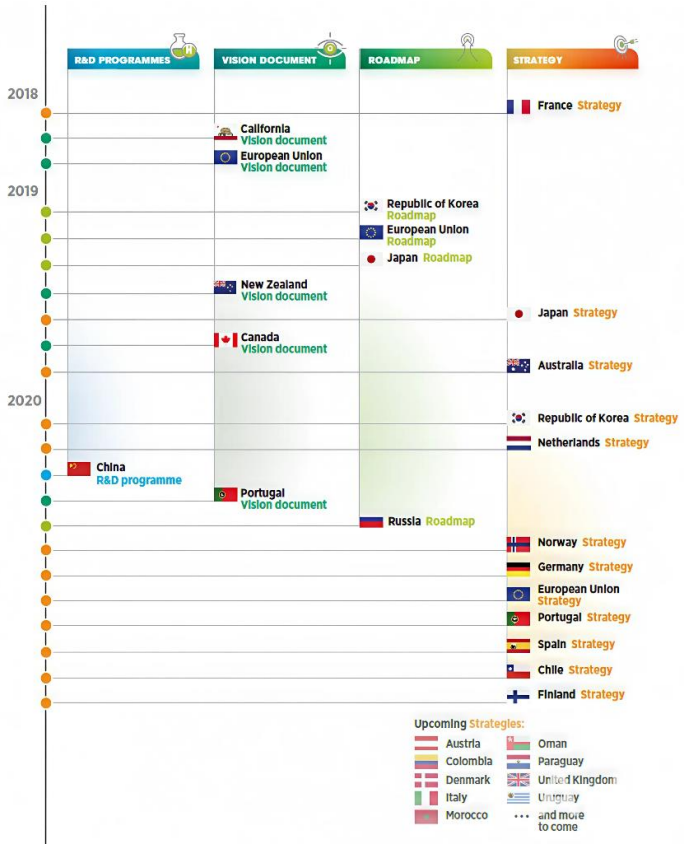

Figure 1.8 Recent hydrogen policies and strategies. Image taken from [25].

Among the most ambitious goals for hydrogen production cost reduction, there are those of Australia and Chile. Australia would like to bring hydrogen production costs under 2 AUD/kg of H_2, supported by important state funding of $14 billion, while Chile has set a target of 1.5 USD/kg by 2030.

Also emerging economies like Brazil, India and South Africa are going on with hydrogen strategies. Brazil is investing in low carbon emission technologies, while India would like to produce 5 million tons (Mt) of hydrogen by 2030.

Japan and South Korea are integrating hydrogen in many sectors, as electric energy production, heating, and transport, with investment of about $18.2 billion in Japan and $16.26 billion in Korea. The US aims to reduce green hydrogen cost to 2 $/kg by 2030, to enhance domestic and commercial demand [61].

Within this global context, the European Union (EU) promotes the most ambitious strategy, accounting for 85% of globally anticipated projects [44]. EU sets a target of 40 GW of electrolysis capacity by 2030, supported by national policies from France, Germany, Netherlands, Portugal, and Spain, aiming to get 6.5 GW, 5.0 GW, 3.0-4.0 GW target, respectively. In Figure 1.9, it is possible to see how this capacity will be shared between the different members. The EU also aims to get a production volume of 10 million tonnes of hydrogen per year (MtH2 /year) by aiming for 40 GW of electrolysis capacity also in neighbouring countries (North Africa) by 2030 [61].

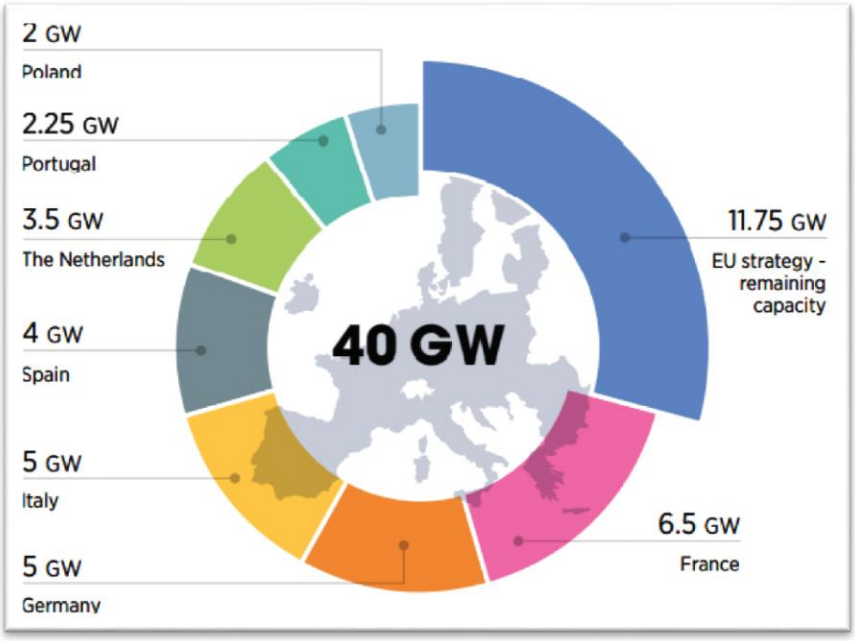

Figure 1.9 Electrolyzer capacity targets in European hydrogen strategies, 2030. Image taken from [26].

EU is developing a series of policies to promote hydrogen as key vector in energy transition and to reinforce energy security, a process accelerated by the crisis derived by Ukraine war. Among the most relevant initiative there are REPowerEU, which aims to reduce the dependence from Russian fuels by 2027, enhancing the domestic hydrogen production, the diversification of energetic sources and the building of new infrastructure. In parallel, the Fit for 55 plans introduce the requirement of development of refueling station along the net, and the use of almost 40% of renewable energy in the energy mix by 2030. It establishes also the creation of an internal market for gases and renewable hydrogen coordinated by an European network of operators [62,63].

Furthermore, to promote innovation technology, EU approved IPCEI Hy ("Important Project of Common European Interest"). This project involves 99 companies, from 16 states members, promoting the development of innovative technologies for hydrogen value chain, boosting the decarbonization of mobility and industrial sectors. This project includes up to €18.9 billion State aid which is expected to unlock more than €27.1 billion of additional private investment [64].

Despite the efforts undertaken, more ambitious actions need to be made to make green hydrogen a really key component of energy transition. In particular, the substitution of 7.9 Tons of fossil hydrogen by green hydrogen, that is nowadays used in industrial processes in Europe, requires a huge expansion of electrolytic capacity, of 79 GW, 300 times higher than the currently installed capacity. In Figure 1.10 it is possible to see Europe's water electrolysis projects to get 88 GW_{el} power by 2030 [65]. However, to get this transformation, there is a need for specific national targets for industrial investment and coordinated international efforts to reduce green hydrogen cost and share technological know-how between countries. It will also be essential to increase investment in the manufacturing capacity of

renewable power generation, without which large-scale hydrogen production will not be feasible.

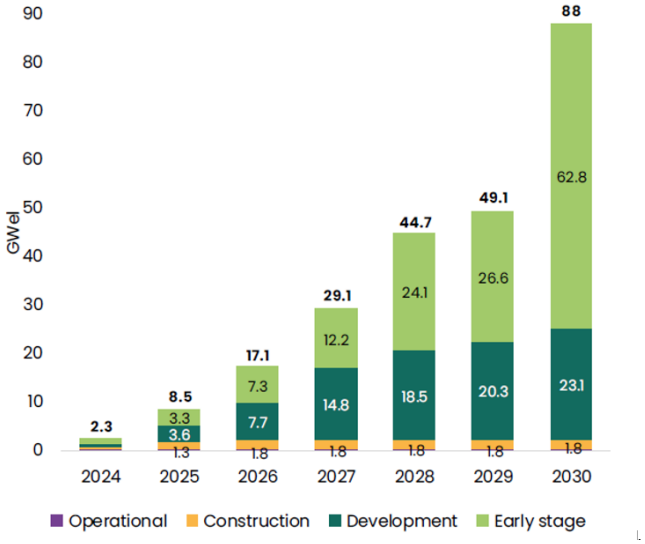

Figure 1.10 Cumulative operational and planned water electrolysis projects in Europe by the year 2024 -2030 in GW_{el}. Image taken from [65].

A further challenge is that green hydrogen is still not competitive under current free-market conditions The current production costs are very high, and there is also a lack of transport and storage infrastructure [66]. In addition, the production of electrolyzers relies on critical raw materials such as platinum and iridium**.** These elements are scarce, energy-intensive to extract, and have a high environmental footprint, but they are also crucial to ensure long-term operation under low overpotential conditions [21]. Figure 1.11 illustrates the global warming potential and cumulative energy demand associated with such materials.

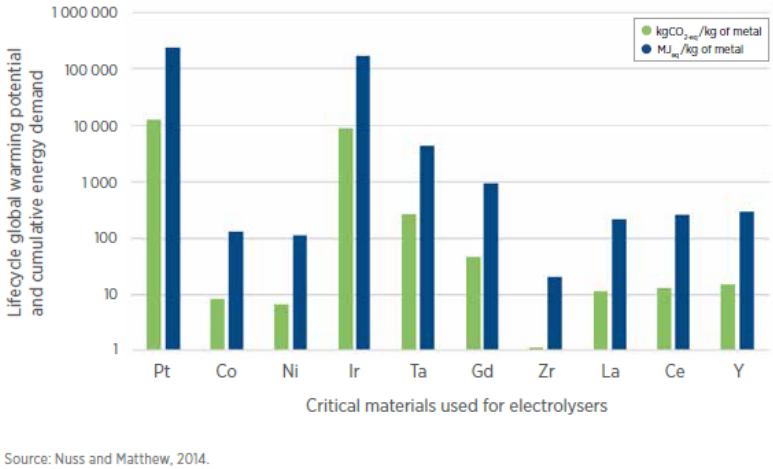

Figure 1.11 Global warming potential and cumulative energy demand for critical materials. Image taken from [25].

To face these challenges, it is necessary a reduction of electrolysis facility cost by 40% in the short term and by 80% in the long term [25]. Despite in the past 10 years, electrolyzer's costs have declined more than 50%, further progress is

fundamental. According to IEA and Hydrogen council, production costs of green hydrogen are going to decrease, depending on the scenario and market conditions, between 30% and 70% [67]. This path is supported by a steadily decreasing production cost of green renewable energy and public interest for clean energy sources [24]. In combination with that, hydrogen-based fuel cells are becoming cheaper, more durable, and secure, expanding hydrogen applications in a zero-emission transport sector, in industry or energy supply security in remote areas [68]. Their evolution is fundamental to guarantee efficiency and flexibility of an energetic system based on low emissions vectors.

In conclusion, the development of a hydrogen-based economy requires a coherent mix of industrial policies, public and private funding, technology innovation, and international cooperation. Only in that way would it be possible to overcome the economical and structural barriers, making hydrogen a foundation of climate neutrality by 2050.

1.2 Water electrolysis

1.2.1 Principle of water electrolysis

The key process, for green hydrogen production is water electrolysis, i.e. an electrochemical process in which electrical energy is used for the splitting of water in hydrogen and oxygen [69].

An electrolyzer consists of two electrodes, immersed in an electrolyte, separated by a diaphragm or a membrane, and connected to an external generator. The electrodes must be made with materials with a high corrosion resistance, good electrical conductivity, effective electrocatalytic activity, and a solid and long-term mechanical stability. The electrolyte must be chemically stable during electrolysis process, avoiding reactions with the electrodes, which would cause alteration or contamination. It is necessary also to use a separator between the two compartments, to prevent the recombination of hydrogen and oxygen. It must avoid short-circuits, thanks to its electrical resistance, but at the same time it should provide a good ion conductivity, and must remain chemically and physically stable over time [70].

The overall reaction occurring is:

$$H_2O(l) \rightarrow H_2(g) + \frac{1}{2}O_2(g) \qquad \text{Eq. 1.1}$$

During electrolysis process, hydrogen evolution reaction (HER) takes place at the cathode, according to the following reactions:

Acid environment:

$$2H^+ + 2e^- \rightarrow H_2 \qquad \text{Eq. 1.2}$$

Alkaline environment:

$$2H_2O + 2e^- \rightarrow H_2 + 2OH^- \qquad \text{Eq. 1.3}$$

At the positive charged anode oxygen is formed, by water oxidation:

Acid environment:

$$H_2O \rightarrow \frac{1}{2}O_2 + 2e^- + 2H^+$$ Eq. 1.4

Alkaline environment:

$$2OH^- \rightarrow \frac{1}{2}O_2 + H_2O + 2e^-$$ Eq. 1.5

Thermodynamics plays a key role in this process because it determines the energy requirements of the process [71,72]. Electrolysis is an endothermic (ΔH >0), and non-spontaneous process (ΔG >0), so it needs energy from the external source to occur. At constant temperature and pressure, the required energy, corresponds to the enthalpy change ΔH >0, which is partly supplied as electrical energy (ΔG) and partly as heat (Q = TΔS):

$$\Delta H = \Delta G + T\Delta S$$ Eq.1.6

The energy consumption of the process, and so the cell voltage, depends strongly on temperature. In Figure 1.12 it is possible to notice the variation of the process energy consumption at standard pressure for temperature range from 298 K to 1273 K (from 25 °C to 1000 °C). As temperature increases, the electrical energy requirement ΔG decreases with temperature, while the thermal demand TΔS increases [70]. At high temperatures the electric energy consumption is very low, for that reason high-temperature electrolysis has such a great potential.

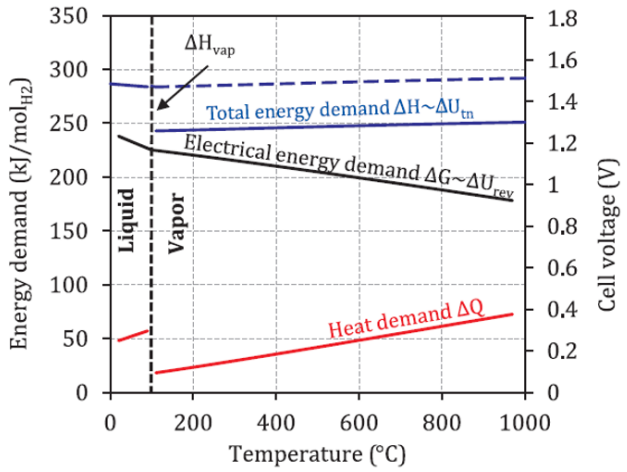

Figure 1.12 Total (ΔH), thermal (Q) and electrical (ΔG) energy demand of an ideal electrolysis. Image taken from [73].

The reversible Equilibrium cell voltage, or electromotive force, E_{eq}, is the minimum required voltage and, at the standard condition (P = 1 atm, T = 25 °C), it is expressed as:

$$E_{eq}^0 = -\frac{\Delta G^\circ}{z}$$ Eq. 1.7

Where:

- ΔG° is the change in Gibbs free energy under standard conditions.
- z is the number of electrons transferred per mole of hydrogen (z = 2).
- F is the Faraday constant, representing the charge of a mole of electrons (96485 C/mol).

At standard conditions ΔG°=237.21 kJ/mol, and E°=1.229 V.

Under non-standard conditions, E_{eq} can be calculated defined by Nernst Equation [74,75]:

$$E_{eq}[V] = E°_{eq} + \frac{RT}{zF}\ln\left(\frac{P_{H_2}\cdot\sqrt{P_{O_2}}}{a_{H_2O}}\right) \quad \text{Eq. 1.8}$$

Where:

- R is the absolute gas constant (8.314 J/(K*mol)),
- p_{O2} and p_{H2} are products' partial pressure,
- a_{H2O} is water activity.

When a direct current (DC) is supplied to the cell, the cell voltage E_{cell} is higher than $E_{eq.}$ This is caused by cell irreversibility and overvoltage, which generate energy losses.

$$E_{cell} = E_{eq} + E_{ohm} + E_{act} + E_{conc} \quad \text{Eq. 1.9}$$

Where:

- E_{ohm} is an overvoltage caused by all the ohmic contribution of the cell, first the electrolyte, and the separator, but also all the electrodes, current collectors, interconnections. This contribution is proportional to the electric current flowing through the cell,
- The term $E_{conc,}$ known as concentration overvoltage, is caused by mass transport phenomena inside the cell, reducing reactant concentration at the electrodes or H_2 and O_2 accumulation at the reaction sites,
- E_{act} represents the activation overvoltage; related to the energy barrier for electrode reactions, usually described by the Tafel equation. Anodic activation losses are generally higher than cathodic [76,77].

By varying current density, the contribution of every overvoltage became predominant with respect to the others, as it is possible to see from Figure 1.13. At low current density, the relationship between the cell voltage and the current is logarithmic, while it becomes linear as the current increases. At the beginning of the curve, activation phenomena are predominant, while for high currents, ohmic and, to a lesser extent, concentration phenomena, start to become important [78].

Commercial electrolyzers usually do not work with high current density, reaching the concentration overpotential zone, to prevent excessive cell degradation and efficiency losses. Also, it is possible to see that the curve at high temperature is lower than that at 25 °C since electric work is compensated for by heat energy.

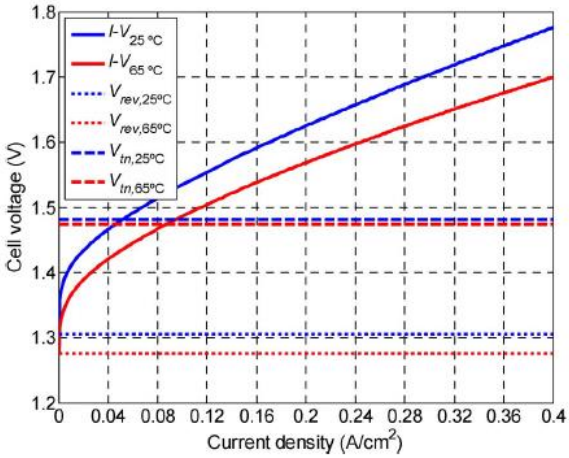

Figure 1.13 I–V characteristic curves of an alkaline electrolysis cell for temperatures of 25 °C and 65 °C at 20 bar. Image taken from [70].

Hydrogen molar rate produced by the cell $\dot{n_{H_2}}$, is proportional to the electric current, according to Faraday law [79]:

$$\dot{n_{H_2}}\left(\frac{mol}{s}\right) = \eta_{far}\,\frac{I}{2 \cdot F} \qquad \text{Eq. 1.10}$$

Where, η_{far} is Faradaic efficiency [70], representing the ratio between the theoretical electrical current to make electrolysis process happen, and the electric current flowing inside the cell. So, it is a parameter giving information about the fraction of current that is dispersed or involved in parasitic reactions.

$$\eta_{far} = \frac{I_{th}}{I} \qquad \text{Eq 1.11}$$

The overall efficiency is defined as the ratio of energetic content of produced hydrogen and the total energy used to make electrolysis happen. The first term could be the Lower Heating Value (LHV) or the Higher Heating Value (HHV), according to the application [73].

$$\eta_{tot_{HHV}} = \frac{\dot{V_{H_2}} \cdot (HHV)_{H_2}}{n_c \cdot E_{cell}} \qquad \text{Eq. 1.12}$$

$$\eta_{tot_{LHV}} = \frac{\dot{V_{H_2}} \cdot (LHV)_{H_2}}{n_c \cdot E_{cell}} \qquad \text{Eq. 1.13}$$

Where:

- $\dot{V_{H_2}}$ is the hydrogen volumetric flow rate, expressed in Nm^3/h.
- HHV is hydrogen Higher Heating Value, expressed on a volumetric basis.
- LHV is hydrogen Lower Heating Value, expressed on a volumetric basis.
- n_c is the number of electrolytic cells constituting the electrolyzer.
- E is the cell's electric potential.
- I is the electric current flowing through every cell.

1.2.2 Electrolysis technologies

Several electrolysis technologies exist. Below is a summary of the main types, with a higher focus on alkaline electrolyzers, which are the most widespread and market-mature option, as well as the focus of this thesis.

Temperature and pH are the two parameters that allow us to classify electrolyzer type. As water is not a good ionic conductor, due to its high resistivity, it could not be used in its pure form in an electrolyzer. Therefore, to enhance ionic conductivity, an electrolyte must be added to the system; it could be an acid, salt, or a basis.

Despite their differences, all the electrolyzers have the same basic architecture, made of two electrodes, an electrolyte, and a separator.

Also, temperature plays a key role as was seen in the previous paragraph, because raising it lowers the system's energy demand [25].

Based on these parameters, electrolyzers can be divided in two categories:

1. **Low temperature electrolyzers** (LTE):
   - Alkaline (AWE)
   - Anion exchange membrane (AEMWE)
   - Proton exchange membrane (PEM)
2. **High temperature electrolyzers** (HTE):

- Solid oxide electrolysis cells (SOEC)

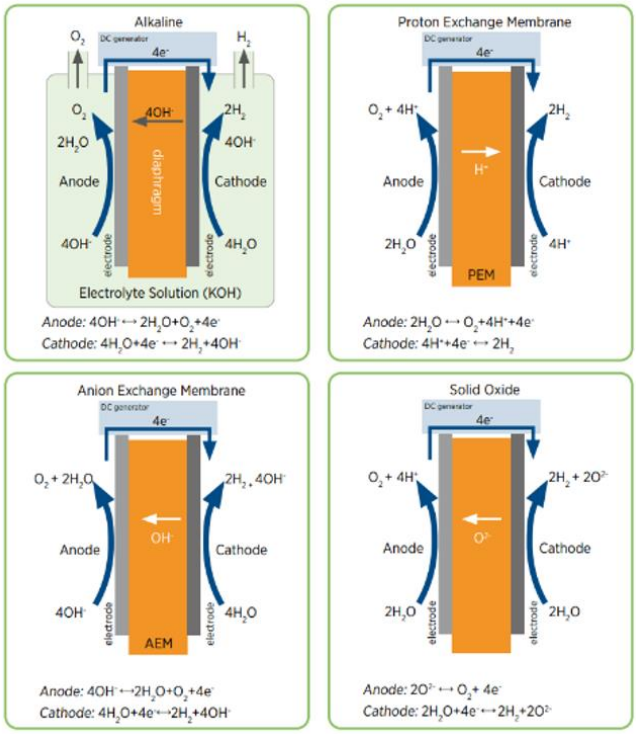

Figure 1.14 Different types of commercial water electrolysis technologies. Image taken from [80].

There are two configurations for common electrolytic cell:

1. The ‘Gap cell’ is a configuration in which the electrodes and the membrane are separated by a finite distance (micrometres to millimetres). Smaller gaps reduce ionic resistance but risk excessive gas accumulation in the narrow volume; an optimal distance depends on current density and operating conditions.
2. In the ‘Zero-gap cell’ configuration there is no space between the electrode and the membrane, so the electrolyte is contained within it. The electrodes must be porous to be used in this cell. It is possible to get a higher current density with a less significant increase in cell potential. The zero-gap configuration is the most used today for commercial electrolyzers [74].

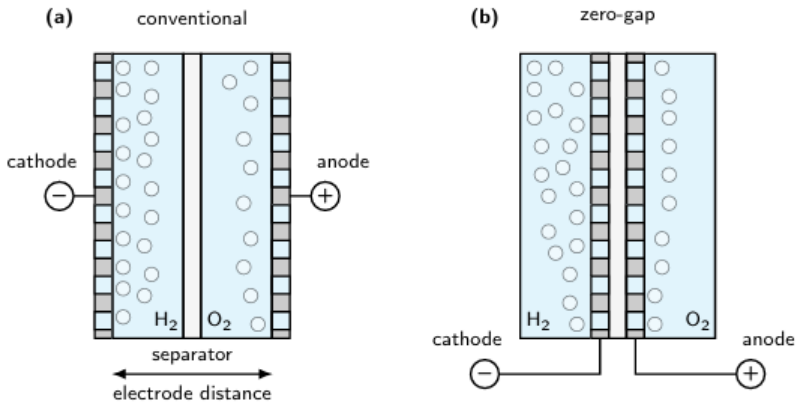

Figure 1.15 Gap cell and zero-gap configuration of electrolysis cell. Image taken from [81].

A single electrolysis cell can produce only a small amount of hydrogen; therefore, to increase production, multiple cells are combined to form an electrolyzer stack. Two possible configurations exist, depending on the electrical connection as shown in Figure 1.16 [81].

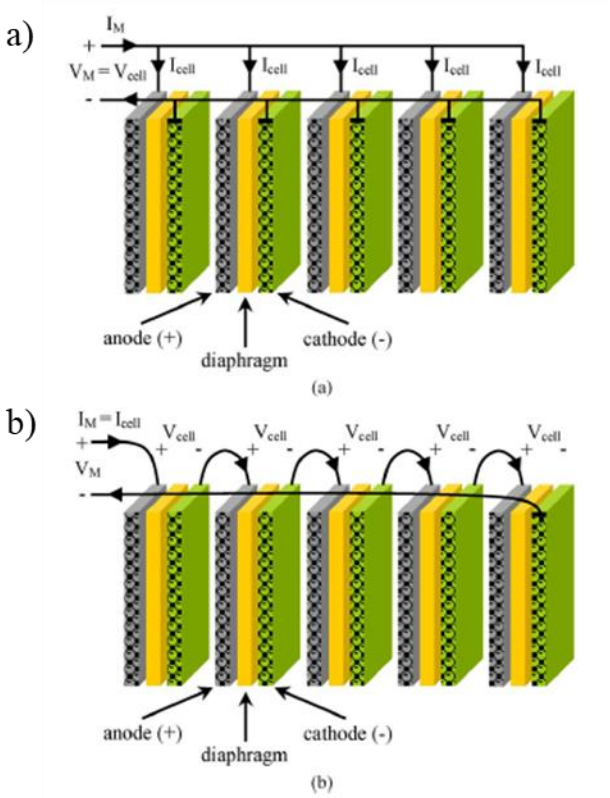

Figure 1.16 Configuration of an electrolysis module: (a) unipolar module b) bipolar module. Image taken from [70].

- In the monopolar configuration, the cells are connected in parallel. The supply voltage is equal to that of a single cell, and the total current is the sum of the current circulating on a single cell. This arrangement requires more space, but in case of failure of a single cell, it can be easily removed and replaced, without the need to shut down the entire system.
- The bipolar configuration, the commercial standard. The cells are connected in series, so the supply voltage is the sum of the voltage of the single cells. The cathode of a cell is connected to the anode of the next, but each electrode has both polarities.

Because monopolar systems require many external connections, they suffer additional losses and non-uniform current distribution when cell resistances differ. Typical figures [81]:

Monopolar: low supply voltage,1.9–2.5 V, but very high stack currents for the same H_2 rate.

Bipolar: per-cell voltages 1.7–1.9 V; for a given H_2 rate, lower current flows than in monopolar stacks.

PROTON EXCHANGE MEMBRANE ELECTROLYSIS

The first water electrolyzer characterized by a solid polymer electrolyte was developed by General Electric® in the 1960s, when a solid sulfonated polystyrene

membrane was used as the electrolyte [82]. In this type of electrolyzer a solid membrane is employed to separate the cathodic and anodic half-cells that are immersed in deionized water. The membrane allows the transport of H^+ ions generated at the anode. The two half reactions that happen inside the cell are Eq. 1.2 and 1.4.

The oxygen evolution reaction takes place at the anode, releasing H^+ ions, that get to the cathode, to be reduced, by passing through the polymeric ion-exchange membrane, while the electrons flow through the external circuit. For PEM, the bipolar configuration is the most spread.

The materials that are usually employed for the electrolyte membrane are Nafion® or Fumapem®, which are characterized by high proton conductivity and exceptionally good gas impermeability [73,82]. PEM electrolyzers can operate at high current density, more than 2 A cm^{-2}, thanks to the thickness of the membrane, reducing OPEX.

The presence of a solid electrolyte makes it is possible to build a compact and mechanically robust electrolyzer, which can operate at high pressure (up to 35 bar), with the same pressure, or a differential in both compartments. In the case of differential configuration, the pressurized half-cell is the cathodic one, to avoid the risk of handling pressurized oxygen, and to prevent the titanium autoignition in oxygen-rich environments. In this way it is possible to produce pressurized hydrogen, without downstream compression for processes like ammonia/methanol. Drawbacks of high-pressure operation include increased gas crossover, necessitating thicker membranes and to keep H_2 concentrations in O_2 below the safety threshold (3.8% vol.). PEM electrolyzers usually work up to 35 bars. The operating temperature is usually below 80 °C, due to the presence of the polymeric membrane. The purity of produced hydrogen is higher than in AWE electrolysis, typically above 99.99 vol.% (in some cases up to 99.999 vol.%) without the need of auxiliary equipment [74].

Since these cells work in a very corrosive environment, and under a high applied cell voltage (2 V), the materials that are used for the membranes, catalysts, separator plates and current collectors are rare and expensive. Oxygen evolution catalysts are usually made of RuO_2 or IrO_2, while Platinum is the material used for the hydrogen evolution reaction. Separator plates and current collectors are usually made of titanium. Despite that, their lifetime is low if compared with AWE technology [82,83].

Cell efficiency is about 50-60%, like alkaline technology. Their major strength is their operation flexibility; in fact, they can work on the entire nominal power range since there is no problem with gas permeability, with very fast response time. This makes this technology very suitable to be used coupled with fluctuating renewable sources [73].

The main issue related to PEM electrolysis is the high capital cost of the system (1400-2100 €/kWh) if compared with AWE technology, due to the material cost and membrane life (60-100000 h) [73].

PEM electrolyzers are commercially available for low-scale production plants. The maximum hydrogen output is in the order of 30 Nm^3/h with a power

consumption of 174 kW. There are only a few companies manufacturing this kind of technology [84,85][86][87]. Development perspective aims a reduction of costs thanks to economies of scale, new compact stack designs, and above all, the reduction of noble metal loading per cell.

ALKALINE WATER ELECTROLYSIS

Alkaline electrolysis is a mature technology, applied to hydrogen large scale production since the early 20th century [88].

The cell of an AWE electrolyzer consists of two electrodes immersed in an aqueous electrolytic solution, where a porous diaphragm acts as a separator between cathodic and anodic compartments, allowing ionic conduction, while remaining impermeable to gases.

At the electrodes, the semi-reactions number 1.3 and 1.5 take place, contributing to the overall water splitting.

Maintaining similar pressure on both sides preserves diaphragm integrity and prevents H_2 ingress into the anode compartment. The operating temperature of AWE electrolysis, as for LTE technologies, ranges between 60 °C and 80 °C. While the operating pressure is usually in the range of 1 bar and 30 bar. AWE operate at moderate current densities (~ 0.2 – 0.45 A/cm²), lower than the current that is possible to achieve with membrane-based technologies [73].

As said, water is not a good ionic conductor, so it is necessary to use an electrolyte, that consists in an aqueous solution of Potassium Hydroxide, KOH, or Sodium Hydroxide, NaOH, dissociated into K^+, OH^- and Na^+, OH^-, respectively. They offer high conductivity while being less corrosive than acids, allowing non-precious electrode materials with low overpotentials. The solution's conductivity must be the highest possible at the operating temperature of the cell.

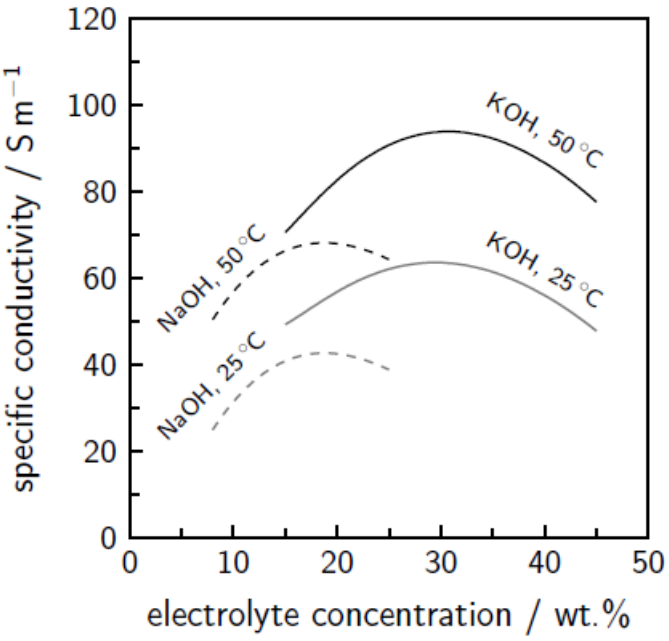

Figure 1.17 Specific electrolyte conductivity as a function of the electrolyte concentrations. Image taken from [81].

As it is possible to notice from the Figure 1.17, in the operating temperature range, the optimal mass concentration of NaOH is about 22%, with an average conductivity of 1 $\Omega^{-1}cm^{-1}$, while for KOH the optimal value is about 30%, with an average conductivity of 1.25 $\Omega^{-1}cm^{-1}$. So ohmic overvoltage is lower in the case KOH solution is used, while activation overvoltage does not depend on nature and concentration of the electrolyte. Also, it is important to notice that the corrosive effect of NaOH is slightly higher than that of KOH, on the electrodes, therefore KOH use is most common [81,89]. In the case of alkaline electrolysis, electrodes are usually made of Nichel (Ni), Cobalt (Co), and Molybdenum (Mo). Despite the electrode itself acts as a catalyst, it is usually covered by a more active cover, to promote charge transfer, reducing reactions' activation energy. The cathode coating is usually made of Nichel, in alloy with other metals (Mo, Zn, Fe, Cr, Co) or with metal oxide (MoO_2, MoO_3, CeO_2, IrO_2, RuO_2). The anode is usually made of Nichel or cobalt. Iron addition improves oxygen evolution efficiency, helping to reduce the activation overvoltage [69].

Electrodes morphology affects the ohmic resistance of the electrolytic cell, because the evolution of the gaseous products from the electrodes could lead to significant overvoltage concentration, reducing the electrolysis efficiency [90]. Designs that increase wetted area and promote bubble removal, like meshes, screens, foams, improve performance.

The separator's function is to divide the electrolytic cell into two parts: one cathodic and one anodic, allowing the transfer of ions. It must be stable under the electrolyzer's operating conditions, immersed in an alkaline solution, and withstand very oxidizing conditions at the anode, and highly reducing conditions at the cathode. In the past, asbestos diaphragms were used, but due to their toxicity, today they have been substituted by composite materials based on microporous polymers or ceramic materials [74].

Between the drawbacks of the use of this technology there is low current density, the use of corrosive electrolytes, and a lower purity of products (99.5% vol-99.9% vol) [91], if compared to PEM technologies. The contamination could be caused by a gas crossover to the diaphragm. Although hydrogen tends to diffuse toward the oxygen side more easily, oxygen can also diffuse toward the hydrogen side. Therefore, when a higher product purity is required than what the electrolyzer can provide, an additional purification stage is necessary. Under low current conditions, the rate of production of hydrogen and oxygen decreases, while the gas permeability is constant. This could lead to dangerously high hydrogen concentrations in the anodic compartment, so it is better off not operating at extremely low loads. To avoid the formation of explosive mixtures (the upper safety limit is set at 3.8% mol H_2 at atmospheric pressure and 80°C) [92] , since hydrogen diffusion increases exponentially with the decreasing of current density, it is better to work in a range between 20% and 100% of the electrolyzer's nominal power [93–95].

The technological maturity of AWE electrolysis, together with its proven durability, availability, and low specific costs, are the main advantages that make it the most widely used technology on an industrial scale. The overall yield of these systems is in the range of 50% to 60%, with specific energy consumption between 50 and 60 kWh/kg_{H_2} [95]. From an economic point of view, AWE technology is characterized by the lowest specific investment costs (in the range of €800–1500 per installed kW) and low maintenance costs (2–3% of capital annually), thanks to the absence of noble metal catalysts and the use of relatively inexpensive materials [73].

These electrolyzers are the most effective for large-scale hydrogen production. Some manufacturers fabricate units with high production capacities in the 500–760–Nm^3/h range, corresponding to electric power consumptions of about 2150–3534 kW [70].

A new developing technology is alkaline electrolysis with a solid polymer electrolyte, AEMWE electrolysis. It puts together the advantages of PEM and AWE electrolysis. Unlike PEMs, AEMs (anion exchange membranes) are permeable to OH^- ions (hydroxide ions) instead of protons. In this configuration, KOH solution is typically fed to the anode, where it is oxidized forming O_2, and OH^-; these anions can migrate through the membrane to the cathode, where water is reduced generating H_2. In contrast to PEM, anionic membranes are not conductive by themselves, so there is a need to use a small amount of KOH solution to make them wet.

The AEMWE cell reminds a PEM, electrodes are installed on the membrane surface, allowing for more compact configurations, and reducing the ohmic drop. In this way it is possible to get higher current density, and better electrolysis' efficiency, producing high purity gases [96,97]. Some examples of AEMs are: Zirfon®, a porous composite composed of a polysulfone matrix and ZrO_2 [98,99], Ryton ® [100,101], a membrane made of polyphenyl sulfide, and the most used PiperION®, a high-performance anion exchange membrane based on a poly(aryl piperidinium) backbone [102,103]. Thanks to the alkaline environment within the AEMWE cell, it is possible to use non-precious catalysts and materials, drastically reducing the cost, and also dependency on critical materials (no platinum, no iridium, no fluorinated membranes). AEMWEs have key advantages respect to classical AWE electrolysis: they operate at higher current densities thanks to the lower ohmic resistance and consequently have a smaller volumetric footprint. Furthermore, it is possible to produce pressurized hydrogen, thus facilitating its subsequent storage, distribution, and final utilization; because thanks to the presence of the polymeric membrane, the safety of the system is significantly improved [96]. This technology presents the greatest potential for future improvement, emerging as the optimal solution for green hydrogen production, having together the robustness and low cost of alkaline systems with the purity and operational flexibility of PEM technology.

SOLID OXIDE WATER ELECTROLYSIS

Solid oxide water electrolysis (SOEC) is an advanced concept which consists of water, or rather, steam electrolysis at high temperatures (600 °C- 900 °C). At the cathode, water is fed in the form of steam, that is reduced, producing H_2 and O^{2-}. These ions migrate to the anode through a ceramic separator, where they are oxidized forming O_2 [104]. The semi reactions are:

At the cathode: $H_2O + 2e^- \rightarrow H_2 + O^{2-}$ Eq. 1.14

At the anode: $O^{2-} \rightarrow \frac{1}{2}O_2 + 2e^-$ Eq. 1.15

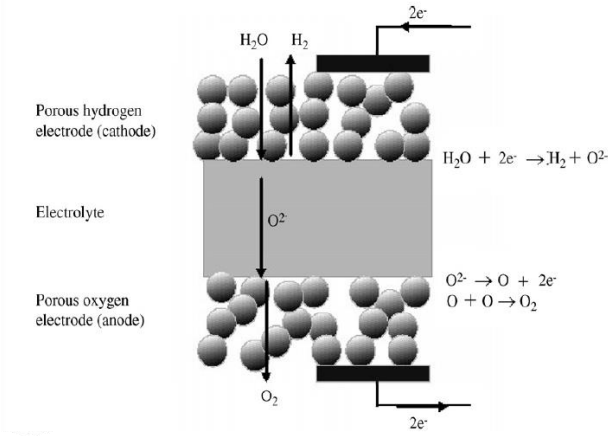

Figure 1.18 Operating mechanisms of solid oxide cells. Image taken from [105].

The reactions evolve with the electrodes in contact with a gas or vapor phase, so it is essential to maximize the interface between the electrodes and gaseous reactants. Furthermore, since the cell must withstand temperatures between 600 °C and 800 °C, the materials are usually ceramics. The electrodes consist of a porous ceramic composite material, characterized by a pore size suitable to form conductive networks for electron transfer and, at the same time, supporting the mass transport of oxygen, hydrogen, and steam. The electrolyte must exhibit low electronic conductivity, good ionic conductivity, and must be chemically stable at these elevated temperatures. It is usually made of a mixed oxide based on zirconium oxide stabilized with yttrium oxide, known as YSZ (yttria-stabilized zirconia), and acts as a ceramic membrane, with a thickness as low as possible, to reduce ohmic overpotential. O^{2-} ion transport occurs through its crystalline structure thanks to a mechanism that involves the oxygen vacancies present in the mixed oxide lattice [100]. The cathode consists of a cermet usually of nickel and YSZ, while the anode is commonly a composite of YSZ and perovskites such as lanthanum manganite ($LaMnO_3$), ferrites ($LaFeO_3$) or cobaltite ($LaCoO_3$) [106,107].

High temperature electrolysis requires less electrical energy than low temperature technologies because a significant amount of energy is supplied from heat. Going from 25 °C to 1000 °C, the electromotive force E_{rev} decreases from 1.23 to 0.91 V. As a result, theoretically up to 40.1% of the energy required to

produce hydrogen from steam electrolysis can be supplied as heat at that temperature [104]. Since the electrical efficiency is really high, the SOEC cell can convert nearly 100% of the input electrical energy into H_2 [73]. Although SOEC electrolyzers are very efficient, they are not technologically mature compared to low temperature technologies. Even without precious metals, the extreme temperatures demand costly materials and complex fabrication. The components of a cell can be characterized by different thermal expansion coefficients, so frequent on/off cycles can potentially damage the contact surfaces between electrodes and the electrolyte. Also, at the cathode-side nickel electrodes suffer deactivation, caused by hardening and gradual agglomeration and reoxidation during electrolysis. Furthermore, to enhance conductivity every component of the cell must be as thin as possible, so the stack is very fragile, and its assembly is really challenging. Also, the stream leaving the cathode is a mixture of hydrogen and steam that needs to be further processed, resulting in extremely high capital costs of SOECs compared to low temperature technologies [104].

Finally, since there is a need for a continuous heat source, the use of SOEC technology can be advantageous, in situations in which a large amount of waste heat is available, or in regions, reach renewable sources such as geothermal energy [83,108].

So, SOEC electrolysis is a promising technology in terms of energy efficiency and operating potential, but the materials, components, and systems must be optimized before it can achieve the technological maturity of AWE and PEM electrolysis.

Comparison between different technologies

In Table 1.1 it is possible to see a final comparison among the analysed technologies.

Table 1.1 Comparison among different electrolysis technologies [73,74].

Feature	Alkaline Electrolysis (AWE)	PEM Electrolysis (PEM)	Anion Exchange Membrane (AEMWE)	Solid Oxide Electrolysis (SOEC)
Current density range	0.25–0.45 A/cm²	1–2 A/cm² (and beyond)	0.2–1 A/cm² (still improving)	0.3–1 A/cm²
Electrical efficiency	55–75%	60–70% (like AWE)	55–70% (promising, close to PEM)	>100% (LHV basis)
Operating temperature	25–120 °C	50–80 °C	30–90 °C	700–1000 °C
Electrolyte / membrane	Aqueous KOH	Perfluorosulfonic acid	Anion-exchange polymer membrane	Ceramic oxide
Catalysts	Non-critical metals (Ni, Co, Fe oxides)	Noble metals (Pt, Ir)	Non-precious metals (Ni, Fe, Co)	Ceramic-based (Ni-YSZ, perovskites)
Capital cost	Low (cheap materials)	High (noble metals + membranes)	Low–moderate (no CRMs, cheaper membranes)	Very high (complex ceramics, high T)
System compactness	Low (large electrodes required)	High (compact stacks possible)	Medium–high (more compact than AWE)	Moderate (lab/R&D scale)
Durability	Long (>60,000–100,000 h)	Medium (10,000–50,000 h)	Still limited (5,000–20,000 h, improving)	Limited (500–20,000 h)
Flexibility	Good, robust	High (dynamic operation possible)	Promising (good flexibility expected)	Limited
Maturity	Commercial, mature	Growing, industrializing	Emerging, under development	Still R&D / pilot stage

Also, in Figure 1.19, it is possible to see a final comparison between the different technologies, based current density (horizontal axis), electrical efficiency based on the lower heating value (LHV) (vertical axis), and specific hydrogen production per cell area (upper scale).

Alkaline electrolysis can work in a limited current density range (0.25–0.45 A/cm²), with moderate but stable electrical efficiencies (55–75%). The use of non-critical metals results in low capital costs, but at the same time there is a need for larger electrode surfaces to achieve production levels comparable to other technologies. PEM technology operates in a larger current density range (1–2 A/cm² and beyond), enabling higher specific H_2 production and more compact systems. The capital costs associated with PEM systems are higher than AWE, and the operational costs are similar since they have a similar efficiency.

Finally, SOEC, can achieve electrical efficiencies above 100% (LHV). But at the same time, its operating current density range is limited (0.3–1 A/cm²), and capital and plant costs are still high due to the elevated operating temperatures and the complexity of the ceramic materials.

Overall, it is difficult to say which is the optimal technology; it is a question of compromise between electrical efficiency, production rate, investment cost, and operational flexibility. In that contest, AWE technologies, and in particular the latest developments based on AEMWE electrolysis, emerge as a balanced solution: characterized by low operating costs, with non-critical materials and promising efficiency, while maintaining a simpler and more scalable technological structure compared to more advanced alternatives [73].

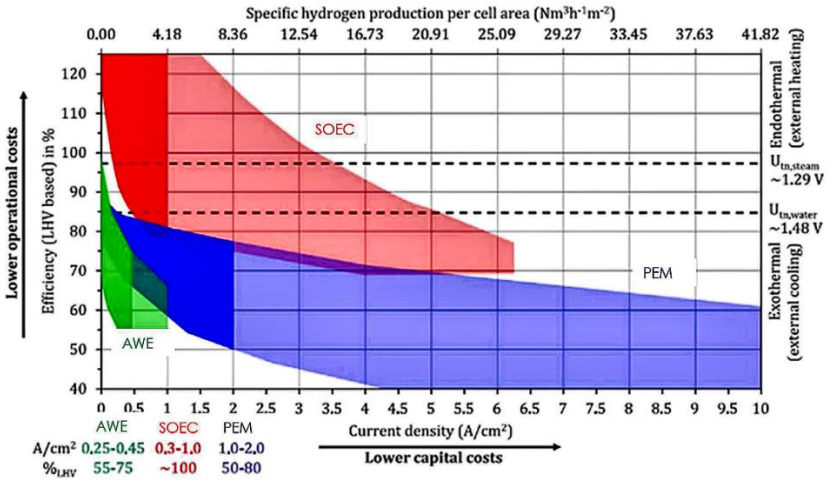

Figure 1.19 Summary of efficiency and operational range of AEL Summary of efficiency and operational range of AWE, PEM and SOEC cells or stacks. Image adapted from [73].

1.3 Oxygen Evolution Reaction and state of the art about Catalytic Material Development

1.3.1 OER bottleneck and mechanism

The Oxygen Evolution Reaction (OER) is often considered the main bottleneck of water splitting, because it suffers of slow kinetics and large energy barriers, with respect to HER [109–112]. In alkaline media, the reaction is:

$$4OH^- \rightarrow O_2 + 2H_2O + 4e^- \quad \text{Eq.1.16}$$

The mechanism takes place through a series of proton-coupled electron transfer (PCET) steps, with the formation of adsorbed intermediates (*OH, *O, *OOH) [113,114]. Each of these steps needs energy, and even efficient non-noble catalysts typically exhibit overpotentials (η) of about 250–400 mV, significantly above the equilibrium potential of 1.23 V vs RHE [109,110].

Working in alkaline conditions allows the use of non-noble transition metals, which is an advantage compared to acidic media [25,102,107]. However, the reaction is slowed down by the low availability of protons: while protons are abundant in acidic electrolytes, in alkaline medium they must be taken from water or OH^-, which means breaking strong O–H bonds. This extra energy requirement makes the proton transfer couplet PCET steps less efficient and leads to higher Tafel slopes (40–120 mV dec^{-1}), showing that a larger overpotential is needed to drive the same current density [110,116].

Another problem is the formation of oxygen bubbles on the electrode surface, which cover active sites and increase resistance [110,111]. This issue is more problematic at high current densities or with compact electrodes. Mitigation strategies involve the use of nanostructured surfaces, with some roughness, or supported on 3D conductive materials, which help bubbles detach and improve electrolyte flow [116].

Mass transport adds another issue: local OH^- gradients, limited diffusion inside pores, and dissolved oxygen accumulation can all reduce efficiency [110,116].

At the same time, the stability of the catalyst is still a concern. Transition metal oxides and hydroxides (Ni, Co, Fe, Mn) often can reconstruct or dissolve under strong oxidative conditions [114].

Finally, CO_2 from air can dissolve in the electrolyte and form carbonates, lowering conductivity and increasing ohmic losses [110,117].

Most of limitations originate from the molecular pathways through which OER occurs. Several mechanistic models have been proposed, each associated with distinct intermediates, active sites, and kinetic features [110,114,118]:

1.Adsorbate Evolution Mechanism (AEM) / Water Nucleophilic Attack (WNA).

The classical pathway involves the sequential formation of *OH, *O, and *OOH intermediates on a single metal site:

- $M + OH^- \rightarrow M–OH + e^-$ Eq.1.17
- $M–OH + OH^- \rightarrow M{=}O + H_2O + e^-$ Eq.1.18

- $M{=}O + OH^- \rightarrow M{-}OOH + e^-$ Eq.1.19
- $M{-}OOH + OH^- \rightarrow M + O_2 + H_2O + e^-$ Eq.1.20

The formation of M-OOH is usually the rate-determining step (RDS), since it requires the coupling between a strongly bound oxygen and an incoming OH^-. This explains the large overpotentials typically observed. Tafel slopes close to 60 mV dec^{-1}, are consistent with a rate-limiting second electron transfer [109]. Importantly, the AEM is controlled by the so-called scaling relationships, i.e. nearly linear correlations between the adsorption energies of *OH, *O, and *OOH [114,118,119]. These relations prevent the independent optimization of each intermediate: stabilizing *OH would destabilize *OOH, and vice versa. As a result, the AEM is subject to a theoretical minimum overpotential of ~0.37 V, often visualized in the form of a volcano plot that relates OER activity to adsorption-energy descriptors [117–119].

2. *Dual-Site Mechanism (DSM) / Interaction of Two M–O (I2M)*

In multimetallic oxides and layered double hydroxides (LDHs) , two neighboring metal–oxo species (M=O) can directly couple to form an M–O–O–M intermediate, which subsequently evolves O_2 [109]This route bypasses the high-energy *OOH step and is therefore associated with lower overpotentials and Tafel slopes around 40 mV dec^{-1}. This explains why NiFe- and CoFe-based LDHs display superior performance compared to single-metal oxides [110,114].

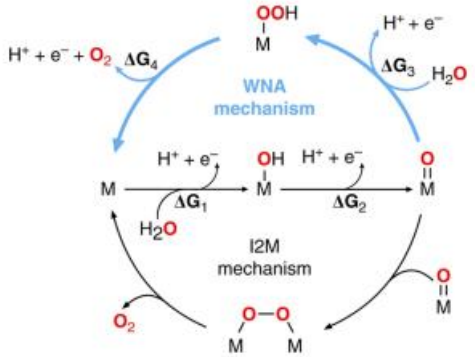

Figure 1.20 OER cycling process of proposed alternative mechanisms. Image taken from [114].

3.Lattice Oxygen Mechanism (LOM).

A more recently recognized pathway involves the direct participation of lattice oxygen in the catalytic reaction. In perovskites and complex oxides (e.g., $LaNiO_3$, $SrCoO_3$), oxygen evolution is coupled to the formation of lattice oxygen vacancies, which are subsequently refilled by OH^- from the electrolyte [110,114,119]. This mechanism is of particular interest because it can overcome the scaling relations that limit the AEM, thereby potentially reducing the overpotential below 0.37 V [119]. However, it comes with the drawback of possible structural instability, since repeated participation of lattice oxygen can lead to irreversible reconstruction or degradation. Reported Tafel slopes for the LOM vary between 30 and 80 mV dec^{-1}, depending on the extent of lattice involvement [114].

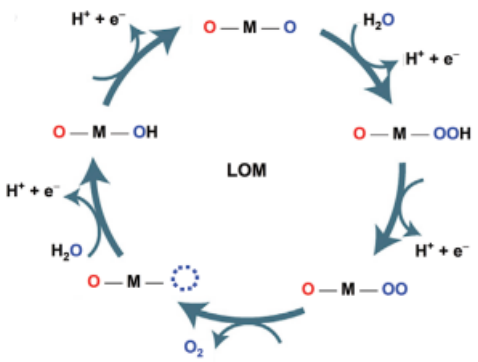

Figure 1.21 LOM mechanism. Image taken from [110].

In summary, the OER in alkaline media is constrained by thermodynamic scaling relations and kinetic bottlenecks. While different mechanisms (AEM, DSM, LOM) highlight alternative pathways, their identification and comparison rely critically on robust measurement protocols. From a metrological standpoint, distinguishing these contributions through reliable and reproducible electrochemical characterization is essential to correctly assess catalyst performance.

1.3.2 OER state of the art catalysts

The mechanistic framework provides the basis to discuss the catalysts employed to realize efficient OER. The following sections examine these materials in detail.

1. Noble catalysts

IrO_2 and RuO_2 are the benchmark OER catalysts [120,121], they are CRM-based and expensive, limiting their large-scale application, and being mostly used in acidic environment. In alkaline conditions, non-precious metal-based catalysts (NPMCs) such as Ni, Fe, Co, and Mn compounds have emerged as promising alternatives thanks to their abundance, low cost, and lower toxicity [110,122,123]. The catalytic activity can be explained by the volcano plot, which correlates OER activity with the adsorption energy of the reactive intermediates (*OH, *O, and *OOH). Materials with excessively strong adsorption (such as certain Ni or Fe oxides) exhibit sluggish kinetics due to the difficulty of releasing intermediates, while those with too weak adsorption (e.g., MnO_2) fail to stabilize the species required for the reaction. RuO_2 and IrO_2 are located near the vertex of the "volcano," representing the ideal catalysts. To bridge the gap, research on NPMCs has focused on strategies like doping, introducing oxygen vacancies, and tuning electronic structures, enabling performance closer to that of noble oxides [114,118].

2. *Transition-Metal Oxides and (Oxy)Hydroxides*

Transition-metal oxides represent one of the most extensively studied class of catalysts for OER in alkaline media [122]. In this group, we can distinguish three main classes: simple oxides, spinels, and perovskites.

Simple oxides such as NiO, Co_3O_4, MnO_2, and Fe_2O_3 have been the first materials to be tested for OER. NiO usually acts as a precursor of NiOOH, which is the truly active phase [109]. Co_3O_4 is charachterized by the coexistence of Co^{2+} and Co^{3+}, which facilitates redox processes [124]. MnO_2 is an highly stable catalyst but it presents a very low conductivity and high overpotentials [125], as also hematite (Fe_2O_3) suffers of low activity [109]. Overall, oxide performance is modest, with typical overpotentials of 300–400 mV at 10 mA cm^{-2} [109,122], yet they remain relevant as benchmarks and as precursors of more active in situ phases.

Spinels (AB_2O_4) such as Co_3O_4, $NiCo_2O_4$, and $NiFe_2O_4$ take advantage from the possibility of distributing cations between tetrahedral and octahedral sites, a structural feature which promotes a wide range of redox processes. They exhibit overpotentials in the range of 300–350 mV [122]. Although spinels are less active than NiFe layered double hydroxides (LDHs), they provide advantages such as higher electronic conductivity, mechanical robustness, and structural stability. Improvement strategies include multimetallic doping, introduction of oxygen vacancies, and direct growth on three-dimensional conductive supports [126].

Perovskites (ABO_3) are a very versatile class, where controlled substitution at the A and B sites allows the tuning of oxygen vacancy concentration and metal oxidation states [127]. The state of the art of perovskite is $Ba_{0.5}Sr_{0.5}Co_{0.8}Fe_{0.2}O_3$-δ (BSCF) [128], which can outperform IrO_2 activity [120,129], though it suffers from cation leaching and surface amorphization [130]. Other systems, such as $PrBaCoO_3$-δ and doped derivatives, have shown good compromise between activity and stability [131]. An other outstanding perovskite is $BaCo_{0.98}Ti_{0.02}O_{3-\delta}$:$Co_3O_4$ [132], coming from $BaCoO_3$ [133] with Co_3O_4 excess and Ti doping. This composition leads to high OER current densities and greater stability, thanks to the reduced oxygen vacancies in its crystal structure. Optimized perovskites reach overpotentials of 280–320 mV and Tafel slopes of 50–70 mV dec^{-1}[122,127]. Recent strategies to improve activity and stability include multimetallic doping to stabilize oxygen-deficient cubic phases, self-supported architectures, and hybrid heterostructures with conductive materials [126,129].

Transition-metal (oxy)hydroxides, in particular NiFe-LDHs, represent the state of the art for the OER in alkaline media. The synergy between Ni and Fe is essential: Fe stabilizes high-valence Ni species (Ni^{3+}/Ni^{4+}) and optimizes the adsorption energy of intermediates (*OH, *O, *OOH), lowering the kinetic barriers [122]. NiFe-LDHs typically exhibit overpotentials of 230–270 mV at 10 mA cm^{-2} and Tafel slopes below 40 mV dec^{-1} [109,122], outperforming noble-metal oxides RuO_2 and IrO_2 [126]. This class of catalysts combines high intrinsic activity, low cost, and compatibility with commercial electrodes. However, they presents some limitations as poor electronic conductivity, partial Fe dissolution, and structural transformations during long-term operation [109,114].

Mitigation strategies include multimetallic doping (Co, Mn, V), anion intercalation (phosphates, carbonates), nanosheet structuring, and the development of self-supported electrodes [109,122]. Among the synthesis methods, electrodeposition is particularly attractive for its simplicity, scalability, and strong film adhesion [134].

Besides the NiFe system, other LDHs (CoFe-LDH, NiCo-LDH, and ternary or multimetallic variants) have been investigated, offering improved stability or conductivity in some cases, though none have yet obtained the efficiency of NiFe-LDHs [109,122].

3. Phosphides and Chalcogenides

Transition-metal phosphides (Ni_2P, CoP, NiFeP) and chalcogenides (Ni_3S_2, CoS_2, $NiSe_2$, $CoSe_2$) have attracted interest because they can act as conductive precatalysts. Under anodic conditions, they turn into Ni-, Fe-, or Co-based oxyhydroxides, which are the real active phases [109,122].

Phosphides are characterized by an high conductivity, furthermore they can directly growth on metal supports, showing overpotentials of 250–300 mV at 10 mA cm^{-2}, their stability can be limited by P leaching [126]. Chalcogenides exhibit even higher conductivity. Their activity can approach that of NiFe-LDHs, but long-term stability remains an issue [114].

4. Carbides and Nitrides

Transition-metal carbides (Mo_2C, WC, TiC) and nitrides (VN, TiN, MoN) are not highly active OER catalysts, but are considered for their metallic conductivity and mechanical robustness [109,122]. In composite or core–shell architectures (Mo_2C/NiFeOOH, TiN/$NiSe_2$), they can achieve overpotentials of 280–320 mV at 10 mA cm^{-2} with improved durability, acting more as conductive supports than as primary active phases [135,136].

5. Metal-organic frameworks (MOFs)

Metal–organic frameworks (MOFs) are hybrid materials composed of metal nodes or clusters (such as Ni, Co, Fe, Mn) coordinated by an organic ligand [135–137]. Several important properties of MOFs, such as porosity, functionalities and structure, can be modified by changing the synthesis route [138–142]. From a catalytic perspective, MOFs offer three key advantages: very high surface area, enhancing exposure of active sites; ordered porosity, improving ion and bubble transport; well-defined metal centers [141,143–147]. MOFs can be used also as excellent precursors: by means of pyrolysis or calcination, metal nodes are transformed into oxides, phosphides or sulfides, while the organic ligands form a conductive carbon matrix. The resulting catalysts preserve porosity and accessibility of active sites, with improved conductivity [136]. Traditionally they

are synthesized by solvothermal/hydrothermal methods, requiring costly ligands and toxic solvents, and limiting in this way scalability. Recently, electrochemical deposition has emerged as a promising route, allowing direct growth on conductive supports (e.g. Ni foam) and the fabrication of binder-free self-supported electrodes, attractive for industrial implementation [135,148–151]. Several MOF systems have shown promising OER performance: NiFe-MOF nanosheets with terephthalate linkers (BDC) reached η_{50} = 270 mV with a Tafel slope of =49 mV dec^{-1}, while NiCo-MOF nanosheets (BDC-based) achieved $\eta_{10} \approx$ 250 mV [136]. In addition, ZIF-67 (a Co-MOF with 2-methylimidazole ligands), after conversion into porous oxides or sulfides, maintained $\eta_{10} \approx$ 250mV and a Tafel slope of 57 mV dec^{-1} [136].

6. *Single-Atom Catalysts (SACs).*

Finally, the emergence of SACs has introduced a new mechanistic complexity in electrocatalysis. In these systems, isolated metal atoms anchored on supports often follow a chemistry closer to molecular catalysts than extended surfaces [114,119].

Both experimental and theoretical studies have identified the stabilization of unconventional intermediates such as $M(OH)_2$ (*OH–*OH), M(O)(OH) (*OH–*O), $M(O)_2$ (*O–*O), and $M(O_2)$ ($*O_2$). These alternative routes allow, in principle, to bypass classical scaling constraints. However, they usually involve multi-electron, which explains the high Tafel slopes (≥120 mV dec^{-1}) often reported for SACs [113].

In Table 1.2 electrochemical performances of main OER electrocatalysts are reported.

Table 1.2 OER state of the art transition metal catalysts.

Class	Representative example	η 10 mA cm^{-2}	Tafel slope	Reference
LDH	NiFe-LDH	230–270 mV	30–40 mV dec^{-1}	[122]
Simple oxides	Co_3O_4	~350 mV	49–60 mV dec^{-1}	[124]
Spinels	$NiCo_2O_4$	340 mV	70 mV dec^{-1}	[126]
Perovskites	$Ba_{0.5}Sr_{0.5}Co_{0.8}Fe_{0.2}O_{3-\delta}$ (BSCF)	300 mV	55-60mV dec^{-1}	[118,131]
Phosphides	Ni_2P	260–280 mV	40–50 mV dec^{-1}	[119,122]
Chalcogenides	$NiSe_2$	240–270 mV	70 mV dec^{-1}	[122]
Carbides/ Nitrides	Mo_2C	280–320 mV	55–65 mV dec^{-1}	[126,135]
MOF and derivatives	NiFe-MOF	250 mV	~50 mV dec^{-1}	[135,136]
SACs	FeNi SAs/NC	280–450 mV	60-150 mV dec^{-1}	[119,152]

7. Self-Supported Electrodes vs Powder Catalysts

After we have analyzed the main classes of OER catalysts, it is important to distinguish between powder-based and self-supported. Powder catalysts are typically deposited with polymeric binders (e.g., Nafion, PVDF) on conductive supports such as Ni foam or carbon cloth. They are easy to prepare but face significant drawbacks like: additional ohmic resistance from binders, poor adhesion with delamination during long-term operation, and limited, non-uniform catalyst loadings that hinder scale-up [109]. On the other hand, self-supported electrodes overcome these issues by directly growing the active material on conductive substrates (Ni, Ti, Cu, steels) without binders. In this way we will get an intimate electrical contact, a high and uniform catalyst loadings, an improved mechanical stability, and a facilitated and efficient oxygen bubble release, with long-term durability [122,126]. Among the synthesis methods, electrodeposition emerges as the most promising methods: it allows fine control over morphology and thickness, provides superior adhesion through direct electrochemical growth, is scalable under mild aqueous conditions, and enables controlled co-deposition of multiple metals (e.g., Ni–Fe, Ni–Co–Fe LDH) [109,124]. For these reasons, it represents the most suitable strategy for the fabrication of robust and industrially relevant OER anodes.

In this thesis, two self-supported type- electrodes were selected to test and validate the measurement protocols for characterization: a $SrCoO_3$-based perovskite and a Ni/ NiFe metal–organic framework (MOF).

The perovskite was chosen for the possibility of tuning its composition through doping and oxygen defects, which makes it possible the study of the relationship between crystal structure and catalytic performance.

The MOF, on the other hand, was selected because its porous architecture and the presence of organic linkers allow exploring how the protocol performs on materials with highly tunable structures, representative of a rapidly emerging class of OER catalysts. It was the effective electrocatalytic layer and was composed by Ni, Fe and a non-toxic and available organic ligand, as succinate [153–156] or tartrate [157–159] anion, derived by the deprotonation of succinic acid and tartaric acid respectively. They are electrodeposited, directly on a low-cost 304 stainless steel (SS) mesh, which acts as substrate of the electrocatalytic layer, but could be employed at the same time as porous transport layer for next-generation zero-gap water alkaline electrolyzers.

1.4 State of the art of OER catalyst characterization protocols

As discussed earlier, producing green hydrogen through water electrolysis is one of the most sustainable options for storing renewable energy. The oxygen evolution reaction, which occurs at the anode, is the limiting process in terms of both kinetics and stability. Many OER catalysts have been suggested in alkaline media, such as transition metal-based materials like nickel, iron, and cobalt, spinels, perovskites, and MOFs, the last two of these are the focus of this study. However, there is no widely accepted protocol to assess the activity and stability of these catalysts, creating a significant gap in the field [160–163].

Protocols that are currently available combine essential electrochemical techniques, that we analyze in detail in the materials and method Section 2.2, to evaluate OER catalyst performance. Linear sweep voltammetry (LSV) is widely used to study the overpotential needed to achieve standard current densities, in the order of 10 mA/cm². Tafel analysis is used to estimate the logarithmic slope of the current-potential curve, which is a key factor in assessing reaction kinetics. Electrochemical impedance spectroscopy (EIS), performed at a fixed potential, is used to analyse the contributions of the system, including ohmic resistance, double-layer capacitance, and charge transfer resistance. Steady-state techniques like chronopotentiometry (CP) and chronoamperometry (CA) are used for long-term stability tests where the catalytic activity is evaluated over time. Cyclic voltammetry (CV), together with EIS, is used for the estimation of double-layer capacitance, which helps in calculating the electrochemically active surface area (ECSA). In table 1.3 the typical parameters used in these techniques are presented.

Table 1.3 Typical characterization techniques and related parameters for OER catalysts.

Technique	Typical Parameters	Purpose	Ref
LSV	*Scan rate*: 1–10 mV/s *Potential range*: up to 1.7–1.8 V vs RHE - *iR correction*: yes	Evaluate OER onset, overpotential, and activity	[161,164]
CV	*Scan rate*: 10–800 mV/s *Potential range*: non-faradaic region (usually for C_{DL})	Estimate C_{DL} →ECSA, ALT test	[89,165]
EIS	*Frequency*: 100 kHz – 0.1 Hz *AC amplitude*: 5–10 mV - Measured at: *fixed potential*, often ~1.6–1.65 V vs RHE	Analyze charge transfer resistance, iR drop, C_{DL} ECSA	[164,166]
CP/CA	*Constant current*: e.g., 10 mA/cm² - *Duration:* 2–100 hours (depending on protocol) *Temperature*: room T or elevated (some up to 80°C)	Assess catalyst stability over time	[161,162,166]

In addition to electrochemical measurements, a full characterization of OER catalysts requires physicochemical and structural techniques. Scanning Electron Microscopy (SEM) analyses surface morphology and elemental composition. X-ray Photoelectron Spectroscopy (XPS) determines surface chemical composition and oxidation state. X-ray Diffraction (XRD) identifies the crystalline structure of the material. Fourier Transform Infrared Spectroscopy (FTIR) analyses chemical bonds and functional groups on the surface [167].

Many studies focused on creating the best formulation for effective catalysts for the OER in alkaline solutions, but the scientific community has not agreed on a common experimental protocol for electrochemical testing. Several reference articles [160,161,167,168], suggest measurement protocols that combine different electrochemical techniques. However, they differ in operating conditions, cell configuration, type of electrodes, support treatment, electrolyte concentration, iR compensation, and normalization criteria, making it hard to compare results accurately. Key parameters that change between labs include:

• The electrolyte concentration, particularly the molarity of KOH, or NaOH, can vary greatly across different protocols, usually from 0.1 M to 6 M. Lower concentrations, such as 0.1 to 1 M, are commonly used in academic studies that focus on comparative screening. While higher concentrations, up to 6 M, are often used to emulate industrial conditions or for speeded-up stability tests. In addition to concentration, also the electrolyte temperature can affect catalyst performance, solution conductivity, and the diffusion rate of reactants. Most academic protocols work at room temperature, around 25 °C, without active thermal control, while in more advanced setups or in systems that simulate real cells, tests may be done at higher temperatures, such as 60 °C to 80 °C, emulating the real operating conditions of an alkaline electrolyzer [90,169].

• The electrochemical cell configuration, which can range from laboratory batch cells (classic three-electrode setup) or more advanced flow-through cells, mimicking the MEA conditions, or MEA (membrane electrode assembly) setups, used in pre-industrial scale studies. The choice of cell configuration is crucial, because it affects aspects such as current distribution, evolved gas management, and reproducibility. Most studies employ batch three-electrode cells, often combined with a rotating disk electrode (RDE) to mitigate mass transport limitations. While RDE improves reproducibility and kinetic analysis, both setups remain far from industrially relevant conditions, where flow or MEA configurations prevail [168].

• Another difference among various studies is the type of electrode and conductive support used for the catalyst. In some studies catalysts are deposited in the form of thin films on flat electrodes, like glassy carbon. These setups allow for good experimental control and make it easier to compare materials, but often there are problems with bubble detachment, and in those cases, it is preferable to use a rotating disk electrode RDE. Specifically, the RDE reduces mass transport effects

because the controlled rotation of the electrode creates steady-state and reproducible conditions. Other studies keep three-dimensional porous supports, like nickel foam or stainless steel meshes. These supports better represent practical setups but are harder to analyse quantitatively, particularly for measuring the electroactive surface area [170].

• The reference electrode used in the protocols varies widely and is a major source of inconsistency in the data reported in the literature. Ag/AgCl electrode is used in some studies, but it is not stable in concentrated KOH solutions, since there is the risk of releasing Cl^- ions. Hg/HgO is particularly common in OER protocols under alkaline conditions. Since the potential relies on pH, to facilitate the comparison between different labs, measured potentials are usually referred to the RHE scale, which is the standard reference for comparing catalytic performance. This conversion is done using the equation:

$$E_{RHE} = E_{Hg/HgO} + E_{vsHg/HgO} + 0.059 \cdot pH \qquad \text{Eq.1.21}$$

Where $E_{Hg/HgO}$ is the standard potential of the electrode, which depends on the electrolyte used, and $E_{vsHg/HgO}$ is the potential measured vs the reference electrode. An incorrect or missing conversion can result in errors when interpreting the overpotentials and assessing catalytic activity [163,168,169].

• The counter electrode should not disturb the process occurring at the working electrode. It must be able to deliver or accept electrons quickly, sustaining the current required without introducing limitations. Pt wires, foils or meshes, are commonly employed, as they can sustain large currents for both hydrogen evolution and oxygen evolution, balancing in this way the charge at the working electrode. To avoid constraining the reaction rate, the counter electrode should have a larger surface area than the working electrode and be positioned to ensure a homogeneous electric field between the two [161].

• The measurement parameters for basic techniques like LSV, CV, EIS, and CP scan rate, (frequencies, potentials, and test duration) as it is possible to see in table can differ among various studies.

• The criteria used for normalizing data, since current density can be expressed as a function of: the geometric area of the electrode as in [167,168], the estimated ECSA [166], the catalyst loading or the mass of active material. In addition, there could be differences also in the method adopted for iR compensation, which is, the correction for the ohmic voltage drop (i·R) between the working and reference electrodes. If iR is not compensated, there could be errors in the overpotential lecture and distortion of the Tafel slope. Some studies make a manual correction based on EIS, others rely on automatic dynamic compensation by the potentiostat, which can introduce errors if not carefully controlled. The absence of a universal standard makes it extremely hard to compare different results.

The differences in the results obtained by international interlaboratory studies highlight the essential importance of standardization. Without a standard procedure, it is not possible to ensure the repeatability, comparability, and reliability of published data. An example is the study of Appelhaus et al. (2024) [162], in which eleven laboratories participated in a round-robin test. All the laboratories used the same cell, equipped with the same components. Nevertheless, the obtained results presented significant differences, especially in terms of cell efficiency and stability. This fact demonstrates the importance of deeper metrological control, including aspects such as material purity and instrument calibration. Every measurement must be repeatable and controllable to ensure reliability.

Different studies have been suggested with the aim to mitigate the lack of standardization. Among these, it is important the contribution of McCrory et al. (2013) [166], which introduced a clear and replicable protocol for the evaluation of catalysts activity using electrochemical techniques as LSV, Tafel analysis, EIS, and CV. It also underlines the importance of data normalization with respect to geometric area and ECSA, the use of potentials converted to the RHE reference, and the need to compensate for ohmic drop.

A similar work was conducted by Peters et al. (2015) [160],developing a more general guide for the characterization of OER and HER catalysts. This work underlines the importance of including durability tests (via CP or CA), to the report of detailed experimental conditions (electrolyte, temperature, cell type), and standardizing performance criteria (for example $\eta(10\ mA/cm^2)$). However, even this authoritative protocol, it still leaves space for variations in practical implementation.

A relevant contribution to this field is given by Zhou et al. (2017) [165], who specified a set of suggestions to improve the quality and comparability of electrochemical data related to the study of OER catalysts. Their protocol includes standard practices such as iR compensation, current density normalization to either geometric area or ECSA, and Tafel slope analysis. For stability study, they used repeated CV as a diagnostic method. This approach allows for monitoring changes in electrocatalytic activity over time. This study provides a useful reference for comparative tests at the laboratory scale.

In 2019, Wei et al. [168] introduced in their work the presence of reference catalysts such as NiFe LDH and IrO_2. Their protocol includes a combination of techniques (LSV, CV, EIS, CP) and proposes clear criteria for normalization to geometric area, ECSA, or active mass. Their kinetic evaluation is based on the Tafel and R_{ct} and they also make considerations of long-term stability. Emphasis is also placed on iR drop compensation.

Also, as it is reported by the study of Thissen et all. [170], most of laboratories conduct their electrochemical tests in conditions that do not adequately represent the industrial operation. The electrolyte that is often used is KOH (≤1 M), the tests are held at room temperature, using flat electrodes and reaching relatively low current densities, while commercial electrolyzers operate at elevated temperatures (60–80°C), using a concentrated solution of KOH (≥5 M), with porous three-

dimensional supports, and current densities above 0.5 A/cm². This study therefore highlights the importance of adequate academic protocols to industry-relevant conditions, recommending a gradual adoption of more realistic parameters even at the laboratory scale, suggesting quantitative criteria to more coherent comparisons.

Another contribution is that of Wu et al. (2025) [161], which represents one of the most comprehensive critical analyses of electrochemical protocols used in literature for the characterization of oxygen evolution reaction (OER) catalysts in alkaline media. Furthermore, they suggested a protocol that combines classical techniques with advanced electrochemical metrology approaches, including the use of PEIS (Potentiostatic EIS), cyclic voltammetry, and the evaluation of intrinsic activity through TOF (turnover frequency). This protocol also accounts for contamination effects and long-term degradation, making it particularly valuable for pre-industrial studies and high–surface-area materials.

In parallel to academic research, regulatory entities and European initiatives have worked on this. In 2021, the Joint Research Centre (JRC) of the European Commission released document EUR 30752 EN [89], which proposes standardized protocols for the characterization of low-temperature electrolyzers (including alkaline systems). While the primary focus of this document is on validating complete devices, many of the specifications can be effectively adapted for component test.

The European project ANIONE [171], which is focused on developing AEMWE cells, has also created a reference protocol for testing components, emphasizing metrological traceability and data reproducibility.

A main summary of these results is presented in the following table:

Table 1.4 State of the art of OER catalyst characterization protocols.

Reference	Electrolyte	LSV/CV	EIS	Stability test	Morphological characterization
McCrory (2013) [166]	1 M NaOH, 25 °C	10 mV/s, RDE, sweep 1–1.7 V, iR drop 85%	100 kHz–100 Hz, for ECSA and iR	2–12 h, 10 $mAcm^{-2}$, CP	XPS, SEM, FTIR
Zhou et al,(2017 [165]	1 M KOH 25 °C	RDE, CV for ECSA, from 0.8 to 1 V RHE, LSV 2 mV/s from 1.3 to 1.65 V	100 kHz–100 Hz, for ECSA and iR, at OCP, 1.5 and 1.65 V RHE	10000 cycles CV 100 mV/s from 0.8 to 1 V RHE	x
Wei (2019) [168]	0.1 M KOH, 25 °C	10 mVs^{-1}, RDE, Tafel extrapolation	100 kHz–0.1 Hz, for iR	x	XPS, SEM
Appelhaus (2024) [162]	30 wt% KOH, 80 °C	Polarization curves built by galvanostatic steps, 0.1–2 Acm^{-2} (AEM configuration)	x	24 h CP 2V	EDX
Thissen (2023) [170]	6 M KOH, 80 °C	manual iR correction, current steps . 10, 100, 500 and 1,000 $mAcm^{-2}$	Galvanostatic eis 100 kHz–0.1 Hz at each step	CP 100, 500 or 1000 $mAcm^{-2}$ 2h/AST 100, 500, 1000 $mAcm^{-2}$ 2h	x
Wu et al. (2025) [161]	1 M KOH, 25 °C RDE o MEA	LSV 5 mV/s to a 1.8 V RHE, CV for Cdl (10–200 mVs^{-1}), iR manual correction. Steady state polarization curve (for tafel)	100 kHz–0.1 Hz, 10 mV, a 1.6–1.65 V	CP 10 mA/cm^2, 24–48 h, 1000 CV Cycling	SEM, XRD, XPS, FTIR
Peters et al. (2015) [160]	1 M NaOH, 25 °C	LSV 5–10 mV/s, sweep LSV 1.0–1.8 V RHE, RDE raccomended; CV for ECSA. Current step from 0.1 to 20 mA cm^2, potential step from eta0 to 0.6 V (85% ir Drop)	Optional, for Rct e iR	CP 10 $mAcm^{-2}$, 2 h/24h	SEM e XPS
ANIONE [171]	1M KOH 25 °C (AEM)	Galvanostatic step of 50 mA cm^{-2} to 2 V RHE	100 kh-100 mhz Galvanostatic 0.1 A cm^{-2} and 1 A cm^{-2}	CP 2.2 V 100h AST variation every 2h between 0.2 and 1 A cm^{-2}	SEM, XPS, ICP-OES, FTIR
JRC (2021) [89]	(AEM, PEM, alkaline)	Galvanostatic step from 0.1 A cm^{-2} to 2 A cm^{-2}	100 khz-100 mHz at constant current	1000 h 0.5 A $cm^{-2,}$ AST	XRD, SEM, Square/Triangle/R wave

At the end, although several electrochemical methods and strategies have been proposed for the evaluation of OER catalysts, a universally accepted standard still doesn't exist. Current guidelines, while valuable, permit subjective interpretation or are not specifically tailored to particular classes of catalysts. Most available

protocols are based mainly on direct current (DC) electrochemical measurements, principally aiming the assessment of catalytic activity and stability under steady-state or dynamic polarization conditions.

Several recent approaches also combine DC measurements with alternating current (AC) techniques such as EIS; however, these are often employed qualitatively or under non-comparable experimental conditions, which limits their complementary value [162,172]. In this context, the present work introduces a systematic and standardized integration of AC and DC electrochemical measurements, where both approaches are combined within a consistent framework to ensure a quantitative, and traceable evaluation of electrocatalyst performance.

This combined approach enables the correlation between steady-state activity, derived from DC measurements, and dynamic interfacial behaviour, captured through AC analysis, thus providing deeper insight into degradation mechanisms and enhancing inter-laboratory comparability [173,174].

Starting from these considerations, to establish robust evaluation criteria is essential a deeper understanding of the potential of AC and DC electrochemical techniques and how they complement each other.

1.5 AC and DC Electrochemical measurement techniques

In the context of the electrochemical characterization of catalysts for the Oxygen Evolution Reaction, in order to obtain a whole understanding of the electrocatalytic behaviour, it is essential to combine DC and AC measurements. Indeed, each class of electrochemical techniques offers complementary evidence of the electrochemical processes happening at the electrode-electrolyte interface. Although both techniques rely on the principles of charge transfer and potential control, they differ in the type of perturbation applied to the system and in the analysis of the response [173].

DC measurements analyse the response of the system when a constant or slowly varying potential is applied, simulating the working conditions in electrolytic devices, and are therefore used to study electrocatalytic activity and durability of the catalysts under real operating conditions. Traditional DC methods intrinsically combine in the measured signal the effects of several processes occurring simultaneously: solution resistance, ohmic drop, charge and mass transport, double-layer charge and discharge, and pseudo-capacitive contributions, making it difficult to isolate and quantify specific parameters such as the charge-transfer resistance (R_{ct}) [175,176].

In contrast, AC techniques, above all EIS, investigate how the system reacts to a small sinusoidal perturbations across a wide frequency range, allowing the decomposition of the overall electrochemical behaviour into its resistive, capacitive, and diffusive components, associated to characteristic time scales, providing more information about the phenomena that take place at the interface during electrochemical reactions [177]. Neither DC nor AC techniques are

considered to be enough to fully describe the electrochemical behaviour of a real catalyst [174].

1.5.1 Direct-Current (DC) measurement techniques

The most frequently used DC techniques for OER catalyst characterization are CV, LSV, and galvanostatic tests, such CP at constant current.

CV is a technique in which, the electrode potential is cycled within a potential range at a controlled scan rate, recording the current. This type of measurement enables the evaluation of double-layer capacitance, the identification of onset potentials and activation/deactivation processes. The LSV method, indeed, is characterized by a monotonic potential sweep, and allows the determination of key kinetic parameters such as the Tafel slope, and the overpotential needed to obtain a certain current density value [172,178].

CP is a technique in which a constant current is applied and the potential response is monitored. It is used to evaluate catalysts durability and material degradation. These steady-state experiments are also useful for constructing quasi-stationary Tafel plots [89,161].

DC techniques together give us information about electrocatalytic performance under controlled operating conditions, allowing the extrapolation of activity and stability parameters such as exchange current densities, Tafel slopes, and sustained current at constant voltage. However, the recorded presents an overlap of multiple contributions, representing an integrated response of the entire electrochemical system [179].

Furthermore, DC techniques lack a frequency-domain perspective: during the application of a constant potential or a sweep, fast and slow processes occur at the same time, making it difficult to clearly discriminate between kinetic, diffusional, and capacitive contributions [179].

From a metrological standpoint, DC methods also provide limited possibilities for internal data validation, while AC techniques, can be checked mathematically through Kramers–Kronig analysis.

In summary, DC techniques are essential tools for evaluating operational performance and stability. Nevertheless, their overlapping nature emphasizes the importance of complementary techniques capable of distinguish the various physical contributions and enhancing the reliability of data interpretation [174].

1.5.2 Alternating-Current (AC) measurement techniques

AC techniques, such as Electrochemical Impedance Spectroscopy, rely on the analysis of the system’s response to periodic perturbations. It consists in the application of a small sinusoidal voltage or current perturbation, typically a few millivolts or microamperes in amplitude to ensure linear behaviour, to the electrode, recording the resulting current or potential across a wide frequency range. From the measure of the system's response to the perturbation, a transfer function is calculated, which in the case of electrochemical systems is referred to as electrochemical impedance, expressed as:

$$Z(\omega) = \frac{\Delta V}{\Delta I} = Z_{re} + jZ_{im}$$ Eq. 1.22

where ω is the angular frequency, related to the frequency (Hz) by ω=2πf.

When the input and output are in phase, the imaginary part has value zero and the impedance will have only a real contribution, Z_{re}. If the input and output are out of phase by 90 °, the real part has value zero and the impedance has only an imaginary contribution, Z_{im} [180]. EIS is a type of measurement allowing the analysis of linear time-invariant systems by transfer functions [180].

EIS provides a frequency-domain study of electrochemical systems, allowing the separation of different processes in relation to their characteristic time constants. By varying the range of frequencies, it is possible to distinguish fast phenomena, such as double-layer charging and interfacial electron transfer, from slower ones linked to diffusion of species involved in the reaction. As a result, EIS is a powerful diagnostic tool capable of decompose the overlapping processes that remain combined under DC operation [174,181,182].

The variation of impedance with frequency can be visualized in several ways. In the Bode diagram, log |Z| and φ are plotted as a function of log ω, whereas when the imaginary component Z_{im} is plotted as a function of the real component Z_{re}, an alternative representation of impedance, the Nyquist diagram, is obtained [181,183].

In a Nyquist plot, specific electrochemical processes are linked to different region. Purely resistive contributions appear along the real axis, with the ohmic resistance corresponding to high-frequency intercept, and slower processes such as diffusion or adsorption phenomena dominant at lower frequencies.

To extract significant information from EIS spectra, it is essential to fit data modeling the electrochemical behaviour of the system with an equivalent electric circuit (ECC), since the recorded impedance represents the overall electrical response due to the presence of several physical processes occurring at the same time in the electrochemical system. Each process is characterized by a specific dynamic behaviour that can be modelled by an idealized electrical analogue. Fitting the impedance data with such model allows the extraction of parameters with physical meaning, such as the charge-transfer resistance, double-layer capacitance, or diffusion coefficient. This approach allow a quantitative and mechanistic interpretation of the system's behaviour [174,177,179].

To perform a good fit, consistent boundary conditions must be imposed, in order to obtain physically meaningful results. Moreover, fitting an appropriate EEC to the EIS data over the entire frequency spectrum presents its own challenges [175,179,184].

The simulation of an impedance spectrum with more than one circuit is possible, as some circuits are mathematically identical, for that reason the quality of the data modelling to a specific equivalent electrical circuit is assessed by the chi-square (χ^2) value. Large χ^2 value means bad fit, small value−good fit [185,186].

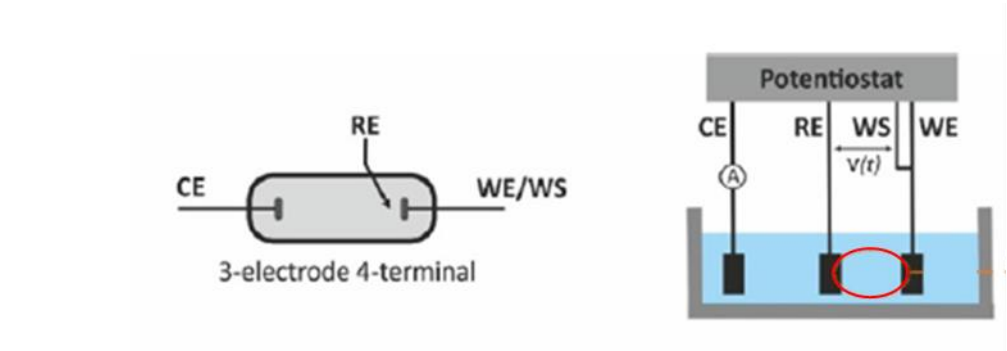

Figure 1.22 3 Electrodes configuration, Image taken from [187].

In a 3 electrode, 4 terminal configuration, the voltage is applied between working electrode (WE) and reference electrode (RE) [187] (see Figure 1.22).

When a redox process occurs, the application of a sinusoidal perturbation to a DC potential result in a faradaic EIS, shown in Figure 1.23 in Nyquist representation.

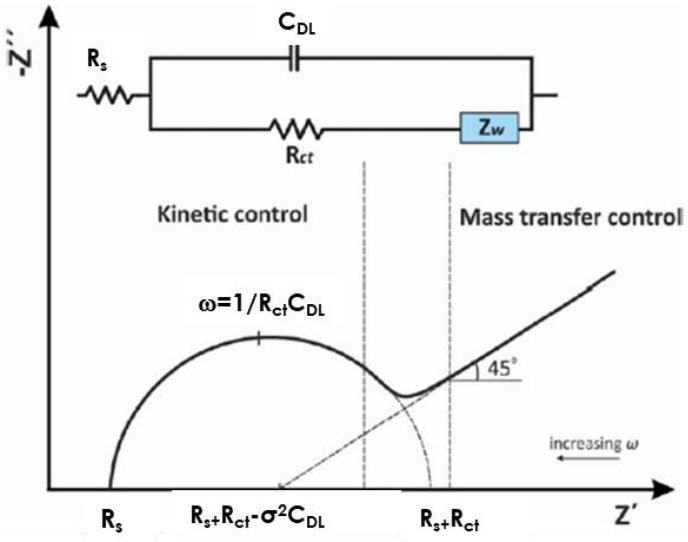

Figure 1.23 Randles equivalent electrical circuit over a wide frequency. Image adapted from [187].

The corresponding EEC is called Randles circuit, made by:

- R_s the ohmic resistance, is the electrolyte resistance between working and reference electrode, depending on the distance and the conductivity of the electrolyte. It can contain also the contribution of the electrolyte cables, that is usually negligible.
- C_{DL}, double layer capacitance. Simulating the electric double layer at the interface, acting as a capacitor under an AC perturbation with an impedance expressed as:

$$Z = \frac{1}{jwC_{dl}} \qquad \text{Eq. 1.23}$$

- R_{ct}, charge-transfer resistance, the rate of current potential curve in steady state conditions, linked to the process kinetics.

$$R_{ct} = \frac{\Delta V}{\Delta i} \quad \text{Eq. 1.24}$$

- Z_w, a Warburg impedance due to mass transport issues [185].

When the electrode is perfectly smooth, the EIS spectra in Nyquist representation is a perfect semicircle, and the capacitive behaviour is ideal. In practice, when the electrode presents some roughness, the behaviour is not ideal, and the semicircle is depressed or inclined. To describe such distributed capacitive behaviour, the constant phase element (CPE) is introduced [177,179,185].

Its impedance is:

$$Z_{CPE} = \frac{1}{Y_0(jw)^n} \quad \text{Eq. 1.25}$$

Where:

- Y_0, which contains capacity information ($F*s^{n-1}$),
- n, define the deviation from ideal behaviour.
  n = 1 CPE = C_{dl} ideal capacity
  n = 0 CPE = R (resistance)
  n = 0.5 CPE = Z_W (Warburg)

The acquisition of reliable data presents several issues, especially at high and low frequencies.

At high frequencies, the response can be dominated by inductance contributions, typically attributed to the connection between the cell and the measurement instrument cables.

At low frequencies, the measurement requires an increasing amount of time, resulting in the risk of changes in the cell's state during an extremely long acquisition [182].

To limit measurement uncertainties, the following aspects must be considered:

- repeatability (repetition of measurements and reproducibility by using identical cells),
- temperature (calibration, ability to maintain a temperature setpoint),
- sensitivity of the measuring instrument, influence of the experimental setup, connections, etc [182].

A crucial aspect of EIS is the validation of experimental data using Kramers–Kronig (K–K) criteria, which assess if the analysed system respects the conditions of linearity, causality, and stability [177,181]:

- A system is linear when the output signal contains only the frequency of the input signal.
- According to the causality principle there is an exclusive cause-effect relationship between the applied signal and the system's response, without external influences.
- A system is considered stable if, when is perturbed by an external stimulus, it can return to its original state once the perturbation is removed.

This validation is essential to ensure that the equivalent circuit models used to simulate the data are reliable [89]. These relations allow the calculation of the real part of the impedance from the imaginary part, and vice versa by using the following equations [177]:

$$Z_r(\omega) = Z_{r,\infty} - \frac{2}{\pi}\int_0^{\infty} \frac{xZ_i(x) - \omega Z_i(\omega)}{x^2 - \omega^2} dx \quad \text{Eq. 1.26}$$

$$Z_i(\omega) = -\frac{2\omega}{\pi}\int_0^{\infty} \frac{Z_r(x) - Z_r(\omega)}{x^2 - \omega^2} dx \quad \text{Eq. 1.27}$$

Kramers–Kronig relations constitute important validation tool, since the algorithms based on that relations make it possible to verify if a measured impedance spectrum corresponds to a physically consistent system or deviates from it due to noise, or non-linear behaviour. This type of validation doesn't present direct counterpart in DC methods.

The main strength of EIS is linked to its ability to combine quantitative modelling with data validation, obtaining physically meaningful parameters correlated to the mechanisms characterizing electrocatalytic activity. It provides a level of detail not accessible through DC techniques and has become a fundamental tool in electrochemical characterization.

Table 1.5 DC and AC techniques characteristics.

	DC Techniques	**AC Techniques (EIS)**
Signal type	Constant or slowly varying (potential/current)	Small sinusoidal perturbation
Domain	Time domain	Frequency domain
Main information	Global activity and stability (η, Tafel slope, current density)	Interfacial and kinetic parameters (R_{ct}, C_{DL})
Data nature	Integrated response of all processes	Separation of resistive, capacitive, and diffusive effects
Validation	Based on reproducibility	Verified by Kramers–Kronig criteria
Advantages	Simple, direct performance evaluation	Quantitative insight into kinetics and interfaces
Limitations	Convoluted signals, no internal validation	Requires model fitting and correct circuit selection

1.5.3 Complementarity and Integration of AC and DC Techniques

To obtain a complete and reliable characterization of electrocatalyst behaviour it is essential to combine the use of DC and AC electrochemical techniques. As said in previous paragraph, each methods provides different but complementary information. DC measurements provide information about the overall electrode performance under operating conditions, giving direct parameters such as overpotential, Tafel slope, and stability. AC techniques, and in particular EIS, allow the separation of resistive, capacitive, and diffusive contributions, showing the physical processes that are behind the observed electrochemical behaviour [174].

When used together, these two methods allow to obtain a complete and reliable interpretation of the data. The link between the overpotential at a specific potential extracted from DC analysis and R_{ct} obtained from EIS is a clear example: catalysts showing a lower overpotential, and therefore faster reaction kinetics, in general also present lower R_{ct} values. Both parameters describe the same process but from different perspectives: DC techniques analyse it in the time domain, while EIS captures it through the frequency response of the system [173–175].

Both CV and EIS can be used to estimate the C_{DL} and, so, the electrochemically active surface area (ECSA), although the two methods are based on different principles. CV provides a rapid estimation of C_{DL} by measuring the capacitive current in a non-faradaic potential window at different scan rate, giving information on surface activity under operating conditions. However, this region often contains pseudocapacitive or weak redox contributions, which can bring to an overestimation of the true C_{DL} value [179,188,189].

EIS, on the other hand, separates the capacitive response from resistive and diffusive by analysis of the system in the frequency domain. The fitting of the spectra with an appropriate equivalent electric circuit models allow the determination of a C_{DL} value that better reflects the real electrochemically active surface. Therefore, while CV offers a quick estimation of surface activity, EIS provides a more reliable and quantitative evaluation [175,176,179,188].

From a methodological perspective, combining DC and AC data helps the improving of both consistency and validation. DC techniques provide direct operational information but lack intrinsic tools for checking data quality. In contrast, EIS permits a verification through the Kramers–Kronig relations. Overall, the two approaches are complementary: DC gives the practical performance picture, while AC reveals its physical origin [174,179].

Therefore, the objective of this study is to design and implement a clear, well-defined testing protocol that accounts for both the structural and electrochemical properties of the investigated catalysts, specifically, thin-film perovskites and metal–organic frameworks (MOFs) supported on stainless-steel mesh, integrating

AC and DC measurements in a unified methodology. In doing so, this work aims to provide a comprehensive evaluation of performance and durability under relevant operating conditions, while contributing to the broader effort toward standardization in the OER research community.

2. Materials and methods

2.1 Electrodes production

2.1.1 MOF on SS mesh

The technique selected in this work for the preparation of MOF electrocatalysts is electrodeposition, for the combination of simplicity, versatility, and control over the deposition process. In literature it is possible to find alternative methods such as sol–gel synthesis, hydrothermal or solvothermal routes, co-precipitation, impregnation, and chemical vapor deposition (CVD), to produce transition metal-based catalysts. But these techniques have some drawbacks, since they often require high-temperature treatments, long reaction times, or the use of surfactants and templating agents, which can affect the reproducibility of the final material [149,151,190].

In contrast, electrodeposition is a technique that requires very mild conditions, it can be carried out at room-temperature, allowing the direct formation of active material on the conductive support, without the need of using binders, or post-synthesis calcination. Moreover, thanks to the control of the applied potential and the deposition time, it is possible to control the thickness, and morphology, which affect the catalytic performance [149–151].

In this thesis, a potentiostatic approach has been used. A stainless steel (AISI 304) mesh (provided by Molino Inox, mesh 91, wire diameter: 100 μm) was used as conductive support. The use of a SS mesh as substrate for OER electrocatalyst is currently spread [191–194]. The mesh was pretreated before the deposition through an immersion in acetone for 5 min and in an aqueous solution 0.5 M of H_2SO_4 for 10 min in ultrasonic bath. The deposition was carried out in a three-electrode cell, using the SS mesh as working electrode (WE), two Pt nets as counter electrodes (CE), to have a uniform deposition on the substrate, and an Ag/AgCl/3.5 M KCl electrode as reference. A constant electrical potential has been applied to the working electrode with respect to the reference electrode, enabling the selective activation of redox reactions at the electrode–electrolyte interface, to form a solid layer on it [194]. The SS mesh has the role not only of the support for the electrocatalytic layer but could also work as a porous transport layer to be employed in next-generation AEMWE electrolyzers [194–196].

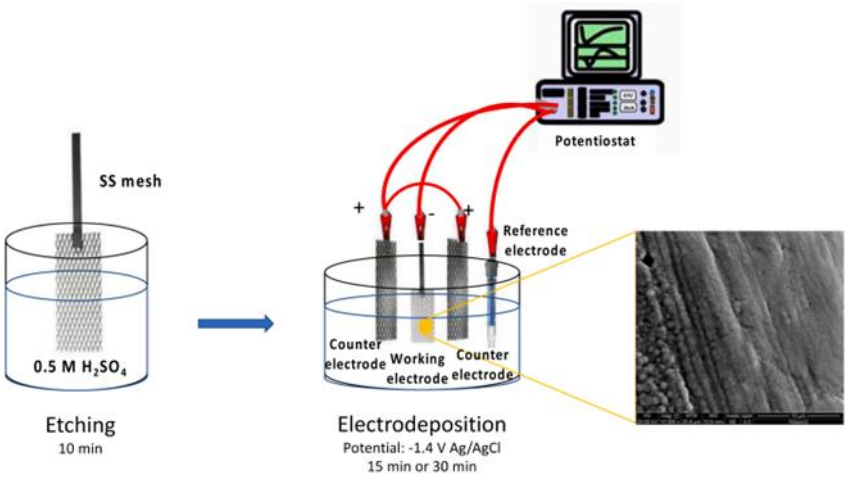

Figure 2.1 Sketch of the preparation process of MOF electrodes. Image taken from [194].

This technique is commonly employed for the deposition of metals and oxides, but recently it has been extended to the synthesis of materials such as MOFs or organic linker coordinated with metals ions.

In conventional metal electrodeposition [190], the following reaction describes the reduction of metal ions:

$$M^{n+} + ne^- \rightarrow M(s) \qquad \text{Eq. 2.1}$$

To make the electrodeposition occur, it is necessary to apply a potential more negative than the equilibrium one, to overcome the kinetic barriers. The difference between the applied and the equilibrium potential is named overpotential η.

The equilibrium potential and therefore the potential to apply, depend on the pH of the medium. Pourbaix diagrams are thermodynamic diagrams, providing a map of the stability regions of various redox species (metal ions, metallic solids, oxides) and it is used to identify the potential–pH conditions suitable for metal deposition [197].

However, in the case of MOF electrodeposition, the mechanism is different, it is not a purely redox-driven process, but it is based on an electrochemically induced local pH modulation. In this case it is necessary to apply a sufficient potential to start the hydrogen evolution reaction, causing the local alkalinization of the zone near the electrode.

This local variation of pH to alkaline conditions during electrodeposition process, move the dissociation equilibrium toward the deprotonation of organic ligands (e.g., terephthalic acid, succinic acid, tartaric acid), leading to the formation of active anions (e.g., terephthalate^{2-}, succinate^{2-}), which coordinate with metal cations in solution, forming in this way a MOF structures [151,190,198–200].

$$(CH_2)_2(COOH)_2 \rightleftarrows (CH_2)_2(COO)^{2-} + 2H^+ \qquad \text{Eq. 2.2}$$

$$2H^+ + 2e^- \rightarrow H_2\uparrow \qquad \text{Eq. 2.3}$$

$$Ni^{2+} or\ Fe^2 + (CH_2)_2(COO)^{2-} \rightarrow Ni(CH_2)_2(COO) or\ Fe(CH_2)(COO)$$

Commonly, to increase the environment local pH, also a pro-base can be used to generate a base that induce ligand deprotonation [201,202]. In this case, no pro-base was used as the local pH increases because of the HER occurring, consuming H^+ ions.

However, if the applied potential is more negative than the standard potential of the Mn^+/M redox couple, even if the overpotential of hydrogen evolution is higher of the potential for direct reduction of the metal, this second process may also occur [194].
This technique was also chosen for its compatibility with relevant substrates and its potential for upscaling in industry.

The electrodeposition parameters used for the preparation of each catalyst, are presented in the following table.

Table 2.1 Electrodeposition parameters of MOF electrodes.

Electrode	Solution composition	Solution PH	Potential applied	Deposition time
Ni-Suc	8.75 mM succinic acid ($C_4H_6O_4$), 7.5 mM of $NiCl_2$	3	1.4 V Ag/AgCl	15 or 30 min
Ni-Tar	8.75 mM tartaric acid ($C_4H_6O_6$), 7.5 mM of $NiCl_2$	3	1.4 V Ag/AgCl	15 or 30 min
Fe-Suc	8.75 mM succinic acid $C_4H_6O_4$, 7.5 mM $FeSO_4*7H_2O$	3.3	1.4 V Ag/AgCl	15 or 30 min
NiFe-Suc	8.75 mM of succinic acid $C_4H_6O_4$, 7.5 mM $NiSO_4*6H_2O$, 7.5 mM $FeSO_4*7H_2O$	3.3	1.4 V Ag/AgCl	15 or 30 min

2.1.2 Perovskite thin film

Perovskite thin films have been prepared by means of a chemical bath deposition method, in which a precursor solution has been deposited by means spin coating technique on a platinized substrate.

Platinized Silicon substrate

A (100) silicon wafer with a native oxide layer is coated with 30 nm of platinum using magnetron sputtering. A thin intermediate layer of approximately 5 nm of titanium nitride (TiN) is applied, to improve adhesion. The substrate has been pretreated with acetone and isopropanol followed by water rinsing. Then it has been annealed at a temperature of 700°C for 15 min, obtaining a (111) texture, functional to the preparation of the thin film.

Chemical Solution Deposition (CDS)

Chemical Solution Deposition is a thin film synthesis technique based on the deposition of liquid precursor solutions [203]. To prepare the precursor solution, the components, particularly metal salts such as metalcarboxylates or other metal organic compounds, are dissolved in an appropriate solvent. Metalcarboxylates are carbonic acid salts (R-COOH), where R is an alkyl. Among that, metalacetates and pentanedionates have shown good performance within the metallo-organic decomposition process (MOD) for perovskite synthesis [130,131,204]. Among the deposition method of the precursor solution such as spin coating, dip coating or spray coating, spin coating was selected, for its high ability to produce highly uniform and controllable thin film coating on a flat surface. After the formation of a wet film on top of the substrate, polymerization leads to the development of a chemical gel film, and organic components are removed by pyrolysis. The result is an amorphous thin film, which crystallizes at elevated air temperatures, in air [130,203]. The solubility of the metalcarboxylates in the solvent will not be too high, to make the precursor stable and preventing sedimentation. During pyrolysis step, all organic compounds are removed.

SPIN COATING

Spin coating is a technique used for the fabrication of thin films to apply a uniform coating on a flat surface [205]. This technique is performed in four steps: deposition, spin up, spin off, and evaporation. During the deposition, a controlled amount of liquid material is applied to the center of the substrate, then spin up and spin off occur in sequence, so the rotation speed of the substrate is increased up to the desired value, and the centrifugal force distributes the liquid outward, while viscous forces regulate the thickness. In the meantime, solvent in the solution evaporates, determining the final film thickness. High spinning speed and longer time result in thinner layers [206]. The final properties of the film depends on several parameters, such us spin speed, acceleration profile, solution viscosity, impurities on the substrate, ambient temperature and humidity, as well as solvent volatility. If there are small fluctuations in these variables there would be significantly impact the thickness, uniformity, and microstructure of the film. Therefore, it is important to have a precise control of process conditions and rigorous standardization of the experimental protocol, to achieve good reproducibility [207].

In that work, a modified propionic acid-based route [130–132,208] was applied for the deposition of $SrCoO_{3-\delta}$ (SCO) and $SrCoO_{3-\delta}$:Co_3O_4 (SCO:CB) materials. The precursor solution was made by $Co(OOCCH_3)_2$, $Sr(OOCCH_3)_2$, suspended in a mixture of propionic acid and propionic acid anhydride 1:5, to remove the constitutional water of the acetate. Co_3O_4 admixture was obtained with the reduction of Sr/Co ratio down to 0.75 in the precursor solution. Various levels of Ti doping in the $SrCo_{1-x}Ti_xO_{3-\delta}$:$Co_3O_4$ (SCT:CB X), was obtained by adding titanium

(IV) oxide bis(2,4-pentanedionate) to the precursor solution. The solution molarity was adjusted to a final concentration of 0.3 M for the cobalt compound and the solution was refluxed for 1 h at 140°C. To deposit the solution on the substrate, spin-coating was performed at 3000 rpm for 30 seconds, the catalyst was then pyrolyzed on a hotplate at 350°C for 2 minutes. This coating and pyrolysis sequence was repeated 5 times, and the samples were subsequently subjected to a thermal treatment at 800°C for 15 min in air [209].

The following table presents a report of the synthesized catalyst, with their composition.

Table 2.2 Composition of thin film catalysts.

Catalyst name	Sr:Co:Ti ratio	Stechiometry
SCO	1:1:0	$SrCoO_{3-\delta}$
SCO CB	0.75:1:0	$SrCoO_{3-\delta}$:Co_3O_4
SCT CB 1	0.75:0.99:0.01	$SrCo_{0.99}Ti_{0.01}O_{3-\delta}$:Co_3O_4
SCT CB 2	0.75:0.98:0.02	$SrCo_{0.98}Ti_{0.02}O_{3-\delta}$:Co_3O_4
SCT CB 3	0.75:0.97:0.03	$SrCo_{0.97}Ti_{0.03}O_{3-\delta}$:Co_3O_4

2.2 Characterization Techniques

A whole understanding of performances of OER Catalysts, requires the use of a huge spectrum of characterization techniques, which can provide a complementary insight between the electrochemical and morphological features of the materials.

Electrochemistry has a pivotal role in the evaluation of the activity, stability, and durability of catalysts, by using DC and AC techniques. These methods allow the simulation of real operating conditions and the investigation of phenomena occurring at the electrode/electrolyte interface.

At the same time, morphological and structural characterization techniques, such as electron microscopy, X-ray diffraction, and photoelectron spectroscopy, give a deep insight into the surface morphology and internal structure, providing details that can be used to correlate physical properties with observed electrocatalytic performance.

The aim of this study is to integrate the results of these different techniques to obtain a comprehensive view of catalyst behaviour, assessing at the same time the influence of experimental setups. Furthermore, to enhance data reliability and allowing a better comparison with existing literature, a standardized characterization procedure is proposed.

2.2.1 Electrochemical measurements

Electrochemical measurements were performed in a three-electrode cell configuration, controlled by a Parstat 4000. In this setup, the investigated electrode acted as the WE, the CE was an inert electrode (DSA, gold plate or Pt net) to close the circuit and an Hg/HgO 1M NaOH electrode was used as RE. A solution of KOH at different concentrations (Chapter 3) was employed as electrolyte. Scheme of this configuration is presented in Figure 2.2 As we will see in Chapter 3, the configuration of the cell we used, changes depending on the catalyst material and substrate.

To better understand the catalysts' behaviour during the OER, a combination of electrochemical techniques was used to evaluate their performances. By combining both DC and AC techniques, it was possible to get a more complete picture about activity, stability, kinetics and interface phenomena. LSV and CA were used to evaluate activity and durability under operating conditions, while CV helped to study the stability during stress conditions. CP was also used to analyse the kinetics and extrapolate useful parameters like Tafel slope. Regarding AC techniques, EIS allowed us to study what happens at the electrode/electrolyte interface, such as charge transfer and ion diffusion.

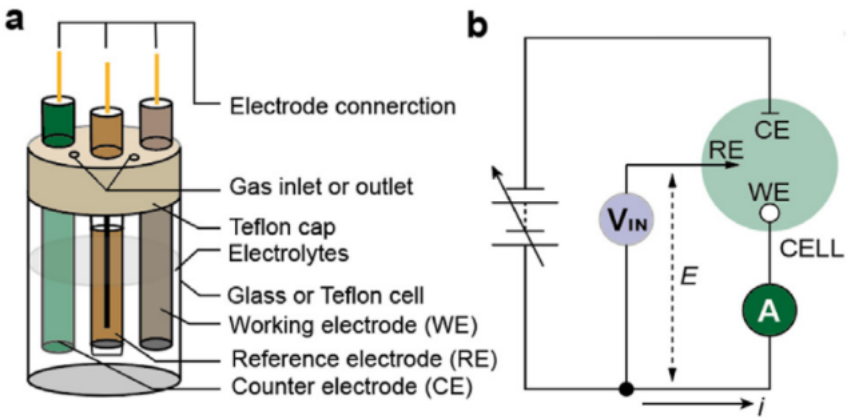

Figure 2.2 (a) Three-electrode set-up configuration, corresponding electrical circuit. Image taken from [161].

ACTIVITY EVALUATION

To evaluate OER activity, polarization curves are recorded using Linear sweep Voltammetry. LSV is a potentiodynamic technique in which, an increasing potential from 0.9 V RHE is applied to the working electrode, and the resulting current is recorded [164]. The applied potential sweep is 10 mV s^{-1}, chosen not too high, to minimize the effect of capacitive charges and to work near steady state conditions. [161]. Reported results have been already corrected considering a 95 % iR compensation.

This technique is used to extrapolate important parameters like the onset potential of the OER, which marks the beginning of significant catalytic activity, or the overpotential at a given current density. The *overpotential* is defined as the

excess potential above the thermodynamic value required (1.23 V under standard conditions) to generate oxygen.

$$\eta = E - E_{eq} \quad \text{Eq. 2.5}$$

The equilibrium potential is determined by the *Nernst equation*, while the actual electrode potential is measured experimentally.

$$E_{eq} = E^0 + \frac{RT}{zF} \ln\left(\frac{a_{ox}}{a_{red}}\right) \quad \text{Eq. 2.6}$$

E^0 is the standard reduction potentials of the species involved, measured respect the hydrogen standard electrode, and $a_{ox}/_{red}$ is the activity of oxidized and reduced species. F=96458 C*mol^{-1} is the Faraday constant and R=8.314 J* (mol*K)$^{-1}$ is the universal gas constant.

In the case of oxygen evolution, at 25 °C [210,211]:

$$E_{eq} = 1.23 - 0.059 * pH \quad \text{Eq. 2.7}$$

Lower overpotential values (typically measured at a specific current density) demonstrates that the catalyst is more active. A current density of 10 mA cm^{-2} is typically used as a benchmark value, it corresponds to the photocurrent density required to have an efficiency of 10% for a solar-to-hydrogen photoelectrochemical devices [212].

Another important parameter derived from the polarization curve is the *Tafel slope*.

It is extracted from the linear region of the polarization curve, measured under steady-state conditions, typically obtained by means of chronopotentiometry. In this technique, a series of fixed potentials is applied for 10 minutes, and the resulting steady-state current is recorded [178,213]. Unlike LSV and CV, chronopotentiometry allows the system to reach a quasi-steady-state, reducing the influence of capacitive currents and providing more accurate kinetic data.

The Tafel slope, is derived from the semi-logarithmic relationship between current and potential (Tafel equation). It is an indicator of the reaction kinetics: a lower Tafel slope indicates a more kinetically active catalyst, since a smaller increase in potential corresponds to a larger increase in current density.

The generic expression of the current *vs* overpotential for an electrochemical reaction is the Butler and Volmer equation (in the case of kinetic control related to charge transfer):

$$i = i_0 \left(e^{-\frac{\alpha nF}{RT}\eta} - e^{\frac{(1-\alpha)nF}{RT}\eta}\right) \quad \text{Eq. 2.8}$$

Where, i_0 is the exchange current density and α is the charge transfer coefficient.

The Tafel slope is calculated by linearizing the kinetically controlled region of the polarization curve, which typically corresponds to high overpotential values.

So, for $\eta \longrightarrow -\infty$, this expression of the Butler and Volmer equation can be derived:

$$\eta = 2.3\frac{RT}{\alpha nF}\log i_0 - 2.3\frac{RT}{\alpha nF}\log i \qquad \text{Eq. 2.9}$$

That can be approximated with the Tafel equation:

$$\eta = a + b\log i \qquad \text{Eq. 2.10}$$

The *Tafel intercept, a* is directly proportional to the logarithm of the *exchange current density, i_0*, and therefore reflects the intrinsic electrocatalytic properties of the material, *b,* defined as *the slope of the Tafel plot*, provides mechanistic insights into the rate-determining step of the OER. The exchange current density i_0 depends not only on the nature of the electrode material but also on physical parameters such as surface roughness [161].

The value of the Tafel slope can be linked to the rate-determining step of the overall OER, which in turn consists of multiple elementary reaction steps, as reported in Section 1.3 [116,214,215].

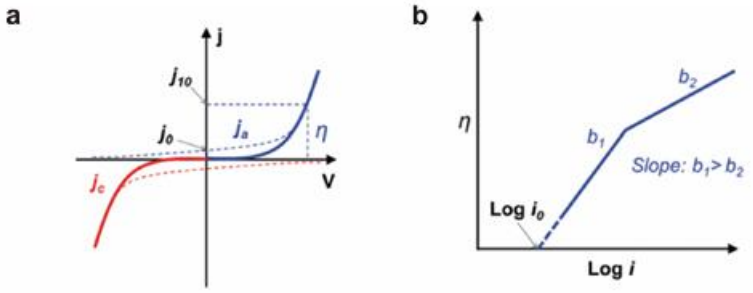

Figure 2.3 a)Anodic and cathodic polarization curve, b)) η vs. $\log_i$ plot , and extrapolation of the exchange current density,i_0. Image taken from [161].

Ideal OER catalysts show small Tafel slopes (40–60 mV/dec or lower in alkaline media) [216]. A high value of Tafel plot could be related not only to a slow kinetic, but also to difficulties in mass transport, for example a harsh oxygen degassing at the electrode [217].

From the Tafel plot, it is also possible to extrapolate the exchange current density i_0 (representing the intrinsic activity at zero overpotential).

As said in section 1.5, another valuable tool in electrochemistry for the quantitative evaluation of catalyst performance is Electrochemical Impedance Spectroscopy. EIS, which is an AC technique can distinguish the contribution of the various physicochemical processes occurring at the electrode–electrolyte interface [181,182].

In our study EIS spectra were recorded, in a 3-electrode configuration and for the best catalyst also in a 2, at different potentials, see Chapter 3. The applied frequency range varies from 0.1 Hz to 100 kHz with an a.c. signal amplitude of 10 mV. The recorded spectra were subsequently fitted with the following equivalent electric circuit using ZSimpWin software.

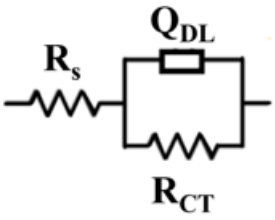

Figure 2.4 Equivalent electric circuit used to model the electrochemical behaviour of the analyzed samples.

It is characterized by a series between R_s, representing the electrolyte resistance, and a parallel between R_{ct}, the charge transfer resistance, and Q_{DL}, representing the non-ideal capacitive behaviour of the electrode-electrolyte interface.

The most significant parameters obtained from EIS for the evaluation of catalyst activity is the charge transfer resistance R_{ct}, which indicates how efficient the electron transfer between the electrode and the redox species in solution is [218]. A high electrocatalytic activity is reflected by a low R_{ct} value, meaning a reduced kinetic barrier for electron transfer. This parameter is particularly relevant in the study of oxygen evolution reaction, where kinetic limitations are the main issue.

From a metrological perspective, the measure of R_{ct} at different applied potentials is particularly significant, because a reduction of its value increasing overpotential provides a direct estimation of the catalyst's kinetic efficiency and the reaction rate. Furthermore, EIS have also been used to monitor electrode behaviour during long-term stability tests, since changes in R_{ct} or C_{DL} over time could reflect, for example, a loss of electrochemically active surface area, the accumulation of reaction products on the electrode surface, or structural changes in the material [181]. As it is possible to see in the next paragraph, the measurement of C_{DL} is also relevant, especially for the evaluation of the electrochemical active surface area.

Electrochemical active surface area (ECSA)

The electrochemically active surface area is a fundamental parameter for evaluating catalyst activity. It is used to normalize the current measured during electrochemical tests, thereby enabling the assessment of the intrinsic OER activity of the catalyst.

Two methods have been used for ECSA estimation: EIS and CV. Both methods are based on the estimation of C_{DL} [116]. From this value it is possible to

calculate the roughness factor r, defined as the ratio between the C_{DL} of the examined electrode and $C_{DL(flat)}$, that is a specific capacity of a flat mirror electrode, whose value usually ranges between 10 μF cm^{-2} and 50 μF cm^{-2} [219].

$$r = \frac{C_{dl}}{C_{dl\,(flat)}} \qquad \text{Eq. 2.11}$$

A 3-electrode configuration was employed. The value of C_{DL} must be evaluated under non-faradaic conditions. For this purpose, a solution of 0.1 M of ammonium diborate was used as electrolyte (pH=9), and purged with Ar to create an inert atmosphere, thereby preventing the occurrence of the oxygen reduction reaction (ORR). A Pt mesh served as counter electrode, while an Ag/AgCl 3.5M KCl was used as reference.

EIS spectra, were recorded at 0.1 V RHE to avoid any faradaic contribution, using an a.c. signal amplitude of 10 mV with frequencies from 0.1 to 10^5 Hz through the PARSTAT 4000. The recorded impedance spectra were then fitted by means of ZSimpWin software, with a suitable equivalent electric circuit. For our electrodes it consists of a series connection between R_s, that is the electrolyte resistance, and a parallel connection between R_{ct}, the charge transfer resistance, and $Q_{DL,el}$, the CPE, used to model the non-ideal electric double layer capacitance.

The C_{DL}, is obtained from $Q_{DL,el}$ with the so-called Brug formula [220]:

$$C_{DL,el} = Q_{DL,el}^{\frac{1}{n}} \; R_s^{\frac{(1-n)}{n}} \qquad \text{Eq. 2.12}$$

As it was said in the previous section, the accuracy of the model can be evaluated with χ^2 parameter, having in this way a verification of the result accuracy.

Regarding CV method, CV were recorded in a potential range in which no faradaic process can occur (between 0.1 RHE and 0.42 RHE), by varying the scan rate (10 mV s^{-1}, 20 mV s^{-1}, 50 mV s^{-1}, 100 mV s^{-1} and 200 mV s^{-1}). In the middle of the potential window, the current, which is almost constant, is a double-layer capacitive current, i_{DL}. Plotting i_{DL} as a function of the scan rate v it is possible to notice a linear behaviour, given by [176,189,221]:

$$I_{DL} = vC_{DL} \qquad \text{Eq. 2.13}$$

The slope of the resulting curve represents the C_{DL}.

In general, the inaccuracy can arise by an incorrect evaluation of the non-faradaic range, that can be different by varying the material and to the presence of pseudo capacities.

The C_{DL} values measured by EIS and CV are consistent within 15%, but EIS method is considered more reliable and reproducible [175,189]. Moreover, the measurement uncertainties are increased by the fact that electrochemical methods, alone, cannot determine whether the capacitance comes only from double-layer charging or also involves the adsorption of charged species [188,222].

STABILITY EVALUATION

Stability evaluation for OER catalysts is a crucial aspect for their characterization, especially considering real-scale operation applications.

In this thesis catalyst durability has been evaluated by using three approaches for this purpose: a galvanostatic measurement, a chronoamperometric measurement and an *Accelerated Life Tests (ALT)* [164].

In the galvanostatic test, a constant current of 50 $mA*cm^{-2}$ has been applied to the working electrode and the evolution of the potential has been recorded over time. The overpotential value required to sustain this current was monitored for 100 hours.

In the Chronoamperometric measurement a potential of 2 V was applied for 40 h, and the resulting current was monitored.

The approach of these two methods is similar, since the increase of overpotential or a decrease of current value could indicate a deterioration in catalytic performance. Such deterioration is typically due to phenomena such as chemical degradation of the active material, formation of passivating layers, or loss of electroactive surface area. These techniques allow monitoring the catalyst's stability under conditions close to real operation and is particularly useful for estimating long-term degradation resistance. After this test, LSV are recorded again to assess catalyst activity after long term operation [161].

The second method is an *Accelerated Life Test* [165], involving the continuous repetition of potential cycles within a voltage range from 1.0 V vs RHE to 2 V vs RHE, until catalyst failure. Although CV does not imitate realistic operating conditions, it is a fast and effective tool to test material stability, since it simulates, in brief time, the degradation mechanisms occurring during catalyst's actual operation [209]. The cyclic redox stress imposed by accelerated cyclic voltammetry can induce different phenomena such as active metal dissolution, surface restructuring or recrystallization, formation of oxides or electrochemically inactive species, and delamination of the material from the conductive support [223].

During the test, for each cycle, various parameters can be analysed, including variation in anodic current, changes in the onset potential, increases in the overpotential required to reach a given current density.

Among the advantages of accelerated cyclic voltammetry there are rapid execution compared to galvanostatic measurement, and good reproducibility. However, this test doesn't reflect realistic operational environments [164].

At the end of the stability tests, additional morphological and structural characterizations (e.g. SEM, TEM, XPS, XRD) can be performed to identify the modifications undergone by the catalyst.

2.2.2 Morphological analysis

Morphological and structural characterization techniques are useful to link electrocatalysts' electrochemical performance with their physical structure. Among these, *Scanning Electron Microscopy* gave an important picture of the

microstructure of catalyst coatings, since it provides high-resolution surface images (ranging from microns down to ~10 nm) by means the scanning of the sample area by a focused electron beam. From these images it is possible to study catalyst's morphology (e.g., particulate, nanosheet-like, porous), particle size and distribution, as well as the presence of agglomerates, cracks, or other defects in the coating. It is possible to use this technique to monitor morphological changes during synthesis or processing, as the variation of density as a function of deposition parameters, as we will see in the case of MOF deposition. The sample must be posed vertically on a metallic stub using copper conductive adhesive, in a vacuum chamber, typically under high vacuum conditions (~10^{-5} Torr) [224]. The sample must be electrically conductive, to prevent the accumulation of electrostatic charges—which would interfere with the detection of secondary electrons. For that reason, if the material is insulating or poorly conductive, as for MOF sample, a thin gold coating, is often applied to its surface to enhance conductivity and image quality, by sputtering under argon atmosphere using an Edwards Scancoat Six, operating at 30 mA for 20 seconds [225]. The primary electron beam is generated via thermionic emission from a tungsten filament and accelerated by an applied potential typically ranging from 0.3 to 30 kV. The beam is then focused and across the sample surface using a system of electromagnetic lenses. At the point where the electron beam interacts with the sample, it usually forms a probe (spot size) of about 5 nm in diameter, for tungsten filament sources, scanning the surface area line by line. As the beam interacts with the sample, it generates several signals, including secondary electrons. Dedicated detectors collect these electrons and turn them into an image that shows the surface topography. SEM systems often include an Energy Dispersive X-ray System (EDX) detector, which allow local elemental analysis, by detecting the characteristic X-rays emitted from the sample under electron beam excitation [224]. In this study surface images were acquired by using a FEI Quanta 200 FEG SEM instrument, using EDX.

X-ray Diffraction is a non-destructive technique, used to study the crystalline structure of materials. It provides valuable information on phase composition and crystallinity and structural properties. This technique is based on the principle of constructive interference between monochromatic X-rays and the atomic planes in a crystalline solid. This interaction follows Bragg's Law:

$$n\lambda = 2d\,sin\theta \qquad \text{Eq. 2.14}$$

where n is the order of diffraction, λ the X-ray wavelength, d the interplanar spacing, and θ the angle of incidence. When this condition is met, the diffracted X-rays are in phase, producing measurable intensity peaks. The XRD instrument generates an X-ray beam that strikes the sample, part the radiation in phase is diffracted. The goniometer precisely moves the detector and sample to measure diffracted intensity at various angles. The resulting pattern consists of a series of

diffraction peaks at specific 2θ angles, which act as a fingerprint of the crystal structure [226].

In this study XRD patterns were recorded using a PANalytical Empyrean diffractometer equipped with a PIXcel1D (tm) detector using the CuKα radiation (λ = 0.15405 nm), operating at 40 kV and 40 mA.

XRD can be performed in different instrumental setup depending on the nature of the sample and the depth of analysis needed. The most used configuration is Bragg–Brentano geometry (also known as symmetric θ–2θ scan), for bulk powders and polycrystalline materials. In our case it was used to analyze the phase composition of MOF sample. In this arrangement, both the X-ray source and detector move symmetrically with respect to the sample, allowing efficient collection of diffraction signals from the entire sample volume. However, when analysing thin films or surface coatings, as in the case of perovskite thin films, the signal from the substrate can dominate and obscure the contribution from the film. In that case a Grazing Incidence X-ray Diffraction (GIXRD) configuration is employed, the incidence angle of the X-ray beam is fixed at a shallow value (typically <2°), which greatly limits the penetration depth into the material. As a result, GIXRD enhances surface sensitivity and allows for selective analysis of nanostructured layers, catalytic coatings, or functional films deposited on substrates [227].

Fourier Transform Infrared Spectroscopy is a non-destructive technique used to study the chemical bonds and molecular interactions within materials. In the study of MOFs, this technique plays a crucial role in the identification of functional groups, confirming the formation of the framework structure [228]. This method relies on the measure of the absorbed infrared radiation by molecules, which causes the vibration of chemical bonds. Each vibrational mode, such us stretching, bending, scissoring, rocking, etc., absorbs energy at specific frequencies (or wavenumbers), constructing a characteristic IR spectrum (interferogram). The application of a Fourier Transform is then used to convert this interferogram into an IR spectrum, providing information on functional groups and molecular structure [229].

FTIR spectroscopy was performed at room temperature, with a Perkin-Elmer FT-IR/NIR Spectrum 400 spectrophotometer in a wavenumber range of 4000–400 cm^{-1}.

To obtain additional vibrational information, *Raman spectroscopy* was employed as a complementary technique to FTIR. This technique is based on the Raman effect, characterized by the inelastic scattering of monochromatic light by molecules [230].When a sample is hit by a laser beam, some photons are elastically scattered, while a small fraction of them exchange energy with the vibrational modes of the molecules. This energy shift shows a characteristic fingerprint of the material [231]. Raman spectra were collected with a Renishaw InVia Raman microscope equipped with a 532 nm diode-pumped solid-state laser. The laser beam was focused on the sample through a Leica DMLM microscope with a 100× long-working-distance objective, producing a spot of about 1 μm.

Although both Raman and FTIR spectroscopy study vibrational mode, they are based on different physical principles. FTIR distinguishes vibrations that can originate a change in the dipole moment of a molecule, for that reason it is mostly sensitive to polar bonds such as O–H, N–H, and C=O. In contrast, Raman spectroscopy responds to vibrations that modify the polarization of the molecule, making it really useful for the observation of symmetric stretching modes such as C=C or M–O–M. The combination of the two techniques, make it possible to obtain a more comprehensive picture of the functional groups, bonding characteristics of and coordination complexes [228,232].

X-ray Photoelectron Spectroscopy is a powerful technique based on the photoelectric effect. In XPS, a beam of monochromatic X-rays irradiates the sample, leading to the emission of core-level electrons. These electrons, known as photoelectrons, are emitted from inner atomic orbitals, such as 1s or 2p. Their kinetic energy is measured by an electron energy analyzer, and the binding energy of each electron is calculated using the equation:

$$E_B = h\nu - E_k - \phi. \quad \text{Eq. 2.15}$$

In which, $h\nu$ represents the photon energy, E_k is the measured kinetic energy, and ϕ is the spectrometer's work function. Each chemical element has characteristic binding energies. The presence of little variations in binding energy, known as chemical shifts, due to the surrounding chemical environment allow to distinguish between different oxidation states and chemical species [233].

XPS measurements were carried out using a PHI 5000 VersaProbe II scanning XPS Microprobe$^{(TM)}$ equipped with monochromatic Al-Kα radiation (hν = 1486.6 eV) from an X-ray source, operating at a spot size of 100 μm, an applied power of 25 W, and an acceleration voltage of 15 kV. The high-resolution XPS spectra were acquired using the hemispherical analyzer with a pass energy of 23.5 eV, an energy step size of 0.05 eV, and a photoelectron take-off angle of 45° relative to the sample surface. Peak fitting was performed using MultiPak 9.9.0.8 software (ULVAC-PHI, Inc), employing a Gaussian-Lorentzian model and a Shirley type background.

XPS is particularly useful to investigate materials because it allows for the precise determination of surface elemental composition and the identification of oxidation states, such as Ni^0, Ni^{2+}, and Ni^{3+} [234]. This technique is also used to monitor chemical changes resulting from, electrochemical activation. One of XPS's major strengths is its exceptional surface sensitivity. It typically probes only the outermost 5 to 10 nm of the material. This is different from techniques like EDX, which provides bulk elemental composition. EDX may detect signals from both the active layer and the substrate. In contrast, XPS enables precise analysis of only the surface layer, making it valuable for characterizing thin films and catalytic coatings [235].

3.Experimental setup and protocols

The experimental procedures created for the electrochemical characterization of the two catalysts under examination are provided in this section. The investigated materials, as reported in the previous section, are MOF electrodeposited on stainless SS mesh and $SrCoO_3$ perovskite deposited on a silicon plate.

The developed protocols are based on the critical study of the existing methods reported in literature, with the aim to overcome the main limitation which affect the current electrochemical testing protocols for OER catalysts. In particular attention was paid at the lack of standardization, the employed cell configuration, electrolyte composition, and data normalization criteria, because these are issues often leading to limited comparability of results across laboratories. Also, most previously reported protocols, use DC and AC electrochemical techniques independently, without proper integration between the two types of techniques. In contrast, the present work introduces a customized experimental protocol, integrating both DC and AC electrochemical techniques, in order to obtain traceable evaluation of catalyst performance and durability.
A summary of the main experimental challenges and methodological improvements introduced in this work is presented in Table 3.1.

Table 3.1 Proposed approach vs Current situation of protocols for OER catalysts testing.

Aspect	Current Situation	Proposed Approach
Industrial Relevance	Tests typically performed at ≤1 M KOH, RT, on flat electrodes.	Test conducted using realistic supports (SS mesh) under representative operation parameters of T and concentration, and also in **AEMWE configuration**.
Cell Configuration	Typically batch or RDE (3-electrode setup).	Both **batch** and **flow-through** configurations employed, selected according to catalyst morphology.
Data Treatment & Referencing	Reference electrodes and iR correction vary across studies; mixed normalization criteria (geometric/ECSA/mass).	Uniform referencing to Hg/HgO scale, consistent iR compensation, and normalization by geometric area.
Measurement Parameters	Variable scan rate, potential window, and duration.	Fixed potential window and scan rate; reproducible operating points for activity and stability assessment.
Integration of AC and DC Techniques	Techniques often used separately; limited cross-validation.	Combined use of **DC** (CV, LSV, CP) and **AC** (EIS) measurements for cross-verification.

Each protocol includes:

- a detailed description of the **electrochemical cell configuration**,
- the **activity and stability tests** performed using DC (CV, LSV, and chronoamperometry/chronopotentiometry) and AC (EIS) techniques,
- the **experimental conditions** applied for each measurement.
- a series of **morphological and structural characterizations** (FTIR, XRD, XPS, SEM, allowing for a more comprehensive interpretation of the electrochemical behaviour.

3.1 *Protocol for functionalized PTLs*

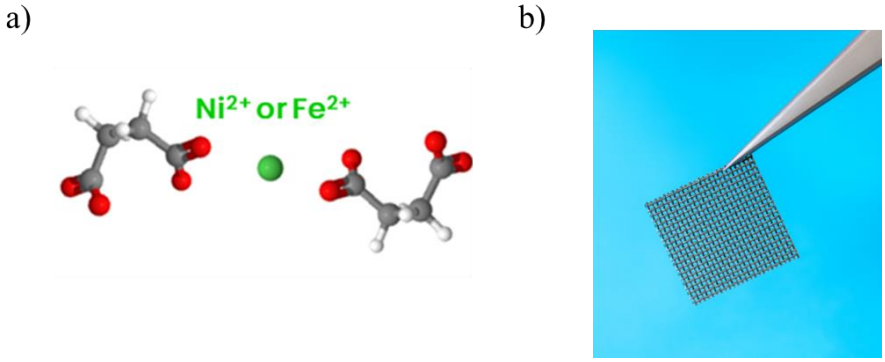

Figure 3.1 a) MOF catalysts chemical structure and b) mesh electrodeposited picture.

For the MOF material electrodeposited on stainless SS mesh, a specific experimental protocol was developed, based on the geometric and morphological characteristics of the substrate, and it will be applied in chapters 4 for NiSuc and Nitar MOF, and in chapter 5 for NiFeSuc MOF.

3.1.1 Cell configuration

The electrochemical tests were performed in a 3-electrode configuration for all electrodes, with two different setups: a batch cell and a flow-through cell. In addition, for the best-performing NiFe-MOF catalyst, measurements were also carried out in an AEMWE electrolyzer using a two-electrode configuration.

In the batch configuration, (Figure 3.2 a) since the catalytic material is deposited on both sides of the mesh, all electrodes are immersed in a single electrolyte compartment. Furthermore, the cell is immersed in a thermostatic bath, allowing tests at different temperatures, to investigate their effect on electrode kinetics.

The flow through configuration more closely mimics the operating conditions of an AEMWE industrial electrolyzer. It is possible to use this set-up since the electrode is deposited on a mesh, which simultaneously acts as a PTL, enabling flow continuously electrolyte flow through the substrate [195]. The cell is made of Teflon, and it is subdivided in two compartments by a fumasep® anionic exchange membrane made of PEEK-reinforced, with a thickness of 130 µm, allowing the ions passage but not the electrons one. The reference electrode is located in the working compartment, immersed within a block positioned behind the working electrode, so as not to interfere with the ions flow between the working and counter electrodes, that in this case is DSA. The electrolyte flow is driven by two peristaltic pumps, one for each compartment, operating at 200 rpm. The exposed active area of the catalyst was 0.78 cm^2. The latter setup was selected for the most representative tests, as it allows for the evaluation of catalytic behaviour under dynamic and mass transport conditions [194].

Potentiostat: Parstat 4000
Working electrode: SS mesh
Counter electrode: Pt mesh/DSA mesh
Reference electrode: Hg/HgO/1 M NaOH
Electrolyte: 1M, 2M, 3M, 5M, 6M KOH
Temperature: 25 °C, 30 °C, 50 °C, 65 °C, 80 °C

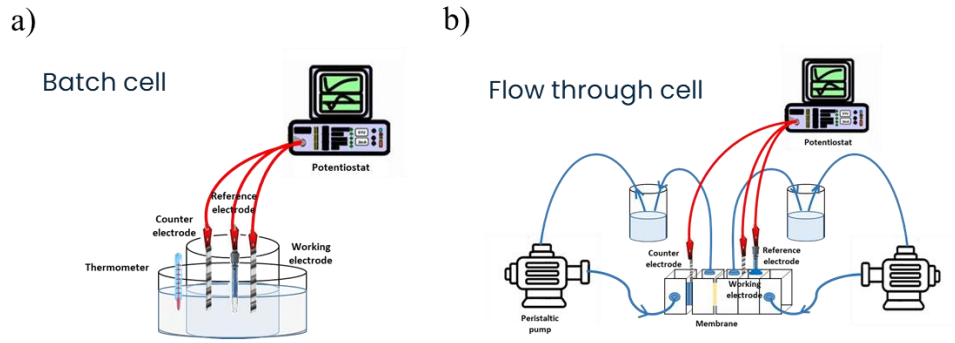

Figure 3.2 Batch and flow through cell configurations. Image taken from [194].

The best sample, NiFe-MOF, as we will see in the following chapters, has also been characterized in an AEMWE electrolyzer.

Potentiostat: Parstat 4000
Working electrode: SS mesh
Counter electrode: Pt/C
Electrolyte: 1M KOH
Temperature: 30 °C, 40 °C, 50 °C, 60 °C

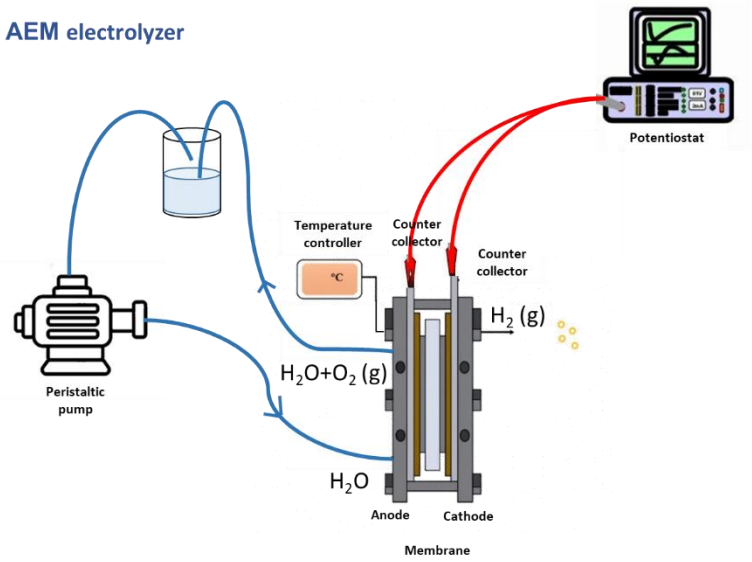

Figure 3.3 AEMWE electrolyzer configuration.

In this configuration, NiFe samples were employed as anodes for the OER, while the cathodes were synthesized by formulating an ink composed of a commercial 40 wt% Platinum on Carbon (Pt/C, Alfa Aesar) and a 20 wt% of FAA3 ionomer (FumaTech), mixed in an ultrasonic bath for 30 min. The resulting ink was deposited onto a Gas Diffusion Layer Sigracet 25-BC (SGL Carbon) by spray coating, with a final loading of 0.5 mg cm^{-2} [236]. A FAA3-50® membrane (FumaTech), about 50 μm thick, was used as AEM. The working area was set to 5 cm^2. The AEMWE electrolyzer was characterized in a single-cell configuration, over a temperature range between 30 °C and 60 °C, supplying a 1 M KOH solution to the anode compartment with a flow rate 5 ml min^{-1} regulated by a peristaltic pump (by Generalcontrol Srl).

3.1.2 ECSA evaluation

The protocol includes a preliminary characterization of the ECSA, essential for normalizing the measured currents and accurately assessing catalytic performance. This is an important characterization in case of MOF structure, because they are characterized by a regular pore structure, adjustable pore size, numerous active sites, and diverse topological structures, which significantly increases the surface area available for electrochemical reactions [136].

As described in the previous section, this measure is based on the C_{DL} determination, by means of EIS and CV. The consistency of the results from both approaches was cross-verified.

In this case a batch set up, with a 3-electrode configuration, was employed, using 0.1 M ABE as electrolyte (pH=8). The cell was sealed and purged with Ar to have an inert atmosphere inside. In this case an Ag/AgCl electrode was used as reference electrode.

EIS spectra at 0.1 V vs. RHE were recorded, over a frequency range from 0.1 Hz to 100 kHz with an a.c. signal amplitude of 10 mV. The recorded spectra were then fitted with an appropriate equivalent electrical circuit using ZSimpWin software.

CV were recorded in a potential range between 0.1 V RHE and 0.42 V RHE, by varying the scan rate (10 mV s^{-1}, 20 mV s^{-1}, 50 mV s^{-1}, 100 mV s^{-1} and 200 mV s^{-1}).

3.1.3 Activity tests

Activity tests were performed under both direct current and alternating current conditions. DC techniques included linear sweep voltammetry, used to determine the overpotential, and chronopotentiometry, employed to extract the Tafel slope and the exchange current density (i_0). AC characterization was carried out by electrochemical impedance spectroscopy, which was used to model the system's electrochemical behaviour.

3-electrode configuration

Concerning *DC measurements*, LSV was recorded from a potential from a starting potential of 0.9 V RHE applied to the working electrode, with a potential sweep of 10 mV s^{-1}. The corresponding Tafel slopes were derived from steady-state measurements to evaluate the electrocatalytic performance.

Regarding *AC measurements*, EIS spectra were collected at electrode potentials of 1.52 V and 1.68 V vs. RHE. An a.c. perturbation with an amplitude of 10 mV was applied over a frequency range spanning from 0.1 Hz to 100 kHz, allowing the analysis of the electrode kinetics and charge-transfer processes.

Tests at 25 °C, and 1 M and 6 M KOH were conducted both in a batch and flow through configuration.

Tests with different electrolyte concentration (1 M, 2 M, 3 M, 5 M, 6 M KOH) and temperatures (25 °C, 30 °C, 50 °C, 65 °C, 80 °C), to evaluate the activation energy, Ea, were conducted in a batch configuration, which allows a control of temperature conditions, only for the most representative electrodes.

AEMWE electrolyzer

DC measurements were carried out by means of LSV, applying a potential sweep rate of 5 mV s^{-1} to the working electrode.

AC measurements were performed through EIS at cell voltages of 1.8 V and 2.0 V, employing an a.c. perturbation of 10 mV within a frequency range from 0.1 Hz to 10 kHz.

Test were conducted using 1M KOH as electrolyte, at different temperatures (30 °C, 40 °C, 50 °C, 60 °C).

3.1.4 Durability tests

3-electrode configuration

Catalyst durability was assessed through chronopotentiometry, applying a constant current density of 50 $mAcm^{-2}$ for 100 hours in 1M KOH and 6M KOH, at 25 °C, reproducing the operating conditions of a real electrolyzer. The severity of these conditions exceeds most of the durability protocols reported in the literature for MOF-based electrodes, both in terms of applied current density [237] and test duration [238]. For that reason, tests were conducted in a flow through configuration in which the electrolyte passes through the material, facilitating the removal of oxygen bubbles generated during the OER. This aspect is crucial, as bubble accumulation on the active surface could partially reduce the catalytic area, introducing noise in the signal, which compromises the metrological assessment of stability [161,219].

AEMWE electrolyzer

A short chronoamperometric test was carried out at an applied voltage of 2 V, using a 1 M KOH aqueous solution for 40 h. Chronoamperometry under constant potential reproduces the voltage-controlled operation of real devices, allowing the evaluation of both catalyst stability and possible degradation effects related to the membrane–electrode assembly [171].

3.1.5 Morphological analysis

Finally, morphological and structural analysis of the catalyst was performed via XRD, FTIR, XPS, and SEM, to correlate electrochemical performance with the physicochemical properties of the material. The tests were conducted before and after the electrochemical tests.

XRD patterns were acquired using a PANalytical Empyrean diffractometer equipped with a PIXcel1D (tm) detector using the CuKα radiation (λ = 0.15405 nm), operating at 40 kV and 40 mA.

Images of the sample's surface were collected by using a FEI Quanta 200 FEG Scanning Electron Microscope, coupled with EDX to have information about the chemical composition of the catalytic layers.

FTIR measurements were carried out at room temperature, with a Perkin-Elmer FT-IR/NIR Spectrum spectrophotometer over a wavenumber range of 4000–400 cm^{-1}.

XPS spectra were recorded using a PHI 5000 VersaProbe II scanning XPS Microprobe (TM) with monochromatic Al-Kα radiation (hν = 1486.6 eV) from an X-ray source operating at a 100 µm spot size, 25 W power, and 15 kV acceleration voltage. The high-resolution XPS spectra were collected using the hemispherical analyzer with a pass energy of 23.500 eV, an energy step size of 0.05000 eV,and a photoelectron take-off angle of 45° with respect to the surface. Peaks fitting was performed with MultiPak 9.9.0.8 (ULVAC-PHI, Inc), using Gauss-Lorentzian model and a Shirley type background.

A summary sketch of the proposed protocol for mesh catalyst characterization is reported in Figure.3.4.

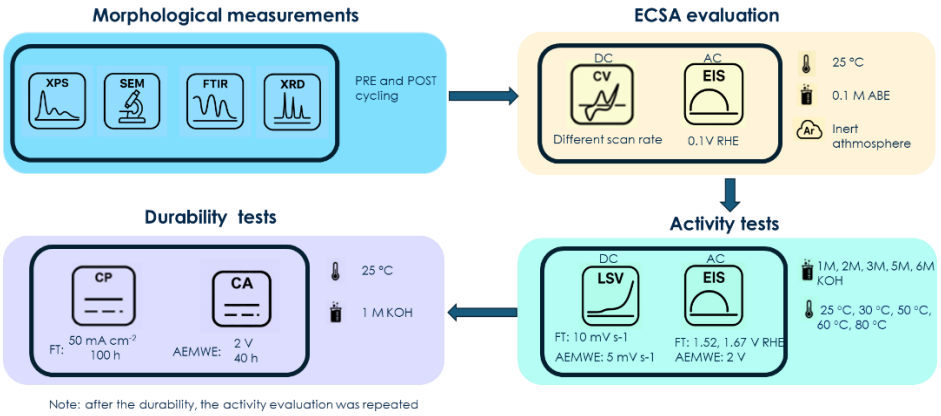

Figure 3.4 Protocol for functionalized PTLs summary.

3.2 *Thin-Film Electrode Protocol*

The second material selected for this study is a perovskite in the form of thin film: $SrCoO_3$, synthesized by a chemical solution deposition method on a platinized Si substrate.

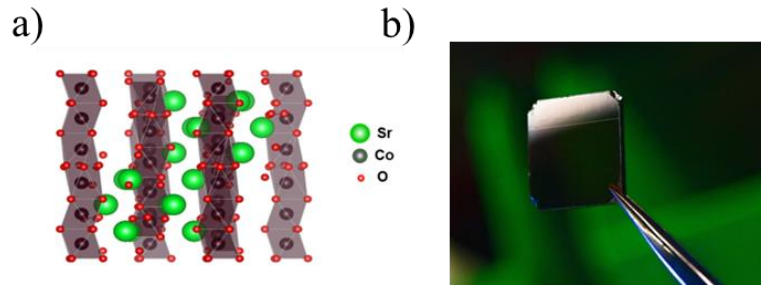

Figure 3.5 a) View on the SCO:CB structure along the [210] direction b) Thin film perovskite on a silicon plate. Image adapted from [209].

3.2.1 Cell configuration

Electrochemical measurements were conducted in a 3-electrode cell configuration, where the investigated electrode served as the working. The experimental configuration was designed considering the flat geometry of the

substrate and the fact that the active layer is present only on one side. All the electrochemical tests were conducted in a self-constructed and membrane-free electrochemical cell, designed for thin film electrodes. The cell has a batch configuration, since the substrate is a sheet deposited on only one side. To ensure that only this side that is exposed to the electrolyte, it is inserted in a holder. A gold plate is used as a counter electrode, inserted in a holder facing the working electrode. The reference electrode (Hg/HgO in 1 M NaOH) was inserted into a capillary tube to minimize contamination of the electrolyte and to maintain a stable reference potential. The cell is contained in a jacket, which can be filled with warm water controlled by a thermostat, to raise the temperature.

Potentiostat: Parstat 4000
Working electrode: Perovskite
Counter electrode: Gold plate
Reference electrode: Hg/HgO/1 M NaOH
Electrolyte: 1M KOH
Temperature: 75°C

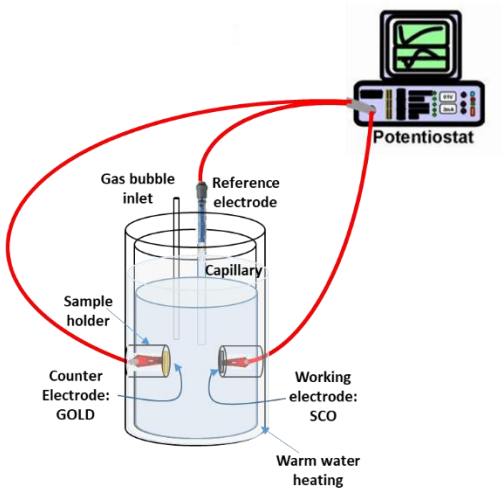

Figure 3.6 Cell configuration used for electrochemical measurements. Image taken from [209].

Since the material is deposited in the form of thin film, its roughness is negligible, so the evaluation of ECSA is not necessary and the activity evaluation was based on the geometric area.

3.2.2 Activity test

The tests were conducted in a 1 M KOH aqueous solution, at a temperature of 75 °C, regulated by an automated thermostat, in order to emulate the operating conditions of a real electrolyzer. Before each measurement, the electrolyte was purged with N_2.

The *DC measurements* consisted of LSV performed in the potential range between 0.9 and 1.9 V vs. RHE, with a scan rate of 10 mV s^{-1}. The Tafel slopes

were derived from steady-state experiments, in which each potential was maintained for about ten minutes to allow the current to stabilise before recording.

The *AC measurements* were based on EIS, carried out at 1.72 V vs. RHE using an AC perturbation of 10 mV amplitude across a frequency range from 0.1 Hz to 10^5 Hz.

3.2.3 Durability test

For catalysts in the form of thin films deposited on conductive substrates, durability was assessed using accelerated cyclic voltammetry (Accelerated Life Test) [239–242]. The protocol is carried out by continuously cycling the sample between 1 V and 2 V RHE at a scan rate of 100 mV s^{-1}, until the loss of catalyst's performance occurs, in agreement with the dynamic test protocol described in the EU technical report for testing of low-temperature water electrolyzers [89]. One of the fundamental issues of perovskite thin films is the leaching of the A-site cation and subsequent amorphization. This test allows researchers to investigate these phenomena by subjecting the material to cyclic redox stresses that trigger degradation mechanisms such as metal dissolution, surface restructuring, or the formation of inactive species, but within a shorter timeframe and with greater control over the rate of stress [243,244].

Moreover, in this cell configuration, the cyclic operation facilitates the removal of oxygen bubbles that, under galvanostatic conditions, would tend to accumulate on the electrode surface, potentially blocking active sites and introducing artifacts in the measurement [161].

3.2.4 Morphological measurements analysis

XRD, XPS, and SEM measurements were carried out to investigate the morphological and structural features of the catalyst and relate them to its electrochemical behaviour.

Characterization of SCT:CB thin films was carried out using Grazing Incidence X-Ray Diffraction method to minimize substrate's contribution. Phase identification was performed using a Philips X'PERT diffractometer with Cu Kα radiation (40 kV, 40 mA). Diffraction patterns were collected over a 2θ range of 10°-65° with a step size of 0.02°.

To track changes in the chemical state of the catalyst surface during degradation an XPS analysis was applied. The measurements were performed using a Phi 5000 VersaProbe II, ULVAC-Phi Inc. All spectras were corrected to C 1s signal with binding energy (BE) of 285 eV.

SEM images were acquired using a FEI Quanta 200 Field Emission Gun Scanning Electron Microscope (FEG-SEM) equipped with an Energy Dispersive X-ray (EDX) detector, which also provided information on the composition of the investigated thin films.

A schematic summary of the proposed protocol for mesh catalyst characterization is shown in Figure 3.7.

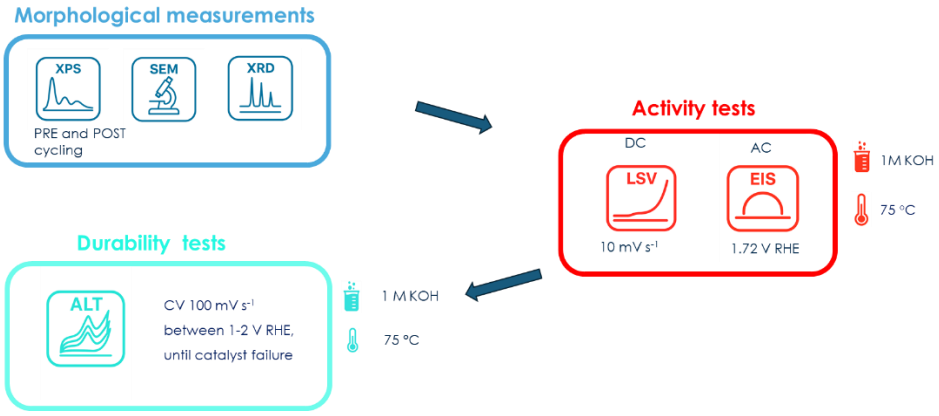

Figure 3.7 Thin-Film Electrode Protocol summary.

4.Electrical and Morphological Assessment of Ni-Coordinated MOF on Stainless Steel for Alkaline Water Electrolysis

In this work it is reported the synthesis and characterization of Ni MOF-based electrodes to improve OER performance in alkaline conditions. These catalysts were characterized by using the *Protocol for functionalized PTLs*, developed in Section 3.1. As it was mentioned in section 2.1.1, the electrodes were prepared by an electrodeposition technique. This is an important approach for the industrial implementation of MOF synthesis, as it enables large-scale MOF production in form of powder and thin film or coating [148–151]. By tuning the parameters of the electrochemical synthesis, MOFs can be tailored for specific applications.

The effective electrocatalytic layer consist of a MOF made by Ni and a non-toxic and simply accessible organic ligand, like succinate [153–156] or tartrate [156,158,159] anion. Actually, MOF was synthesized by cathodic electrodeposition, directly on a cheap 304 SS mesh. This substrate not only worked as the support for the electrocatalytic layer but could also act as a porous transport layer in next-generation zero-gap alkaline water electrolyzers [195,219]. To verify the effective synthesis of the MOF layer, a morphological and compositional analysis of the coatings were performed. The electrochemical performances were evaluated both in 1 M aqueous KOH solution and in 6 M aqueous KOH solution, in batch and flow through configuration, in order to assess catalytic activity and long-term stability.

4.1. MOF electrodeposition

Electrocatalysts were prepared by means an electrodeposition process in aqueous solution containing a Ni-based salt and an organic acid, i.e. succinic or tartaric [194]. Electrodeposition conditions are shown in Section 2.1. Corresponding current density vs time curves are reported in Figure 4.1 a-d.

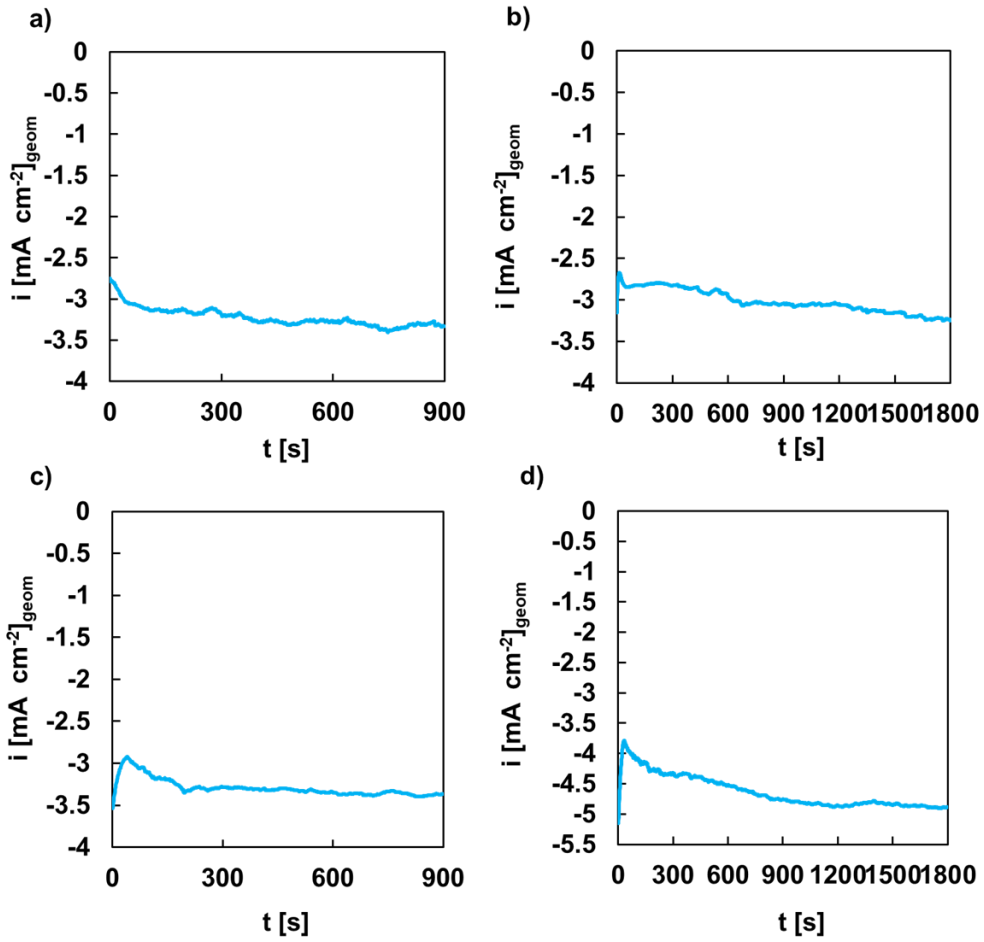

Figure 4.1 Current density vs time curves recorded during the electrodeposition process carried out at -1.4 V (Ag/AgCl) for a) 15 min and b) 30 min in 8.75 mM of succinic acid and 7.5 mM of $NiCl_2$, and for c) 15 min and d) 30 min in 8.75 mM of tartaric acid and 7.5 mM of $NiCl_2$. Image taken from [194].

From a thermodynamic point of view, the following reactions can take place under those electrode potential and pH conditions. [245]:

$$½O_2 + 2H^+ + 2e^- \rightarrow H_2O \qquad E_{eq} = 1.05 \text{ V SHE} \qquad \text{Eq. 4.1}$$

$$2H^+ + 2e^- \rightarrow H_2 \qquad E_{eq} = -0.18 \text{ V SHE} \qquad \text{Eq. 4.2}$$

$$Ni^{2+} + 2e^- \rightarrow Ni \qquad E_{eq} = -0.31 \text{ V SHE} \qquad \text{Eq. 4.3}$$

Under the electrodeposition conditions, the highest overpotential value is associated to reaction (Eq. 4.1) (i.e., oxygen reduction reaction). However, since this reaction occurs in limiting current conditions, due to the low O_2 concentration (i.e. resulting from the poor solubility in water at room temperature) and stagnant hydrodynamics condition, its contribution to the total circulating current is low [246,247]. The overpotential of Reaction Eq. 4.2 is higher than that of reaction Eq. 4.3 so, as confirmed by bubble formation on the mesh during the electrodeposition, hydrogen evolution reaction took place leading a local alkalinization near the cathode. As reported in section 2.1, considering the dissociation equilibria of the

organic acids, related to the presence of hydroxyl and carboxyl groups in Figure 4.2, the localized pH increase occurring during the electrodeposition process shifts the dissociation equilibrium toward the generation of succinate/tartrate anions. These anions subsequently react with metallic cations (Ni^{2+}in this case) leading to the formation of a MOF structure, in which the succinate/tartrate ligands coordinate Ni^{2+}ions [151,194,199]. Particularly, suc^{2-} or tar^{2-} ligand chelate two Ni^{2+} centres, with each of that coordinated by four oxygen atoms thus adopting an octahedral coordination geometry.

Nevertheless, as previously reported for other MOF structures produced by cathodic electrodeposition, it isn't possible to completely exclude the formation of metallic Ni during the electrodeposition process (see below), [148].

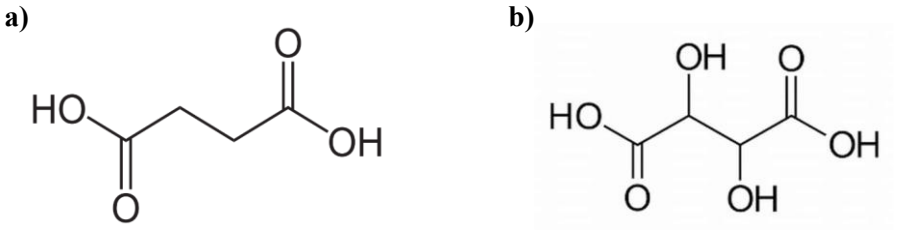

Figure 4.2 Chemical structure of a) succinic acid and b) tartaric acid. Image taken from [194].

Catalyst mass loadings estimated from the mass differences before and after electrodeposition is reported in Figure 4.3.

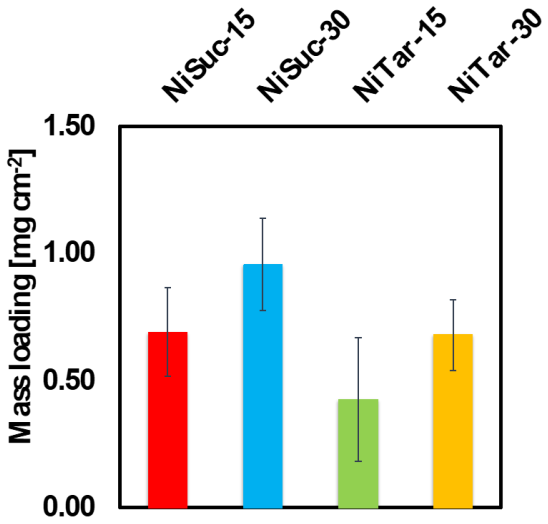

Figure 4.3 Mass loadings for all the investigated MOF electrodes. Image taken from [194].

Table 4.1 Mass loadings for all the investigated MOF electrodes. Table taken from [194].

	NiSuc-15	NiSuc-30	NiTar-15	NiTar-30
Mass loadings	0.68 ± 0.17	0.95 ± 0.17	0.42 ± 0.2	0.67 ± 0.13

4.2. MOF-based electrocatalysts morphology and composition

According to the protocol in section 3.1.5, the catalysts were subjected to a comprehensive morphological and structural investigation through XRD, FTIR, XPS, and SEM analyses, aimed at linking its electrochemical performance with the chemical and morphological characteristics.

To investigate the morphologies of MOF samples, SEM images were recorded and they are presented in Figure 4.4 for NiSuc-15 and NiSuc-30 samples (i.e. electrodeposited using succinic acid with deposition time of 15 and 30 min respectively) and in Figure 4.5 for NiTar-15 and NiTar-30 (i.e. electrodeposited using tartaric acid with deposition time of 15 and 30 min respectively) samples.

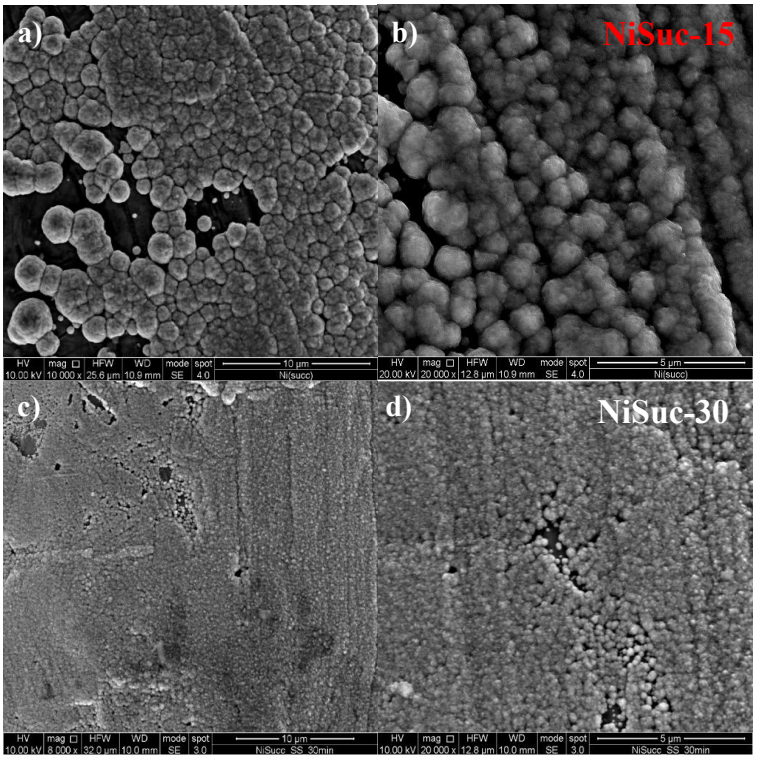

Figure 4.4 SEM images of NiSuc-15 sample at a) 10000x and b) 20000x magnification. SEM images of NiSuc-30 sample at c) 8000x and d) 20000x magnification. Image taken from [194].

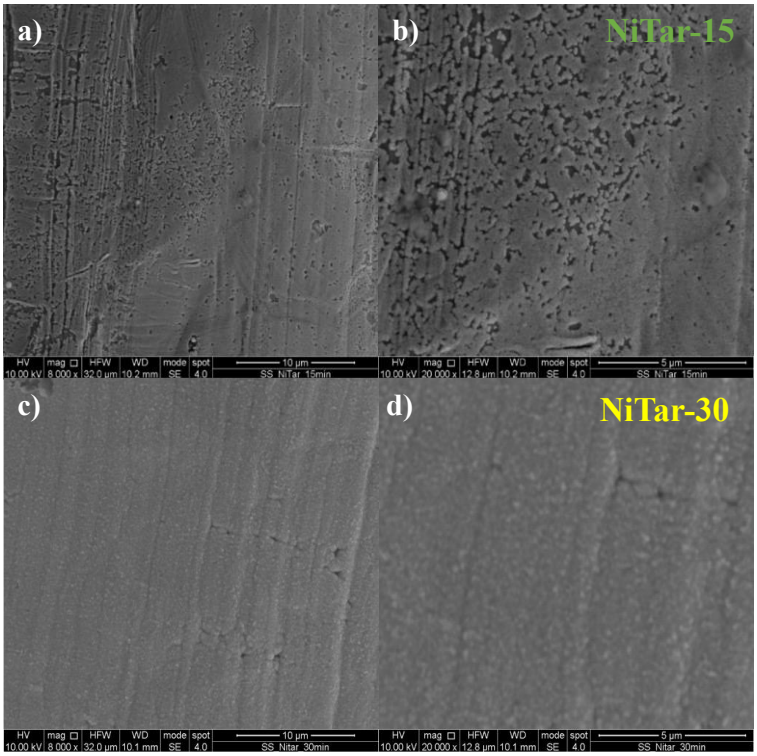

Figure 4.5 SEM images of NiTar-15 sample at a) 8000x and b) 20000x magnification. SEM images of NiTar-30 sample at c) 8000x and d) 20000x magnification. Image taken from [194].

Figure 4.4b) and d) clearly show how deposition time affects the coating morphology on the SS 304 mesh when succinic acid is used. After 15 min, the coating is made of particles with diameters of 1.1 ± 0.4 μm (Figure 4.4 b), while extending the deposition to 30 min produces a more compact layer made of smaller particles with an average size of 0.3 ± 0.1 μm (Figure 4.4 d). This compact structure is similar to that obtained with tartaric acid after 15 min (Figure 4.5 b), while a 30 min deposition time, using the same acid, lead to the formation of a more compact MOF layer, where is hard to notice individual nanoparticles (Figure 4.5 d). Table 4.2 reports the EDX data, showing the atomic composition in terms of C, O, Cr, Fe, and Ni.

Table 4.2 Atomic composition of 304 mesh sample and all the electrodeposited MOF structures obtained by EDX. Table taken from [194].

Sample	C (at%)	O (at%)	Cr (at%)	Fe (at%)	Ni (at%)
304 mesh		10.86	17.97	63.45	7.72
NiSuc-15	17.85	5.16	2.48	7.23	67.28
NiSuc-30	22.99	7.31	2.82	8.30	58.58
NiTar-15	33.19	16.28	9.23	31.19	10.11
NiTar-30	25.1	6.35	2.52	7.7	58.34

The presence of Fe and Cr originate from the 304 SS substrate whereas the presence of C, O and Ni is associated to the coating, even if Ni is also present in the

substrate. C presence is directly linked to the succinate/ tartrate demonstrating a MOF-like structure deposition. In the case of NiTar-15 sample, higher Fe and Cr levels were observed, most likely because the signal from the SS substrate was partially collected.

The hydrophilicity of MOF-based sample was also evaluated by means a water contact angle measurement, which is ~ 80◦ (see Figure 4.6 a and b), for both succinate and tartrate-MOF layers.

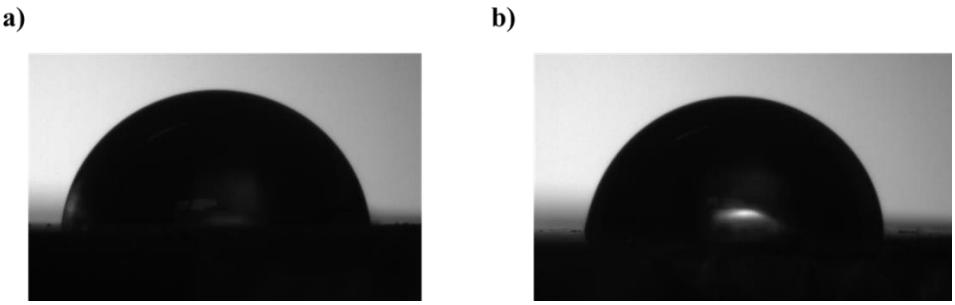

Figure 4.6 Static water contact angle for a) NiSuc-30 and b) NiTar-30 samples. Image taken from [194].

Figure 4.7 shows the XRD patterns of NiSuc-15 and NiTar-15 samples. To have an improved resolution, MOF structures were electrodeposited on a glass/FTO substrate, consequently several peaks of the diffractogram originate from FTO. The diffraction profile indicates that the crystal structure do not change varying the deposition time, or by changing the organic acid employed during the electrodeposition process. It is possible to notice that the diffraction peaks at 44.5◦, 51.86◦ and 76.39◦ correspond to the (111), (200) and (220) planes of face-centered cubic (FCC) metallic Ni [248,249], while the additional peaks are associated to the FTO substrate. The presence of metallic Ni can be explained by considering its possible electrodeposition during electrocatalysts preparation, as the applied potential during the electrodeposition is more negative than equilibrium potential related to the Ni/Ni^{2+} redox couple (Eq. 4.3).

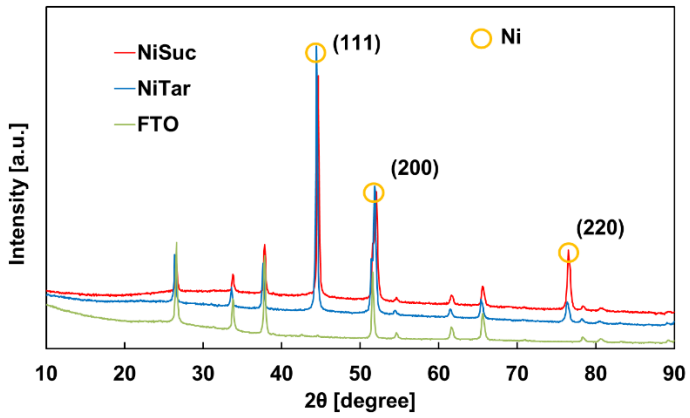

Figure 4.7 XRD patterns of NiSuc-15, NiTar-15 and FTO samples. Image taken from [194].

FTIR spectra of NiSuc-30 and NiTar-30 samples are reported in Figure 4.8.

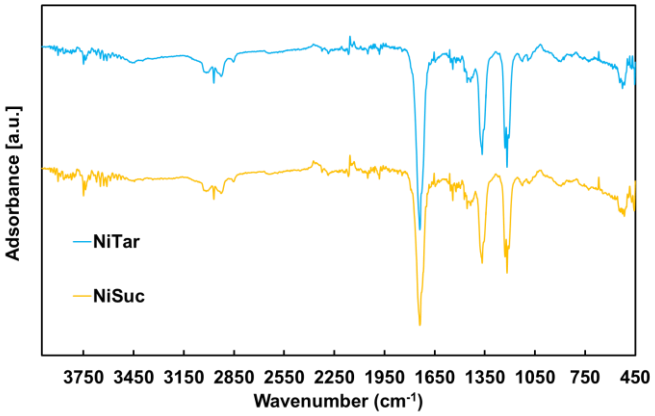

Figure 4.8 FTIR spectra of NiSuc-30 and NiTar-30 samples.

The FTIR spectra show several characteristic bands related to the functional groups of the organic linkers. In particular, bands at 1399 cm^{-1} and 1125 cm^{-1} can be assigned to (C–H), while the signals observed at 1367 cm^{-1} and 1542 cm^{-1} corresponds to the vibration of the carboxylate group ν(C–OO^-), coordinated with Ni^{2+} ions. An additional band at 1081 cm^{-1} is related to ν(C–C) stretching, whereas the vibration at 1450 cm^{-1} can be assigned to the C–OH group. In addition, a broad absorption with a maximum at 2971 cm^{-1} is observed, arising from the O–H stretching vibrations of water ligands; this feature indicates the formation of hydrogen bonds within the complex [228,250,251]. To better understand the role of the organic acids, reference FTIR spectra of pure succinic and tartaric acid were also collected, and are shown in Figure 4.9.

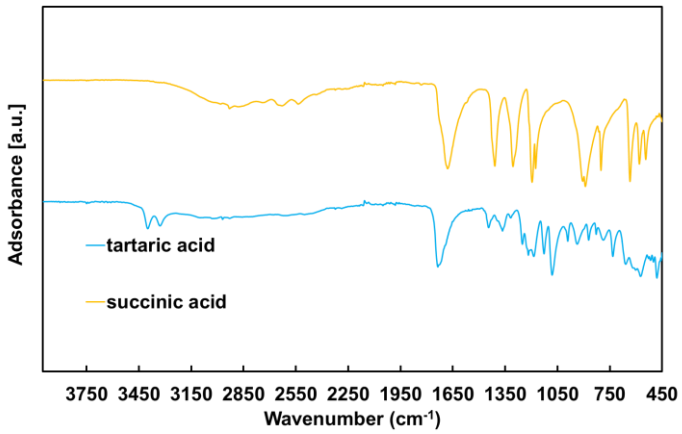

Figure 4.9 . FTIR spectra of Succinic and Tartaric acid samples.

In the case of succinic acid, the stretching vibration of carboxylic groups in the free acid appears at 1681 cm^{-1}. This peak disappears in the electrodeposited sample (see Figure 4.8), demonstrating the complexation of Ni by succinate groups and the formation of a MOF [194,228].

For tartaric acid, a peak visible at 3399 cm^{-1} can be associated with O–H stretching of the carboxyl group [252]. This signal is no longer present in the case of electrodeposited sample, further supporting the complexation of Ni by carboxyl

groups of tartrate ions. Overall, the comparison between pure acids and electrodeposited samples clearly evidences the complexation of Ni by succinate and tartrate ligands. Moreover, the spectral features remain essentially unchanged when varying the deposition time.

XPS was used to investigate the surface chemistry of NiSuc-15. In accordance with the EDX results, the survey spectrum (Figure 4.10) confirms the presence of C, O and Ni, confirming the formation of a structure that combines an organic ligand with a metallic component.

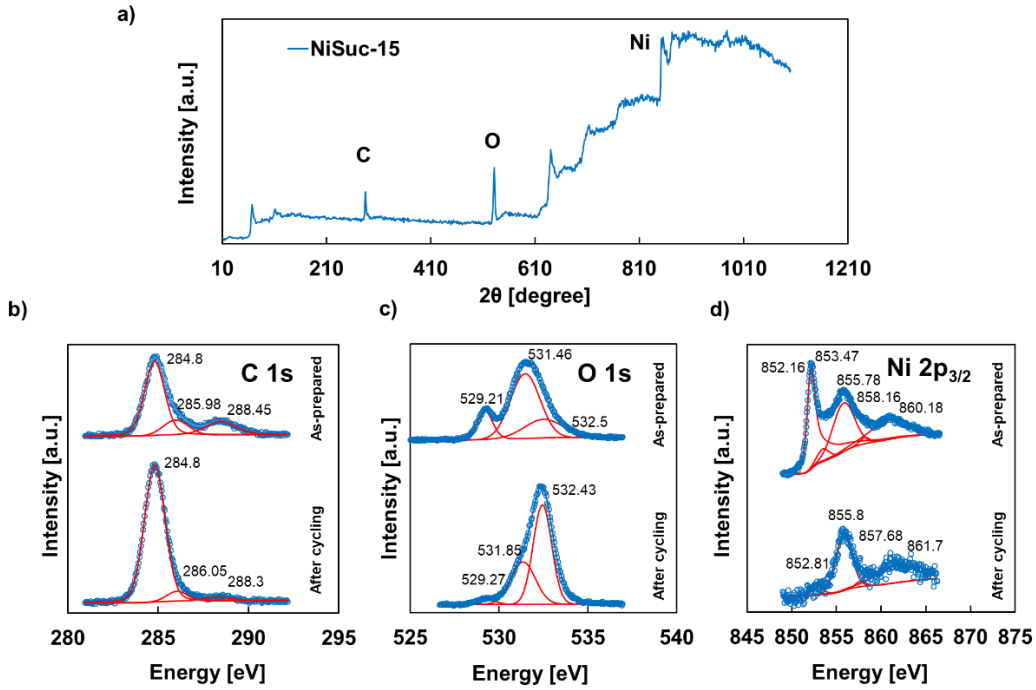

Figure 4.10 XPS analysis of NiSuc sample. a) survey scan spectrum, b) C 1s, c) O 1s, and d) Ni $2p_{3/2}$ spectra, for as-prepared sample and after electrochemical cycling.

In the Ni 2p region, the main $2p_{3/2}$ peak at 855.78 eV and the satellite at 860.18 eV are typical related to Ni^{2+} species, such as in $Ni(OH)_2$ [253,254]. A separate signal at 852.16 eV reveals the presence of metallic Ni (Ni^0), which can be attributed to electrodeposition occurring during the preparation of the catalyst. The C 1s spectrum shows a strong peak at 284.8 eV, due to C–C and C–H bonds from adventitious carbon. Also, the contributions detected at 285.98 eV and 288.5 eV, correspond to C–O and O–C=O groups of the ligand [255]. In the O 1s region, three signals are visible: the one at 532.5 eV is assigned to oxygen in organic groups, the peak at 531.46 eV is related to hydroxyls (–OH), in accordance with the presence of $Ni(OH)_2$. and the component at lower binding energy, 529.21 eV is typical of oxygen bound in metal oxides (M–O) [253,256,257]. After OER it is possible to notice an increase in the peaks related to oxidized species [198].

4.3. Electrochemical measurements

The electrocatalytic performance of the MOF-based electrodes was evaluated following the experimental protocol described in Section 3.1, which included electrochemical measurements with a particular focus on Electrochemical Impedance Spectroscopy. The tests were carried out in both batch and flow-through configurations, as described by the protocol, to evaluate the behaviour of the catalytic layers under different operating conditions. The flow-through setup, in particular, was employed to simulate the practical set-up of a porous transport layer in an industrial electrolyzer.

4.3.1 ECSA evaluation

To properly evaluate the electrocatalytic activity of the MOF-based electrodes, is essential to measure the electrochemically active surface area, as a larger ECSA corresponds to a greater number of active sites and, therefore, improved performance. For this purpose, the electrode C_{DL} was evaluated as an indicator of ECSA, as described in Section 2.2.

Therefore, EIS spectra were recorded in 0.1 M ABE under an inert atmosphere (Ar-saturated) at 0.1 V vs. RHE, ensuring that the measured current arose exclusively from non-faradaic processes, thereby excluding contributions from the oxygen reduction reaction. The Nyquist plots obtained for all samples are presented in Figure 4.11, along with a comparison to the bare 304 SS mesh. To extract meaningful information from the EIS spectra, the data must be fitted by a suitable EEC, capable of reproducing the electrochemical response of the system at the investigated electrode potentials. In the case of MOF-based electrodes, the chosen EEC is an R(RQ), Figure 4.11 b , which consists of the ohmic resistance of the electrolyte (R_s) in series with a parallel branch including the charge-transfer resistance (R_{ct}) and a constant phase element (Q_{DL}), which accounts for the non-ideal capacitive behaviour of the electrochemical double layer. The fitting results obtained with this model are reported in Table 4.3. From Q_{DL} value it is possible to calculate the C_{DL} by means the Eq. 2.18 in Section 2.2.1 [220].

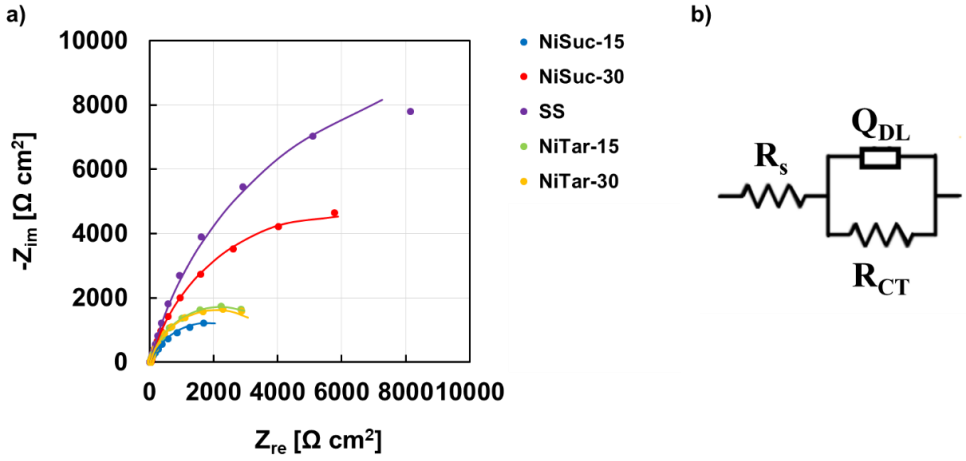

Figure 4.11 a) EIS spectra, reported in Nyquist representation, recorded at 0.1 V RHE, related to all the electrodes, b) Equivalent electric circuit, used for the fitting of EIS. Image taken from [194].

From the analysis of the fitting parameters reported in Table 4.3, and the corresponding value of C_{DL} reported in Table 4.4, it is possible to see that the C_{DL} values do not exhibit a relevant increase after the electrodeposition process. This behaviour can derive from the similar surface roughness, and consequently the comparable electrochemically active area, of the deposited MOF layers relative to the bare 304 SS mesh.

As expected for an ideally polarizable interface, the charge-transfer resistance R_{ct} measured for the 304 SS mesh is relatively high (3×10^4 Ω cm^2), the order of magnitude is the same for the electrodeposited MOF samples. Such elevated R_{ct} values confirm that, under the applied potential and experimental conditions, no Faradaic processes are taking place.

Table 4.3 Fitting parameters of EIS spectra recorded at 0.1 V RHE related to all the electrodes for the evaluation of ECSA. Table taken from [194].

Sample	R_s [Ω cm^2]	R_{ct} [Ω cm^2]	Q_{DL} [S s^n cm^{-2}]	n	χ^2
304 SS mesh	27	2.24×10^4	1.05×10^{-4}	0.85	1.2×10^{-2}
NiSuc-15	28	3.60×10^3	3.33×10^{-4}	0.76	7.4×10^{-3}
NiSuc-30	44	1.15×10^4	1.30×10^{-4}	0.85	1.4×10^{-2}
NiTar-15	31	4.40×10^3	2.18×10^{-4}	0.84	4.4×10^{-2}
NiTar-30	36	4.10×10^3	1.89×10^{-4}	0.84	1.1×10^{-2}

As reported in Section 2.2.1 C_{DL} can also be determined by CV method, performing CV measurements at different scan rates, always within a potential window free from faradaic contributions (e.g., between 0.1 and 0.42 V vs. RHE). CVs curves for all the investigated electrodes are shown in Figures Figure 4.12 a, c, e, and Figure 4.13 a, c. As reported in section 2.2.1. C_{DL} values can be extracted

from the slope of the i_{CL} vs. ν plot [221], reported in Figure 4.12 b, f, h, and Figure 4.13 b, d. The capacitances obtained using this method are in close agreement with those derived from EIS analysis, as reported in Table 4.4, confirming the reliability and consistency of the estimated C_{DL} values.

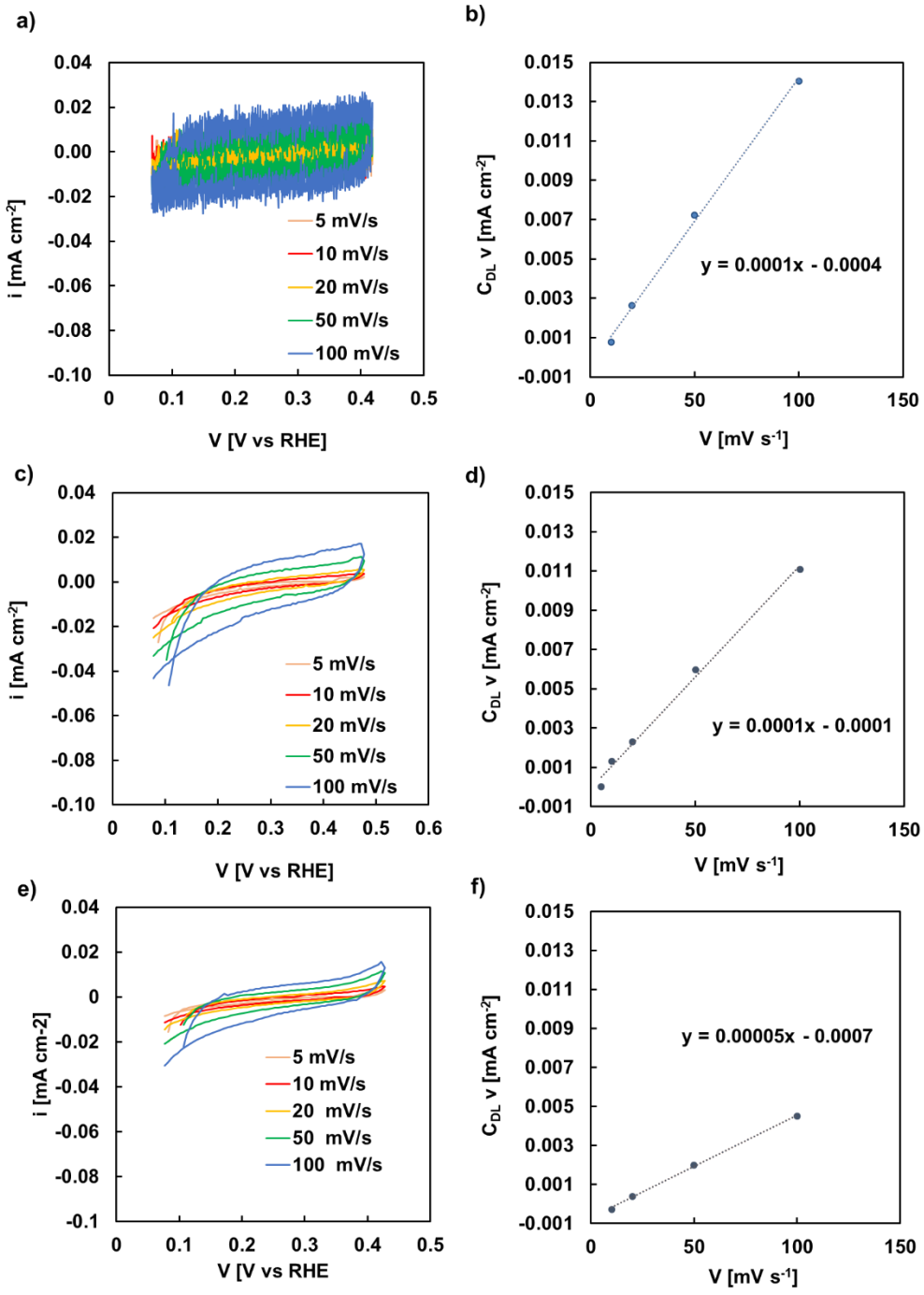

Figure 4.12 CV plots at different scan rates for a) SS, c) NiSuc-15, e) NiSuc-30 and samples, respectively. b), d), f) corresponding C_{DL} v *vs* v plots.

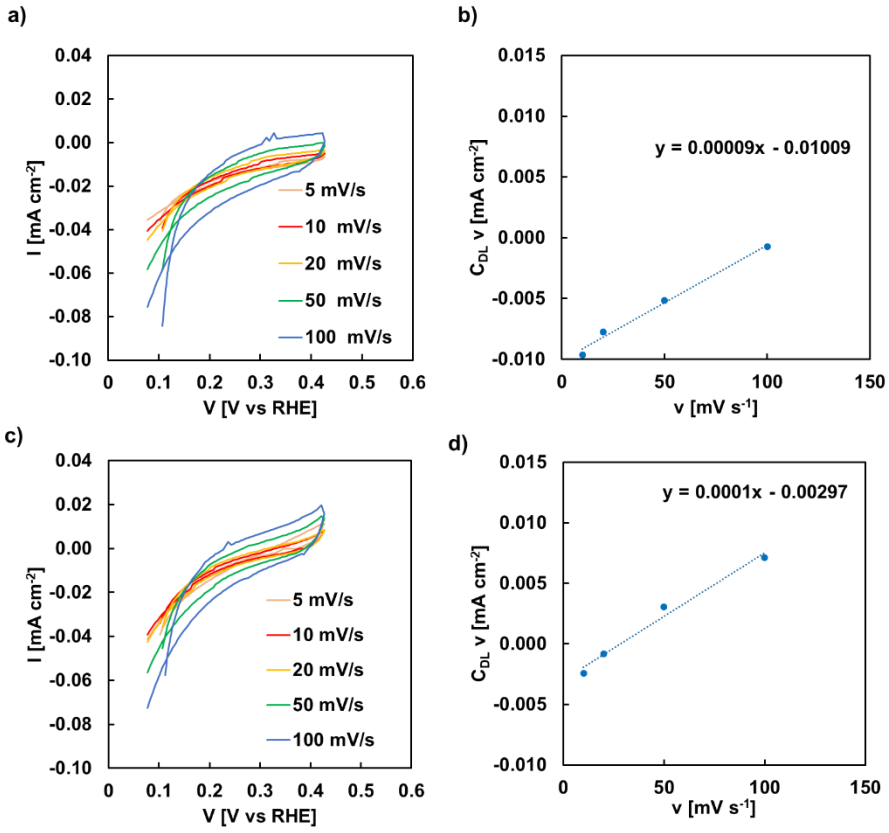

Figure 4.13 CV plots at different scan rates for a) NiTar-15 b s)NiTar-30 samples, respectively. b), d) corresponding C_{DL} v *vs* v plots.

Table 4.4 C_{DL} value [F cm^{-2}] of all MOF structures investigated in this study, calculated by EIS and CV methods.

Sample	EIS	CV
304 SS mesh	3.77×10^{-5}	1×10^{-4}
NiSuc-15	1.1×10^{-4}	1×10^{-4}
NiSuc-30	4.9×10^{-5}	5×10^{-5}
NiTar-15	8.7×10^{-5}	9×10^{-5}
NiTar-30	7.6×10^{-5}	1×10^{-4}

From the obtained C_{DL} values, and considering 50 µF cm^{-2} as the C_{DL} of a mirror-polished AISI 304 surface[219], the roughness factor (*r*) was calculated using Eq.2.17 in section 2.2.1.

The *r* values, determined as the average of those obtained from the two employed methods, are summarized in Table 4.5.

Table 4.5 Roughness factor of all MOF structures investigated in this study. Table taken from [194].

	304 SS mesh	NiSuc-15	NiSuc-30	NiTar-15	NiTar-30
Roughness factor r	1.40 ± 0.3	1.90 ± 0.4	1.05 ± 0.05	1.8 ± 0.1	1.8 ± 0.3

Considering the estimated *r* values and the morphological analysis of the electrodes by SEM Figure 4.4 and Figure 4.5, the ECSA is similar to that of the bare 304 SS mesh. Furthermore, if we combine these results with the catalyst mass loadings (Figure 4.3), it is possible to estimate the specific surface area (SSA) of the MOF coatings. The obtained SSA values range from 0.27 ± 0.08 $m^2\ g^{-1}$ for the NiSuc-15 sample to 0.52 ± 0.26 $m^2\ g^{-1}$ for the NiTar-15 sample.

4.3.2 Activity tests

As described in Section 3.1.3, the evaluation of catalyst activity was performed by means potentiodynamic tests in 1 M KOH, under both batch and flow-through configurations. The resulting polarization curves are presented in Figure 4.14 a and c), while the corresponding Tafel plots are reported in Figure 4.14 b and d.

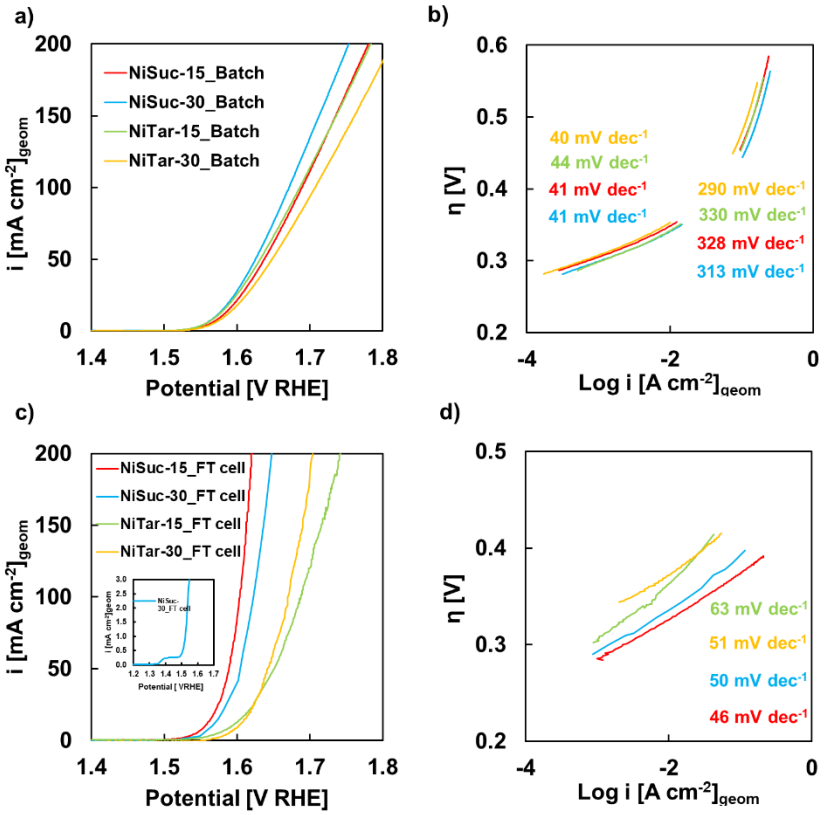

Figure 4.14 Comparison of i vs. potential curves, related to all the investigated electrodes, carried out in a) batch and c) flow through configurations. b) Tafel plot extrapolated from Figure 4.14a) and d) Tafel plot extrapolated from Figure 4.14c). Image taken from [194].

The analysis of the current density vs potential curves clearly shows that the MOF coating is able to fully prevent the happening of transpassive dissolution linked to chromate formation, even when very high anodic potentials are applied. This behaviour can be linked to the protective, passivating effect of the MOF layer, thanks to which there is no presence of current peaks related to Cr(III) [258]. At the same time, at the inset in Figure 4.14c) it is possible to see the well-known oxidation signal corresponding to the Ni^{2+}/Ni^{3+} transition, a process that generates catalytically active sites for enhancing OER activity [259–261].

In batch configuration (Figure 4.14 a), the different MOF electrodes show a similar behaviour. In particular, the onset potential for the OER is observed at 1.5 V vs RHE, corresponding to an onset overpotential (η_{onset}) of about 270 mV. A further relevant information is the overpotential required to reach 10 mA cm^{-2} (η_{10}), as this current density is typically adopted as a reference value for a device which converts solar energy to hydrogen [212]. In batch system configuration, η_{10} ranges between 340–352 mV, which is in line with the performance reported in the literature for MOF-based electrocatalysts [145]. What distinguishes our approach, to other literature catalysts however, is the fabrication route, because our catalysts have been obtained entirely through an electrochemical synthesis method, which could be easily scaled up at industrial level. Moreover, we used nontoxic organic molecules and a low-cost 304 stainless steel substrate, avoiding high expenses associated with more conventional supports such as Ni foams.

Finally, it is important to underline that the mass loadings of our succinate- and tartrate-derived electrocatalysts (Figure 4.3) are relatively low, ranging from 0.42 ± 0.1 to 0.96 ± 0.1 mg cm^{-2}. These values are inferior to those usually reported for MOF-based electrodes [145], which underlines the superior mass activity achieved by our catalysts.

In addition to the overpotential values, another key parameter for evaluating the electrocatalytic behaviour of the electrodes is the slope of the Tafel line, as explained in section 2.2.1. As shown in Figure 4.14 b, at low current densities the extracted Tafel slopes present a low value (40–44 mV dec^{-1}), independent of the specific MOF composition, reflecting a charge-transfer-controlled mechanism. However, when the current density increase up to 200 mA cm^{-2}, the Tafel slope rises to nearly 300 mV dec^{-1}, indicating that the process becomes dominated by non-kinetic effects, mainly related to oxygen bubble accumulation and consequently mass transfer limitations [262].

Moving to the flow-through configuration (Figure 4.14 c), succinate-based MOF electrodes exhibit superior performance compared to their tartrate-based counterparts, not in terms of η_{onset}, which remains essentially the same for all samples, but in terms of Tafel slope values, which is determined by the composition of the catalytic layer (ranging from 46 mV dec^{-1} for NiSuc-15 to 63 mV dec^{-1} for NiTar-15). These values suggest that the rate-determining step of the OER may vary with MOF composition. The flow-through setup also plays a significant role in bubble management, facilitating oxygen detachment from the electrode surface and thus enabling a more efficient reaction pathway. On the other hand, this

configuration may induce additional mechanical stress on the catalytic layer, underlining the importance of long-term stability tests (see below).

Interestingly, in the case of NiSuc-15 and NiSuc-30 electrodes, the Tafel slope remains nearly constant up to 200 mA cm^{-2}, whereas it starts to increase for NiTar-based samples, confirming that both MOF composition and film thickness strongly influence the OER mechanism. The lower Tafel slopes of NiSuc electrodes correspond to reduced η_{10} values, reaching 326 mV and 336 mV for NiSuc-15 and NiSuc-30, respectively. Notably, the minimum Tafel slope of 46 mV dec^{-1} is comparable with those reported for benchmark OER electrocatalysts such as IrO_2 and RuO_2 [120,121], and matches the value obtained by Wang et al. [261] for a fully electrochemically synthesized MOF catalyst, which is regarded among the best performances so far reported for MOF-based electrocatalysts prepared by electrochemical methods [148].

Impedance spectra were recorded in a flow-through configuration at two different electrode potentials, 1.52 V and 1.67 V vs. RHE, by applying an a.c. perturbation of 10 mV over the frequency range 0.1 Hz–100 kHz. The resulting spectra are presented in Figure 4.15 a and b in Nyquist form.

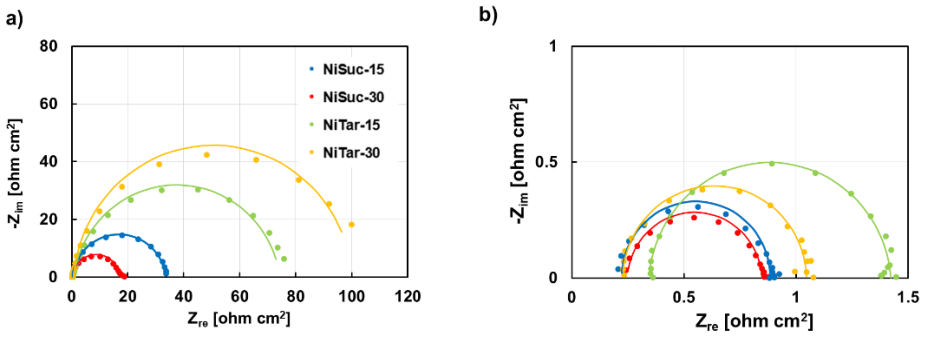

Figure 4.15 Electrochemical impedance spectra recorded at a) 1.52 V RHE and b) 1.67 V RHE for all the investigated electrodes in FT configuration. Fitting data are those reported with continuous lines. Image taken from [194].

To assess the reliability of the data, a Kramers–Kronig validation was performed using ZSimpWin. The results of this analysis are shown in Fig. 4.16 for a) NiSuc-15 and b) NiSuc-30 electrodes, which exhibited the best overall electrocatalytic performances. The excellent agreement between experimental and K–K transformed data confirms the physical consistency of the spectra.

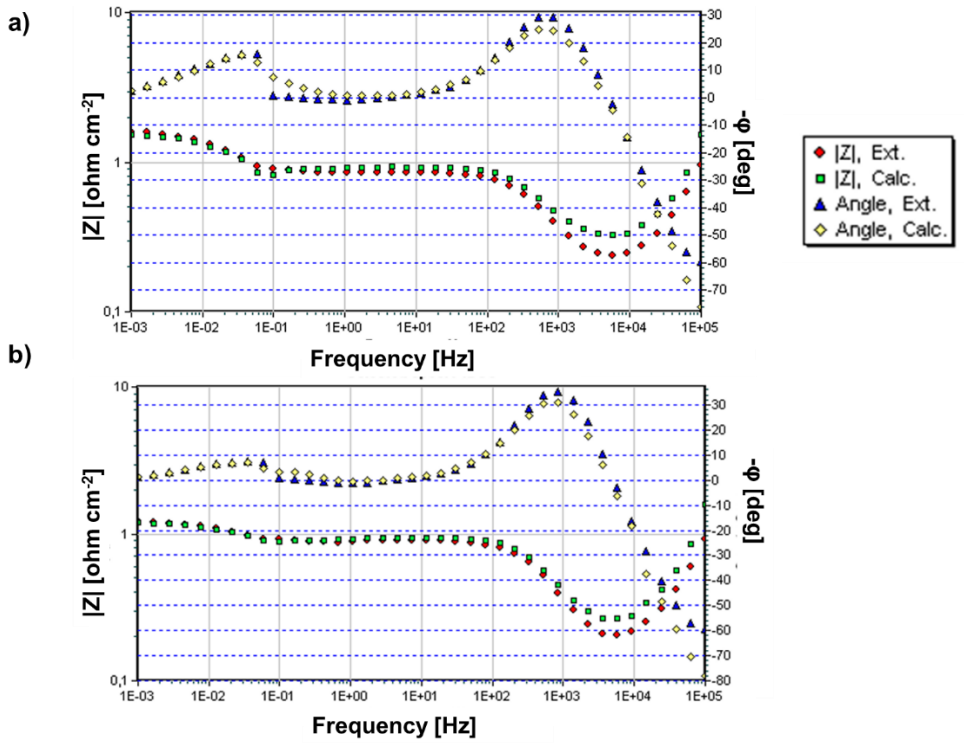

Figure 4.16 Kramer and Kroning validation of 1.67 V RHE spectra related to a) NiSuc-15 and b) NiSuc-30 electrodes in FT configuration.

In order to interpret the EIS spectra, datas have been fitted with an R(RQ) equivalent electrical circuit, Figure 4.11 b. The corresponding fitting parameters are reported in Table 4.6.

Table 4.6 Fitting parameters of EIS spectra recorded at 1.52 V RHE and 1.67 V RHE related to all the electrodes in FT configuration. Table taken from [194].

Sample	V [V RHE]	R_s [Ω cm^2]	R_{ct} [Ω cm^2]	$Q_{DL,el}$ [S s^n cm^{-2}]	n	χ^2
NiSuc-15	1.52	0.20	17	2.1×10^{-3}	0.95	6.5×10^{-2}
	1.67	0.25	0.6	1.1×10^{-3}	0.96	3.6×10^{-2}
NiSuc-30	1.52	0.17	34	2.1×10^{-3}	0.92	3.2×10^{-2}
	1.67	0.22	0.7	7.5×10^{-4}	1	1.2×10^{-2}
NiTar-15	1.52	0.64	74	1.8×10^{-3}	0.90	1.4×10^{-1}
	1.67	0.34	1.1	8.4×10^{-3}	0.95	3.1×10^{-4}
NiTar-30	1.52	0.64	100	1.7×10^{-3}	0.94	2.7×10^{-2}
	1.67	0.23	0.8	6.7×10^{-4}	0.98	1.1×10^{-3}

At 1.52 V vs RHE the reaction is not yet fully activated, as indicated by the relatively high R_{ct} values. When the potential is increased to 1.67 V vs RHE, R_{ct} significantly decreases, with the lowest values observed for NiSuc-15 and NiSuc-30, in agreement with the trends previously shown in Figure 4.14 c.

Electrochemical tests were also carried out in a more concentrated electrolyte, namely 6 M KOH, this electrolyte concentration corresponds to the conditions typically employed at industrial scale in alkaline water electrolyzers. To investigate

the electrode response under these realistic operating conditions, LSV measurements were performed for the NiSuc-30 sample. This sample was selected because it exhibited a very homogeneous MOF coverage, with few defects, and together with NiSuc-15 demonstrated the best overall electrochemical behaviour among the investigated electrodes. The resulting polarization curves, recorded both in batch and in flow-through configurations, are reported in Figure 4.17 a, while the corresponding Tafel plots are shown in Figure Figure 4.17 b.

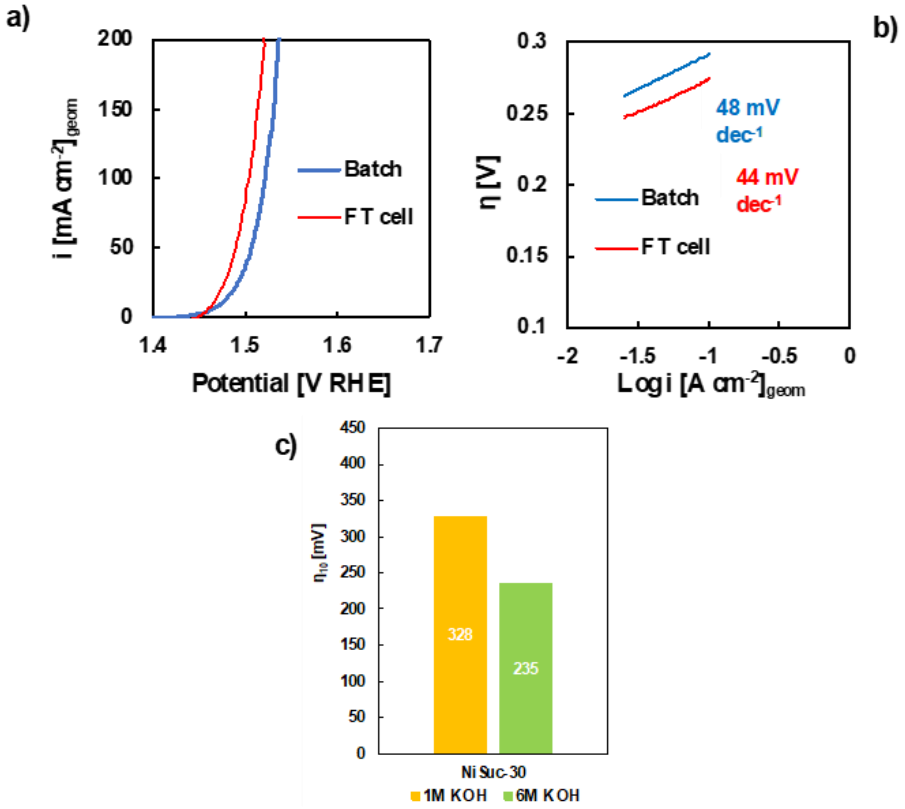

Figure 4.17 a) i vs. potential curves recorded in 6 M KOH aqueous solution in batch and FT configuration related to NiSuc-30 sample, with b) the corresponding tafel slopes values. c) Overpotential values estimated at 10 mA cm^{-2} in 1 M KOH and 6 M KOH aqueous solution. Image taken from [194].

It is important to highlight that, even under this highly alkaline environment, no sign of transpassive dissolution is detected. Moreover, the onset overpotential decreases compared to the measurements in 1 M KOH, reaching a value of 210 mV, while the Tafel slope remains practically unchanged. This behaviour is consistent with the role of OH^- concentration in enhancing the reaction kinetics, and in particular in affecting the i_0. The latter can be generally expressed as [263]:

$$i_0 = Fk^0 C^*_O{}^{(1-\alpha)} C^*_R{}^{\alpha} \qquad \text{Eq.3.1}$$

where, α is the transfer coefficient, k_0 the standard rate constant, and C_O and C_R represent the concentrations of the reacting species or intermediates at the electrode/electrolyte interface. This relation is valid for a generic equilibrium step $O + e^- \leftrightarrow R$, which can be considered the rate-determining step within a multistep process such as the OER. As a direct consequence, the overpotential at 10 mA cm^{-2}

(η_{10}) measured in 6 M KOH is lower than that obtained in 1 M KOH, as shown in Figure 4.17 c.

4.3.3 Durability tests

Another key aspect to be considered for large-scale applications is the long-term stability of the electrodes, which can be evaluated by means of chronopotentiometric measurements. In this work, stability tests were performed under particularly demanding and oxidizing conditions, namely at 0.05 A cm^{-2} in aqueous 1 M KOH for a continuous operation of 100 hours. For this purpose, the best-performing samples, NiSuc-15 and NiSuc-30, were selected and investigated in flow-through configuration. The corresponding stability profiles are presented in Figure 4.18 a and b.

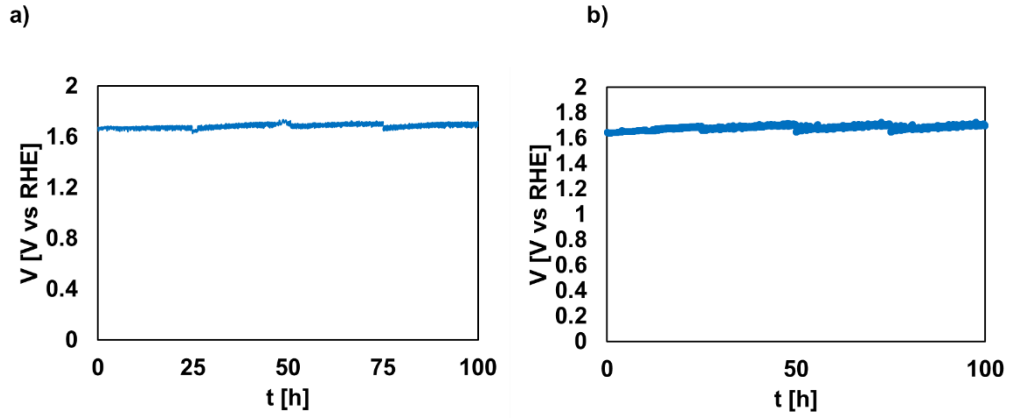

Figure 4.18 Durability test carried out at 0.05 A cm^{-2} in aqueous 1 M KOH solution for a) NiSuc-15 and b) NiSuc-30 samples.

The overpotential required for OER remained essentially stable throughout the 100 h test, with values of 435 ± 6 mV for the NiSuc-15 sample (Figure 4.18 a) and 459 ± 16 mV for NiSuc-30 (Figure 4.18 b), thereby confirming the remarkable durability of both electrodes. Furthermore, post-test SEM analysis (Figure 4.19) revealed no evidence of material detachment or degradation of the catalytic layer, further supporting the mechanical robustness and long-term stability of the MOF coatings under harsh operating conditions.

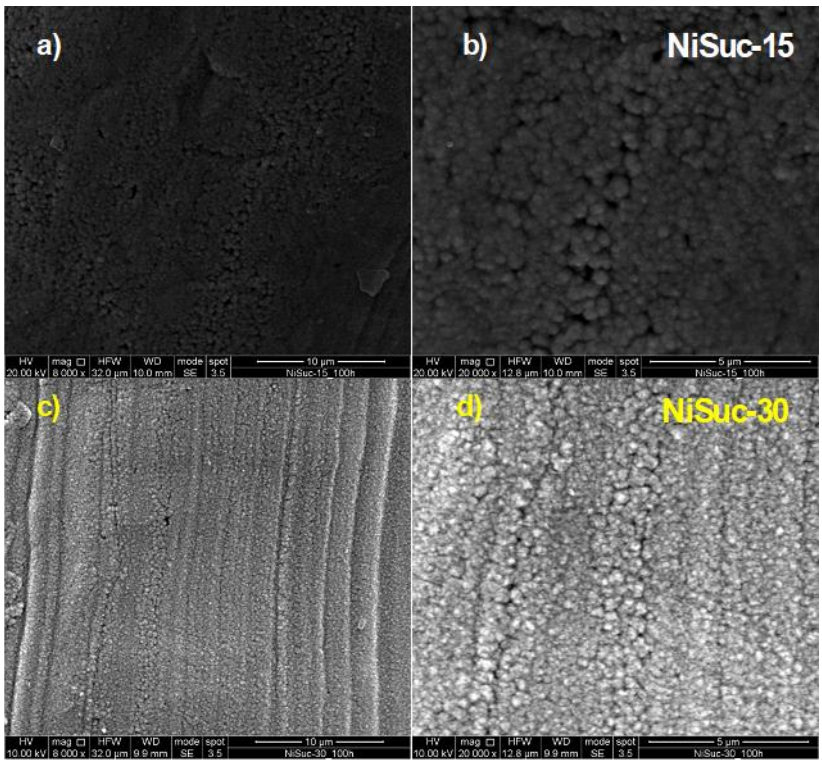

Figure 4.19 SEM images of a),b) NiSuc-15 sample and of c),d) NiSuc-30 sample after durability test in 1 M KOH. Image taken from [194].

After the stability test, LSV curves and EIS spectra were recorded again in order to compare the initial electrocatalytic performance with that obtained after 100 hours of continuous operation.

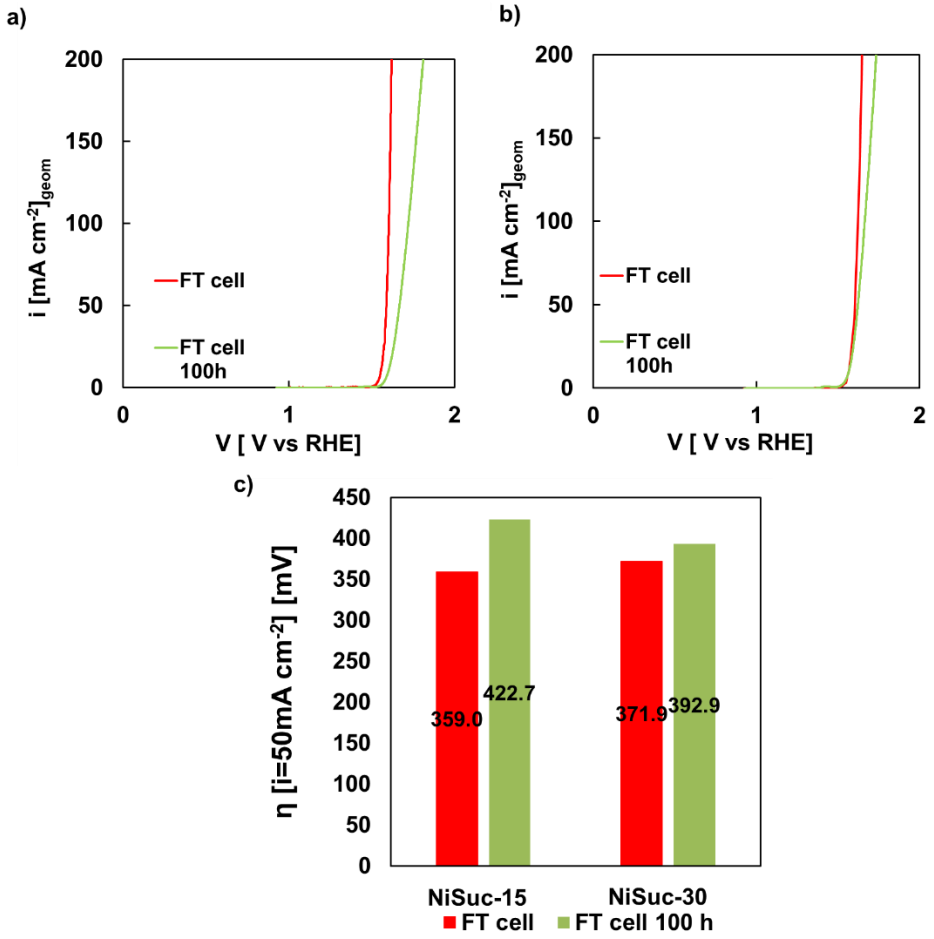

Figure 4.20 Current density vs. electrode potential curves carried in a flow through cell for a new electrode and for an electrode after 100h electrolysis in 1M KOH, related to a) NiSuc-15 and b) NiSuc-30min, recorded in 1 M KOH aqueous solution - c) Overpotential values estimated at 50 mA cm^{-2} for all the electrodes.

After 100 h of electrolysis, polarization curves (Figure 4.20 a, b) show a slight decay in the performance of both samples, lower in the case of NiSuc-30. Nevertheless, both catalysts maintain very good activity for this class of materials, confirming their durability. In Figure 4.20 c, it is possible to notice that, for NiSuc-15**,** the overpotential at 50 mA cm^{-2} increased from 359.0 mV to 422.7 mV, indicating a moderate deterioration in catalytic activity. In contrast, NiSuc-30 exhibited only a slight increase, from 371.9 mV to 392.9 mV, suggesting superior long-term stability.

The EIS spectra, (Figure 4.21) agree with this behaviour. The Nyquist plots displays only a moderate increase in the semicircle diameter after the stability test, indicating a limited growth in charge transfer resistance, as it is possible to see from the fitting parameters showed in Table 4.7.

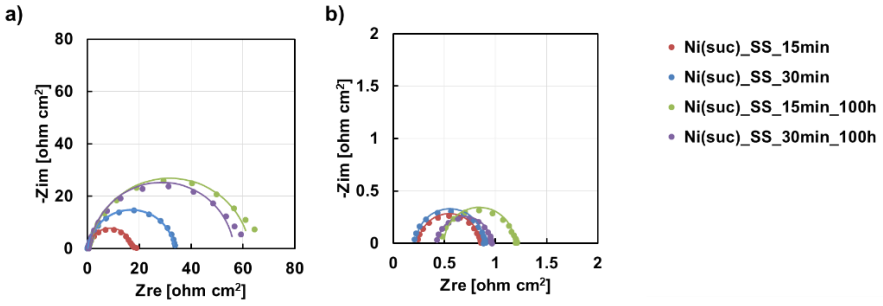

Figure 4.21 . Electrochemical impedance spectra recorded at a) 1.52 V RHE and b) 1.67 V RHE forNiSuc-15 and NiSuc-30 before and after stability test. Fitting data are those reported with continuous lines.

Table 4.7 Fitting parameters of EIS spectra recorded at 1.52 V RHE and 1.67 V RHE related to NiSuc-15 and NiSuc-30 electrodes in FT configuration before and after 100 h

Sample	V [V RHE]	R_s [Ω cm^2]	R_{ct} [Ω cm^2]	$Q_{DL,el}$ [S s^n cm^{-2}]	n	χ^2
NiSuc-15	1.52	0.7	62	2.9×10^{-3}	0.91	1.3×10^{-2}
	1.67	0.5	0.68	1.2×10^{-3}	1	1.2×10^{-3}
NiSuc-30	1.52	0.75	56	2.4×10^{-3}	0.93	1.9×10^{-2}
	1.67	0.43	0.51	1.3×10^{-3}	1	2.6×10^{-3}

To further confirm the reliability of the impedance data, Kramers–Kronig validation was performed on the spectra collected after 100 hours, in

Figure 4.22 the spectra recorded at 1.67 V for both 15 and 30 min are shown. The excellent agreement between experimental and calculated values confirmed that the data satisfy the K–K relations.

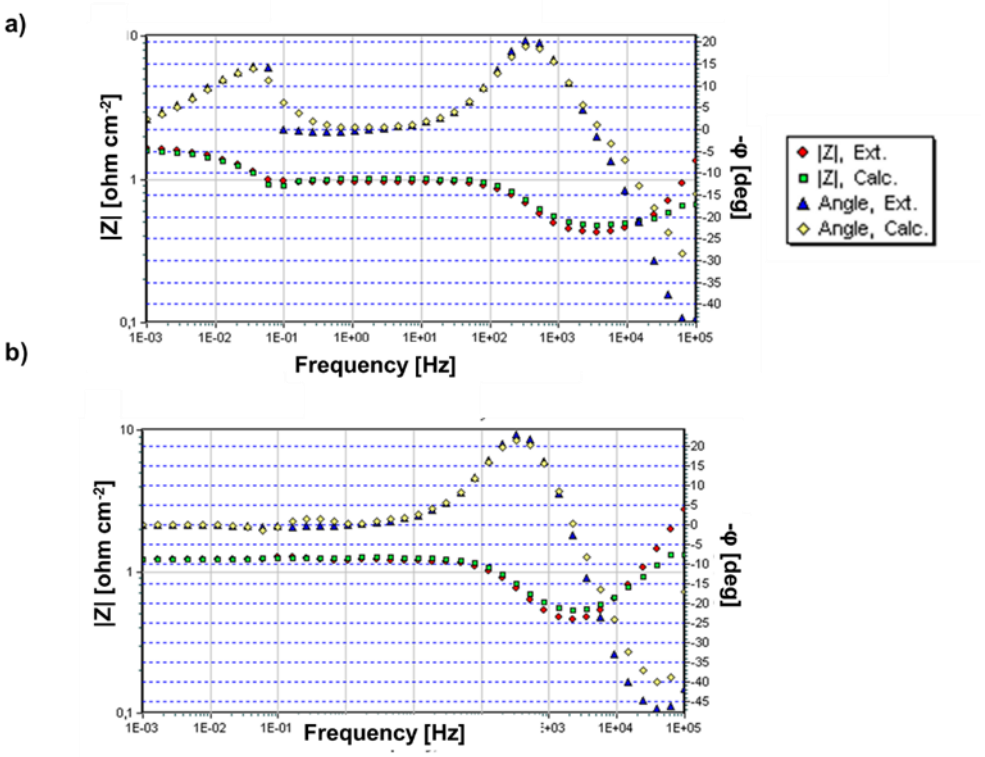

Figure 4.22 Kramer and Kroning validation of 1.67 V RHE spectra related to NiSuc-15 and NiSuc-30 electrodes in FT configuration after 100 h electrolysis.

The stability test was also carried out for the NiSuc-30 sample in 6 M KOH. Under these conditions, assessing the long-term electrocatalytic activity is particularly important, as possible dissolution phenomena may occur at such a high pH. For this purpose, the same 100 h test at 0.05 A cm^{-2} was performed, and the corresponding electrode potential vs. time profile is shown in Figure 4.23 a.

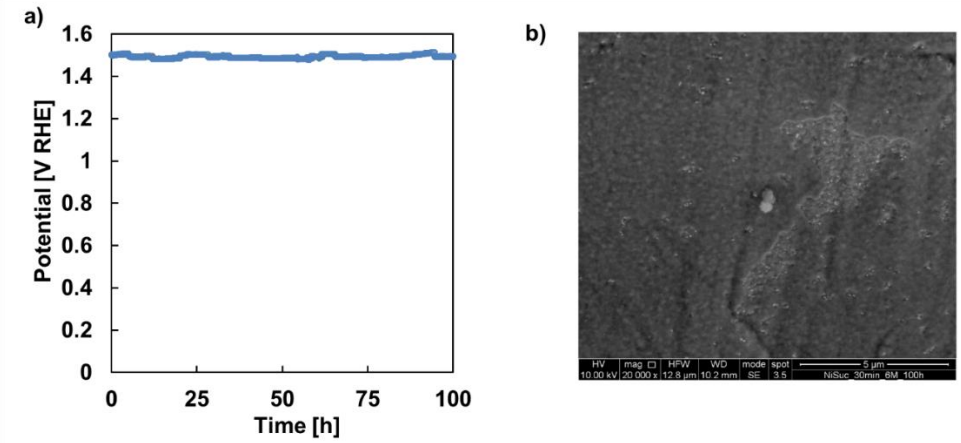

Figure 4.23 Durability test carried out at 0.05 A cm^{-2} in aqueous 6 M KOH solution for) NiSuc-30 sample, b) SEM images NiSuc-30 sample after durability test in 6 M KOH. Image taken from [194].

As can be observed, the electrode potential remains highly stable over the entire 100 h test, with an overpotential of 260 mV, highlighting the remarkable electrocatalytic durability of this succinate-based MOF electrode. Furthermore, the morphology of the catalytic layer is well preserved after the stability test (Figure 4.23 b), and its atomic composition (Table 4.8) is very similar to that measured immediately after the electrodeposition process (Table 4.2).

Table 4.8 Atomic composition of NiSuc-30 sample, obtained by EDX, after durability test in 6 M KOH.

Sample	C (at%)	O (at%)	Cr (at%)	Fe (at%)	Ni (at%)
NiSuc-30	22.4	13.01	4.09	12.53	46.86

The electrochemical behaviour NiSuc-30 electrode in 6 M KOH was further investigated by LSV and EIS measurements after 100 h of operation as shown in

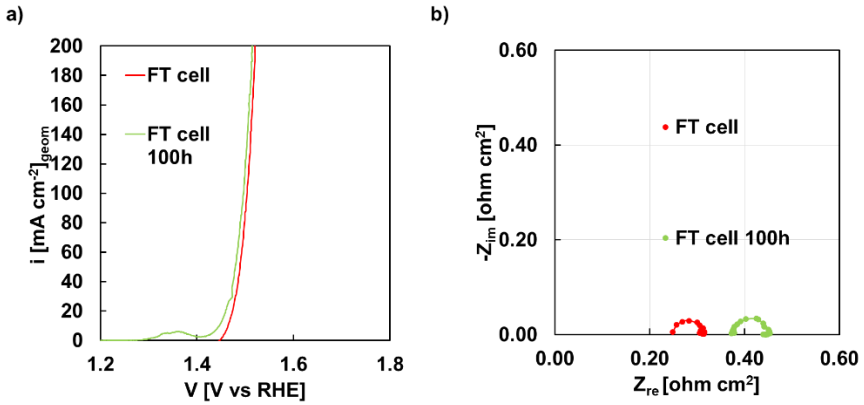

Figure 4.24 Current density vs. electrode potential curves carried in a flow through cell for a new electrode and for an electrode of NiSuc-30 after 100h electrolysis in 6M KOH. Fitting data are those reported with continuous lines.

LSV curves before and after electrolysis are really similar, confirming that the electrode maintains a stable polarization behaviour even in such a concentrated electrolyte. The Nyquist plots reveal a slight increase in the charge transfer resistance (Table 4.9), suggesting preserved electrode kinetics and good durability under these harsh conditions.

To ensure the reliability of the impedance data, K–K validation was carried out at 1.67 V vs. RHE (Figure 4.25), confirming the physical consistency of the data.

Table 4.9 Fitting parameters of EIS spectra recorded at 1.67 V RHE related to a new electrode and an electrode of NiSuc-30 after 100h electrolysis in 6M KOH in flow through configuration.

Sample	V [VRHE]	R_s [Ω cm^2]	R_{ct} [Ω cm^2]	$Q_{DL,el}$ [S s^n cm^{-2}]	n	χ^2
6 M KOH	1.67	0.25	0.06	2.6×10^{-3}	1	2.1×10^{-3}
6M KOH 100h	1.67	0.38	0.07	1.13×10^{-2}	0.94	2.9×10^{-3}

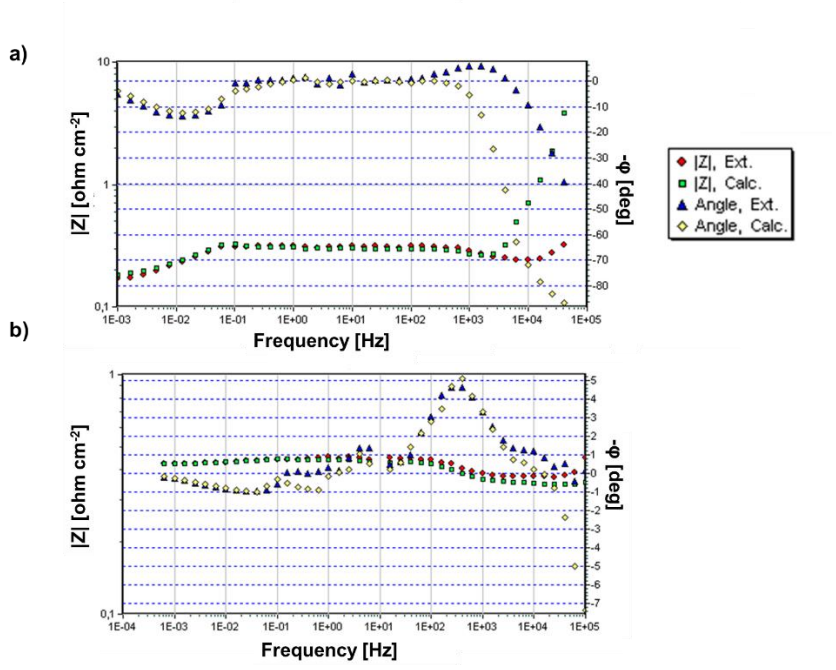

Figure 4.25 Kramer and Kroning validation of 1.67 V RHE spectra related to NiSuc-30 electrodes in FT configuration in 6M KOH before and after 100 h electrolysis.

4.4 Conclusions

In summary, the experimental protocol developed in this work proved to be effective for the reliable characterization of the electrodes, allowing us to combine electrochemical activity and stability tests within a consistent framework. This methodology was then applied to Ni succinate and tartrate-based MOF nanostructures synthesized on SS mesh substrates through an optimized electrodeposition process under mild conditions. The presence of coordinated Ni guaranteed the electrocatalytic activity, while succinate-based electrodes displayed the best performance, with a Tafel slope as low as 46 mV dec^{-1} in flow-through configuration, close to benchmark OER catalysts. In addition, they showed remarkable durability, sustaining 50 mA cm^{-2} for at least 100 h in 1 M KOH without degradation. Even in more aggressive conditions (6 M KOH), typical of industrial alkaline electrolyzers, the succinate-based electrode preserved its stability, maintaining 50 mA cm^{-2} for 100 h at an overpotential of 260 mV. This behaviour can be attributed to the synergistic effect of the highly active Ni centres with the

structural stability provided by the succinate linker. The behaviour of this sample could be also improved by tuning its composition, as we will see in the next chapter.

5. Electrochemical and Structural Investigation of Electrodeposited NiFe-MOF for Oxygen Evolution in AEM Water Electrolysis

In this work the *Protocol for functionalized PTLs,* developed for the characterization of catalyst electrodeposited on mesh, is applied on a Platinum Group Metal-free (PGM-free), NiFe based electrocatalysts, for the Oxygen Evolution Reaction (OER) in alkaline conditions.

As described in the previous chapter for Ni-based electrocatalysts, NiFe samples also synthesized by an optimized electrodeposition process in the presence of succinic acid as organic linker, Fe samples have been deposited for comparison. The material was directly grown on a low-cost 304 SS mesh, avoiding complex synthesis methods that involve the use of high temperature or toxic precursor materials [149,264,265]. In this way it is possible to form an inorganic–organic complex with high activity and durability, deposited on a conductive and mechanically robust support suitable for large-scale applications [136,194].

In particular, spinel-type $NiFe_2O_4$, that is formed after the first OER cycle, has been identified as a highly active material toward OER, thanks to the possibility of tuning its structural and electronic properties [266–271]. Nevertheless, the stability of these catalysts under OER conditions is still a challenge. The use of organic linkers has recently been explored to improve durability, conductivity, and porosity of the catalytic layer, while also affecting the distribution of active sites [142].

The electrodes were characterized according to the customized protocol described in Section 3.1, to systematically investigate their morphology, composition, and structure. Their electrochemical performance was then evaluated under alkaline conditions following the same procedure adopted also in Chapter 4, and the most active electrodes were tested in a single-cell Anion Exchange Membrane Water Electrolyzer, confirming their high current density and good stability under realistic conditions.

5.1. MOF electrodeposition

NiFe and Fe catalysts have been made up by cathodic electrodeposition process, from an aqueous solution containing the carboxylic acid (i.e. succinic acid) and Ni^{2+} and/or Fe^{2+} ions as discussed in section 2.1.1. During the deposition process, a lightly decreasing cathodic current is registered, due to the HER, to

increase a local OH^- concentration. According to literature, alkaline conditions favor the deprotonation of succinic acid, leading to the formation of succinate ions. These ions will interact with metal ions in solution promoting the crystallization of metallic succinate, where succinate ions acts as ligand for Ni^{2+} and Fe^{2+} ions [148,194,198,202,272,273].

At the same time, under these conditions, the formation of metallic Ni and Fe cannot be excluded (see below), particularly due to the applied overpotential with respect to the equilibrium potential at the working pH, as well as it is not possible to exclude the deposition of NiFe hydroxides [273,274]. The current density vs time curves related to the deposition of the analysed sample are reported in Figure. 5.1.

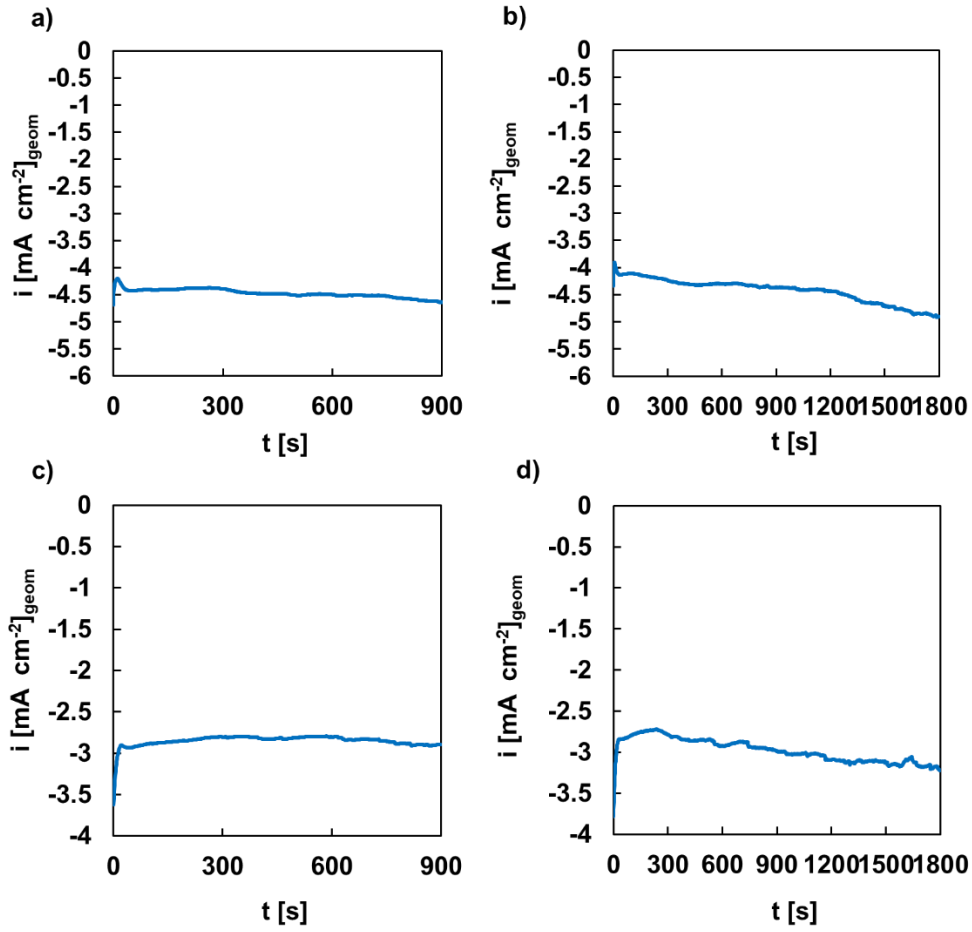

Figure 5.1 Current density vs time curves recorded during the electrodeposition process carried out at -1.4 V (Ag/AgCl) for a) 15 min and b) 30 min in 8.75 mM of succinic acid 7.5 mM of $NiSO_4$ and 7.5 mM of $FeSO_4$, and for c) 15 min and d) 30 min in 8.75 mM of succinic acid and 7.5 mM of $FeSO_4$. Image taken from [198].

Catalyst mass loadings estimated from the mass differences before and after electrodeposition is reported in Figure 5.2.

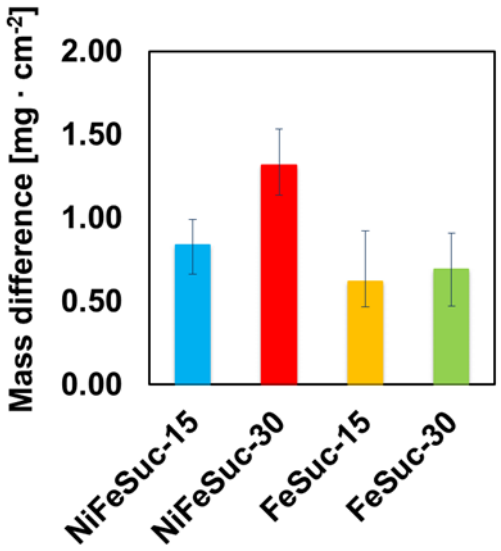

Figure 5.2 Mass loadings for all the investigated MOF electrodes. Image taken from [198].

5.2. MOF-based electrocatalysts morphology and composition

Following the protocol described in Section 3.1, the catalyst was studied through an extensive morphological and structural characterization, using FTIR, XPS, and SEM analyses, with the aim of correlating its electrochemical performance with its chemical and morphological properties.

The surface morphologies of the samples were analysed to understand their structural properties and potential defects. Figure 5.3 presents the surface images at of FeSuc-15 and FeSuc-30 respectively, while Figure 5.4 of NiFeSuc-15 and NiFeSuc-30.

At lower magnification, FeSuc-15 sample surface (Figure 5.3 a) appears irregular and only partially covered, whereas a deposition time of 30 minutes lead to the formation of a more homogeneous coating (Figure 5.3 c). At higher magnification, both FeSuc-15 and FeSuc-30 samples display a cubic-like morphology, with smaller particles decorating the surface of the microcubes (Figure 5.3 b and d).

In contrast, at lower magnification, the overall surfaces of NiFeSuc-15 and NiFeSuc-30 samples appear more uniform and exhibit better coverage (Figure 5.4 a and c, respectively) compared to Fe-based samples. A particle-rich structure is observed, with particle diameters on the order of several hundred nm. Increasing the deposition time to 30 minutes, leads to the formation of larger particles and a thicker multilayer coating (Figure 5.4 c). Particularly, each particle consists of a nanosheet array, which provides an increased surface area at the nanometer scale.

Similar nanosheet array morphologies have also been reported for NiFe-based organic–inorganic structures [253].

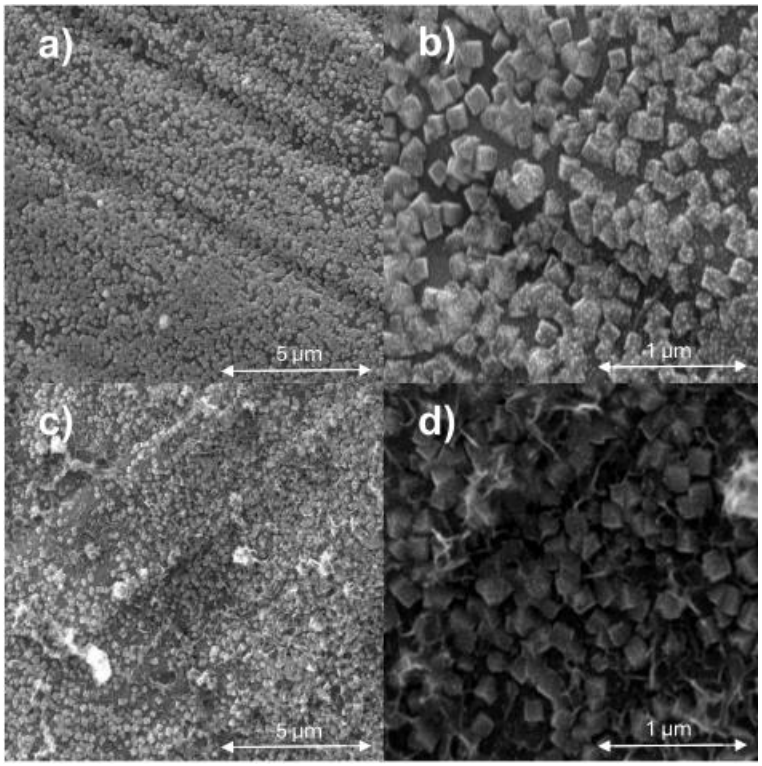

Figure 5.3 SEM images of a), b) FeSuc-15 sample and c), d) FeSuc-30 sample. Magnification: a), c) 20000x and b), d) 80000x. Image taken from [198].

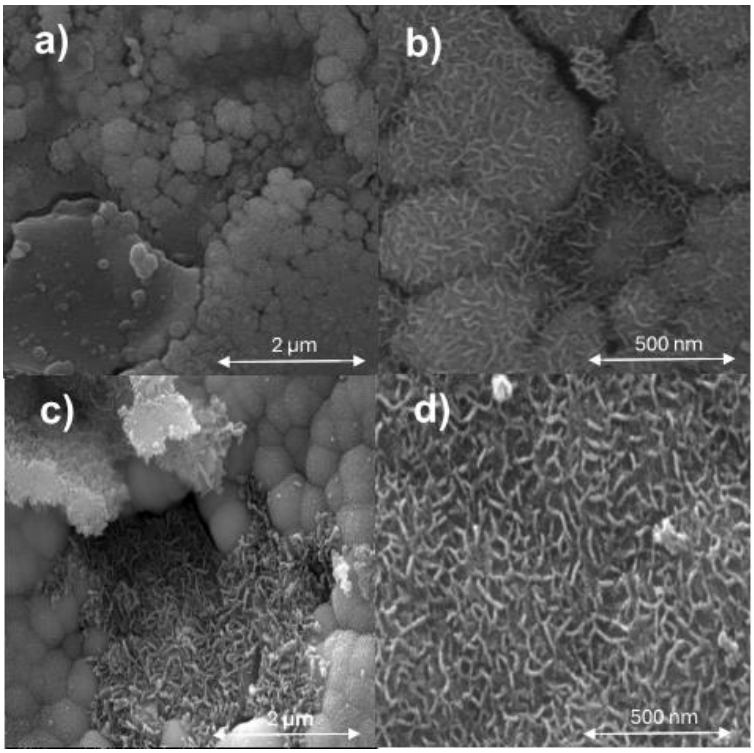

Figure 5.4 SEM images of a), b) NiFeSuc-15 sample and c), d) NiFeSuc-30 sample. Magnification: a), c) 50000x and b), d) 200000x. Image taken from [198].

Table 5.1 summarizes the composition of the coating deposited on SS mesh. Carbon (C) and oxygen (O) signals comes from the coating, whereas the presence of chromium (Cr) originates from SS substrate. Nickel (Ni) and iron (Fe) contribution derives both from the coating and the substrate. In NiFe samples, the Fe content is lower than that in the SS, indicating that the measured fraction meanly originates from the deposited layer. Ni and C amounts increase with deposition time, demonstrating the coating became thicker enhancing the deposition time from 15 to 30 min.

Table 5.1 Atomic composition of 304 mesh sample and all the electrodeposited MOF structures obtained by EDX. Table taken from [198].

Sample	C [at%]	O [at%]	Cr [at%]	Fe [at%]	Ni [at%]
304 mesh		10.86	17.97	63.45	7.72
FeSuc-15	9.58	7.91	16.29	60.62	5.59
FeSuc-30	7.04	8.83	16.23	61.33	5.3
NiFeSuc-15	12.71	22.73	7.53	34.56	20.99
NiFeSuc-30	21.3	25.91	3.92	23.42	24.38

FTIR analysis offers relevant information on the molecular composition of the analysed samples. The spectra collected for FeSuc and NiFeSuc samples and for pure succinic acid, are reported in Figure 5.5. Succinic acid FTIR spectra presents a characteristic peak around 1700 cm^{-1}, which corresponds to the C=O stretching of the carboxylic group [155]. In FeSuc-15 and NiFeSuc-15 spectra, it is possible to notice that this peak is shifted toward lower wavenumbers, because the succinic acid ligand is coordinated with one or two metal centers, depending on the electrode composition. The broad absorption band in the 3000–3500 cm^{-1} region is attributed to O–H stretching vibrations of water ligands, suggesting that hydrogen bonding are present in the complex [155,228,250,275,276]. Furthermore, the carboxylate group vibrations, ν(C–OO), appearing at approximately 1400 cm^{-1} (symmetric stretching) and 1300 cm^{-1} (asymmetric stretching) in the spectrum of pure succinic acid [155], are also evident in the spectra of both NiFeSuc-15 and FeSuc-15. Importantly, the overall FTIR spectral features remain unchanged as a function of electrodeposition time [198].

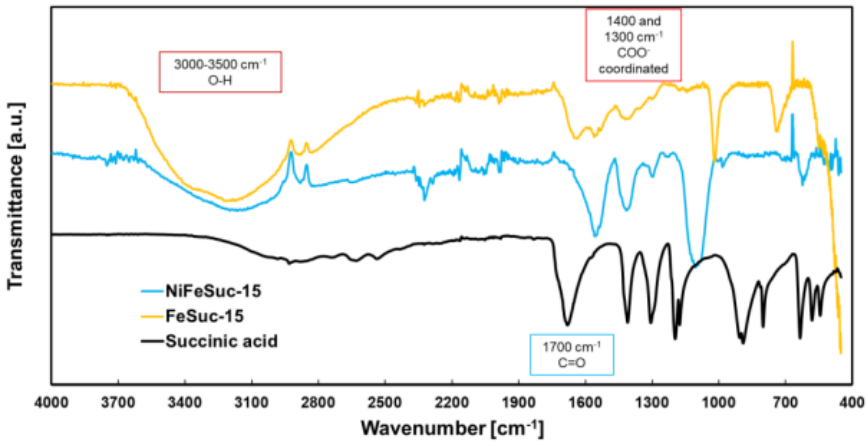

Figure 5.5 FTIR spectrum related to NiFeSuc-15 sample, FeSuc-15 sample and succinic acid powder. Image taken from [198].

XPS analysis was used to investigate the chemical state of the NiFeSuc-15 surface and compared it with those of FeSuc-15 and NiSuc-15. In agreement with EDX results, the survey XPS spectrum of NiFeSuc-15 (Figure 5.6 a) shows the presence of C, O, Ni, and Fe. The finding of these elements provides an additional evidence of the formation of a framework made by an organic ligand and metallic centres (Ni and Fe).

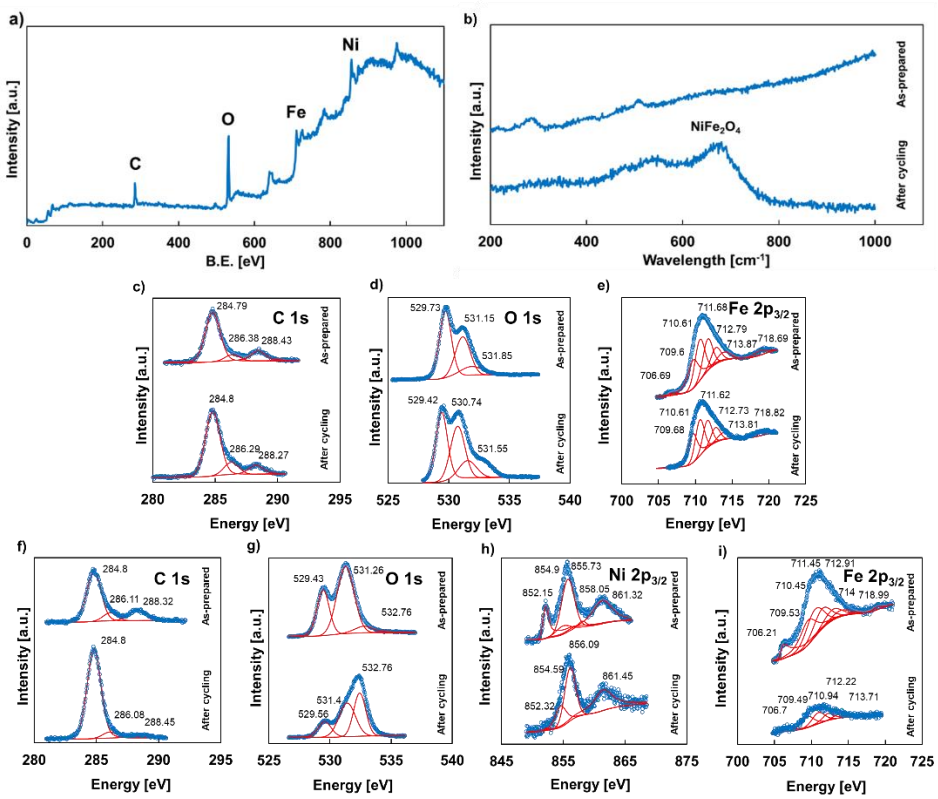

Figure 5.6 XPS analysis of NiFeSuc-15 sample. a) survey scan spectrum, XPS analysis of FeSuc-15 sample, c) C 1s, d) O 1s, e) Fe $2p_{3/2}$, and, NiFeSuc-15 sample, f) C 1s, g) O 1s, h) Ni $2p_{3/2}$. i) Fe $2p_{3/2}$ spectra, for as-prepared sample and after electrochemical cycling. b) Raman spectrum of NiFeSuc-15 sample. Image taken from [198].

Ni $2p_{3/2}$ spectra presents a main peak at 855.7 eV, which together with the shoulder at 861.32 eV, is assigned to Ni^{2+} species, such as those in $Ni(OH)_2$ [253,254], while the peak at 852.15 eV corresponds to metallic Ni (Ni^0). Similarly, the Fe $2p_{3/2}$ envelope at 711.45 eV, with a shoulder at 718.9 eV, is attributed to Fe^{3+} species, such as FeOOH, whereas the peak at 706.21 eV indicates the presence of metallic Fe (Fe^0) [277,278]. Ni^0 and Fe^0 presence can be due to the electrodeposition of metallic species during catalyst preparation, as previously discussed.

The C 1s spectrum of NiFeSuc-15 shows a peak at 284.8 eV, corresponding to C–C and C–H groups from adventitious carbon. Additional peaks at 286.11 eV and 288.32 eV are assigned to C–O and O–C=O groups of the organic ligand, respectively [255]. In the O 1s region, a peak at 532.76 eV is related to oxygen in the organic ligand, while the signal at 531.26 eV is associated with hydroxyl groups (–OH), reliable with the presence of FeOOH and $Ni(OH)_2$. A lower binding energy peak at 529.43 eV is attributed to oxygen in metal oxides (M–O).

Finally, FeSuc-15 display the same oxidation states for C, O, Ni, and Fe as observed in NiFeSuc-15, as confirmed by their XPS spectra [253,256,257].

5.3. Electrochemical measurements

The electrocatalytic performance of the MOF-based electrodes was evaluated following the protocol described in Section 3.1, with a particular emphasis on Electrochemical Impedance Spectroscopy. In addition, the electrodes were tested at varying electrolyte concentrations and temperatures, providing further insights into their electrochemical behaviour and stability. Finally, the best-performing electrode was selected for validation in an AEMWE single-cell setup, in order to confirm its activity under realistic operating conditions.

5.3.1 ECSA evaluation

As reported in the previous paragraph ECSA represents a key parameter for the evaluation of the activity of an electrocatalyst, since it reflects the fraction of the electrode surface which effectively participate in the electrochemical process. A larger ECSA reflects a higher density of active sites, enhancing the efficiency of electrocatalytic reactions.

To determine the ECSA of the samples, as reported in Section 2.2.1, EIS measurements were carried out in an Ar-saturated 0.1 M ABE aqueous solution, at 0.1 V RHE, in order to evaluate the double-layer capacitance (C_{DL}) [220]. The Nyquist plots of all recorded EIS spectra are reported in Figure 5.7 a.

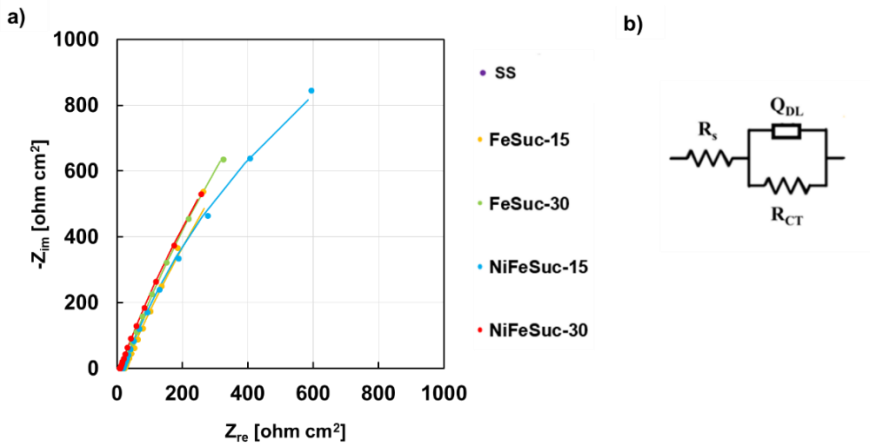

Figure 5.7 .a) Nyquist plot of impedance spectra recorded for the evaluation of ECSA of all the electrodes. Fitting data are those reported with continuous lines. b) Equivalent electrical circuit used for fitting procedure. Image adapted from [198].

For the extraction of relevant information from the EIS data, an R(RQ) circuit have been used Figure 5.7 b. The fitting parameters are reported in Table 5.2.

Table 5.2 Fitting parameters of EIS spectra recorded at 0.1 V RHE related to all the electrodes for the evaluation of ECSA. Table taken from [198].

Sample	R_s [Ω cm^2]	R_{ct} [Ω cm^2]	$Q_{DL.el}$ [S s^n cm^{-2}]	n	χ^2
304 SS mesh	26.7	2.2×10^4	1.05×10^{-4}	0.85	1.2×10^{-2}
NiFeSuc-15	18.9	3.6×10^3	1.2×10^{-3}	0.77	7.4×10^{-3}
NiFeSuc-30	9.4	6.08×10^3	2.4×10^{-3}	0.78	1.1×10^{-3}
FeSuc-15	23.2	7.03×10^3	2.5×10^{-3}	0.74	1.3×10^{-3}
FeSuc-30	19.6	6.4×10^3	1.9×10^{-3}	0.78	9.3×10^{-4}

C_{DL} values can be calculated from Q_{DL} using the given Eq. 2.18 [220], and are reported in Table 5.3

As previously discussed in Section 2.2.1, C_{DL} can be evaluated by the CV method, recording cyclic-voltammograms at different scan rates within a potential window free from faradaic contributions (0.1–0.42 V vs. RHE). CV profiles are reported in Figure 5.8 a, c, e, g). The corresponding C_{DL} values have been extracted from the slope of the i_{CL} *vs.* ν plots [221] (Figure 5.8 b, d, f, h). Also in this case, the capacitances derived by CV are in close agreement with those obtained from EIS analysis (Table 5.3), further confirming the reliability of the method and the consistency of the estimated C_{DL} values.

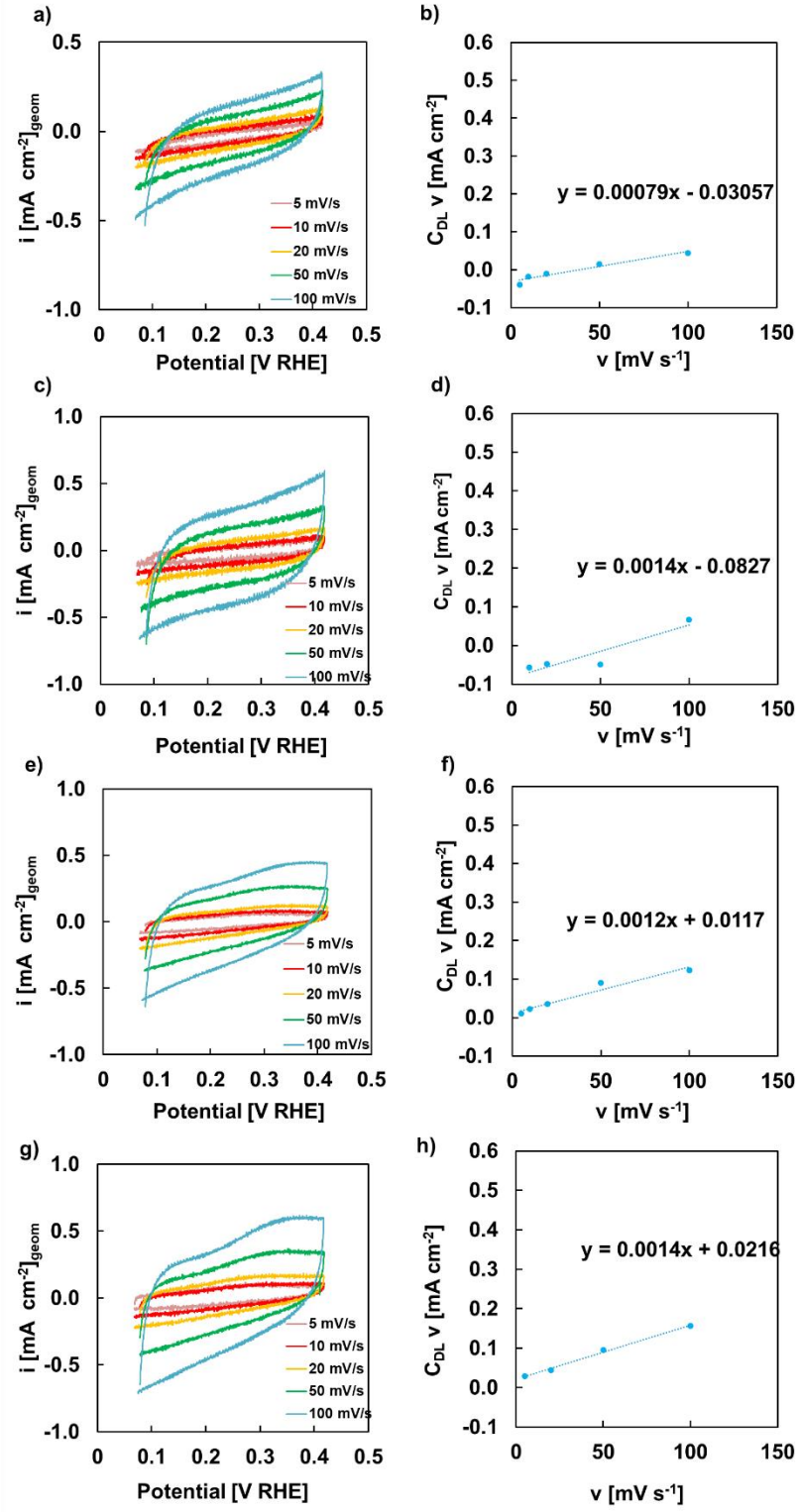

Figure 5.8 CV plots at different scan rates for a) NiFeSuc-15, c) NiFeSuc-30, e) FeSuc-15 and g) FeSuc-30 samples, respectively. b), d), f) h) corresponding C_{DL} v vs v plots.

Table 5.3 C_{DL} value [F cm^{-2}] of all MOF structures investigated in this study.

	304 SS mesh	NiFeSuc-15	NiFeSuc-30	FeSuc-15	FeSuc-30
EIS	3.7×10^{-5}	5×10^{-4}	8.4×10^{-4}	9.7×10^{-4}	8.1×10^{-4}
CV	1×10^{-4}	7×10^{-4}	1.4×10^{-3}	1.2×10^{-3}	1.4×10^{-3}

From the obtained C_{DL} values, and assuming 50 μF cm^{-2} as the reference C_{DL} for a mirror-polished AISI 304 surface[196], the roughness factor (r) have been calculated according to the Eq.17 reported in Section 2.2.1.

Table 5.4 Roughness factor, r, estimated for all the investigated electrodes.

		304 SS mesh	NiFeSuc-15	NiFeSuc-30	FeSuc-15	FeSuc-30
Roughness factor r	EIS	0.75-1	10	16.9	19.52	16.2
	CV	2	14	28	24	28

The roughness factors estimated from both EIS and CV measurements are comparable, confirming the consistency of the two electrochemical methods. The bare 304 SS mesh exhibits a roughness factor close to 1, while FeSuc and NiFeSuc samples display an increased r. This result is further supported by SEM images, where a well-developed and porous microstructure is observed, responsible for the increase in electroactive surface area.

In addition, specific surface area (SSA) values for the MOF structures can be determined based on the mass loadings of the catalysts (Figure 5.2). The SSA values vary from 1.05 ± 0.18 m^2/g for the NiFeSuc-15 sample, 1.31 ± 0.2 m^2/g for the NiFeSuc-30 to 4 ± 0.4 m^2/g for the FeSuc-15 sample and to 2.5 ± 0.7 m^2/g for the FeSuc-30 sample.

5.3.2 Activity tests

First the synergistic effect of coupling Ni and Fe for the OER was studied, comparing the results with the bare metals, in a batch and flow through configuration at 25°C using 1 M KOH as the electrolyte. As it is possible to notice from Figure 5.9, the current density obtained with NiFeSuc samples under those conditions is larger than that obtained wit FeSuc samples, and also higher than NiSuc samples reported in literature [194,279]. Furthermore, at that conditions the

deposition time doesn't significantly affect the electro-catalytic activity of the NiFeSuc samples. In particular, NiFeSuc-15 catalytic layer exhibited very high activity even if it presents the lowest roughness factor, indicating that its superior performance arises from intrinsic electrocatalytic properties rather than from a higher active surface. In contrast, the larger roughness factors observed for the FeSuc samples, indicate an even lower intrinsic electrocatalytic activity.

Moving from the batch to the flow-through configuration, different behaviours emerge, depending on the electrode. For NiFeSuc, the performance remains essentially unchanged: the nanosheet morphology ensures efficient exposure of active sites and rapid bubble detachment already in static conditions, such that the flow does not introduce further improvements. At the contrary, in the case of FeSuc electrodes, a remarkable increase in current density is observed under flow-through operation. In this case, the morphology and sluggish intrinsic kinetics make the system strongly affected by mass transport and bubble accumulation in batch mode. Therefore, the introduction of forced convection improves these limitations, activating a larger fraction of the surface. Nevertheless, even under FT conditions, FeSuc electrodes remain less active than NiFeSuc, due to the intrinsically higher catalytic activity of the Ni–Fe sites compared to Fe-only sites [198].

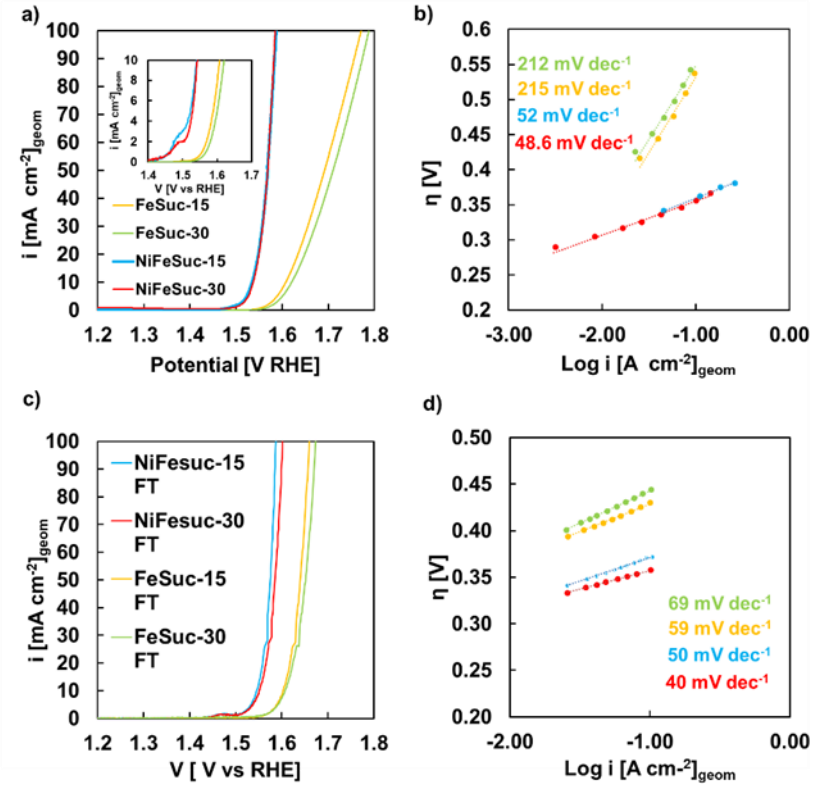

Figure 5.9 Comparison of i vs. potential curves, related to all the investigated electrodes, carried out in a) batch and c) flow through configurations. b) Tafel plot extrapolated from Figure 4.7) and d) Tafel plot extrapolated from Figure 4.7 c). Image adapted from [198].

As it is possible to notice from Figure 5.10, the onset potential for OER depends on the electrode material. In batch configuration, for NiFeSuc, it is about 1.47 V vs. RHE, while for FeSuc electrodes it is 1.55 V vs. RHE. These values correspond to an onset overpotential value, η_{onset}, of 240 mV and 320 mV respectively. Regarding η_{10}, the NiFeSuc samples exhibit an overpotential of 306 mV, while the FeSuc samples show higher values in the range of 378mV and 392 mV. The overpotential observed for NiFeSuc is comparable to those performances reported in literature for best OER electrochemical NiFe-based or SS-based electrodes [198,280]. In FT configuration it is possible to notice an improvement of those values, indeed the onset potential for OER for NiFeSuc shows a value of about 1.44 V vs. RHE, while for FeSuc electrodes it is comprised between 1.54 and 1.52 V vs. RHE. These values correspond to an onset overpotential value, η_{onset}, of 210 mV and between 310 mV and 300 mV respectively. In the field of OER catalysts, NiFeSuc samples performances are similar to RuO_2, characterized by η_{10} = 295 mV and a value of Tafel slope of 71 mV dec^{-1}[193], and outperform commercial IrO_2 deposited on carbon cloth, which present a η_{100} (i.e. 353 mV vs 415 mV for IrO_2) [281].

This result is also noteworthy when considering the mass loadings that are 0.83 ± 0.15 mg cm^{-2} for NiFeSuc-15, 1.31± 0.2 mg cm^{-2} for NiFeSuc-30, 0.5± 0.4 mg cm^{-2} for FeSuc-15 and 0.69 ± 0.2 mg cm^{-2} for FeSuc-30, as it is possible to see in Figure 5.2.

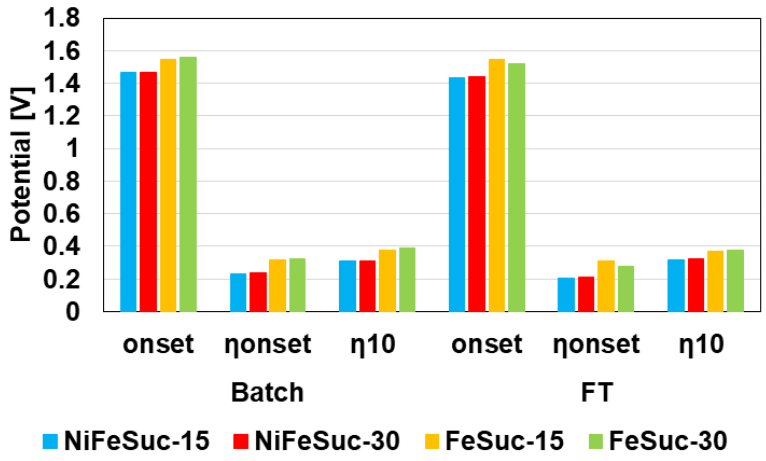

Figure 5.10 Onset potential, onset overpotential and overpotential at 10 mA cm^{-2}, for all the electrodes, in batch and flow throug configuration.

The superior electrochemical performance of NiFeSuc-based electrodes is further confirmed by the slope values of the η vs. log(i) plots (i.e., Tafel slopes), shown in Figure 5.9 b. In batch configuration for NiFeSuc electrodes, the Tafel slopes are approximately 50 mV dec^{-1}, whereas for the FeSuc electrode they are close to 210 mV dec^{-1}. These high values suggest that the lower electrochemical performance of FeSuc derives not from its limited intrinsic kinetic activity, but also from mass transport limitations. In particular, the pronounced Tafel slope can be due by non-kinetic effects, especially severe oxygen bubble formation and detachment at the electrode surface [215,217]. In flow through configuration for

NiFesuc sample the Tafel slope it's almost unchanged, while it is possible to notice a high reduction for Fesuc sample, thanks to an improved bubble detachment and a better mass transport.

These observations are verified by the EIS spectra recorded at 1.52 V RHE and 1.67 V RHE in batch configuration, presented in Figure 5.10 a and b, in Nyquist representation. The electrochemical response was fitted using the equivalent electrical circuit displayed in Figure 5.7 b), and the corresponding fitting parameters are summarized in Table 5.5.

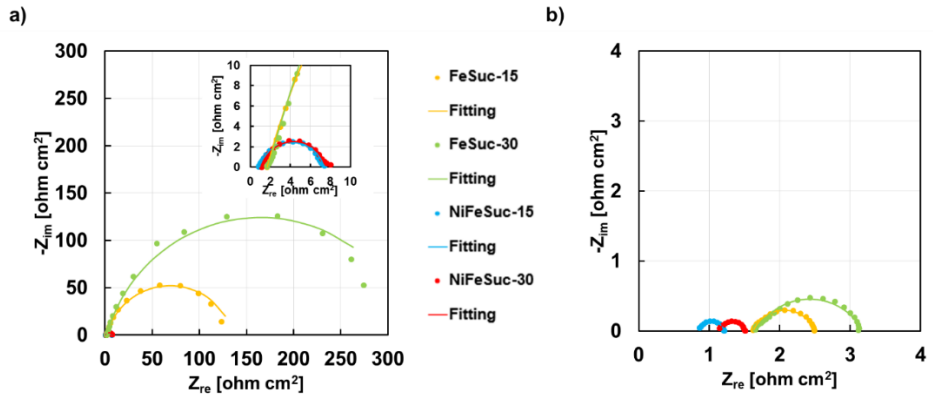

Figure 5.11 Nyquist plot of EIS spectra recorded at a) 1.52 V RHE and b) 1.67 V RHE for all the electrodes in batch configuration. Inset: equivalent electrical circuit used for fitting impedance data. Fitting data are those reported with continuous lines. Image taken from [198].

To verify the reliability of the impedance data, K–K validation was performed at 1.67 V vs. RHE (Figure 5.12), confirming the physical consistency of the data.

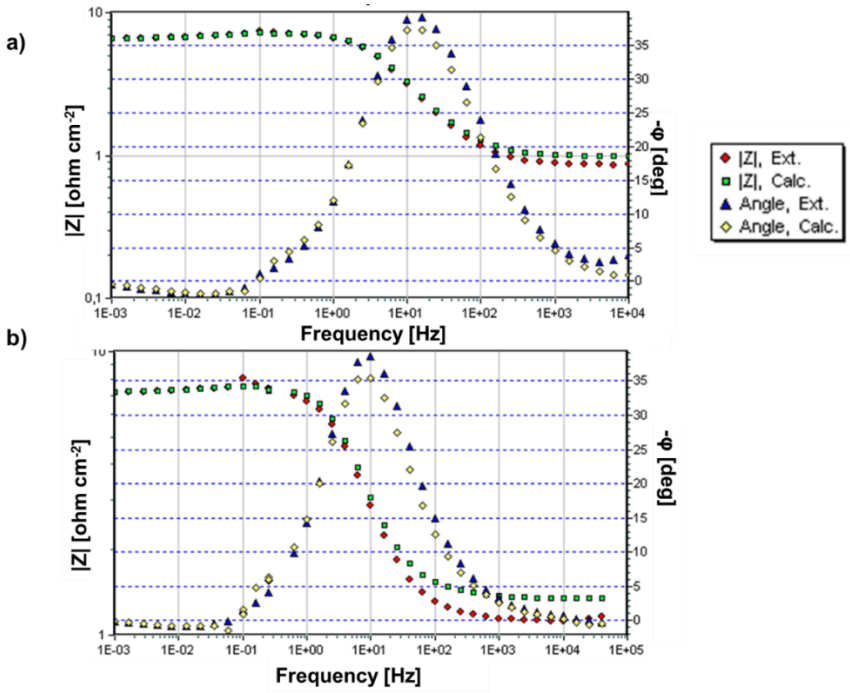

Figure 5.12 Kramer and Kroning validation of 1.52 V RHE spectra related to NiFeSuc-15 and NiFeSuc-30 electrodes in 1 M KOH in batch configuration.

Table 5.5 Fitting parameters related to EIS spectra, recorded at 1.52 and 1.67 V RHE, reported inFigure 5c) and 5d). Table taken from [198].

Sample	V [V RHE]	R_s [Ω cm^2]	R_{ct} [Ω cm^2]	$Q_{DL,el}$ [S s^n cm^{-2}]	n	χ^2
FeSuc-15	1.52	1.709	134.6	1.8×10^{-3}	0.83	2×10^{-3}
	1.67	1.62	0.87	6.5×10^{-3}	0.76	6.5×10^{-5}
FeSuc-30	1.52	1.8	326.1	1.2×10^{-3}	0.82	5.8×10^{-3}
	1.67	1.7	1.5	8.5×10^{-3}	0.7	2.5×10^{-4}
NiFeSuc-15	1.52	0.89	6.46	1.04×10^{-2}	0.81	5.1×10^{-3}
	1.67	0.86	0.36	1.06×10^{-2}	0.82	5.03×10^{-5}
NiFeSuc-30	1.52	1.13	6.47	1.2×10^{-2}	0.84	4.1×10^{-4}
	1.67	1.13	0.38	1.5×10^{-2}	0.8	2.99×10^{-5}

At 1.52 V vs RHE, the FeSuc electrode is still not electrochemically activated, as confirmed by the high R_{ct} values, while the NiFeSuc samples already show clear activation. Increasing the potential to 1.67 V vs RHE, the R_{ct} values further decrease, with NiFeSuc exhibiting lower resistance values, in full agreement with the previously discussed results.

Important evidence were obtained from the XPS analysis performed on the electrodes after electrochemical characterization (Figure 5.6). O 1s spectra, presents a decrease in the signal at 531.26 eV, related to hydroxyl groups, accompanied by an increase of the peak at 529.5 eV, assigned to oxides. In the C 1s spectra, it is possible to notice some modifications in the peaks associated with C–O and O–C=O groups. Furthermore, both the Fe^0 peak at 706 eV and the Ni^0 peak at 852.15 eV decrease in intensity after OER. A reduction and shift of the Fe^{3+} signal to 712.2–713.7 eV suggests the formation of a new phase, namely spinel-type $NiFe_2O_4$, a compound known to be stable and highly active toward OER in alkaline media [266–271,282]. This interpretation is further supported by the shift of the Ni peak from 861.32 to 861.45 eV, consistent with $NiFe_2O_4$ formation. also confirmed by the simultaneously existence of Ni and Fe in different oxidation states [269,270]. The generation of this phase can be attributed to oxidation and structural rearrangement of Ni and Fe species, in line with the oxidation feature observed in the potentiodynamic curve of NiFeSuc samples prior to the OER onset (Figure 5.9 a, c)) [282,283]. These characteristics are not strange and have been widely reported in Ni–Fe based electrocatalysts literature [284–286]. In general, these signals are referred to the redox transitions of Ni(II) to Ni(III) (and sometimes to higher oxidation states), as well as to the possible oxidation of Fe species embedded the Ni matrix. Such transitions are widely recognized as the electrochemical fingerprint of the activation process which give rise to the formation of the real catalytically active oxyhydroxide phase. The appearance of these peaks before the OER onset is typically linked to the formation of the true active sites for oxygen evolution reaction, although it is still debate if whether Ni, Fe, or their synergistic interaction is mainly responsible for the enhanced catalytic activity [286,287]. For the

monometallic electrodes, FeSuc and NiSuc, the XPS spectra also reveal a reduction in metallic signals and an increase in oxidized species; as it was seen also for NiSuc sample in Figure 4.10. However, electrochemical data confirm that these oxides are less active for OER than the $NiFe_2O_4$ spinel detected in NiFeSuc.

After the electrochemical cycling, Raman spectrum of NiFeSuc-15 sample Figure 5.6 b, exhibits a distinct band at about 700 cm^{-1}, commonly attributed to the formation of $NiFe_2O_4$, whilst the band around 530 cm^{-1} can be assigned to residual $Ni(OH)_2$ [72–74].

The impact of temperature on the kinetic parameters of NiFesuc samples was further assessed by performing tests with 1 M KOH as electrolyte, in batch configuration, measuring the activity at 25°C, 30°C, 50°C, 65°C, and 80°C, the latter corresponds to the operating temperature commonly adopted in industrial alkaline water electrolysis. The LSV curves are reported in Figure 5.13 a and b.

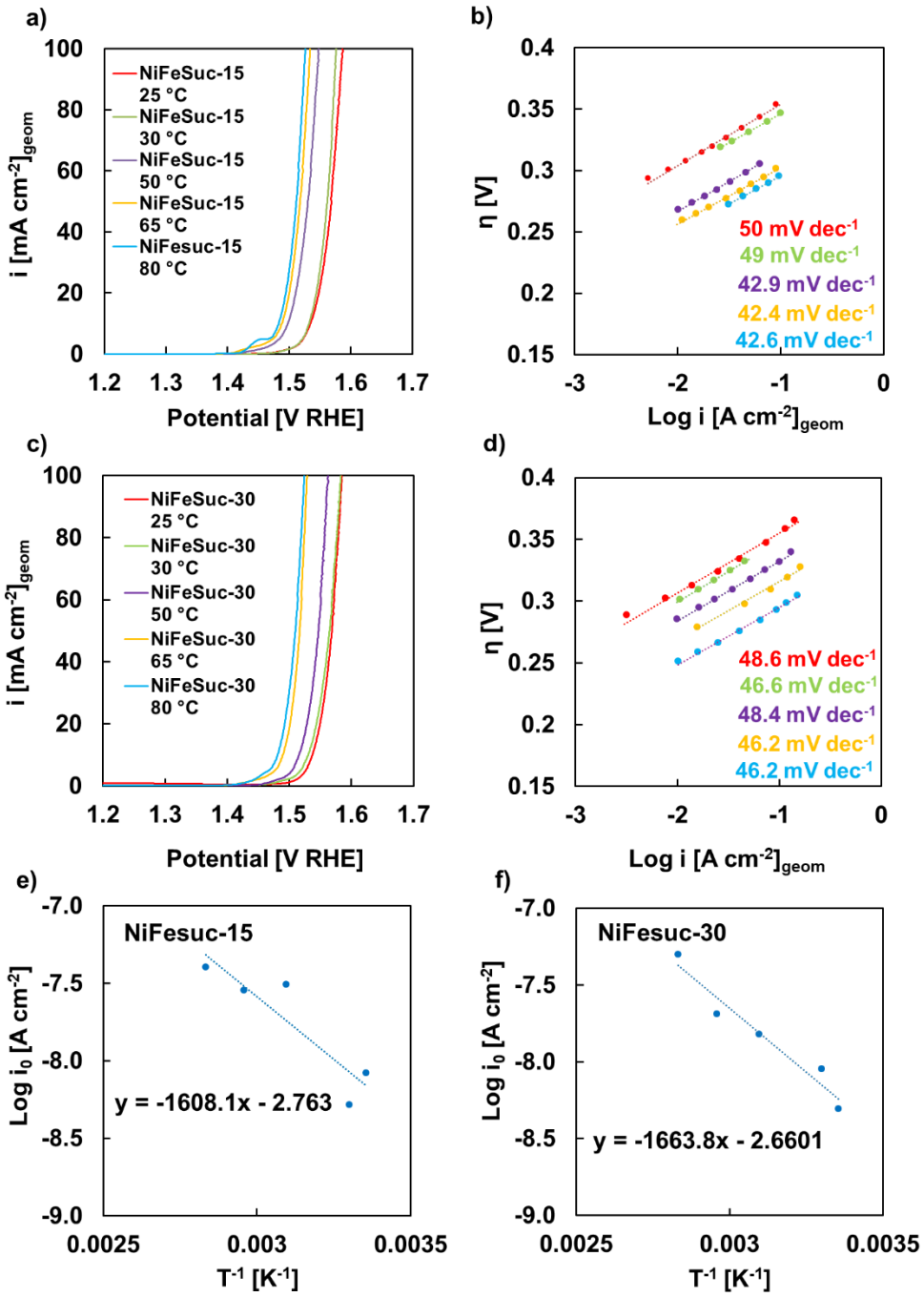

Figure 5.13 Electrochemical performance of a) NiFeSuc-15 and c) NiFeSuc-30 electrodes in 1 M KOH aqueous solution, in batch configuration at different bath temperatures (95% iR correction). b) and d) Corresponding Tafel plots. Arrhenius plots, relating to exchange current density values, for e) NiFeSuc-15 and f) NiFeSuc-electrodes. Image taken from [198].

As temperature increases, the reactions rate increases according to Arrhenius' law, Eq. 5.1, which leads to a decrease in activation overvoltage, and thanks to the improved kinetics it is also possible to see more evident oxydaction peaks befor the onset.

Rising the temperature it is possible to notice also that the polarization curve shifts toward higher current densities and lower potentials due to improved reaction kinetics (Figure 5.13).

The Tafel slope shows only a low dependence on temperature, suggesting that the rate-determining step is not affected by changes in temperature. The exchange current density (i_0) was obtained from the Tafel plots by extrapolating the linear portion of the curve to $\eta = 0$. In the i_0 evaluation, the roughness factor (r) was included, so that i_0 was estimated as $i_0 = i_{0,geom} \times r$. A linear dependence was then observed between $\ln(i_0)$ and $1/T$, in accordance with the Arrhenius law, where the slope of the plot corresponds to $-E_a/R$ [288–290].

$$\frac{\delta \ln(i_0)}{\frac{\delta 1}{T}} = -\frac{E_a}{R} \qquad \text{Eq. 5.1}$$

Where, E_a corresponds to the activation energy of the rate-determining step of the overall electrochemical process, while R denotes the universal gas constant and T refers to the absolute temperature (in K).

By analyzing the slopes of the Arrhenius plots (Figure 5.13 e and f), the activation energy was calculated, obtaining values of 30.7 kJ mol^{-1} for the NiFeSuc-15 electrode and 31.8 kJ mol^{-1} for NiFeSuc-30 [198]. These activation energies fall within the same range as those previously reported in the literature for comparable electrochemical systems [288–290].

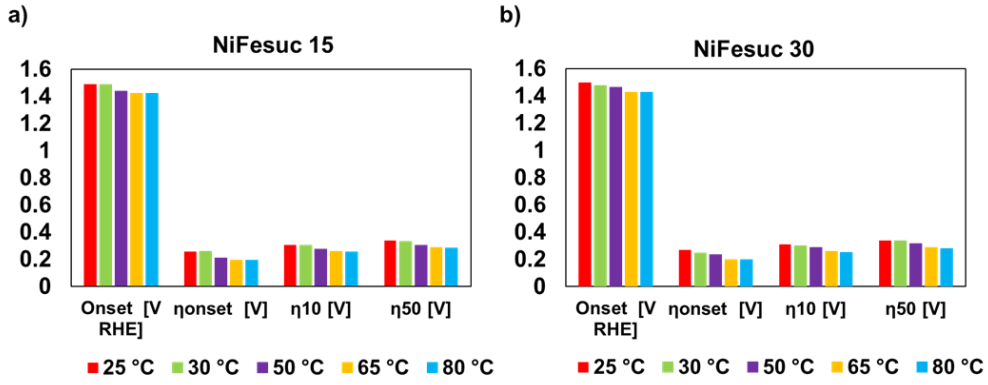

Figure 5.14 Onset, overpotential at onset and 10 and 50 mA cm^{-2} for a) NiFeSuc-15 and b) NiFeSuc-30 varying the temperature.

An increase in the i_0 values is further evidenced by the R_{ct} values obtained as fitting parameters from the EIS spectra (Figure 5.15), recorded at 1.52 V vs RHE in 1 M KOH at different operating temperatures (Table 5.6 and Table 5.7), whose Kramer and Kroning validation is reported in Figure 5.16. Because i_0 varies inversely with R_{ct} [289,290], the observed trend provides additional for the influence of temperature on the reaction kinetics. In particular, for the NiFeSuc-15 electrode, R_{ct} decreases from 6.5 Ω·cm² at 25 °C to 0.8 Ω·cm² at 80 °C, highlighting the improvement in electrochemical kinetics at higher temperatures.

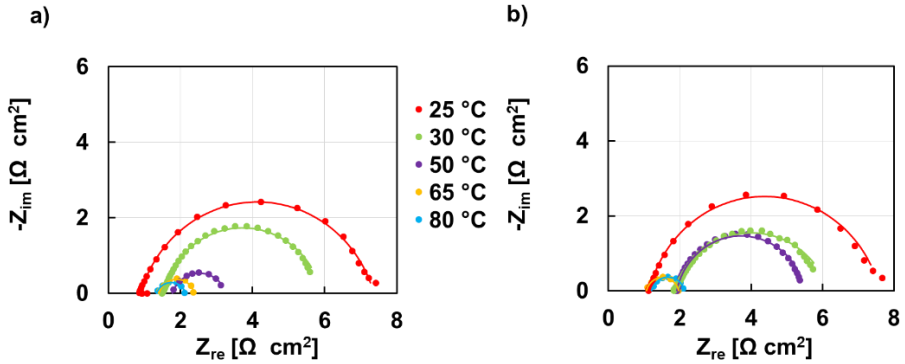

Figure 5.15 EIS spectra in Nyquist representation, recorded at 1.52 V RHE related to NiFeSuc15 a) and NiFeSuc 30 b) electrodes varying the temperature. Image taken from [198].

Table 5.6 Fitting parameters of EIS spectra recorded at 1.52 V RHE related to NiFeSuc15 electrodes varying the temperature. Table taken from [198].

NiFesuc15	R_s [Ω cm^2]	R_{ct} [Ω cm^2]	$Q_{DL,el}$ [S s^n cm^{-2}]	n	χ^2
25 °C	0.89	6.46	1.04×10^{-2}	0.81	5.1×10^{-3}
30 °C	1.5	4.41	8.5×10^{-3}	0.84	3.8×10^{-4}
50 °C	1.7	1.45	2.7×10^{-2}	0.79	1.5×10^{-4}
65 °C	1.4	0.97	2.4×10^{-2}	0.82	8.3×10^{-5}
80 °C	1.3	0.79	2.9×10^{-2}	0.79	1.04×10^{-4}

Table 5.7 Fitting parameters of EIS spectra recorded at 1.52 V RHE related to NiFeSuc30 electrodes varying the temperature. Table taken from [198].

NiFesuc30	R_s [Ω cm^2]	R_{ct} [Ω cm^2]	$Q_{DL,el}$ [S s^n cm^{-2}]	n	χ^2
25 °C	1.13	6.47	1.2×10^{-2}	0.84	4.1×10^{-4}
30 °C	1.86	4.3	1.1×10^{-2}	0.79	3.7×10^{-4}
50 °C	1.91	3.6	4.6×10^{-2}	0.87	3.2×10^{-4}
65 °C	1.06	0.9	1.5×10^{-2}	0.85	1.7×10^{-4}
80 °C	1.2	0.93	1.3×10^{-2}	0.84	1.2×10^{-4}

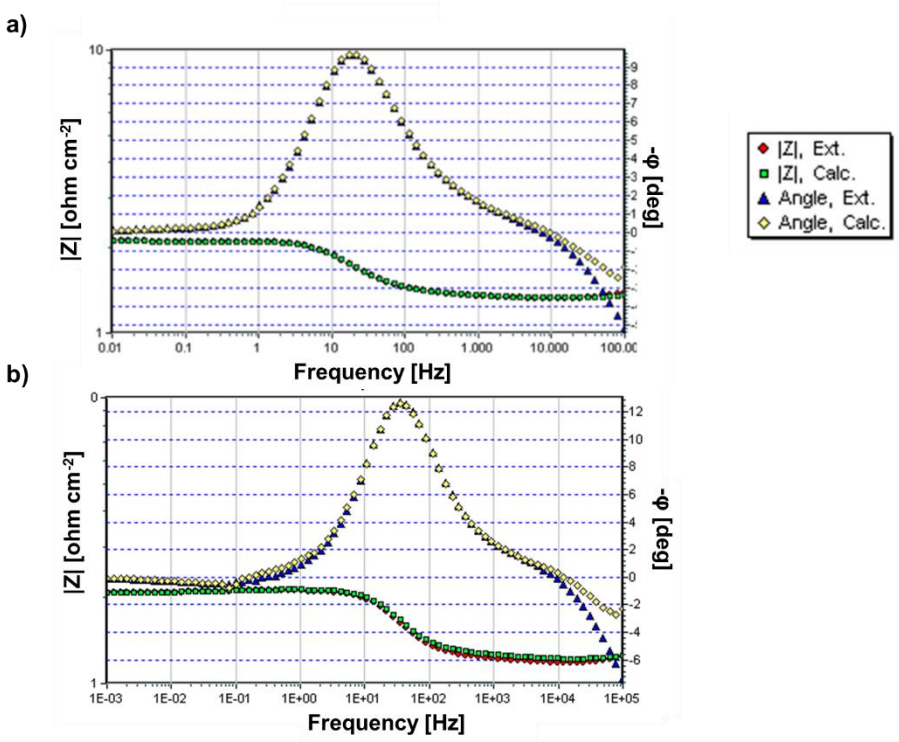

Figure 5.16 Kramer and Kroning validation of 1.52 V RHE spectra related to NiFeSuc-15 and NiFeSuc-30 electrodes in 1 M KOH at 80 °C in batch configuration.

The same electrodes were also characterized in aqueous KOH solutions with concentrations rising from 1 M to 6 M (Figure 5.17), in batch configuration. These results demonstrate that the electrodes are suitable for operation in conventional alkaline water electrolyzers, which typically employ KOH concentrations in the range of 4–8 M [290,291].

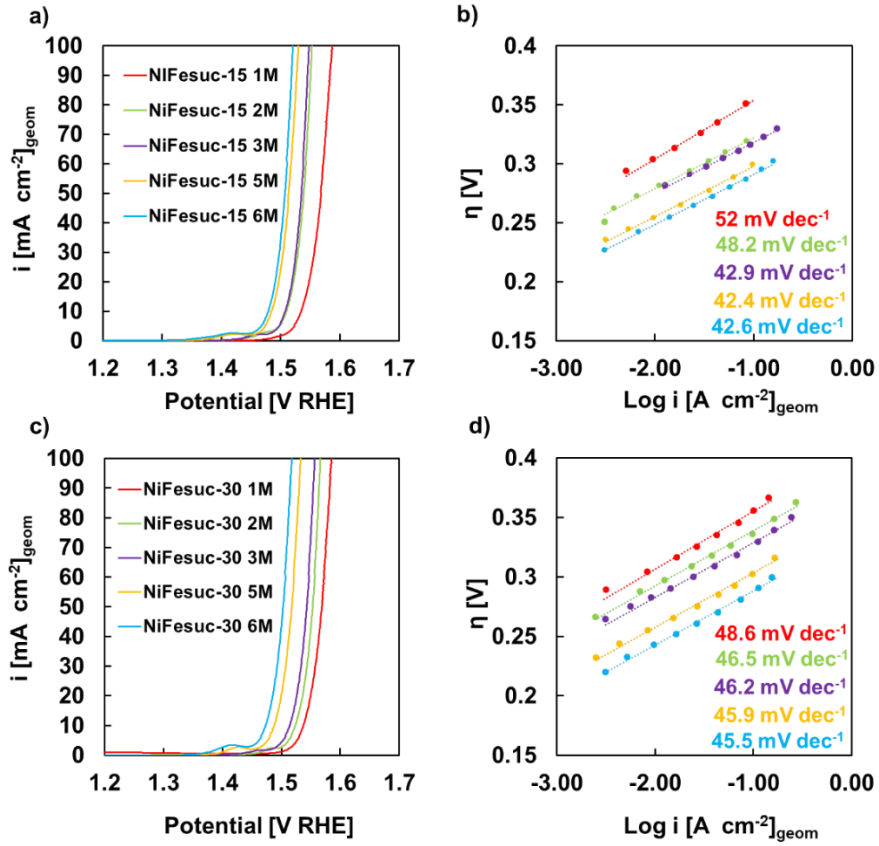

Figure 5.17 Comparison of i vs. potential curves, related to electrodes a) NiFeSuc-15 and c) NiFeSuc 30 electrodes, varying electrolyte composition., in batch configuration. b) Tafel plot extrapolated from Figure a) and d) Tafel plot extrapolated from Figure c). Log i0 vs logC for e) NiFeSuc-15 and f) NiFeSuc-30. Image taken from [198].

Varying the electrolyte concentration, it is possible to notice a modification in the polarization curve due to the impact on mass transfer, electrolyte resistance and on the reaction rate. In particular at low current, it is possible to notice a reduction in the activation overpotential because a higher concentration of reactive species in the electrolyte tends to favour reactions at the electrode surface. Thus, it can be seen that as the concentration increases, the polarization curve shifts toward higher current densities and lower potentials, improving the performance of the electrochemical system, as it is possible to notice in Figure 5.18.

The Tafel slope, as it is possible to see from Figure 5.17 b and d is almost unchanged with the concentration of the electrolyte, which means that the rate determining step is the same in all the conditions. This indicates that the observed improvements are mainly due to enhanced mass transport and increased ionic conductivity, rather than to a change in the reaction mechanism.

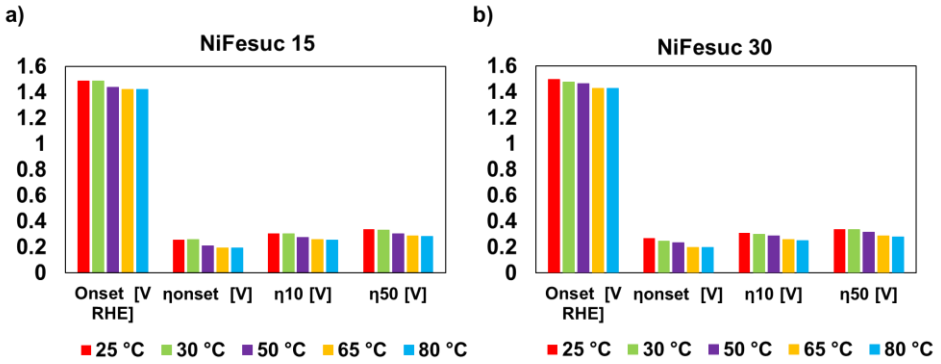

Figure 5.18 Onset, overpotential at onset and 10 and 50 mA cm^{-2} for a) NiFeSuc-15 and b)NiFeSuc-30 varying the concentration of electrolyte.

EIS spectra recorded at 1.52 V RHE and 25 °C, varying the concentration of the electrolyte are shown in Nyquist representation in Figure 5.19. The EIS spectra were tuned using the equivalent electrical circuit shown in Figure 5.7. The fitting parameters for all electrodes are detailed in Table 5.8 for NiFeSuc-15 and Table 5.9 for NiFeSuc-30. The fitting parameters show that R_{ct} decreases with electrolyte concentration, from values above 6 Ω·cm² in 1 M KOH to below 0.6 Ω·cm² in 6 M KOH, both for NiFeSuc-15 and NiFeSuc-30. This trend reflects the reduction in activation overpotential and the significant enhancement of charge transfer kinetics at higher electrolyte concentrations. On the other hand, the values of R_s do not exhibit a clear monotonic decrease with concentration. This behaviour is likely related to the manual positioning of the electrodes during assembly: since the electrode–electrode distance was not perfectly constant across all tests, the solution resistance does not strictly reflect the variation in bulk conductivity.

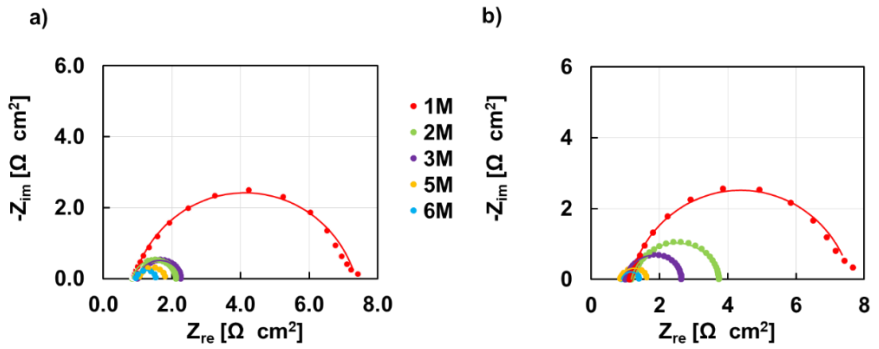

Figure 5.19 EIS spectra in Nyquist representation, recorded at 1.52 V RHE related to NiFeSuc15 a) and NiFeSuc 30 b) electrodes varying the electrolyte concentration.

Table 5.8 Fitting parameters of EIS spectra recorded at 1.52 V RHE related to NiFeSuc-15 electrodes varying the composition of the electrolyte.

NiFesuc15	R_s [Ω cm^2]	R_{ct} [Ω cm^2]	$Q_{DL,el}$ [S s^n cm^{-2}]	n	χ^2
1M	0.89	6.46	1.04×10^{-2}	0.81	5.1×10^{-3}
2M	0.84	1.29	1.8×10^{-2}	0.87	1.06×10^{-4}
3M	1.013	1.27	1.6×10^{-2}	0.86	2.3×10^{-4}
5M	1.045	0.78	1.6×10^{-2}	0.86	9.5×10^{-5}
6M	0.958	0.6	2.3×10^{-2}	0.83	1.8×10^{-4}

Table 5.9 Fitting parameters of EIS spectra recorded at 1.52 V RHE related to NiFeSuc-30 electrodes varying the composition of the electrolyte.

NiFesuc30	R_s [Ω cm^2]	R_{ct} [Ω cm^2]	$Q_{DL,el}$ [S s^n cm^{-2}]	n	χ^2
1M	1.13	6.47	1.2×10^{-2}	0.84	4.1×10^{-4}
2M	1.17	2.63	1.4×10^{-2}	0.84	2.6×10^{-4}
3M	1.01	1.65	9.6×10^{-3}	0.88	2.3×10^{-4}
5M	0.85	0.8	1.1×10^{-2}	0.84	1.7×10^{-5}
6M	0.88	0.54	2.5×10^{-2}	0.84	8.7×10^{-5}

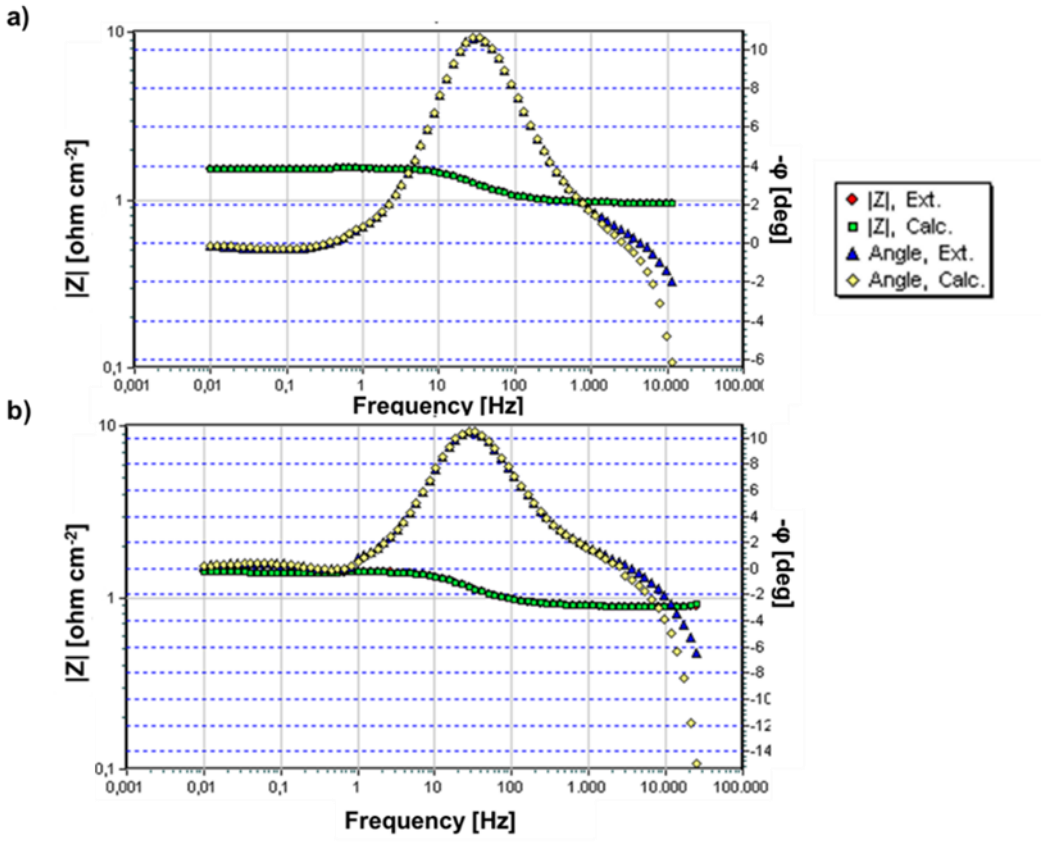

Figure 5.20 Kramer and Kroning validation of 1.52 V RHE spectra related to NiFeSuc-15 and NiFeSuc-30 electrodes in 6M KOH at 25 °C in batch configuration

5.3.4 Durability tests

The electrochemical stability of the catalysts was examined by carrying out a chronopotentiometric test on the best-performing electrode, NiFeSuc-15, by applying a constant current density of 50 mA cm^{-2} in 1 M KOH for 100 hours. The measurements were conducted in a flow-through configuration, in order to emulate the operating conditions of a real AEMWE electrolyzer.

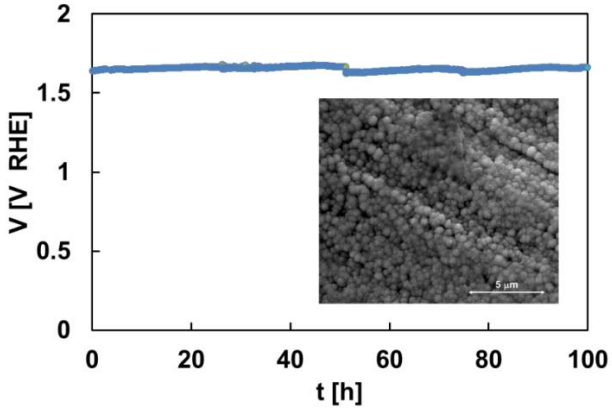

Figure 5.21 Durability test carried out at 0.05 A cm^{-2} in aqueous 1 M KOH solution for) NiFeSuc-15 sample. Inset: SEM image of the sample after chronopotentiometric test. Image taken from [198].

The OER overpotential stays nearly constant for at least 100 hours, at 420 ± 11 mV, confirming the remarkable durability of the NiFeSuc-15 electrode under severe oxidizing conditions. Also, from the SEM image in Figure 5.21 it is possible to see that after durability tests a particle rich structure is still present on sample's surface [198].

After 100 h of electrolysis, (Figure 5.22) the polarization curves reveal a moderate deterioration in the performance of the sample, which in any case remains very good for this class of catalysts, confirming their durability. Specifically, the overpotential at 50 mA cm^{-2} increased from 345.0 mV to 423 mV, indicating a moderate deterioration in catalytic activity.

This trend is further supported by the EIS spectra. The Nyquist plots display only a moderate increase of the semicircle diameter after the stability test, suggesting a limited increase in charge transfer resistance. This behaviour is consistent with the fitting parameters reported in Table 5.10. The Kramer and Kroning relation, further validated the reliability of that EIS spectra (Figure 5.23).

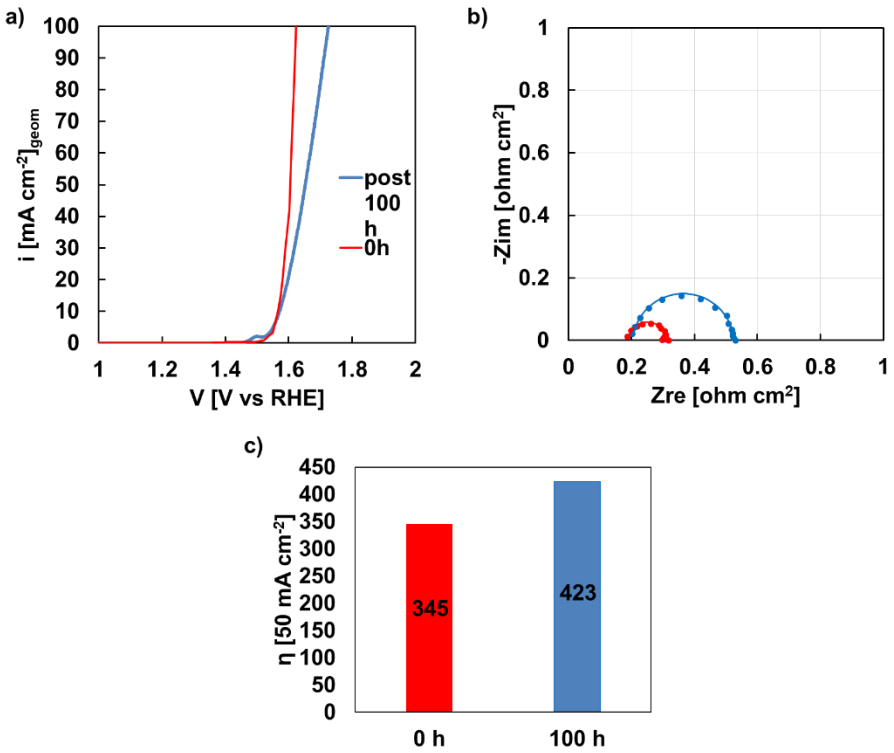

Figure 5.22 a)Current density vs. electrode potential curves carried in a flow through cell for a new electrode and for an electrode of NiFeSuc-15 after 100h electrolysis in 1 M KOH b) EIS recorded at 1.67 V RHE c) overpotential in mV estimated before and after 100 h electrolysis.

Table 5.10 Fitting parameters of EIS spectra recorded at 1.67 V RHE related to NiFeSuc15 electrodes in FT configuration before and after 100 h electrolysis

Sample	R_s [Ω cm^2]	R_{ct} [Ω cm^2]	$Q_{DL.el}$ [S s^n cm^{-2}]	n	χ^2
NiFeSuc-15	0.19	0.11	4.6×10^{-3}	1	1.8×10^{-3}
NiFeSuc-15 Post 100h	0.2	0.32	5.5×10^{-3}	0.95	1.1×10^{-3}

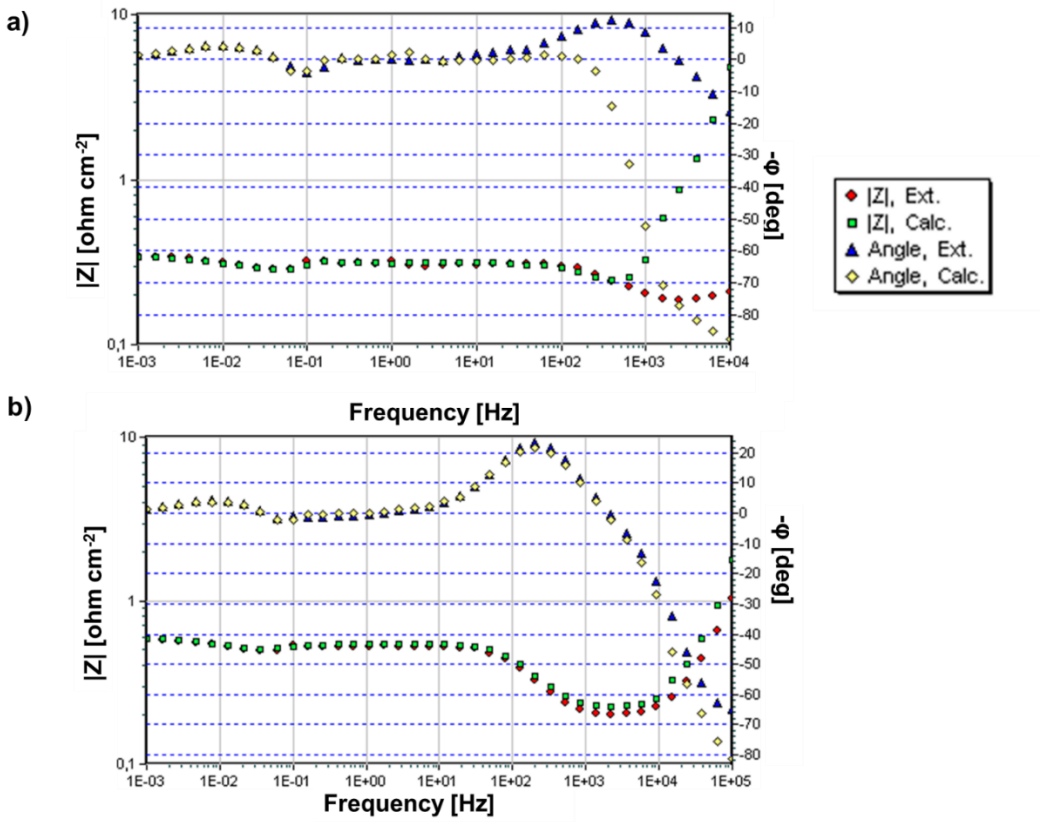

Figure 5.23 Kramer and Kroning validation of 1.67 V RHE spectra related to NiFeSuc-15 before and after 100 h electrolysis in FT configuration in 1M KOH

5.4 AEM electrolyzer testing

To further validate the performance of the electrodeposited material, the electrodeposition process was scaled up, producing a NiFeSuc-15 electrode, integrated as the anode in a single-cell electrolyzer, as reported in Section 3.1. The electrolyzer module consisted of nickel plates with a single-serpentine flow field (active area: 5 cm²), positioned between external gold current collectors. The membrane–electrode assembly (MEA) comprised the NiFeSuc-15 anode, an FAA3-50® anion exchange membrane and a Pt/C catalyst supported on a carbon

backing layer as the cathode. Electrochemical characterization was carried out by LSV, using 1 M KOH as the feed at the anode side. Measurements were performed at operating temperatures ranging from 30 °C to 60 °C, with the resulting LSV profiles shown in Figure 5.24 a.

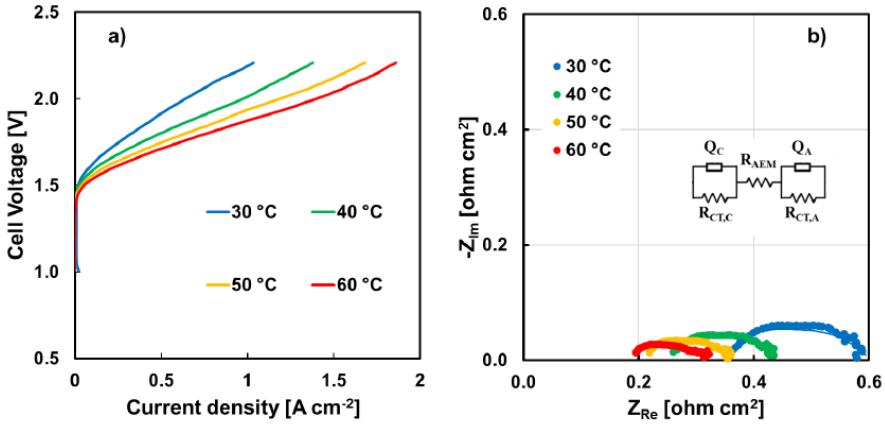

Figure 5.24 a) LSVs recorded at different temperatures employing NiFeSuc-15 electrode as anode in an AEM electrolyzer and b) EIS spectra in Nyquist representation recorded at 1.8 V using the same experimental setup. Fitting: continuous lines. Inset: EEC used to fit the data. Image taken from [198].

As commonly recognized in the literature, the electrochemical performance of AEM electrolyzers enhances by using a higher operating temperatures [292–296]. This improvement mainly derives from a reduction in the activation losses, due to a faster HER and OER kinetics at the electrodes, together with the enhanced ionic conductivity of the AEM [292]. In our case, increasing the temperature from 30 °C to 60 °C led to a slight reduction in the onset cell voltage along with a substantial enhancement in the maximum current density at 2.2 V, which rose from 1.0 A cm^{-2} at 30 °C to 1.86 A cm^{-2} at 60 °C.The temperature-dependent behaviour is further verified by EIS analysis in Figure 5.24 b, which shows the spectra collected at 1.8 V across the same described temperature range. The overall electrochemical response of the device can be modeled by using the EEC showed in the inset of Figure 5.24 b. This model includes two parallel RQ elements, attributed to the anodic and cathodic processes, arranged in series with an ohmic resistance [218,297], the dominant contribution is the ionic resistance of the AEM (R_{AEM}). The corresponding fitting parameters are summarized in Table 5.11.

Table 5.11 Fitting parameters related to EIS spectra, recorded at 1.8 V at different operating temperatures, reported in Figure b. Table taken from [198].

T (°C)	R_{AEM} [Ω·cm²]	$R_{ct,C}$ [Ω·cm²]	Q_C [S·sⁿ·cm⁻²]	n (C)	$R_{ct,A}$ [Ω·cm²]	Q_A [S·sⁿ·cm⁻²]	n (A)
30	0.35	0.06	7×10^{-3}	0.86	0.19	0.14	0.56
40	0.25	0.05	9×10^{-3}	0.83	0.14	0.19	0.56
50	0.20	0.02	7×10^{-3}	0.97	0.15	0.19	0.50
60	0.18	–	–	–	0.068	0.04	0.67

It is possible to observe that an increase in operating temperature led to a reduction in the series resistance, thanks to the improved OH^- conductivity of the AEM. The resistance decreased from 0.35 Ω·cm² at 30 °C to 0.18 Ω·cm² at 60 °C.

The R_{AEM} values obtained from EIS analysis are in agreement with those estimated from the ohmic drop region in Figure 5.24 a, which range from 0.52 Ω·cm² at 30 °C to 0.32 Ω·cm² at 60 °C. Furthermore, the overall cell impedance decreases with temperature, reflecting enhanced electrode kinetics for both HER and OER. This is evident from the R_{ct} values reported in Table 5.11, which decrease by increasing temperature. Importantly, $R_{ct,C}$ values remain an order of magnitude lower than $R_{ct,A}$ under all conditions, as expected due to the Pt/C cathode catalyst. At 60 °C, the HER charge-transfer resistance becomes negligible, effectively removing the cathodic contribution from the equivalent circuit. The presence of additional time constants in the impedance spectra may be associated with other loss mechanisms, such as ionic transport within the catalyst layer [298].

To further assess stability, a short-term durability test (~40 h) was conducted in potentiostatic mode at 2 V using the NiFeSuc anode. The corresponding chronoamperometric profile is presented in Figure 5.25.

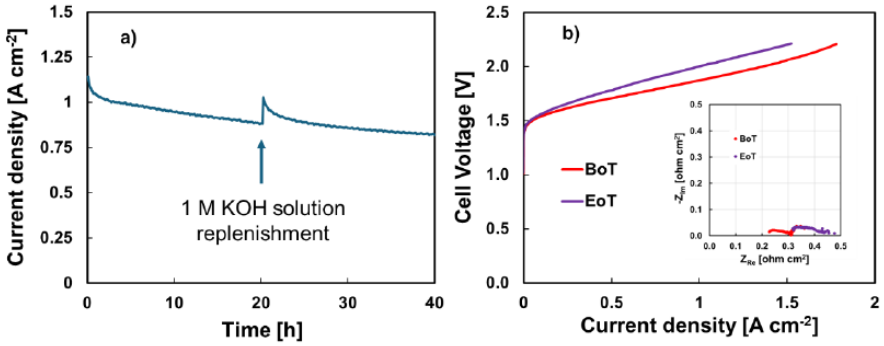

Figure 5.25 a) Chronoamperometric durability test carried out at 2 V at 60 °C employing NiFeSuc-15 electrode as anode in an AEMWE. b) LSVs recorded before (BoT) and after (EoT) the durability test at 60 °C. Inset: EIS spectra in Nyquist representation recorded at 2 V before (BoT) and after (EoT) the durability test using the same experimental setup. Image taken from [198].

As it is possible to see, the current density gradually decreased over time, with the most evident drop occurring during the first few hours of the test. Toward the end, however, the decrease became less pronounced. The current density peak at around 20 h can be attributed to the restart of the test following the replenishment of the 1 M KOH solution. This trend is consistent with previous studies, where similar drops in current density were linked to mechanisms such as membrane degradation, carbonate formation in the presence of CO_2, catalyst deactivation, or electrode-related issues (e.g., difficulties in removing gas bubbles from the electrode surface) [293,296].

To further investigate possible degradation mechanisms, LSV and EIS experiments were carried out before (BoT, Beginning of Test) and after (EoT, End of Test) the chronoamperometric measurements at 60 °C (Figure 5.25 a). As expected, the LSV results indicated reduced cell performance at EoT, with a higher ohmic drop leading to a current density of 1.05 A cm^{-2} at 2 V. This is also evident from the impedance spectra (inset of Figure 5.25 b) recorded at 2 V under BoT and EoT conditions, which show an increase in R_{AEM} and a slight rise in overall impedance. These changes suggest possible electrode degradation during the short-

term stability test. Nonetheless, the performance of this AEMWE remains superior to that reported in in the literature, evaluated at BoT [299–301].

5.5 Conclusions

In this chapter, the application of the *Protocol for functionalized PTLs* on a NiFe-based catalyst, used as the anode in anion-exchange membrane electrolyzers (AEMWE) was presented. Morphological and electrochemical characterization revealed that the material consisted of microparticles composed of nanosheet arrays, resulting in a significant higher electrochemically active surface area. Impedance spectroscopy further confirmed this enhancement through double-layer capacitance measurements, while XPS analysis highlighted the formation of catalytically active $NiFe_2O_4$ species after electrochemical cycling.

From a performance perspective, the developed electrode exhibited a lower onset potential compared to the Fe-only electrode, as well as a competitive overpotential at 10 mA cm^{-2} with respect to the best PGM-free catalysts reported in the literature. When integrated into an AEMWE electrolyzer, the catalyst enabled high current densities (1.86 A cm^{-2} at 60 °C and 2.2 V), maintaining stable operation for 40 hours with minimal degradation.

These results should not only be interpreted as a technological advancement but, more importantly, as a validation of the applied metrological protocol. The systematic and reproducible electrochemical measurements allowed a clear correlation between cell performance and possible electrode degradation mechanisms, underlining the importance of a proper measurement methodology in the study of innovative materials. In this sense, the work carried out demonstrates how a metrological approach represents an essential tool not only to ensure data reliability but also to guide the development of platinum-group-metal-free electrocatalysts for application in AEMWE electrolyzers.

6. Comprehensive Characterization of $SrCoO_3$-δ and $SrCo_{1-x}Ti_xO_3$-δ Perovskites as Electrocatalysts for Oxygen Evolution in Alkaline Media

In this chapter, the results concerning the application of the *Thin-Film Electrode Protocol* to a $SrCoO_3$-δ (SCO) perovskite-based electrocatalysts for the Oxygen Evolution Reaction in alkaline environment are presented. As discussed in the introductory sections, the design of active and durable catalysts is crucial for enabling green hydrogen production through water electrolysis, while avoiding the use of PGMs. Perovskite oxides represent a particularly promising class of non-precious metal catalysts, due to their tunable electronic structure, compositional flexibility, and high intrinsic activity toward OER [118,302].

SCO has been identified as one of the most active perovskite compositions, although its practical application is hindered by limited structural stability under reaction conditions [303,304]. To address these limitations, thin-film SCO electrodes were synthesized by a chemical solution deposition method, and their properties were tuned through cobalt excess (SCO + Co_3O_4) and titanium doping, with the aim of enhancing both activity and long-term stability [132,305].

The electrodes were systematically characterized according to the customized protocol described in Section 3.2, in order to assess their morphology, composition, and crystalline structure. Their electrochemical performance was then evaluated under alkaline conditions (1 M KOH, 75 °C), following the same electrochemical protocol adopted in the previous chapters. In addition, durability was investigated by means of an Accelerated Life Test, carried out according to the EU technical protocol for low-temperature water electrolyzers, which allows to reproduce dynamic and demanding operating conditions [89].

The following sections present and discuss the morphological, structural, and electrochemical results, with particular emphasis on the correlation between electrode composition, catalytic activity, and stability, and on the potential of these perovskite-based electrodes for large-scale, PGM-free alkaline water electrolysis.

6.1 Perovskite synthesis

$SrCoO_3$ perovskites catalysts have been synthesized by a chemical solution deposition method [306], on platinized Si substrates, as described in detail in the

section 2.1.2. Precursor solutions were prepared by suspending $Sr(OOCCH_3)_2$ and $Co(OOCCH_3)_2$ in a mixture of propionic acid and propionic anhydride; the deposition was performed by spin coating on Pt substrates. The perovskite crystalline structure was obtained through a crystallization step at 800 °C for 15 min. These catalyst have been prepared with a simple manufacturing process respect to methods that are generally used for thin film production [307,308].

The effect of cobalt excess was investigated by preparing $SrCoO_{3-\delta}$ with Co_3O_4 admixture (SCO:CB), by reducing Sr/Co ratio down to 0.75 in the precursor solution. In addition, the influence of Ti doping was studied in the series $SrCo_{1-x}Ti_xO_{3-\delta}:Co_3O_4$ (SCT:CB X). In this notation, *CB* indicates the presence of the Co_3O_4 secondary phase and *X* corresponds to the titanium content. Specifically, samples with 1, 2, 3, 4, and 5 at.% Ti were synthesized, named SCT:CB 1, SCT:CB 2, and SCT:CB 3 respectively.

6.2 Morphological characterization

Following the protocol described in Section 3.2, the catalysts were subjected to extensive morphological and structural characterization by XRD**,** SEM and XPS analyses, with the aim of correlating their electrochemical performance with their chemical composition and morphological features.

SEM images of platinized Si substrate and SEM image of SCO sample are reported in Figure 6.1 a and b respectively.

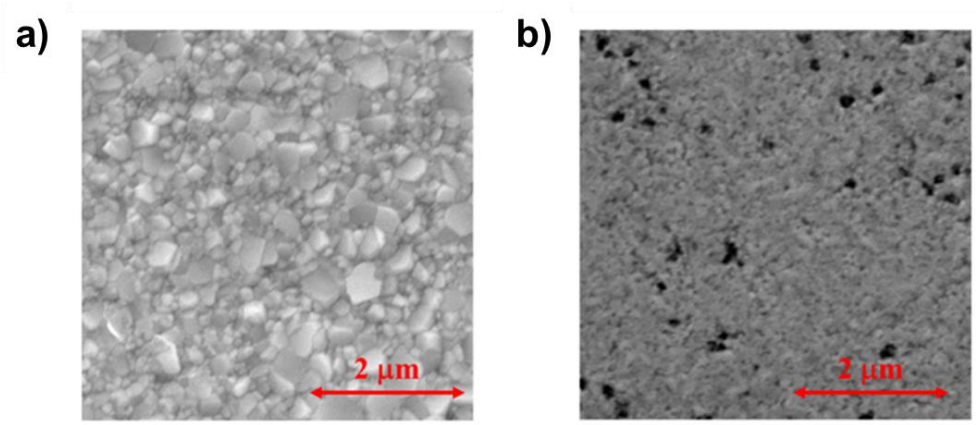

Figure 6.1 a), SEM image related to platinized Si substrate (20000x) and b) SEM image related to SCO sample (20000x). Image taken from [209].

From this images it is not possible to distinguish any relevant features neither before and after the deposition of perovskite thin films through the CSD technique. Previous studies [130–132] reported surface roughness values ranging between 1 and 10 nm. Surface morphology isn't affected by the deposition conditions, neither changing adding Co excess (i.e. SCO:CB sample) or Ti doping (i.e. SCT:CB samples).

Figure 6.2 a, displays the X-ray diffractograms of the SCO:CB reference and the SCT:CB series with Ti doping ranging from 1 at.% to 3 at.%, while, Figure 6.2 b shows the structure of SCO:CB along the [210] direction. All samples crystallized in the 6R perovskite-type structure, with trigonal symmetry ($R\bar{3}$, No. 148), as reported by Sun *et al.* (ICSD No. 81312) [309]. In this structure, $Co^{3+/4+}$ ions form chains of CoO_6 octahedra oriented along the [001] direction, separated by trigonal prisms. Diffraction analysis reveals the main picks at 2θ values of 18.67°, 28.63°, 32.64°, 43.82°, and 55.69°. In SCT:CB samples, the lattice constants vary with Ti doping: for the undoped compound, they are a = 9.49 Å and c = 12.41 Å, whereas with 2% Ti doping, they become a = 9.49 Å and c = 12.49 Å.

At 3 at.% Ti doping, additional diffraction planes appear, suggesting the formation of a new polymorph. This structural modification is accompanied by a reduction of the c parameter (c = 12.41 Å) and by the appearance of two additional peaks at 2θ = 31.3° and 38.6°, whose intensity is attenuated due to the applied scaling of the graph. However, due to the limited crystallinity of the samples, it is difficult to obtain an accurate identification of this phase. Up to 2 at.% Ti, the 6R structure is preserved, and a low crystallinity at 2% is observed, most likely arising from lattice strain induced by the ionic radius mismatch between Ti^{4+} and $Co^{3+/4+}$. For Ti contents of 3 at.%, lattice relaxation appears to drive the stabilization of a new phase. In all cases, a collateral Co_3O_4 phase (ICSD No. 27497) [310] was also detected, with its characteristic peaks observed at 2θ = 36.97° and 44.96° [209].

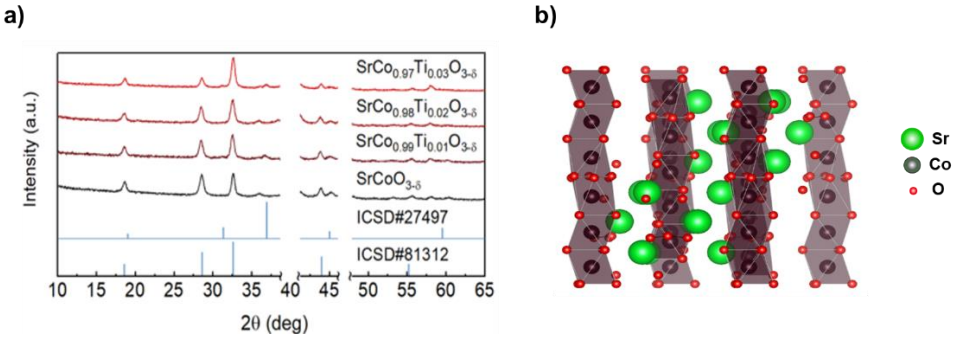

Figure 6.2 a) GIXRD patterns of the SCO, SCO:CB and SCT:CB samples and b) view on the SCO:CB structure along the [210] direction. Image adapted from [209].

To investigate the surface chemistry of the as-prepared SCT:CB catalysts, XPS spectra were collected in the Sr 3d, Co $2p_{3/2}$, and Ti 2p regions (Figure 5.2). The composition of the investigated samples, measured by means XPS measurement, are reported in Table 6.1.

Table 6.1 Samples composition estimated through XPS measurements. Table taken from [209].

Sample	C 1s [at.%]	O 1s [at.%]	Ti 2p [at.%]	Co $2p_{3/2}$ [at.%]	Sr 3d [at.%]	Pt 4f [at.%]
SCO:CB	22.2	59	-	3.3	12.4	3.1
SCT:CB 1	24.3	58.2	0.2	6.6	9.5	1.2
SCT:CB 2	21	58.8	0.4	8.3	8.8	2.6
SCT:CB 3	23	58	0.6	5.9	10	2.6

It is important to underline that the presence of Pt in sample's composition results from the platinized Si substrate. For the Sr 3d core levels, four distinct peaks were observed (Figure 6.3), corresponding to both $3d_{3/2}$ (BE = 134.0 eV and 135.8 eV) and $3d_{5/2}$ (BE = 132.9 eV and 134.6 eV) doublets, corresponding to Sr^{2+} state [311]. In agreement with literature data, the lower binding energy component is attributed to Sr within the lattice ($Sr_{lattice}$), whereas the higher binding energy contribution originates from surface Sr species ($Sr_{surface}$) [312]. Upon Ti doping (Figure 6.3 b–c), an increase of the $Sr_{lattice}$ contribution was detected, indicating a reduced leaching tendency of Sr from the lattice.

To track the surface chemical changes in initial structure of SCT:CB under operation XPS gave been recorded also after electrochemical cycling, in particular after 100 CV cycle. After electrochemical aging, the Sr 3d spectrum evolved into a single doublet (Figure 6.3 a–c), with the Sr $3d_{5/2}$ peak positioned between 133.5–133.1 eV and the Sr $3d_{3/2}$ peak between 135.2–134.8 eV, depending on Ti doping level therefore with a higher BE with respect to as-formed samples.
These values correspond to higher binding energies compared to the as-prepared samples, reflecting changes in the Sr chemical environment.

Surface cobalt was found in mixed Co^{2+}/Co^{3+} oxidation states, consistent with reference data for Co_3O_4 (BE = 779.6 eV [313]) and $ZnCo_2O_4$ (BE = 780.4 eV [314]). Co^{3+}/Co^{2+} ratio can be determined from the at.% values of Co_3O_4 and Co^{3+} species obtained by fitting the Co $2p_{3/2}$ XPS spectrum. Since the spinel Co_3O_4 structure consists of CoO (Co^{2+}, tetrahedral sites) and Co_2O_3 (Co^{3+}, octahedral sites) in a 1:2 ratio [315,316], this ratio can be easily calculated. SCO:CB exhibited the highest Co^{3+}/Co^{2+} ratio prior to cycling, with a value of 3.11, while Ti-doped samples displayed values around 2. This finding is significant because Co^{3+} is considered the precursor of electrocatalytically active Co^{4+}, formed under anodic polarization. Therefore, the Co^{3+} excess in SCO:CB provides a greater quantity of species that can undergo the Co^{3+}/Co^{4+} transition during OER. The lower overpotential measured for SCO:CB is therefore related to its higher initial Co^{3+} content, which facilitates and stabilizes the Co^{3+}/Co^{4+} redox equilibrium under operating conditions.

Ti addition led to a partial reduction of Co^{3+} ions, with a BE shift, upon doping with 2% Ti [317]. Titanium species were identified as Ti^{4+} (BE = 458.2 eV, typical

of TiO_2 [318]) with a splitting energy Δ = 5.7 eV. For cobalt, cycling led to an increased Co^{3+}/Co^{2+} surface ratio across all Ti-doped samples, from 2 to 6.76 in the SCT:CB 1 sample and from 2 to 2.2 in the case of 3% Ti substitution, confirming that higher-valence cations play a key role in stabilizing the structure under operation [319]. Ti surface species maintained the original splitting energy but shifted toward higher binding energies, suggesting modifications in ion coordination. Splitting into two doublets is suggested to indicate an agglomeration of remaining Ti species in the vicinity of leached Sr cations. In addition, the Sr/Co ratio increases with Ti doping, rising from 0.056 in the SCO:CB sample to 0.079 in SCT:CB 3. This trend suggests that the enhanced electrochemical stability of SCT:CB 3 (as we will see in the next section), is linked to the higher Sr content retained during cycling, confirming the role of $Ti^{4+}$with its highest oxidation state, as a stabilizer of A-sites in perovskites [132].

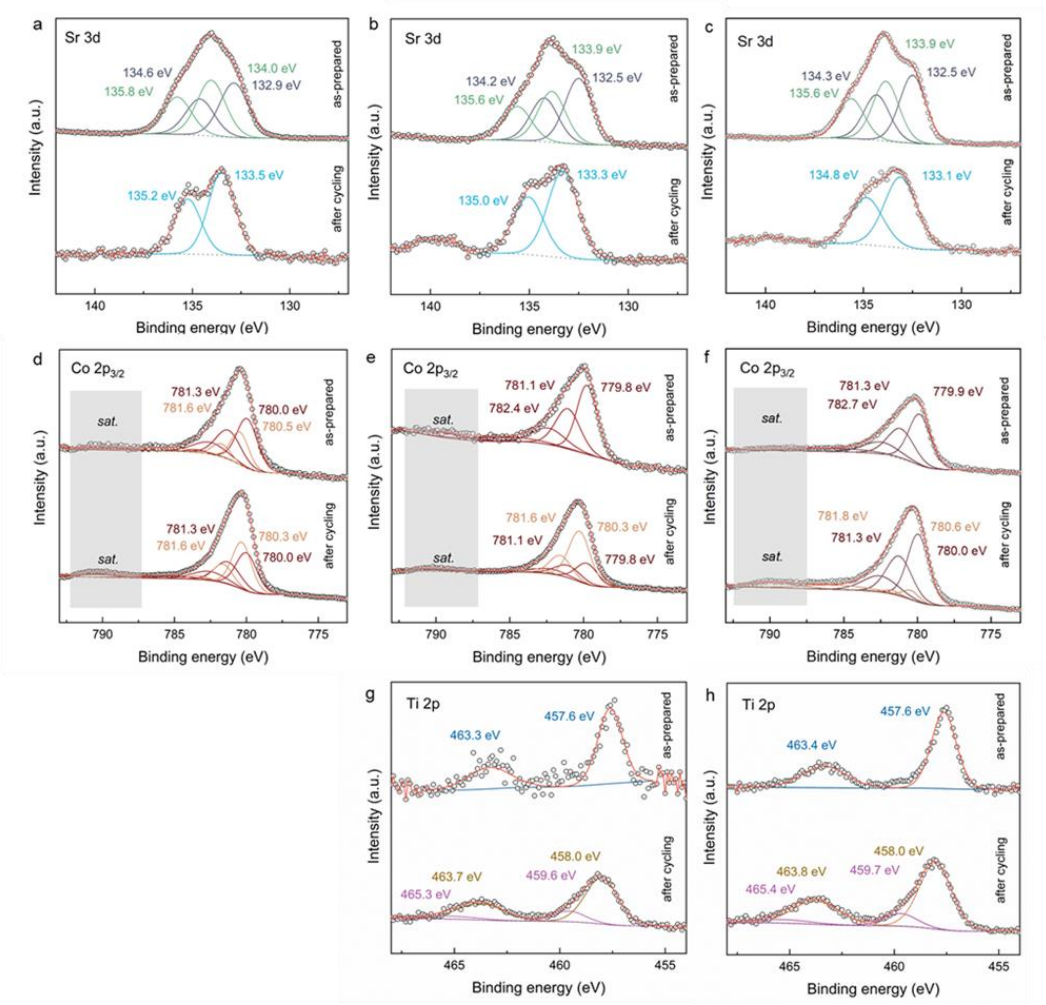

Figure 6.3 Sr 3d and Co $2p_{3/2}$ and Ti 2p XPS fitted spectra on as-prepared and after 100 CV cycles in 1 M KOH for SCO:CB (a, d), SCT:CB 1 (b, e, g), SCT:CB 3 (c, f, h). Image taken from [209].

6.3 Electrochemical characterization

6.3.1 Activity tests

Electrochemical measurements were performed to assess the OER activity of the synthesized perovskites by means of LSV and impedance spectroscopy. The LSV curves, recorded at 10 mV s^{-1} and corrected for 95% iR-drop, are reported in Figure 6.4 a.

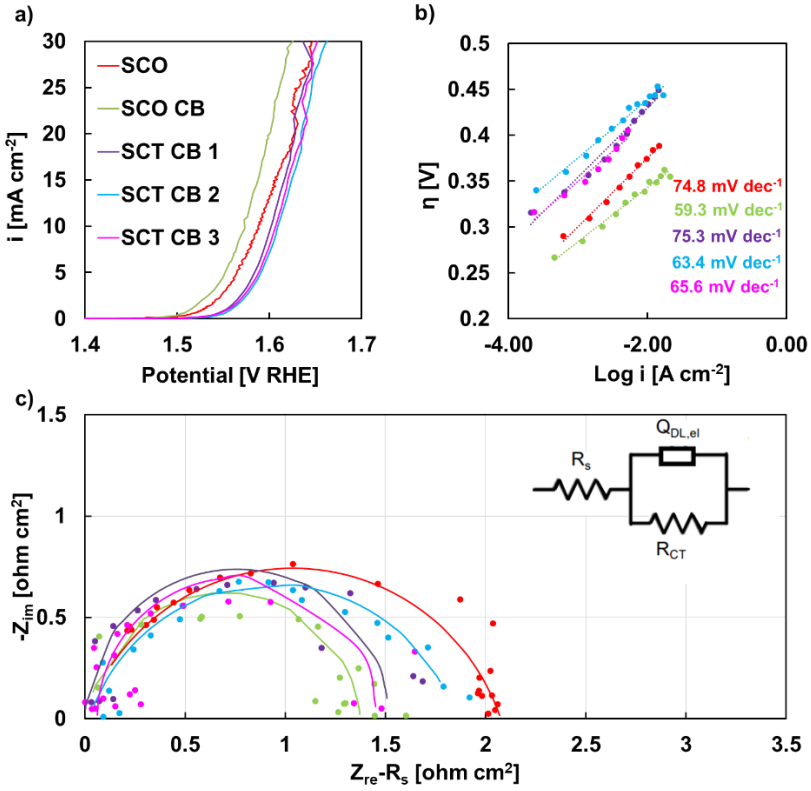

Figure 6.4 a) Current density vs. potential curves, b) Steady State Tafel plots and c) Electrochemical impedance spectra recorded at 0.8V Hg/HgO for all the investigated electrodes. Inset: equivalent electrical circuit used for spectra fitting procedure. Continuous lines: fitting data.

The OER performance of the studied perovskite thin films was evaluated by measuring two key parameters: η_{onset}, defined at a current density of 1 mA cm^{-2}, and η_{10}. The results for each sample are listed in Table 6.2.

Table 6.2 η_{onset} and η_{10} values estimated from LSV reported in Figure 6.4 a.

Sample	η_{onset} [mV]	η_{10} [mV]
SCO	298	357
SCO:CB	284	343
SCT:CB 1	322	372
SCT:CB 2	327	379
SCT:CB 3	323	376

As can be observed, cobalt excess (B-site substitution) improves the catalytic activity of the SCO sample, resulting in a lower value of η_{onset} and . $\eta_{10,}$ of 284 mV and 343 mV for SCO:CB, respectively, compared to 298 mV and 357 mV for the pristine SCO. This trend is coherent with literature data on the BCO ($BaCo_{0.98}Ti_{0.02}O_{3-\delta}$) perovskite system, where cobalt excess enhances activity but compromises long-term stability [132]. The effect can be attributed to the generation of additional active sites thanks to Co excess, and to the modification of oxygen stoichiometry, with an increase in oxygen vacancies that improve conductivity, oxygen diffusion, and oxygen release [302].

It is well known that OER on perovskites can follow two possible pathways: the conventional AEM and the LOM [320,321], as it was mentioned in Section 1.3. In the AEM pathway, O_2 forms through adsorbed intermediates (OH*, O*, OOH*) on the catalyst surface, while in the LOM pathway, lattice oxygen actively participates, generating oxygen vacancies and promoting O_2 release. This second mechanism is favored in materials with high oxygen mobility and low vacancy formation energy [302]. In $SrCoO_{3}$–δ, the LOM is generally considered dominant, due to its electronic structure and high oxygen vacancy concentration, which enhances lattice oxygen transport [322]. Under anodic polarization, lattice oxygen can thus be directly oxidized, rather than following the conventional pathway with adsorbed intermediate. On the other hand, a high vacancy concentration can also promote Sr ions diffusing out of the lattice.

Ti incorporation is expected to mitigate these drawbacks, by means for Ti doping. In particular, Ti presence could change the oxidation level of Co, because Co^{2+}/Co^{3+} species can be partially replaced by Ti^{4+}, as described by Kröger–Vink notation:

$$2Co_{Co}^{x} + V_{O}^{\cdot\cdot}(SrCoO_{3-\delta}) \xrightarrow{2TiO_2} 2Ti_{Co}^{\cdot} + O_{O}^{x} + Co_2O_3 \qquad \text{Eq.6.1}$$

This substitution reduces the concentration of oxygen vacancies. According to previous studies, replacing B-site cations with Ti^{4+} helps reduce oxygen deficiency, since the formation of strong Ti–O bonds suppresses the creation of oxygen vacancies [316,323]. This effect may lower overall conductivity, because the

reduction of oxygen possible pathways, but can improve structural stability and suppress excessive lattice oxygen evolution [305,324].

If it is possible to see by LSV curves, on average, Ti-doped samples showed higher onset potentials compared to SCO:CB, and reduced activity. The lowest onset was obtained for SCT:CB 1 (1.552 V vs. RHE), while the highest was observed for SCT:CB 2 (1.557 V vs. RHE). Despite this performance reduction, these values remain comparable to those of PBCO and lower than those of BSCF (≈1.60 V vs. RHE) [130]. The catalytic activity of samples with Ti doping between 1–3 % was similar, worse than non-doped samples, with η_{10} values between 372 and 379 mV. These results suggest that while Ti doping reduces activity, in combination with cobalt excess it may help balance catalytic performance and stability. If we compared η_{onset} and η_{10} values related to $SrCoO_{3-\delta}$ and $SrCo_{1-x}Ti_xO_{3-x}$ samples perovskites with those reported in previous studies, it is possible to note that SCO:CB performance surpassed many others perovskites materials, including also that with both A-site and B-site doping [325,326], considering that samples studied in this work had no binder, as typically used in literature for improving electrochemical performances.

Tafel slopes have been obtained by taking into account the current density value recorded by applying electrode potential values until a steady state current density value was reached, they are presented in Figure 6.4 b.

For both SCO and SCT:CB samples, Tafel slopes ranged between 60–70 mV dec^{-1}. These values are consistent with previously reported studied for OER-active perovskites [325–327].

EIS was carried out at 0.8 V vs. Hg/HgO, (i.e. 1.72 V RHE) and the corresponding Nyquist plots for all tested samples are shown in Figure 6.4 c. The electrochemical response of the electrodes was tuned by using the equivalent electric circuit illustrated in the inset of Figure 6.4 c. This model includes a single time constant, consisting of the series resistance R_s and the parallel combination of R_{ct} with $Q_{DL,el}$, which accounts for the non-ideal behaviour of the electrode double-layer capacitance. Since a lower R_{ct} reflects superior electrocatalytic activity, the electrochemical performance can be compared by matching these values. The lowest R_{ct} values, 1.3 $\Omega \cdot cm^2$, was obtained for SCO:CB, consistent with the LSV results in Figure 6.4 a. In contrast, the highest R_{ct} values were observed for SCO, nearly double those of the best-performing samples, while the other samples exhibited intermediate R_{ct} values.

For the SCO:CB sample, the lowest Tafel slope and R_{ct} values were obtained, confirming the dominant role of the LOM mechanism [328]. The introduction of Ti resulted in reduced performance, as indicated by the increase in both Tafel slope and R_{ct}. Nonetheless, with Ti doping, these parameters remained nearly unchanged and in line with values previously reported for perovskite-based OER catalysts [326].

Kramers–Kronig relations were used to validate the consistency of the impedance spectroscopy data, ensuring compliance with causality and linearity requirements of the system, the results for SCO:CB are showed in Figure 6.5.

Table 6.3 Fitting parameters of EIS spectra recorded at 0.8 V Hg/HgO, (i.e. 1.72 V RHE). Rs = 7 Ω cm^{-2}.

Sample	R_{ct} [Ω cm^2]	$Q_{DL,el}$ [S s^n cm^{-2}]	n	χ^2
SCO	2.1	2.8×10^{-3}	0.79	2.5×10^{-4}
SCO:CB	1.3	2.7×10^{-4}	0.94	3.5×10^{-4}
SCT:CB 1	1.5	1.2×10^{-3}	0.98	3.4×10^{-4}
SCT:CB 2	1.8	2.5×10^{-3}	0.79	3.1×10^{-4}
SCT:CB 3	1.4	9.1×10^{-4}	0.99	3.9×10^{-4}

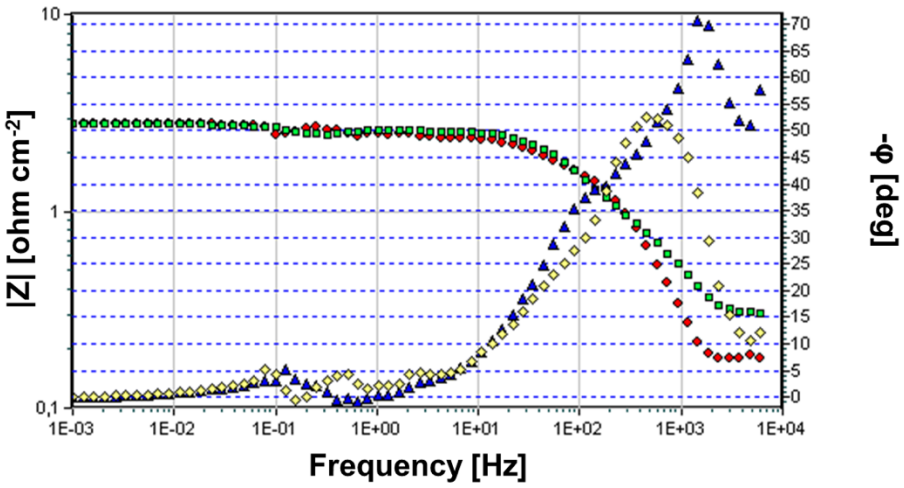

Figure 6.5 Kramer and Kroning validation of 1.8 V RHE spectra related to SCO CB

6.3.2 Durability tests

To evaluate the electrochemical durability of the catalysts, an Accelerated Lifetime Test was performed by continuously cycling the electrodes at a scan rate of 100 mV s^{-1} in the potential window of 1–2 V vs. RHE [239–242]. The stability results for all tested samples are presented in Figure 6.6, where the current density measured at 2 V RHE is plotted against the cycle number. A decline in current density was taken as the endpoint of the test, corresponding to the complete degradation of the catalytic layer.

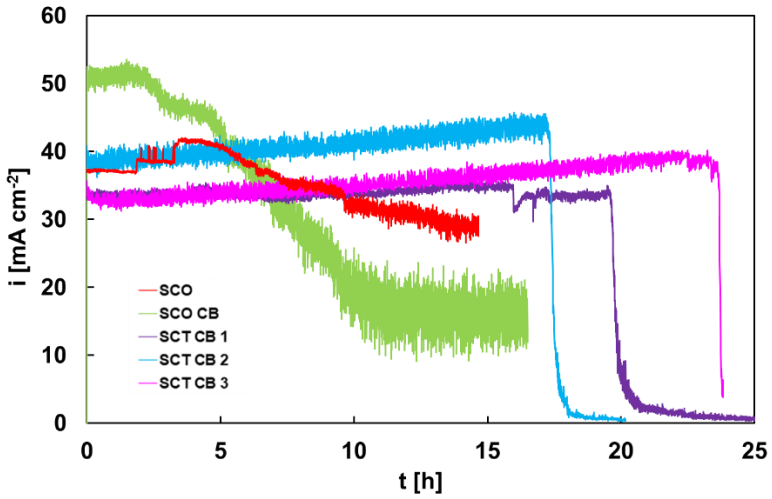

Figure 6.6 ALT related to all the investigated electrodes using the current density i at 2 V RHE during CV sweeps at 100 mV s-1 and 75°C in 1 M KOH.

According to the LSV results, SCO:CB exhibited the highest initial electrocatalytic activity, as evidenced by the maximum current density at the onset of the stability test. However, this sample also showed the poorest durability, indicating that Ti incorporation enhances the lifetime of the electrocatalyst regardless on the specific thin-film composition. Among the investigated materials, SCT:CB 3 demonstrated the best stability, maintaining activity for up to 24 hours before complete degradation caused by full leaching of the thin film.

When compared to state-of-the-art perovskite OER catalysts reported in the literature, such as PBCO and BSCF [132], the SCT:CB samples revealed superior durability while retaining their electrocatalytic performance over longer periods. Although BSCF initially delivers a higher current density (68 mA cm^{-2}), its performance rapidly declines after only 200–300 cycles. Conversely, PBCO mantains a current density of approximately 48 mA cm^{-2} for ~11 hours, which is lower to the stability recorded for the worst durable sample in this study (SCO). As previously discussed, the substitution of Co with Ti reduces oxygen vacancy formation and consequently limits Sr mobility within the lattice framework [324].

6.4 Conclusions

In this chapter, the *Thin-Film Electrode Protocol* was applied to study the electrochemical performance and durability of $SrCoO_{3-\delta}$ and Ti-doped $SrCo_{1-x}Ti_xO_{3-\delta}$ perovskite thin films, for OER inn alkaline media. Structural tuning was achieved by introducing cobalt excess and by partial substitution of B-site cations with Ti^{4+}.

Electrochemical measurements revealed that cobalt-enriched SCO:CB displayed the best activity, with an onset potential of 1.50 V vs. RHE (ηonset = 280 mV), a Tafel slope of 59 mV dec^{-1}, and the lowest charge transfer resistance (1.3 Ω

cm²). Ti incorporation, while not directly enhancing catalytic activity, was found to significantly improve the durability of the films. In particular, SCT:CB 3 maintained stable performance for 24 h, more than double the stability of the Co-rich sample.

XPS analyses performed both on as-prepared films and after electrochemical cycling provided direct insight into the surface chemistry under operation. After cycling, SCO-based films exhibited Sr leaching accompanied by surface reorganization, whereas Ti-doped samples showed a reduced extent of Sr migration. Furthermore, Ti preserved its oxidation state while undergoing coordination changes, suggesting its role as a structural stabilizer of the A-site. These findings confirm that Ti^{4+} doping suppresses excessive lattice oxygen involvement in the OER pathway and mitigates degradation driven by Sr depletion.

Beyond the specific results, this study demonstrates the value of a combined experimental protocol that integrates linear sweep voltammetry, Tafel analysis, impedance spectroscopy validated through Kramers–Kronig relations, accelerated lifetime tests, and XPS characterization performed before and after electrochemical cycling. The systematic and reproducible application of this methodology enabled a consistent correlation between catalytic performance and degradation mechanisms, ensuring data reliability and providing a framework for the rational design of perovskite-based OER electrocatalysts.

Conclusions

This doctoral research has addressed the metrological challenges associated with the electrochemical characterization of electrodes for the oxygen evolution reaction, contributing to the development of a more robust and traceable measurement framework for green hydrogen technologies, such as alkaline water electrolysis, in a research field still lacking standardized protocols.

A central outcome of this work was the definition of two dedicated experimental protocols, designed according to the nature of the investigated materials. In particular, a *Protocol for functionalized PTLs* was established for nanostructured electrodes grown on stainless steel mesh, while a *Thin-Film Electrode Protocol* was developed for electrocatalysts deposited as thin film compact layers on plate substrates. Both frameworks combine activity and durability tests with morphological and spectroscopic analyses, integrating DC and AC techniques, the latter validated through Kramers–Kronig relations to ensure data consistency and reproducibility.

Functionalized stainless steel mesh with Ni-based MOF nanostructures, synthesized by electrodeposition, was studied. The use of succinate as an organic linker ensured both high activity and remarkable stability. The superior performance of the succinate-based electrodes could be attributed to the synergistic effect of Ni active sites and the structural stability imparted by the organic framework, highlighting the potential of MOF-derived materials as scalable OER catalysts.

Simirarly, an analogous experimental approach was employed to investigate a NiFe-based electrocatalyst prepared by a one-step electrodeposition process, tested also in a anion-exchange membrane water electrolyzers .The optimized synthesis yielded a hierarchical nanostructure that significantly enhanced the electrochemically active surface area, while XPS analyses confirmed the formation of $NiFe_2O_4$ species as the catalytically active phase. The electrode demonstrated competitive activity compared to state-of-the-art PGM-free catalysts and, when integrated into an AEMWE electrolyzer, enabled high current densities with stable operation.

Perovskite electrocatalysts, namely $SrCoO_{3-\delta}$ and Ti-doped $SrCoO_{3-\delta}$, synthesized by chemical bath deposition, were also studied due to their tunable electronic structure and promising activity toward oxygen evolution in alkaline environments. While films with Co excess exhibited the best catalytic activity, Ti incorporation strongly enhanced stability by mitigating Sr leaching during the OER process. This study demonstrated the crucial role of structural tuning in improving

catalyst durability and confirmed the ability of the proposed methodology to consistently link structural modifications with electrochemical behaviour.

Overall, the results presented in this dissertation contribute to the field of electrochemical metrology applied to water electrolysis, by demonstrating how standardized and reproducible characterization protocols are essential to obtain reliable insights into catalyst performance and degradation. Beyond the specific materials investigated, this work highlights the importance of metrology not only as a tool to validate experimental results but mainly as a guide for the rational design of innovative OER electrocatalysts.

Future perspectives include the extension of the proposed protocol approach to other emerging classes of catalytic materials, as well as its validation under real operating conditions in electrolyzer cells. Such developments could support the establishment of standardized best practices in electrocatalysis characterization allowing a large-scale development of efficient, durable, and sustainable hydrogen production technologies.

References

[1] M. Sol, Green Energy by Hydrogen Production from Water Splitting , Water Oxidation Catalysis and Acceptorless Dehydrogenative Coupling, (2023).

[2] F. Environment, Energy Technologies and Environment Sustainable Solutions : The Role of Renewable Energy in Creating an Eco-, 1 (2023) 81–88. https://doi.org/10.58567/ete01010005.

[3] F. Martins, C. Felgueiras, M. Smitkova, N. Caetano, Analysis of fossil fuel energy consumption and environmental impacts in european countries, Energies 12 (2019) 1–11. https://doi.org/10.3390/en12060964.

[4] S. Yi, K. Raza Abbasi, K. Hussain, A. Albaker, R. Alvarado, Environmental concerns in the United States: Can renewable energy, fossil fuel energy, and natural resources depletion help?, Gondwana Res. 117 (2023) 41–55. https://doi.org/10.1016/j.gr.2022.12.021.

[5] H. van Asselt, K. Kulovesi, Seizing the opportunity: tackling fossil fuel subsidies under the UNFCCC, Int. Environ. Agreements Polit. Law Econ. 17 (2017) 357–370. https://doi.org/10.1007/s10784-017-9357-x.

[6] R. Alfiana, A. Hidayat, M.I. Irfany, D.A. Haq, Household Activities and Greenhouse Gas Emissions Value: Lessons from a Neglasari Household Survey, Bus. Sustain. 3 (2024). https://doi.org/10.58968/bs.v3i1.418.

[7] D.J. Wuebbles, A.K. Jain, Concerns about climate change and the role of fossil fuel use, Fuel Process. Technol. 71 (2001) 99–119. https://doi.org/10.1016/S0378-3820(01)00139-4.

[8] H. Council, How hydrogen empowers the energy transition (2017), Verfügbar Unter Https//Hydrogencouncil. Com/Wp-Content/Uploads/2017/06/Hydrogen-Council-Vision-Document. Pdf. Zugriff Am 13 (2017) 1–28.

[9] H.E. Armstrong, The Paris Observatory, Nature 127 (1931) 600–601. https://doi.org/10.1038/127600a0.

[10] IRENA, World energy transitions outlook 2023: 1.5°C Pathway, 2023. https://www.irena.org/Publications/2023/Jun/World-Energy-Transitions-Outlook-2023.

[11] S. Shafiee, E. Topal, When will fossil fuel reserves be diminished?, Energy Policy 37 (2009) 181–189. https://doi.org/10.1016/j.enpol.2008.08.016.

[12] K. Gunawardane, Evolution of hydrogen energy and its potential opportunities around the globe, Elsevier Inc., 2023. https://doi.org/10.1016/B978-0-443-15329-7.00007-7.

[13] T.N. Veziroğlu, S. Şahin, 21st Century's energy: Hydrogen energy system, Energy Convers. Manag. 49 (2008) 1820–1831. https://doi.org/10.1016/j.enconman.2007.08.015.

[14] IRENA, Reaching Zero With Renewables: Eliminating CO2 emissions from industry and transport in line with the 1.5 °C climate goal, Int. Renew. Energy Agency (2020) 216. https://www.irena.org/-/media/Files/IRENA/Agency/Publication/2020/Sep/IRENA_Reaching_zero_2020.pdf%0A.

[15] R. Merzian, T. Bridges, Hydrogen and Climate: Trojan Horse or Golden Goose | The Australia Institute, Aust. Inst. (2019) 1–20. https://apo.org.au/node/230061%0Ahttps://pdfs.semanticscholar.org/88d8/665867092ee2c95e924274d0a6f3962c3b18.pdf%0Ahttps://www.tai.org.au/content/hydrogen-and-climate-trojan-horse-or-golden-goose.
[16] C. Li, D. Wu, Innovation and future development direction of hydrogen fuel cell vehicles, Highlights Sci. Eng. Technol. 116 (2024) 53–59. https://doi.org/10.54097/a8n0cr21.
[17] goal-7-affordable-and-clean-energy, (n.d.). https://sdgresources.relx.com/goal-7-affordable-and-clean-energy.
[18] A.I. Osman, N. Mehta, A.M. Elgarahy, M. Hefny, A. Al Hinai, H. Al Muhtaseb, D.W. Rooney, Hydrogen production , storage , utilisation and environmental impacts : a review, Springer International Publishing, 2022. https://doi.org/10.1007/s10311-021-01322-8.
[19] J.C. Ruth, G. Stephanopoulos, Synthetic fuels: what are they and where do they come from?, Curr. Opin. Biotechnol. 81 (2023) 102919. https://doi.org/10.1016/j.copbio.2023.102919.
[20] T. Ahmad, D. Zhang, A critical review of comparative global historical energy consumption and future demand: The story told so far, Energy Reports 6 (2020) 1973–1991. https://doi.org/10.1016/j.egyr.2020.07.020.
[21] IRENA, Making the breakthrough: Green hydrogen policies and technology costs, 2021. https://www.irena.org/-/media/Files/IRENA/Agency/Publication/2020/Nov/IRENA_Green_Hydrogen_breakthrough_2021.pdf?la=en&hash=40FA5B8AD7AB1666EECBDE30EF458C45EE5A0AA6.
[22] J.D. Holladay, J. Hu, D.L. King, Y. Wang, An overview of hydrogen production technologies, Catal. Today 139 (2009) 244–260. https://doi.org/10.1016/j.cattod.2008.08.039.
[23] M. Dvoynikov, G. Buslaev, A. Kunshin, D. Sidorov, A. Kraslawski, M. Budovskaya, New concepts of hydrogen production and storage in Arctic region, Resources 10 (2021) 1–18. https://doi.org/10.3390/resources10010003.
[24] S. Bourne, The future of fuel: The future of hydrogen, Fuel Cells Bull. 2012 (2012) 12–15. https://doi.org/10.1016/S1464-2859(12)70027-5.
[25] IRENA, Green Hydrogen cost reduction: Scaling up electrolysers to meet the 1.5 °C climate goal, Abu Dhabi, 2020.
[26] International Renewable Energy Agency, Green Hydrogen: A Guide to Policy Making, 2021.
[27] J.M.M. Arcos, D.M.F. Santos, The Hydrogen Color Spectrum: Techno-Economic Analysis of the Available Technologies for Hydrogen Production, Gases 3 (2023) 25–46. https://doi.org/10.3390/gases3010002.
[28] R. Kumar, R. Singh, S. Dutta, Review and Outlook of Hydrogen Production through Catalytic Processes, Energy and Fuels 38 (2024) 2601–2629. https://doi.org/10.1021/acs.energyfuels.3c04026.
[29] P. Afanasev, A. Askarova, T. Alekhina, E. Popov, S. Markovic, A. Mukhametdinova, A. Cheremisin, E. Mukhina, An overview of hydrogen production methods: Focus on hydrocarbon feedstock, Int. J. Hydrogen Energy 78 (2024) 805–828. https://doi.org/10.1016/j.ijhydene.2024.06.369.
[30] B.S. Zainal, P.J. Ker, H. Mohamed, H.C. Ong, I.M.R. Fattah, S.M.A. Rahman, L.D. Nghiem, T.M.I. Mahlia, Recent advancement and assessment of green hydrogen production technologies, Renew. Sustain. Energy Rev.

189 (2024) 113941. https://doi.org/10.1016/j.rser.2023.113941.
[31] I. Renewable, E. Agency, Green hydrogen for industry: A guide to policy making, Abu Dhabi, 2022.
[32] World Energy Council in collaboration with EPRI and PwC, National Hydrogen Strategies, Hydrog. Horiz. Ready, Almost Set, Go? (2021) 1–20. https://www.worldenergy.org/assets/downloads/Working_Paper_-_National_Hydrogen_Strategies_-_September_2021.pdf%0Ahttps://www.worldenergy.org/publications/entry/working-paper-hydrogen-on-the-horizon-national-hydrogen-strategies.
[33] Y. Luo, Z. Zhang, M. Chhowalla, B. Liu, Recent Advances in Design of Electrocatalysts for High-Current-Density Water Splitting, Adv. Mater. 34 (2022). https://doi.org/10.1002/adma.202108133.
[34] H. Sun, X. Xu, H. Kim, W.C. Jung, W. Zhou, Z. Shao, Electrochemical Water Splitting: Bridging the Gaps Between Fundamental Research and Industrial Applications, Energy Environ. Mater. 6 (2023) 1–21. https://doi.org/10.1002/eem2.12441.
[35] A. González-Garay, N. Mac Dowell, N. Shah, A carbon neutral chemical industry powered by the sun, Discov. Chem. Eng. 1 (2021). https://doi.org/10.1007/s43938-021-00002-x.
[36] V.A. Panchenko, Y. V. Daus, A.A. Kovalev, I. V. Yudaev, Y. V. Litti, Prospects for the production of green hydrogen: Review of countries with high potential, Int. J. Hydrogen Energy 48 (2023) 4551–4571. https://doi.org/10.1016/j.ijhydene.2022.10.084.
[37] L. Eicke, N. De Blasio, Green hydrogen value chains in the industrial sector—Geopolitical and market implications, Energy Res. Soc. Sci. 93 (2022) 102847. https://doi.org/10.1016/j.erss.2022.102847.
[38] G. Kakoulaki, I. Kougias, N. Taylor, F. Dolci, J. Moya, A. Jäger-Waldau, Green hydrogen in Europe – A regional assessment: Substituting existing production with electrolysis powered by renewables, Energy Convers. Manag. 228 (2021). https://doi.org/10.1016/j.enconman.2020.113649.
[39] I.R.E. Agency, Renewable Power Generation Costs in 2019, 2020. https://www.irena.org/-/media/Files/IRENA/Agency/Publication/2018/Jan/IRENA_2017_Power_Costs_2018.pdf.
[40] M.R.G. Pangestu, Z. Malaibari, A. Muhammad, F.N. Al-Rowaili, U. Zahid, Comprehensive Review on Methane Pyrolysis for Sustainable Hydrogen Production, Energy and Fuels 38 (2024) 13514–13538. https://doi.org/10.1021/acs.energyfuels.4c01551.
[41] J.L. Aleixandre-Tudó, L. Castelló-Cogollos, J.L. Aleixandre, R. Aleixandre-Benavent, Renewable energies: Worldwide trends in research, funding and international collaboration, Renew. Energy 139 (2019) 268–278. https://doi.org/10.1016/j.renene.2019.02.079.
[42] T. Kurbatova, T. Perederii, Global trends in renewable energy development, 2020 IEEE KhPI Week Adv. Technol. KhPI Week 2020 - Conf. Proc. (2020) 260–263. https://doi.org/10.1109/KhPIWeek51551.2020.9250098.
[43] Q. Hassan, S. Algburi, A.Z. Sameen, T.J. Al-Musawi, A.K. Al-Jiboory, H.M. Salman, B.M. Ali, M. Jaszczur, A comprehensive review of international renewable energy growth, Energy Built Environ. (2024). https://doi.org/10.1016/j.enbenv.2023.12.002.
[44] A.I. Osman, N. Mehta, A.M. Elgarahy, M. Hefny, A. Al-Hinai, A.H. Al-Muhtaseb, D.W. Rooney, Hydrogen production, storage, utilisation and

environmental impacts: a review, 2022. https://doi.org/10.1007/s10311-021-01322-8.
[45] T. da Silva Veras, T.S. Mozer, D. da Costa Rubim Messeder dos Santos, A. da Silva César, Hydrogen: Trends, production and characterization of the main process worldwide, Int. J. Hydrogen Energy 42 (2017) 2018–2033. https://doi.org/10.1016/j.ijhydene.2016.08.219.
[46] Cost of hydrogen production, (n.d.). https://observatory.clean-hydrogen.europa.eu/hydrogen-landscape/production-trade-and-cost/cost-hydrogen-production?utm.
[47] P. Psarras, Technoeconomic Comparison of Hydrogen Production from Steam Methane Reforming with Carbon Capture and Renewably Powered Electrolysis, Exaere Consult. LLC 16 (2020) 39–55.
[48] S.W. Sharshir, A. Joseph, M.M. Elsayad, A.A. Tareemi, A.W. Kandeal, M.R. Elkadeem, A review of recent advances in alkaline electrolyzer for green hydrogen production: Performance improvement and applications, Int. J. Hydrogen Energy 49 (2024) 458–488. https://doi.org/10.1016/j.ijhydene.2023.08.107.
[49] D. Franzmann, H. Heinrichs, F. Lippkau, T. Addanki, C. Winkler, P. Buchenberg, T. Hamacher, M. Blesl, J. Linßen, D. Stolten, Green hydrogen cost-potentials for global trade, Int. J. Hydrogen Energy 48 (2023) 33062–33076. https://doi.org/10.1016/j.ijhydene.2023.05.012.
[50] P. Cavaliere, Water Electrolysis for Hydrogen Production, Springer International Publishing, Cham, 2023. https://doi.org/10.1007/978-3-031-37780-8.
[51] C.A. Schoeneberger, C.A. McMillan, P. Kurup, S. Akar, R. Margolis, E. Masanet, Solar for industrial process heat: A review of technologies, analysis approaches, and potential applications in the United States, Energy 206 (2020) 118083. https://doi.org/10.1016/j.energy.2020.118083.
[52] L. Kruitwagen, K.T. Story, J. Friedrich, L. Byers, S. Skillman, C. Hepburn, A global inventory of photovoltaic solar energy generating units, Nature 598 (2021) 604–610. https://doi.org/10.1038/s41586-021-03957-7.
[53] A.M. Oliveira, R.R. Beswick, Y. Yan, A green hydrogen economy for a renewable energy society, Curr. Opin. Chem. Eng. 33 (2021) 100701. https://doi.org/10.1016/j.coche.2021.100701.
[54] T.R. Ayodele, J.L. Munda, Potential and economic viability of green hydrogen production by water electrolysis using wind energy resources in South Africa, Int. J. Hydrogen Energy 44 (2019) 17669–17687. https://doi.org/10.1016/j.ijhydene.2019.05.077.
[55] N. Naseri, S. El Hani, M. Machmoum, E. Elbouchikhi, A. Daghouri, Energy Management Strategy for a Net Zero Emission Islanded Photovoltaic Microgrid-Based Green Hydrogen System, Energies 17 (2024) 1–19. https://doi.org/10.3390/en17092111.
[56] W. He, L. Chen, X. Qing, F. Qian, Towards a net-zero future for refineries: A case study on capacity configuration for hydrogenation demands in a refinery, AIChE J. 71 (2025). https://doi.org/10.1002/aic.18742.
[57] A.I. Atteya, D. Ali, M. Hossain, N. Sellami, A Comprehensive Review on The Empowering the Low-Carbon Economy : Development Status , Ongoing Trends, Green Energy Environ. Technol. 2 (2023) 1–53.
[58] J. Plunkett, C. White, S. Salerno, D. Gray, IGCC: Current status and future potential, AIChE Annu. Meet. Conf. Proc. (2007) 1–29.
[59] A.M. Hamed, T.N.A.T. Kamaruddin, N. Ramli, M.F.A. Wahab, A review on

blue and green hydrogen production process and their life cycle assessments, IOP Conf. Ser. Earth Environ. Sci. 1281 (2023). https://doi.org/10.1088/1755-1315/1281/1/012034.
[60] E.R. Sadik-Zada, Political economy of green hydrogen rollout: A global perspective, Sustain. 13 (2021). https://doi.org/10.3390/su132313464.
[61] H.P.S. Yalamati, R.K. Vij, R. Srivastava, Green hydrogen revolution: Mapping G20 nations' policies and geopolitical strategies in the net-zero emission era, Wiley Interdiscip. Rev. Energy Environ. 13 (2024) 1–18. https://doi.org/10.1002/wene.538.
[62] Commissione europea, Piano REPowerEU, Bruxelless, 2022.
[63] Geopolitica info, (n.d.). https://www.geopolitica.info/idrogeno-politiche-eu/.
[64] Approved IPCEIs in the Hydrogen value chain, (n.d.). https://competition-policy.ec.europa.eu/state-aid/ipcei/approved-ipceis/hydrogen-value-chain_en?utm.
[65] M. Muron, G. Pawelec, D. Fraile, Clean Hydrogen Production Pathways Report 2024, (2024). https://hydrogeneurope.eu/wp-content/uploads/2024/06/2024_H2E_CleanH2ProductionPathwaysReport.pdf.
[66] I. Renewable, E. Agency, HYDROGEN : A RENEWABLE, 2019.
[67] Mckinsey, Path to hydrogen competitiveness A cost perspective, Hydrog. Counc. (2020). www.hydrogencouncil.com.
[68] World Bank, Green Hydrogen in, Energy Sect. Manag. Assist. Progr. (2020).
[69] E. Arian, C. Zamfirescu, A review on water electrolysis, Tcjst 4 (2004) 41–71.
[70] A. Ursua, P. Sanchis, L.M. Gandia, Hydrogen Production from Water Electrolysis : Current Status and Future Trends, Proc. IEEE 100 (2012) 410–426.
[71] R.L. LeRoy, C.T. Bowen, D.J. LeRoy, The Thermodynamics of Aqueous Water Electrolysis, J. Electrochem. Soc. 127 (1980) 1954–1962. https://doi.org/10.1149/1.2130044.
[72] K. Onda, T. Kyakuno, K. Hattori, K. Ito, Prediction of production power for high-pressure hydrogen by high-pressure water electrolysis, J. Power Sources 132 (2004) 64–70. https://doi.org/10.1016/j.jpowsour.2004.01.046.
[73] A. Buttler, H. Spliethoff, Current status of water electrolysis for energy storage, grid balancing and sector coupling via power-to-gas and power-to-liquids: A review, Renew. Sustain. Energy Rev. 82 (2018) 2440–2454. https://doi.org/10.1016/j.rser.2017.09.003.
[74] S.A. Grigoriev, V.N. Fateev, D.G. Bessarabov, P. Millet, Current status, research trends, and challenges in water electrolysis science and technology, Int. J. Hydrogen Energy 45 (2020) 26036–26058. https://doi.org/10.1016/j.ijhydene.2020.03.109.
[75] A. Ursúa, P. Sanchis, Static-dynamic modelling of the electrical behaviour of a commercial advanced alkaline water electrolyser, Int. J. Hydrogen Energy 37 (2012) 18598–18614. https://doi.org/10.1016/j.ijhydene.2012.09.125.
[76] A. Gharib, A. Arab, Decomposition of formic acid via carboxyl mechanism on the graphene nanosheet decorated by Cr, Mn, Fe, Co, Ni, Pd, Ag, and Cd metals: A DFT study, 2023. https://doi.org/10.1016/j.ijhydene.2022.09.203.
[77] K. Zhang, X. Liang, L. Wang, K. Sun, Y. Wang, Z. Xie, Q. Wu, X. Bai, M.S. Hamdy, H. Chen, X. Zou, Status and perspectives of key materials for PEM

electrolyzer, Nano Res. Energy 1 (2022) 1–8. https://doi.org/10.26599/NRE.2022.9120032.
[78] M. Dreoni, F. Balduzzi, F.M. Ferro, G. Fagioli, K. Panichi, G. Ferrara, A. Bianchini, Multi-physics model development and application to real-case alkaline electrolyzer, J. Phys. Conf. Ser. 2648 (2023). https://doi.org/10.1088/1742-6596/2648/1/012060.
[79] P. Olivier, C. Bourasseau, P.B. Bouamama, Low-temperature electrolysis system modelling: A review, Renew. Sustain. Energy Rev. 78 (2017) 280–300. https://doi.org/10.1016/j.rser.2017.03.099.
[80] IRENA, Green hydrogen cost reduction: Scaling up electrolysers to meet the 1.5 °C climate goal, Abu Dhabi, 2020.
[81] J. Brauns, T. Turek, Alkaline water electrolysis powered by renewable energy: A review, Processes 8 (2020). https://doi.org/10.3390/pr8020248.
[82] M. Carmo, D.L. Fritz, J. Mergel, D. Stolten, A comprehensive review on PEM water electrolysis, Int. J. Hydrogen Energy 38 (2013) 4901–4934. https://doi.org/10.1016/j.ijhydene.2013.01.151.
[83] M. El-Shafie, Hydrogen production by water electrolysis technologies: A review, Results Eng. 20 (2023) 101426. https://doi.org/10.1016/j.rineng.2023.101426.
[84] Your shift to clean energy starts here, (n.d.). http://www.hydrogenics.com.
[85] No Title, (n.d.). https://nelhydrogen.com/support/.
[86] No Title, (n.d.). https://www.ginerinc.com/.
[87] No Title, (n.d.). https://www.treadwellcorp.com/.
[88] W. Kreuter, H. Hofmann, Electrolysis: the important energy transformer in a world of sustainable energy, Int. J. Hydrogen Energy 23 (1998) 661–666. https://doi.org/10.1016/S0360-3199(97)00109-2.
[89] Georgios Tsotridis, A. Pilenga, Eu H2 Protocols, 2021. https://doi.org/10.2760/58880.
[90] S.K. Mazloomi, N. Sulaiman, Influencing factors of water electrolysis electrical efficiency, Renew. Sustain. Energy Rev. 16 (2012) 4257–4263. https://doi.org/10.1016/j.rser.2012.03.052.
[91] J. Ivy, Summary of electrolytic hydrogen production, Small (2004) 27. http://www.nrel.gov/docs/fy04osti/35948.pdf.
[92] V. Schröder, B. Emonts, H. Janßen, H.P. Schulze, Explosion limits of hydrogen/oxygen mixtures at initial pressures up to 200 bar, Chem. Eng. Technol. 27 (2004) 847–851. https://doi.org/10.1002/ceat.200403174.
[93] H. Janssen, J.C. Bringmann, B. Emonts, V. Schroeder, Safety-related studies on hydrogen production in high-pressure electrolysers, Int. J. Hydrogen Energy 29 (2004) 759–770. https://doi.org/10.1016/j.ijhydene.2003.08.014.
[94] L.M. Gandía, R. Oroz, A. Ursúa, P. Sanchis, P.M. Diéguez, Renewable hydrogen production: Performance of an alkaline water electrolyzer working under emulated wind conditions, Energy and Fuels 21 (2007) 1699–1706. https://doi.org/10.1021/ef060491u.
[95] M. Sánchez, E. Amores, L. Rodríguez, C. Clemente-Jul, Semi-empirical model and experimental validation for the performance evaluation of a 15 kW alkaline water electrolyzer, Int. J. Hydrogen Energy 43 (2018) 20332–20345. https://doi.org/10.1016/j.ijhydene.2018.09.029.
[96] C. Santoro, A. Lavacchi, P. Mustarelli, V. Di Noto, L. Elbaz, D.R. Dekel, F. Jaouen, What is Next in Anion-Exchange Membrane Water Electrolyzers? Bottlenecks, Benefits, and Future, ChemSusChem 15 (2022). https://doi.org/10.1002/cssc.202200027.

[97] S. Sebbahi, A. Assila, A. Alaoui Belghiti, S. Laasri, S. Kaya, E.K. Hlil, S. Rachidi, A. Hajjaji, A comprehensive review of recent advances in alkaline water electrolysis for hydrogen production, Int. J. Hydrogen Energy 82 (2024) 583–599. https://doi.org/10.1016/j.ijhydene.2024.07.428.
[98] P. Vermeiren, W. Adriansens, J.P. Moreels, R. Leysen, Evaluation of the zirfon® separator for use in alkaline water electrolysis and Ni-H2 batteries, Int. J. Hydrogen Energy 23 (1998) 321–324. https://doi.org/10.1016/s0360-3199(97)00069-4.
[99] M.T. de Groot, A.W. Vreman, Ohmic resistance in zero gap alkaline electrolysis with a Zirfon diaphragm, Electrochim. Acta 369 (2021). https://doi.org/10.1016/j.electacta.2020.137684.
[100] K. Rajeshwar, R. McConnell, S. Licht, Solar hydrogen generation: Toward a renewable energy future, Sol. Hydrog. Gener. Towar. a Renew. Energy Futur. (2008) 1–318. https://doi.org/10.1007/978-0-387-72810-0.
[101] Q. Zhu, T. Zhang, X. Zhu, J. Zhang, M. Shan, Z. Hu, G. Xu, M. Zhu, Rigid-flexible coupling poly (phenylene sulfide) fiber membrane: a highly stable chemical and thermal material for energy and environmental applications, Energy Mater. 4 (2024). https://doi.org/10.20517/energymater.2023.85.
[102] D. Henkensmeier, W.C. Cho, P. Jannasch, J. Stojadinovic, Q. Li, D. Aili, J.O. Jensen, Separators and Membranes for Advanced Alkaline Water Electrolysis, Chem. Rev. 124 (2024) 6393–6443. https://doi.org/10.1021/acs.chemrev.3c00694.
[103] B. Rutjens, K. von Foerster, B. Schmid, H. Weinrich, S. Sanz, H. Tempel, R.A. Eichel, Impact of the PiperION Anion Exchange Membrane Thickness on the Performance of a CO2-to-HCOOH Three-Compartment Electrolyzer, Ind. Eng. Chem. Res. 63 (2024) 3986–3996. https://doi.org/10.1021/acs.iecr.3c04459.
[104] M. Ni, M.K.H. Leung, D.Y.C. Leung, Technological development of hydrogen production by solid oxide electrolyzer cell (SOEC), Int. J. Hydrogen Energy 33 (2008) 2337–2354. https://doi.org/10.1016/j.ijhydene.2008.02.048.
[105] M. Sohal, J. O'Brien, C. Stoots, M. McKellar, Challenges in Generating Hydrogen by High Temperature Electrolysis Using Solid Oxide Cells, Development (2008). http://www.inl.gov/technicalpublications/Documents/3920063.pdf.
[106] J. Kong, Y. Zhang, C. Deng, J. Xu, Synthesis and electrochemical properties of LSM and LSF perovskites as anode materials for high temperature steam electrolysis, J. Power Sources 186 (2009) 485–489. https://doi.org/10.1016/j.jpowsour.2008.10.053.
[107] C. Yang, A. Coffin, F. Chen, High temperature solid oxide electrolysis cell employing porous structured (La0.75Sr0.25)0.95MnO3 with enhanced oxygen electrode performance, Int. J. Hydrogen Energy 35 (2010) 3221–3226. https://doi.org/10.1016/j.ijhydene.2010.01.056.
[108] J. Sigurvinsson, C. Mansilla, P. Lovera, F. Werkoff, Can high temperature steam electrolysis function with geothermal heat?, Int. J. Hydrogen Energy 32 (2007) 1174–1182. https://doi.org/10.1016/j.ijhydene.2006.11.026.
[109] M. Plevová, J. Hnát, K. Bouzek, Electrocatalysts for the oxygen evolution reaction in alkaline and neutral media. A comparative review, J. Power Sources 507 (2021). https://doi.org/10.1016/j.jpowsour.2021.230072.
[110] X. Xie, L. Du, L. Yan, S. Park, Y. Qiu, J. Sokolowski, W. Wang, Y. Shao, Oxygen Evolution Reaction in Alkaline Environment: Material Challenges

and Solutions, Adv. Funct. Mater. 32 (2022). https://doi.org/10.1002/adfm.202110036.
[111] Y. Luo, Z. Zhang, M. Chhowalla, B. Liu, Recent Advances in Design of Electrocatalysts for High-Current-Density Water Splitting, Adv. Mater. 34 (2022) 1–18. https://doi.org/10.1002/adma.202108133.
[112] T. Reier, M. Oezaslan, P. Strasser, Electrocatalytic oxygen evolution reaction (OER) on Ru, Ir, and pt catalysts: A comparative study of nanoparticles and bulk materials, ACS Catal. 2 (2012) 1765–1772. https://doi.org/10.1021/cs3003098.
[113] I. Barlocco, L.A. Cipriano, G. Di Liberto, G. Pacchioni, Does the Oxygen Evolution Reaction follow the classical OH*, O*, OOH* path on single atom catalysts?, J. Catal. 417 (2023) 351–359. https://doi.org/10.1016/j.jcat.2022.12.014.
[114] Y. Zhao, D.P. Adiyeri Saseendran, C. Huang, C.A. Triana, W.R. Marks, H. Chen, H. Zhao, G.R. Patzke, Oxygen Evolution/Reduction Reaction Catalysts: From In Situ Monitoring and Reaction Mechanisms to Rational Design, Chem. Rev. 123 (2023) 6257–6358. https://doi.org/10.1021/acs.chemrev.2c00515.
[115] A.W. Tricker, T.Y. Ertugrul, J.K. Lee, J.R. Shin, W. Choi, D.I. Kushner, G. Wang, J. Lang, I. V. Zenyuk, A.Z. Weber, X. Peng, Pathways Toward Efficient and Durable Anion Exchange Membrane Water Electrolyzers Enabled By Electro-Active Porous Transport Layers, Adv. Energy Mater. 14 (2024) 1–12. https://doi.org/10.1002/aenm.202303629.
[116] G. Li, L. Anderson, Y. Chen, M. Pan, P.-Y. Abel Chuang, New insights into evaluating catalyst activity and stability for oxygen evolution reactions in alkaline media, Sustain. Energy Fuels 2 (2018) 237–251. https://doi.org/10.1039/C7SE00337D.
[117] S. Wang, A. Lu, C.J. Zhong, Hydrogen production from water electrolysis: role of catalysts, Nano Converg. 8 (2021). https://doi.org/10.1186/s40580-021-00254-x.
[118] W.T. Hong, M. Risch, K.A. Stoerzinger, A. Grimaud, J. Suntivich, Y. Shao-Horn, Toward the rational design of non-precious transition metal oxides for oxygen electrocatalysis, Energy Environ. Sci. 8 (2015) 1404–1427. https://doi.org/10.1039/c4ee03869j.
[119] A. Higareda, D.L. Hernández-Arellano, L.C. Ordoñez, R. Barbosa, N. Alonso-Vante, Advanced Electrocatalysts for the Oxygen Evolution Reaction: From Single- to Multielement Materials, Catalysts 13 (2023). https://doi.org/10.3390/catal13101346.
[120] Y. Lee, J. Suntivich, K.J. May, E.E. Perry, Y. Shao-Horn, Synthesis and activities of rutile IrO 2 and RuO 2 nanoparticles for oxygen evolution in acid and alkaline solutions, J. Phys. Chem. Lett. 3 (2012) 399–404. https://doi.org/10.1021/jz2016507.
[121] E. Tsuji, A. Imanishi, K.I. Fukui, Y. Nakato, Electrocatalytic activity of amorphous RuO2 electrode for oxygen evolution in an aqueous solution, Electrochim. Acta 56 (2011) 2009–2016. https://doi.org/10.1016/j.electacta.2010.11.062.
[122] D. Zhou, P. Li, W. Xu, S. Jawaid, J. Mohammed-Ibrahim, W. Liu, Y. Kuang, X. Sun, Recent Advances in Non-Precious Metal-Based Electrodes for Alkaline Water Electrolysis, ChemNanoMat 6 (2020) 336–355. https://doi.org/10.1002/cnma.202000010.
[123] B. Zhang, L. Sun, Ru-bda: Unique Molecular Water-Oxidation Catalysts

with Distortion Induced Open Site and Negatively Charged Ligands, J. Am. Chem. Soc. 141 (2019) 5565–5580. https://doi.org/10.1021/jacs.8b12862.
[124] J.A. Koza, Z. He, A.S. Miller, J.A. Switzer, Electrodeposition of crystalline Co 3O 4-A catalyst for the oxygen evolution reaction, Chem. Mater. 24 (2012) 3567–3573. https://doi.org/10.1021/cm3012205.
[125] H. Sun, Z. Yan, F. Liu, W. Xu, F. Cheng, J. Chen, Self-Supported Transition-Metal-Based Electrocatalysts for Hydrogen and Oxygen Evolution, Adv. Mater. 32 (2020) 1–18. https://doi.org/10.1002/adma.201806326.
[126] H. Sun, Z. Yan, F. Liu, W. Xu, F. Cheng, J. Chen, Self-Supported Transition-Metal-Based Electrocatalysts for Hydrogen and Oxygen Evolution, Adv. Mater. 32 (2020). https://doi.org/10.1002/adma.201806326.
[127] R. Khan, M.T. Mehran, S.R. Naqvi, A.H. Khoja, K. Mahmood, F. Shahzad, S. Hussain, Role of perovskites as a bi-functional catalyst for electrochemical water splitting: A review, Int. J. Energy Res. 44 (2020) 9714–9747. https://doi.org/10.1002/er.5635.
[128] J. Suntivich, K.J. May, H.A. Gasteiger, J.B. Goodenough, Y. Shao-Horn, A perovskite oxide optimized for oxygen evolution catalysis from molecular orbital principles, Science (80-.). 334 (2011) 1383–1385. https://doi.org/10.1126/science.1212858.
[129] X. Xu, C. Su, W. Zhou, Y. Zhu, Y. Chen, Z. Shao, Co-doping strategy for developing perovskite oxides as highly efficient electrocatalysts for oxygen evolution reaction, Adv. Sci. 3 (2015) 1–6. https://doi.org/10.1002/advs.201500187.
[130] D.S. Bick, A. Kindsmüller, G. Staikov, F. Gunkel, D. Müller, T. Schneller, R. Waser, I. Valov, Stability and Degradation of Perovskite Electrocatalysts for Oxygen Evolution Reaction, Electrochim. Acta 218 (2016) 156–162. https://doi.org/10.1016/j.electacta.2016.09.116.
[131] D.S. Bick, J.D. Griesche, T. Schneller, G. Staikov, R. Waser, I. Valov, Pr x Ba 1-x CoO 3 Oxide Electrodes for Oxygen Evolution Reaction in Alkaline Solutions by Chemical Solution Deposition , J. Electrochem. Soc. 163 (2016) F166–F170. https://doi.org/10.1149/2.0311603jes.
[132] D.S. Bick, A. Kindsmüller, D.-Y. Cho, A.Y. Mohamed, T. Bredow, H. Laufen, F. Gunkel, D.N. Mueller, T. Schneller, R. Waser, I. Valov, Self-Assembling oxide catalyst for electrochemical water splitting, ArXiv (2017). https://doi.org/10.48550/arXiv.1707.03346.
[133] T. Tabari, M. Kobielusz, D. Singh, J. Yu, W. Macyk, Cobalt-/Copper-Containing Perovskites in Oxygen Evolution and Reduction Reactions, ACS Appl. Eng. Mater. 1 (2023) 2207–2216. https://doi.org/10.1021/acsaenm.3c00288.
[134] M.B. Kale, R.A. Borse, A. Gomaa Abdelkader Mohamed, Y. Wang, Electrocatalysts by Electrodeposition: Recent Advances, Synthesis Methods, and Applications in Energy Conversion, Adv. Funct. Mater. 31 (2021) 1–24. https://doi.org/10.1002/adfm.202101313.
[135] J. Du, F. Li, L. Sun, Metal-organic frameworks and their derivatives as electrocatalysts for the oxygen evolution reaction, Chem. Soc. Rev. 50 (2021) 2663–2695. https://doi.org/10.1039/d0cs01191f.
[136] X. Qin, D. Kim, Y. Piao, Metal-organic frameworks-derived novel nanostructured electrocatalysts for oxygen evolution reaction, Carbon Energy 3 (2021) 66–100. https://doi.org/10.1002/cey2.80.
[137] B. He, Q. Zhang, Z. Pan, L. Li, C. Li, Y. Ling, Z. Wang, M. Chen, Z. Wang, Y. Yao, Q. Li, L. Sun, J. Wang, L. Wei, Freestanding Metal-Organic

Frameworks and Their Derivatives: An Emerging Platform for Electrochemical Energy Storage and Conversion, Chem. Rev. 122 (2022) 10087–10125. https://doi.org/10.1021/acs.chemrev.1c00978.
[138] Q. Liang, J. Chen, F. Wang, Y. Li, Transition metal-based metal-organic frameworks for oxygen evolution reaction, Coord. Chem. Rev. 424 (2020) 213488. https://doi.org/10.1016/j.ccr.2020.213488.
[139] D. Li, H.Q. Xu, L. Jiao, H.L. Jiang, Metal-organic frameworks for catalysis: State of the art, challenges, and opportunities, EnergyChem 1 (2019) 100005. https://doi.org/10.1016/j.enchem.2019.100005.
[140] H. Furukawa, K.E. Cordova, M. O'Keeffe, O.M. Yaghi, The chemistry and applications of metal-organic frameworks, Science (80-.). 341 (2013). https://doi.org/10.1126/science.1230444.
[141] H.F. Wang, L. Chen, H. Pang, S. Kaskel, Q. Xu, MOF-derived electrocatalysts for oxygen reduction, oxygen evolution and hydrogen evolution reactions, Chem. Soc. Rev. 49 (2020) 1414–1448. https://doi.org/10.1039/c9cs00906j.
[142] K. Biradha, A. Goswami, R. Moi, Coordination polymers as heterogeneous catalysts in hydrogen evolution and oxygen evolution reactions, Chem. Commun. 56 (2020) 10824–10842. https://doi.org/10.1039/d0cc04236f.
[143] Y. Guo, C. Zhang, J. Zhang, K. Dastafkan, K. Wang, C. Zhao, Z. Shi, Metal-Organic Framework-Derived Bimetallic NiFe Selenide Electrocatalysts with Multiple Phases for Efficient Oxygen Evolution Reaction, ACS Sustain. Chem. Eng. 9 (2021) 2047–2056. https://doi.org/10.1021/acssuschemeng.0c06969.
[144] F. Shahbazi Farahani, M.S. Rahmanifar, A. Noori, M.F. El-Kady, N. Hassani, M. Neek-Amal, R.B. Kaner, M.F. Mousavi, Trilayer Metal-Organic Frameworks as Multifunctional Electrocatalysts for Energy Conversion and Storage Applications, J. Am. Chem. Soc. 144 (2022) 3411–3428. https://doi.org/10.1021/jacs.1c10963.
[145] H. Wu, W. Zheng, R. Zhu, M. Zhou, X. Ren, Y. Wang, C. Cheng, H. Zhou, S. Cao, Modulating coordination structures and metal environments of MOFs-Engineered electrocatalysts for water electrolysis, Chem. Eng. J. 452 (2023) 139475. https://doi.org/10.1016/j.cej.2022.139475.
[146] Y. Li, Z. Gao, H. Bao, B. Zhang, C. Wu, C. Huang, Z. Zhang, Y. Xie, H. Wang, Amorphous nickel-cobalt bimetal-organic framework nanosheets with crystalline motifs enable efficient oxygen evolution reaction: Ligands hybridization engineering, J. Energy Chem. 53 (2020) 251–259. https://doi.org/10.1016/j.jechem.2020.05.002.
[147] Y. Xie, M. Liu, Y. Li, Z. Zhang, C. Wu, C. Huang, Z. Guo, H. Wang, Toward efficient cobalt-based oxygen evolution reaction: heteropolyatomic anion-inductive effect, Mater. Today Energy 24 (2022). https://doi.org/10.1016/j.mtener.2021.100922.
[148] X. Zhang, K. Wan, P. Subramanian, M. Xu, J. Luo, J. Fransaer, Electrochemical deposition of metal-organic framework films and their applications, J. Mater. Chem. A 8 (2020) 7569–7587. https://doi.org/10.1039/d0ta00406e.
[149] N. Campagnol, T.R.C. Van Assche, M. Li, L. Stappers, M. Dinca, J.F.M. Denayer, K. Binnemans, D.E. De Vos, J. Fransaer, On the electrochemical deposition of metal-organic frameworks, J. Mater. Chem. A 4 (2016) 3914–3925. https://doi.org/10.1039/c5ta10782b.
[150] B. Zhang, P. Huang, J. Chen, X. Dang, Y. Hu, Y. Ai, D. Zheng, H. Chen,

One-step controlled electrodeposition of iron-based binary metal organic nanocomposite, Appl. Surf. Sci. 504 (2020) 144504. https://doi.org/10.1016/j.apsusc.2019.144504.
[151] A. Mariella Babu, A. Varghese, Electrochemical deposition for metal organic Frameworks: Advanced Energy, Catalysis, sensing and separation applications, J. Electroanal. Chem. 937 (2023) 117417. https://doi.org/10.1016/j.jelechem.2023.117417.
[152] D. Yu, Y. Ma, F. Hu, C. Lin, L. Li, H. Chen, X. Han, S. Peng, Dual-Sites Coordination Engineering of Single Atom Catalysts for Flexible Metal–Air Batteries, Adv. Energy Mater. 11 (2021). https://doi.org/10.1002/aenm.202101242.
[153] K.W. Jung, B.H. Choi, S.Y. Lee, K.H. Ahn, Y.J. Lee, Green synthesis of aluminum-based metal organic framework for the removal of azo dye Acid Black 1 from aqueous media, J. Ind. Eng. Chem. 67 (2018) 316–325. https://doi.org/10.1016/j.jiec.2018.07.003.
[154] N. Fajrin, I.R. Saragi, Y.K. Krisnandi, A. Zulys, Synthesis of metal organic framework (MOF) using lanthanum and yttrium metals with succinate acid ligand as adsorbent for cadmium(II) metal ion, AIP Conf. Proc. 2242 (2020). https://doi.org/10.1063/5.0008318.
[155] D.A. Nurani, B.C.B. Butar, Y.K. Krisnandi, Synthesis and characterization of metal organic framework using succinic acid ligand with cobalt and iron metals as methylene blue dye adsorbent, IOP Conf. Ser. Mater. Sci. Eng. 902 (2020). https://doi.org/10.1088/1757-899X/902/1/012055.
[156] A. Sharma, M. Kumari, M. Tahir, S. Jain, S. Sharma, N. Kumar, An energy saving and water- based synthesis of Bi2O3@Fe-succinate MOF: A visible light mediated approach towards water decontamination, J. Mol. Liq. 386 (2023) 122429. https://doi.org/10.1016/j.molliq.2023.122429.
[157] A. Palǒić, A. Puškarić, M. Mazaj, E. Žunkoviǒ, N.Z. Logar, J. Bronić, Structural and degradation studies of a biocompatible Zn-L-tartrate metal-organic framework, J. Solid State Chem. 225 (2015) 59–64. https://doi.org/10.1016/j.jssc.2014.11.028.
[158] U. Huizi-Rayo, X. Gastearena, A.M. Ortuño, J.M. Cuerva, A. Rodríguez-Diéguez, J.A. García, J. Ugalde, J.M. Seco, E.S. Sebastian, J. Cepeda, Influence of Tartrate Ligand Coordination over Luminescence Properties of Chiral Lanthanide-Based Metal–Organic Frameworks, Nanomaterials 12 (2022). https://doi.org/10.3390/nano12223999.
[159] C. Jandl, G. Steinfeld, K. Li, P.K.C. Pang, C.L. Choi, C. Wang, P. Simoncic, I.D. Williams, Absolute Structure Determination of Chiral Zinc Tartrate MOFs by 3D Electron Diffraction, Symmetry (Basel). 15 (2023). https://doi.org/10.3390/sym15050983.
[160] C.C.L. McCrory, S. Jung, I.M. Ferrer, S.M. Chatman, J.C. Peters, T.F. Jaramillo, Benchmarking Hydrogen Evolving Reaction and Oxygen Evolving Reaction Electrocatalysts for Solar Water Splitting Devices, J. Am. Chem. Soc. 137 (2015) 4347–4357. https://doi.org/10.1021/ja510442p.
[161] C. Wu, Y. Tang, A. Zou, J. Li, H. Meng, F. Gao, J. Wu, X. Wang, Recommended electrochemical measurement protocol for oxygen evolution reaction, DeCarbon 8 (2025) 100108. https://doi.org/10.1016/j.decarb.2025.100108.
[162] S. Appelhaus, L. Ritz, S.V. Pape, F. Lohmann-Richters, M.R. Kraglund, J.O. Jensen, F. Massari, M. Boroomandnia, M. Romanò, J. Albers, C. Kubeil, C. Bernäcker, M.S. Lemcke, N. Menzel, G. Bender, B. Chen, S. Holdcroft, R.

Delmelle, J. Proost, J. Hnát, P. Kauranen, V. Ruuskanen, T. Viinanen, M. Müller, T. Turek, M. Shviro, Benchmarking performance: A round-robin testing for liquid alkaline electrolysis, Int. J. Hydrogen Energy 95 (2024) 1004–1010. https://doi.org/10.1016/j.ijhydene.2024.11.288.
[163] E.B. Creel, X. Lyu, G. McCool, R.J. Ouimet, A. Serov, Protocol for Screening Water Oxidation or Reduction Electrocatalyst Activity in a Three-Electrode Cell for Alkaline Exchange Membrane Electrolysis, Front. Energy Res. 10 (2022) 1–7. https://doi.org/10.3389/fenrg.2022.871604.
[164] T. Malkow, A. Pilenga, G. Tsotridis, EU harmonised test procedure: electrochemical impedance spectroscopy for water electrolysis cells, 2018. https://doi.org/10.2760/8984.
[165] b P.-Y.A.C. Guangfu Li, a Lawrence Anderson, a Yanan Chen, a, b Mu Pan, A, Sustainable Energy & Fuels, (2017). https://doi.org/10.1039.
[166] C.C.L. McCrory, S. Jung, J.C. Peters, T.F. Jaramillo, Benchmarking heterogeneous electrocatalysts for the oxygen evolution reaction, J. Am. Chem. Soc. 135 (2013) 16977–16987. https://doi.org/10.1021/ja407115p.
[167] M. Zlatar, D. Escalera-López, M.G. Rodríguez, T. Hrbek, C. Götz, R. Mary Joy, A. Savan, H.P. Tran, H.N. Nong, P. Pobedinskas, V. Briega-Martos, A. Hutzler, T. Böhm, K. Haenen, A. Ludwig, I. Khalakhan, P. Strasser, S. Cherevko, Standardizing OER Electrocatalyst Benchmarking in Aqueous Electrolytes: Comprehensive Guidelines for Accelerated Stress Tests and Backing Electrodes, ACS Catal. 13 (2023) 15375–15392. https://doi.org/10.1021/acscatal.3c03880.
[168] C. Wei, R.R. Rao, J. Peng, B. Huang, I.E.L. Stephens, M. Risch, Z.J. Xu, Y. Shao-Horn, Recommended Practices and Benchmark Activity for Hydrogen and Oxygen Electrocatalysis in Water Splitting and Fuel Cells, Adv. Mater. 31 (2019) 1806296. https://doi.org/10.1002/adma.201806296.
[169] G. Smith, E.J.F. Dickinson, Error, reproducibility and uncertainty in experiments for electrochemical energy technologies, Nat. Commun. 13 (2022) 1–6. https://doi.org/10.1038/s41467-022-34594-x.
[170] N. Thissen, J. Hoffmann, S. Tigges, D.A.M. Vogel, J.J. Thoede, S. Khan, N. Schmitt, S. Heumann, B.J.M. Etzold, A.K. Mechler, Industrially Relevant Conditions in Lab-Scale Analysis for Alkaline Water Electrolysis, ChemElectroChem 11 (2024). https://doi.org/10.1002/celc.202300432.
[171] A. project, D2.1 Harmonised test protocols for assessing AEM electrolysis components, cells and stacks in a wide range of operating temperature and pressure, (2020). www.anione.eu.
[172] C. Wei, R.R. Rao, J. Peng, B. Huang, I.E.L. Stephens, M. Risch, Z.J. Xu, Y. Shao-Horn, Recommended Practices and Benchmark Activity for Hydrogen and Oxygen Electrocatalysis in Water Splitting and Fuel Cells, Adv. Mater. 31 (2019) 1–24. https://doi.org/10.1002/adma.201806296.
[173] J. Guo, Y. Xu, P. Li, K. Pedersen, M. Gaberšček, D.I. Stroe, Can Electrochemical Impedance Spectroscopy be Replaced by Direct Current Techniques in Battery Diagnosis?, ChemPhysChem 25 (2024) 1–9. https://doi.org/10.1002/cphc.202400528.
[174] L. Stolz, M. Gaberšček, M. Winter, J. Kasnatscheew, Different Efforts but Similar Insights in Battery R&D: Electrochemical Impedance Spectroscopy vs Galvanostatic (Constant Current) Technique, Chem. Mater. 34 (2022) 10272–10278. https://doi.org/10.1021/acs.chemmater.2c02376.
[175] M. Schalenbach, H. Tempel, R.A. Eichel, Capacitance Measurements for Evaluating Electrochemical Double-Layer Models and Potentials of Zero

Charge: A Reassessment, ChemPhysChem 26 (2025) 1–10. https://doi.org/10.1002/cphc.202401088.
[176] M. Schalenbach, V. Selmert, A. Kretzschmar, L. Raijmakers, Y.E. Durmus, H. Tempel, R.A. Eichel, How microstructures, oxide layers, and charge transfer reactions influence double layer capacitances. Part 1: impedance spectroscopy and cyclic voltammetry to estimate electrochemically active surface areas (ECSAs), Phys. Chem. Chem. Phys. 26 (2023) 14288–14304. https://doi.org/10.1039/d3cp04743a.
[177] J. Zhang, S. Wang, K. Ono, Electrochemical Impedance Spectroscopy, 2023. https://doi.org/10.1201/9781003299295-11.
[178] T. Malkow, A. Pilenga, G. Tsotridis, EU Harmonised Polarisation Curve Test Method for Low Temperature Water Electrolysis, 2018. https://doi.org/10.2760/179509.
[179] M. Schalenbach, L. Raijmakers, H. Tempel, R.A. Eichel, How Microstructures, Oxide Layers, and Charge Transfer Reactions Influence Double Layer Capacitances. Part 2: Equivalent Circuit Models, Electrochem. Sci. Adv. 5 (2025). https://doi.org/10.1002/elsa.202400010.
[180] J.R. Macdonald, a J. Wiley, Theory , Experiment , and, n.d.
[181] X.-Z. Yuan, C. Song, H. Wang, J. Zhang, Electrochemical Impedance Spectroscopy in PEM Fuel Cells, Springer London, London, 2010. https://doi.org/10.1007/978-1-84882-846-9.
[182] G. Dotelli, R. Ferrero, P.G. Stampino, S. Latorrata, Analysis and compensation of PEM fuel cell instabilities in low-frequency EIS measurements, IEEE Trans. Instrum. Meas. 63 (2014) 1693–1700. https://doi.org/10.1109/TIM.2013.2297632.
[183] E. Giordano, A. Zaffora, L. Iannucci, M. Santamaria, S. Grassini, Study of Methanol Concentration Effect in Direct Methanol Fuel Cells by Electrochemical Impedance Spectroscopy, Conf. Rec. - IEEE Instrum. Meas. Technol. Conf. 2023-May (2023). https://doi.org/10.1109/I2MTC53148.2023.10176090.
[184] L. Deleebeeck, S. Veltzé, Electrochemical impedance spectroscopy study of commercial Li-ion phosphate batteries: A metrology perspective, Int. J. Energy Res. 44 (2020) 7158–7182. https://doi.org/10.1002/er.5350.
[185] A.M. Dhirde, N. V. Dale, H. Salehfar, M.D. Mann, T.H. Han, Equivalent electric circuit modeling and performance analysis of a PEM fuel cell stack using impedance spectroscopy, IEEE Trans. Energy Convers. 25 (2010) 778–786. https://doi.org/10.1109/TEC.2010.2049267.
[186] P.A. Lindahl, S. Member, M.A. Cornachione, S.R. Shaw, S. Member, A Time-Domain Least Squares Approach to Electrochemical Impedance Spectroscopy, IEEE Trans. Instrum. Meas. 61 (2012) 3303–3311. https://doi.org/10.1109/TIM.2012.2210457.
[187] A.C. Lazanas, M.I. Prodromidis, Electrochemical Impedance Spectroscopy─A Tutorial, ACS Meas. Sci. Au 3 (2023) 162–193. https://doi.org/10.1021/acsmeasuresciau.2c00070.
[188] E. Cossar, M.S.E. Houache, Z. Zhang, E.A. Baranova, Comparison of electrochemical active surface area methods for various nickel nanostructures, J. Electroanal. Chem. 870 (2020) 114246. https://doi.org/10.1016/j.jelechem.2020.114246.
[189] Z. Xie, W. Qu, E.A. Fisher, J. Fahlman, K. Asazawa, T. Hayashi, H. Shirataki, H. Murase, Capacitance Determination for the Evaluation of Electrochemically Active Surface Area in a Catalyst Layer of NiFe-Layered

Double Hydroxides for Anion Exchange Membrane Water Electrolyser, Materials (Basel). 17 (2024). https://doi.org/10.3390/ma17030556.
[190] Z. Jia, S. Hao, J. Wen, S. Li, W. Peng, R. Huang, X. Xu, Electrochemical fabrication of metal–organic frameworks membranes and films: A review, Microporous Mesoporous Mater. 305 (2020). https://doi.org/10.1016/j.micromeso.2020.110322.
[191] J. Jian, Z. Wang, Y. Qiao, S. Gao, M. Wang, L. Chang, H. Wang, P. Nie, NiCoP@CoNi-LDH/SSM as a multifunctional catalyst for high-efficiency water splitting and ultra-long-life rechargeable zinc-air batteries, Green Chem. 26 (2024) 6713–6722. https://doi.org/10.1039/D4GC01546K.
[192] Z. Wang, Y. Qiao, X. Xue, M. Wang, P. Nie, Y. Liu, L. Chang, J. Jian, Cobalt Carbide-Nickel Carbide Nanosheets Supported on CoNi Basic Carbonates/Stainless Steel Mesh as a Trifunctional Catalyst for Water Splitting and Zn-Air Batteries, ACS Appl. Nano Mater. 7 (2024) 27620–27627. https://doi.org/10.1021/acsanm.4c05631.
[193] J. Jian, Z. Wang, Y. Qiao, M. Wang, P. Nie, L. Chang, Stainless steel mesh based CoNiSe4/CoNi-layered-double-hydroxides for efficient water-splitting and durable Zn-air battery, J. Power Sources 629 (2025) 235994. https://doi.org/10.1016/j.jpowsour.2024.235994.
[194] V.M. Volanti, A. Zaffora, L. Iannucci, S. Grassini, E. Inico, C. Saetta, G. Di Liberto, M. Santamaria, Design of Ni-coordinated MOF on stainless steel via electrodeposition as efficient and stable oxygen evolution electrode for alkaline water electrolysis, Electrochim. Acta 511 (2025) 145416. https://doi.org/10.1016/j.electacta.2024.145416.
[195] B. Chen, A.L.G. Biancolli, C.L. Radford, S. Holdcroft, Stainless Steel Felt as a Combined OER Electrocatalyst/Porous Transport Layer for Investigating Anion-Exchange Membranes in Water Electrolysis, ACS Energy Lett. 8 (2023) 2661–2667. https://doi.org/10.1021/acsenergylett.3c00878.
[196] A. Zaffora, F. Di Franco, D. Pupillo, B. Seminara, G. Tranchida, M. Santamaria, Highly Active and Stable NiCuMo Electrocatalyst Supported on 304 Stainless Steel Porous Transport Layer for Hydrogen Evolution in Alkaline Water Electrolyzer, Adv. Sustain. Syst. 7 (2023) 1–9. https://doi.org/10.1002/adsu.202200486.
[197] M. Paunovic, M. Schlesinger, Fundamentals of Deposition, 2006.
[198] A. Zaffora, V. Maria, L. Iannucci, S. Grassini, I. Valov, C. Saetta, G. Di, E. Mosca, I. Gatto, V. Baglio, M. Santamaria, Electrodeposited NiFe-succinate for the oxygen evolution reaction in anion exchange membrane water electrolysis, Fuel 407 (2026) 137329. https://doi.org/10.1016/j.fuel.2025.137329.
[199] C. Fei, N. Ma, Q. Zhong, Y. Wang, M. Li, Oxygen-Reduction-Triggered Cathodic Electrodeposition of Mn-Based Metal-Organic Framework Nanoflakes as Oxygen Evolution Electrocatalysts, ACS Appl. Nano Mater. 6 (2023) 20139–20148. https://doi.org/10.1021/acsanm.3c03913.
[200] A. Mariella Babu, A. Varghese, Electrochemical deposition for metal organic Frameworks: Advanced Energy, Catalysis, sensing and separation applications, J. Electroanal. Chem. 937 (2023) 117417. https://doi.org/10.1016/j.jelechem.2023.117417.
[201] V. M. V., G. Nageswaran, Review—Direct Electrochemical Synthesis of Metal Organic Frameworks, J. Electrochem. Soc. 167 (2020) 155527. https://doi.org/10.1149/1945-7111/abc6c6.

[202] M. Li, M. Dinca, Selective formation of biphasic thin films of metal-organic frameworks by potential-controlled cathodic electrodeposition, Chem. Sci. 5 (2013) 107–111. https://doi.org/10.1039/c3sc51815a.
[203] J.E. ten Elshof, Chemical solution deposition of oxide thin films, 2022. https://doi.org/10.1016/B978-0-08-102945-9.00012-5.
[204] R.W. Schwartz, T. Schneller, R. Waser, Chemical solution deposition of electronic oxide films, Comptes Rendus Chim. 7 (2004) 433–461. https://doi.org/10.1016/j.crci.2004.01.007.
[205] B.S. Yilbas, A. Al-Sharafi, H. Ali, Surfaces for Self-Cleaning, 2019. https://doi.org/10.1016/b978-0-12-814776-4.00003-3.
[206] Spin Coating: Complete Guide to Theory and Techniques, (n.d.). https://www.ossila.com/pages/spin-coating.
[207] P.L.G. Jardim, A.F. Michels, F. Horowitz, Spin-coating process evolution and reproducibility for power-law fluids, Appl. Opt. 53 (2014) 1820. https://doi.org/10.1364/ao.53.001820.
[208] U. Hasenkox, C. Mitze, R. Waser, Metal propionate synthesis of magnetoresistive La1-x(Ca,Sr)xMnO3 thin films, J. Am. Ceram. Soc. 80 (1997) 2709–2713. https://doi.org/10.1111/j.1151-2916.1997.tb03180.x.
[209] V.M. Volanti, A. Semenova, A. Zaffora, M. Santamaria, I. Valov, SrCoO3-δ and SrCo1-xTixO3-δ perovskites as electrocatalytic materials for oxygen evolution reaction in alkaline environment, Mater. Chem. Phys. (2025) 131713. https://doi.org/10.1016/j.matchemphys.2025.131713.
[210] G. Hertz, Modern Electrochemistry, 1999. https://doi.org/10.1524/zpch.1999.212.part_2.233.
[211] A.M. Appel, M.L. Helm, Determining the overpotential for a molecular electrocatalyst, ACS Catal. 4 (2014) 630–633. https://doi.org/10.1021/cs401013v.
[212] J. Luo, J.H. Im, M.T. Mayer, M. Schreier, M.K. Nazeeruddin, N.G. Park, S.D. Tilley, H.J. Fan, M. Grätzel, Water photolysis at 12.3% efficiency via perovskite photovoltaics and Earth-abundant catalysts, Science (80-.). 345 (2014) 1593–1596. https://doi.org/10.1126/science.1258307.
[213] T. Shinagawa, A.T. Garcia-Esparza, K. Takanabe, Insight on Tafel slopes from a microkinetic analysis of aqueous electrocatalysis for energy conversion, Sci. Rep. 5 (2015) 1–21. https://doi.org/10.1038/srep13801.
[214] N.T. Suen, S.F. Hung, Q. Quan, N. Zhang, Y.J. Xu, H.M. Chen, Electrocatalysis for the oxygen evolution reaction: Recent development and future perspectives, Chem. Soc. Rev. 46 (2017) 337–365. https://doi.org/10.1039/c6cs00328a.
[215] O. van der Heijden, S. Park, R.E. Vos, J.J.J. Eggebeen, M.T.M. Koper, Tafel Slope Plot as a Tool to Analyze Electrocatalytic Reactions, ACS Energy Lett. 9 (2024) 1871–1879. https://doi.org/10.1021/acsenergylett.4c00266.
[216] T. Shinagawa, A.T. Garcia-Esparza, K. Takanabe, Insight on Tafel slopes from a microkinetic analysis of aqueous electrocatalysis for energy conversion, Sci. Rep. 5 (2015) 1–21. https://doi.org/10.1038/srep13801.
[217] O. van der Heijden, S. Park, J.J.J. Eggebeen, M.T.M. Koper, Non-Kinetic Effects Convolute Activity and Tafel Analysis for the Alkaline Oxygen Evolution Reaction on NiFeOOH Electrocatalysts, Angew. Chemie Int. Ed. 62 (2023). https://doi.org/10.1002/anie.202216477.
[218] S. Siracusano, S. Trocino, N. Briguglio, V. Baglio, A.S. Aricò, Electrochemical impedance spectroscopy as a diagnostic tool in polymer electrolyte membrane electrolysis, Materials (Basel). 11 (2018).

https://doi.org/10.3390/ma11081368.
[219] A. Zaffora, F. Di Franco, D. Pupillo, B. Seminara, G. Tranchida, M. Santamaria, Highly Active and Stable NiCuMo Electrocatalyst Supported on 304 Stainless Steel Porous Transport Layer for Hydrogen Evolution in Alkaline Water Electrolyzer, Adv. Sustain. Syst. 7 (2023). https://doi.org/10.1002/adsu.202200486.
[220] B. Hirschorn, M.E. Orazem, B. Tribollet, V. Vivier, I. Frateur, M. Musiani, Determination of effective capacitance and film thickness from constant-phase-element parameters, Electrochim. Acta 55 (2010) 6218–6227. https://doi.org/10.1016/j.electacta.2009.10.065.
[221] D.M. Morales, M. Risch, Seven steps to reliable cyclic voltammetry measurements for the determination of double layer capacitance, JPhys Energy 3 (2021). https://doi.org/10.1088/2515-7655/abee33.
[222] C. Wei, S. Sun, D. Mandler, X. Wang, S.Z. Qiao, Z.J. Xu, Approaches for measuring the surface areas of metal oxide electrocatalysts for determining their intrinsic electrocatalytic activity, Chem. Soc. Rev. 48 (2019) 2518–2534. https://doi.org/10.1039/C8CS00848E.
[223] S. Zuo, Y. Liao, C. Wang, A.B. Naden, J.T.S. Irvine, Improving the Oxygen Evolution Reaction: Exsolved Cobalt Nanoparticles on Titanate Perovskite Catalyst, Small 20 (2024) 1–9. https://doi.org/10.1002/smll.202308867.
[224] D.M. Kannan, Scanning electron microscopy: principle, components and applications, Textb. Fundam. Appl. Nanotechnol. (2018) 82–92.
[225] Target material selection for coating SEM samples using an SEM sputter coater, (n.d.). https://www.microtonano.com/TIN-Target-material-selection-for-coating-SEM-samples-using-an-SEM-sputter-coater.php?
[226] A.A. Bunaciu, E. gabriela Udriştioiu, H.Y. Aboul-Enein, X-Ray Diffraction: Instrumentation and Applications, Crit. Rev. Anal. Chem. 45 (2015) 289–299. https://doi.org/10.1080/10408347.2014.949616.
[227] G.F. Harrington, J. Santiso, Back-to-Basics tutorial: X-ray diffraction of thin films, J. Electroceramics 47 (2021) 141–163. https://doi.org/10.1007/s10832-021-00263-6.
[228] D. Bieńko, M. Malik-Gajewska, P. Walencik, M. Kaj, W. Zierkiewicz, G. Murtaza, T. Ruffer, S. Ahmad, IR and Raman spectroscopic analysis, DFT modeling, and magnetic properties of a nickel(II) complex, [Ni(succ)(H2O)4]n, J. Coord. Chem. 72 (2019) 2215–2232. https://doi.org/10.1080/00958972.2019.1650351.
[229] P.R. Griffiths, Fourier transform infrared spectrometry, 1983. https://doi.org/10.1126/science.6623077.
[230] R. Spectroscopy, Chapter 3 The Theory of Raman Spectroscopy, 5 (2019).
[231] E. Smith, J. Dent, Modern Raman Spectroscopy: A Practical Approach. John Wiley and Sons, 2004.
[232] C. Farber, J. Li, E. Hager, R. Chemelewski, J. Mullet, A.Y. Rogachev, D. Kurouski, Complementarity of Raman and Infrared Spectroscopy for Structural Characterization of Plant Epicuticular Waxes, ACS Omega 4 (2019) 3700–3707. https://doi.org/10.1021/acsomega.8b03675.
[233] G. Greczynski, L. Hultman, X-ray photoelectron spectroscopy: Towards reliable binding energy referencing, Prog. Mater. Sci. 107 (2020) 100591. https://doi.org/10.1016/j.pmatsci.2019.100591.
[234] M.C. Biesinger, B.P. Payne, A.P. Grosvenor, L.W.M. Lau, A.R. Gerson, R.S.C. Smart, Resolving surface chemical states in XPS analysis of first row transition metals, oxides and hydroxides: Cr, Mn, Fe, Co and Ni, Appl. Surf.

Sci. 257 (2011) 2717–2730. https://doi.org/10.1016/j.apsusc.2010.10.051.
[235] Thermo Fisher Scientific, Application note: 31014_Angle Resolved XPS, East App. Note (2008) 10. https://tools.thermofisher.com/content/sfs/brochures/D16069~.pdf.
[236] A. Carbone, R. Pedicini, I. Gatto, A. Saccà, A. Patti, G. Bella, M. Cordaro, Development of polymeric membranes based on quaternized polysulfones for AMFC applications, Polymers (Basel). 12 (2020) 1–15. https://doi.org/10.3390/polym12020283.
[237] F. Zeng, C. Mebrahtu, L. Liao, A.K. Beine, R. Palkovits, Stability and deactivation of OER electrocatalysts: A review, J. Energy Chem. 69 (2022) 301–329. https://doi.org/10.1016/j.jechem.2022.01.025.
[238] L. Xiao, Z. Wang, J. Guan, 2D MOFs and their derivatives for electrocatalytic applications: Recent advances and new challenges, Coord. Chem. Rev. 472 (2022) 214777. https://doi.org/10.1016/j.ccr.2022.214777.
[239] M.R. Gao, Y.F. Xu, J. Jiang, Y.R. Zheng, S.H. Yu, Water oxidation electrocatalyzed by an efficient Mn3O 4/CoSe2 nanocomposite, J. Am. Chem. Soc. 134 (2012) 2930–2933. https://doi.org/10.1021/ja211526y.
[240] M. Ledendecker, S. Krick Calderón, C. Papp, H. Steinrück, M. Antonietti, M. Shalom, The Synthesis of Nanostructured Ni 5 P 4 Films and their Use as a Non-Noble Bifunctional Electrocatalyst for Full Water Splitting, Angew. Chemie Int. Ed. 54 (2015) 12361–12365. https://doi.org/10.1002/anie.201502438.
[241] J.W.D. Ng, M. Tang, T.F. Jaramillo, A carbon-free, precious-metal-free, high-performance O2 electrode for regenerative fuel cells and metal-air batteries, Energy Environ. Sci. 7 (2014) 2017–2024. https://doi.org/10.1039/c3ee44059a.
[242] F. Paquin, J. Rivnay, A. Salleo, N. Stingelin, C. Silva, Multi-phase semicrystalline microstructures drive exciton dissociation in neat plastic semiconductors, J. Mater. Chem. C 3 (2015) 10715–10722. https://doi.org/10.1039/b000000x.
[243] T. Zhai, H. Wang, S.R. Beaudoin, R. Zhang, M. Kwak, S. Hou, Z. Guo, S.W. Boettcher, Perovskite Catalysts for Pure-Water-Fed Anion-Exchange-Membrane Electrolyzer Anodes: Co-design of Electrically Conductive Nanoparticle Cores and Active Surfaces, J. Am. Chem. Soc. 147 (2025) 15448–15458. https://doi.org/10.1021/jacs.5c01621.
[244] I. Rodriguez-Garcia, J.L. Gomez de la Fuente, D. Galyamin, A. Tolosana-Moranchel, P. Kayser, M.A. Salam, J.A. Alonso, F. Calle-Vallejo, S. Rojas, M. Retuerto, Dy2NiRuO6 perovskite with high activity and durability for the oxygen evolution reaction in acidic electrolyte, J. Mater. Chem. A 12 (2024) 16854–16862. https://doi.org/10.1039/d3ta06788b.
[245] M.J.N. Pourbaix, Atlas of electrochemical equilibria in aqueous solutions, J. Electroanal. Chem. Interfacial Electrochem. (1974) 644.
[246] J. Wang, C.X. Zhao, J.N. Liu, D. Ren, B.Q. Li, J.Q. Huang, Q. Zhang, Quantitative kinetic analysis on oxygen reduction reaction: A perspective, Nano Mater. Sci. 3 (2021) 313–318. https://doi.org/10.1016/j.nanoms.2021.03.006.
[247] G. Zhong, S. Xu, L. Liu, C.Z. Zheng, J. Dou, F. Wang, X. Fu, W. Liao, H. Wang, Effect of Experimental Operations on the Limiting Current Density of Oxygen Reduction Reaction Evaluated by Rotating-Disk Electrode, ChemElectroChem 7 (2020) 1107–1114. https://doi.org/10.1002/celc.201902085.

[248] J.T. Richardson, R. Scates, M. V. Twigg, X-ray diffraction study of nickel oxide reduction by hydrogen, Appl. Catal. A Gen. 246 (2003) 137–150. https://doi.org/10.1016/S0926-860X(02)00669-5.
[249] A.Y. Faid, A.O. Barnett, F. Seland, S. Sunde, Ni/NiO nanosheets for alkaline hydrogen evolution reaction: In situ electrochemical-Raman study, Electrochim. Acta 361 (2020) 137040. https://doi.org/10.1016/j.electacta.2020.137040.
[250] S. Krishnan, C.J. Raj, R. Robert, A. Ramanand, S. Jerome Das, Growth and characterization of succinic acid single crystals, Cryst. Res. Technol. 42 (2007) 1087–1090. https://doi.org/10.1002/crat.200710981.
[251] Y. Hai, L. Liu, Y. Gong, Iron Coordination Polymer, Fe(oxalate)(H2O)2Nanorods Grown on Nickel Foam via One-Step Electrodeposition as an Efficient Electrocatalyst for Oxygen Evolution Reaction, Inorg. Chem. 60 (2021) 5140–5152. https://doi.org/10.1021/acs.inorgchem.1c00170.
[252] S.A. Martin Britto Dhas, M. Suresh, G. Bhagavannarayana, S. Natarajan, Growth and characterization of l-Tartaric acid, an NLO material, J. Cryst. Growth 309 (2007) 48–52. https://doi.org/10.1016/j.jcrysgro.2007.09.008.
[253] X. Gao, D. Chen, J. Qi, F. Li, Y. Song, W. Zhang, R. Cao, NiFe Oxalate Nanomesh Array with Homogenous Doping of Fe for Electrocatalytic Water Oxidation, Small 15 (2019) 1–7. https://doi.org/10.1002/smll.201904579.
[254] M.C. Biesinger, B.P. Payne, L.W.M. Lau, A. Gerson, R.S.C. Smart, X-ray photoelectron spectroscopic chemical state Quantification of mixed nickel metal, oxide and hydroxide systems, Surf. Interface Anal. 41 (2009) 324–332. https://doi.org/10.1002/sia.3026.
[255] P. Taheri, T. Hauffman, J.M.C. Mol, J.R. Flores, F. Hannour, J.H.W. De Wit, H. Terryn, Molecular interactions of electroadsorbed carboxylic acid and succinic anhydride monomers on zinc surfaces, J. Phys. Chem. C 115 (2011) 17054–17067. https://doi.org/10.1021/jp204751z.
[256] X. Wang, D. Du, H. Xu, Y. Yan, X. Wen, L. Ren, C. Shu, NiMn-based metal-organic framework with optimized eg orbital occupancy as efficient bifunctional electrocatalyst for lithium-oxygen batteries, Chem. Eng. J. 452 (2023) 139524. https://doi.org/10.1016/j.cej.2022.139524.
[257] Z. Li, Y. Yao, S. Sun, J. Liang, S. Hong, H. Zhang, C. Yang, X. Zhang, Z. Cai, J. Li, Y. Ren, Y. Luo, D. Zheng, X. He, Q. Liu, Y. Wang, F. Gong, X. Sun, B. Tang, Carbon Oxyanion Self-Transformation on NiFe Oxalates Enables Long-Term Ampere-Level Current Density Seawater Oxidation, Angew. Chemie Int. Ed. 63 (2024). https://doi.org/10.1002/anie.202316522.
[258] G. Tranchida, M. Clesi, F. Di Franco, F. Di Quarto, M. Santamaria, Electronic properties and corrosion resistance of passive films on austenitic and duplex stainless steels, Electrochim. Acta 273 (2018) 412–423. https://doi.org/10.1016/j.electacta.2018.04.058.
[259] M.W. Louie, A.T. Bell, An investigation of thin-film Ni-Fe oxide catalysts for the electrochemical evolution of oxygen, J. Am. Chem. Soc. 135 (2013) 12329–12337. https://doi.org/10.1021/ja405351s.
[260] N. Hales, T.J. Schmidt, E. Fabbri, Reversible and irreversible transformations of Ni-based electrocatalysts during the oxygen evolution reaction, Curr. Opin. Electrochem. 38 (2023) 101231. https://doi.org/10.1016/j.coelec.2023.101231.
[261] L. Wang, Y. Wu, R. Cao, L. Ren, M. Chen, X. Feng, J. Zhou, B. Wang, Fe/Ni Metal-Organic Frameworks and Their Binder-Free Thin Films for Efficient

Oxygen Evolution with Low Overpotential, ACS Appl. Mater. Interfaces 8 (2016) 16736–16743. https://doi.org/10.1021/acsami.6b05375.
[262] O. van der Heijden, S. Park, J.J.J. Eggebeen, M.T.M. Koper, Non-Kinetic Effects Convolute Activity and Tafel Analysis for the Alkaline Oxygen Evolution Reaction on NiFeOOH Electrocatalysts, Angew. Chemie Int. Ed. 62 (2023) 1374. https://doi.org/10.1002/anie.202216477.
[263] R. Holze, Book Review: Electrochemical Methods. Fundamentals and Applications (2nd Edition). By Allen J. Bard and Larry R. Faulkner, Angew. Chemie Int. Ed. 41 (2002) 655–657. https://doi.org/10.1002/1521-3773(20020215)41:4<655::AID-ANIE655>3.0.CO;2-I.
[264] C.P. Wang, Y.X. Lin, L. Cui, J. Zhu, X.H. Bu, 2D Metal–Organic Frameworks as Competent Electrocatalysts for Water Splitting, Small 19 (2023) 1–46. https://doi.org/10.1002/smll.202207342.
[265] C. Yang, H. Ma, R. Yuan, K. Wang, K. Liu, Y. Long, F. Xu, L. Li, H. Zhang, Y. Zhang, X. Li, H. Wu, Roll-to-roll prelithiation of lithium-ion battery anodes by transfer printing, Nat. Energy 8 (2023) 703–713. https://doi.org/10.1038/s41560-023-01272-1.
[266] Z. Feng, P. Wang, Y. Cheng, Y. Mo, X. Luo, P. Liu, R. Guo, X. Liu, Recent progress on NiFe2O4 spinels as electrocatalysts for the oxygen evolution reaction, J. Electroanal. Chem. 946 (2023) 117703. https://doi.org/10.1016/j.jelechem.2023.117703.
[267] L. Mirizzi, M. Muhyuddin, C. Lo Vecchio, E. Mosca, V. Baglio, I. Gatto, E. Berretti, A. Lavacchi, V.C.A. Ficca, R. Viscardi, R. Nisticò, C. Santoro, Amorphous nanostructured Ni–Fe oxide as a notably active and low-cost oxygen evolution reaction electrocatalyst for anion exchange membrane water electrolysis, Ind. Chem. Mater. 3 (2025) 485–497. https://doi.org/10.1039/d5im00008d.
[268] J. Chen, T. Li, G. Shen, Z. Song, S. Zhong, Y. Yang, W. Feng, Synergistic enhancement of oxygen evolution reaction via NiFe2O4-doped hexagonal nickel hydroxide nanosheets for efficient water electrolysis, Fuel 400 (2025) 135730. https://doi.org/10.1016/j.fuel.2025.135730.
[269] X. Zheng, Z. Wang, D. Zeng, Y. Qiao, Z. Li, J. Jian, H. Yuan, NiFe 2 O 4 nanoflowers with Mo doping for self-powered hydrogen production at large current density, J. Mater. Chem. C 13 (2025) 9099–9105. https://doi.org/10.1039/D5TC00624D.
[270] J. Jian, Y. Zhang, Z. Wang, X. Zheng, P. Nie, W. Yang, T. Zhang, L. Chang, One-step synthesized iron foam-based NiFe 2 O 4 applied for self-powered water splitting hydrogen production, J. Mater. Chem. A 13 (2025) 1102–1108. https://doi.org/10.1039/D4TA07904C.
[271] Y. Zhang, Y. Yang, B. Lu, R. Zhang, F. Zhou, D. Sun, Q. Wang, J. Li, Z. Lei, Bimetallic chloride in situ etching of NiFe alloy substrate to synthesize porous coral structure catalyst for efficient oxygen evolution reaction, Fuel 402 (2025) 135909. https://doi.org/10.1016/j.fuel.2025.135909.
[272] Z. Wang, H. Liu, S. Wang, Z. Rao, Y. Yang, A luminescent Terbium-Succinate MOF thin film fabricated by electrodeposition for sensing of Cu2+ in aqueous environment, Sensors Actuators, B Chem. 220 (2015) 779–787. https://doi.org/10.1016/j.snb.2015.05.129.
[273] S.G. Patnaik, G. Vanheusden, A.A. Saleh, P.M. Vereecken, Electrochemically Induced Deposition (ECiD): A Versatile Method that Greatly Extends the Portfolio of Surface Coatings and Materials Fabricated by Electrochemical Deposition, Electrochem. Soc. Interface 33 (2024) 61–

66. https://doi.org/10.1149/2.F11242IF.
[274] A. Zaffora, B. Megna, B. Seminara, F. Di Franco, M. Santamaria, Ni,Fe,Co-LDH Coated Porous Transport Layers for Zero-Gap Alkaline Water Electrolyzers, Nanomaterials 14 (2024). https://doi.org/10.3390/nano14050407.
[275] C.F. Li, L.J. Xie, J.W. Zhao, L.F. Gu, H.B. Tang, L. Zheng, G.R. Li, Interfacial Fe−O−Ni−O−Fe Bonding Regulates the Active Ni Sites of Ni-MOFs via Iron Doping and Decorating with FeOOH for Super-Efficient Oxygen Evolution, Angew. Chemie - Int. Ed. 61 (2022). https://doi.org/10.1002/anie.202116934.
[276] V.T. Yilmaz, S. Demir, O. Andac, W. Harrison, Mixed-ligand metal succinate complexes with 1,10-phenanthroline and ethylenediamine: Synthesis, characterization, spectroscopic and thermal studies. Crystal structure of succinatocobalt(II) complex with phenanthroline, J. Coord. Chem. 55 (2002) 863–872. https://doi.org/10.1080/0095897022000002196.
[277] M.C. Biesinger, L.W.M. Lau, A.R. Gerson, R.S.C. Smart, Resolving surface chemical states in XPS analysis of first row transition metals, oxides and hydroxides: Sc, Ti, V, Cu and Zn, Appl. Surf. Sci. 257 (2010) 887–898. https://doi.org/10.1016/j.apsusc.2010.07.086.
[278] T. Yamashita, P. Hayes, Analysis of XPS spectra of Fe 2+ and Fe 3+ ions in oxide materials, Appl. Surf. Sci. 254 (2008) 2441–2449. https://doi.org/10.1016/j.apsusc.2007.09.063.
[279] J. Zhao, J. Zhang, Z. Li, X. Bu, Recent Progress on NiFe-Based Electrocatalysts for the Oxygen Evolution Reaction, Small 16 (2020). https://doi.org/10.1002/smll.202003916.
[280] L. Magnier, G. Cossard, V. Martin, C. Pascal, V. Roche, E. Sibert, I. Shchedrina, R. Bousquet, V. Parry, M. Chatenet, Fe–Ni-based alloys as highly active and low-cost oxygen evolution reaction catalyst in alkaline media, Nat. Mater. 23 (2024) 252–261. https://doi.org/10.1038/s41563-023-01744-5.
[281] Y. Zhu, Z. Cai, Q. Wei, R. Chen, F. Guo, Y. Jiang, Y. Xiao, J. Guo, Z. Wang, J. Zhong, N. Cheng, Asymmetric Electron Transport-Induced Formation of High-Valent IrO x in NiFeOOH Heterostructure for Efficient Water Oxidation, Adv. Funct. Mater. 35 (2025). https://doi.org/10.1002/adfm.202503692.
[282] Ö.N. Avcı, L. Sementa, A. Fortunelli, Mechanisms of the Oxygen Evolution Reaction on NiFe 2 O 4 and CoFe 2 O 4 Inverse-Spinel Oxides, ACS Catal. 12 (2022) 9058–9073. https://doi.org/10.1021/acscatal.2c01534.
[283] M. Hua, L. Xu, F. Cui, J. Lian, Y. Huang, J. Bao, J. Qiu, Y. Xu, H. Xu, Y. Zhao, H. Li, Hexamethylenetetramine-assisted hydrothermal synthesis of octahedral nickel ferrite oxide nanocrystallines with excellent supercapacitive performance, J. Mater. Sci. 53 (2018) 7621–7636. https://doi.org/10.1007/s10853-018-2052-7.
[284] D.A. Corrigan, S.P. Maheswari, Catalysis of the Oxygen Evolution Reaction By Trace Iron Impurities in Thin Film Nickel Oxide Electrodes., Electrochem. Soc. Ext. Abstr. 85–1 (1985) 934–935.
[285] L. Trotochaud, S.L. Young, J.K. Ranney, S.W. Boettcher, Nickel-Iron oxyhydroxide oxygen-evolution electrocatalysts: The role of intentional and incidental iron incorporation, J. Am. Chem. Soc. 136 (2014) 6744–6753. https://doi.org/10.1021/ja502379c.
[286] D. Friebel, M.W. Louie, M. Bajdich, K.E. Sanwald, Y. Cai, A.M. Wise, M.J.

Cheng, D. Sokaras, T.C. Weng, R. Alonso-Mori, R.C. Davis, J.R. Bargar, J.K. Nørskov, A. Nilsson, A.T. Bell, Identification of highly active Fe sites in (Ni,Fe)OOH for electrocatalytic water splitting, J. Am. Chem. Soc. 137 (2015) 1305–1313. https://doi.org/10.1021/ja511559d.

[287] Y. Zhou, Z. Wang, M. Cui, H. Wu, Y. Liu, Q. Ou, X. Tian, S. Zhang, NiFe-Based Electrocatalysts for Alkaline Oxygen Evolution: Challenges, Strategies, and Advances Toward Industrial-Scale Deployment, Adv. Funct. Mater. 34 (2024). https://doi.org/10.1002/adfm.202410618.

[288] T. Shinagawa, K. Takanabe, New Insight into the Hydrogen Evolution Reaction under Buffered Near-Neutral pH Conditions: Enthalpy and Entropy of Activation, J. Phys. Chem. C 120 (2016) 24187–24196. https://doi.org/10.1021/acs.jpcc.6b07954.

[289] E. Nurlaela, T. Shinagawa, M. Qureshi, D.S. Dhawale, K. Takanabe, Temperature Dependence of Electrocatalytic and Photocatalytic Oxygen Evolution Reaction Rates Using NiFe Oxide, ACS Catal. 6 (2016) 1713–1722. https://doi.org/10.1021/acscatal.5b02804.

[290] M. Suermann, T.J. Schmidt, F.N. Büchi, Comparing the kinetic activation energy of the oxygen evolution and reduction reactions, Electrochim. Acta 281 (2018) 466–471. https://doi.org/10.1016/j.electacta.2018.05.150.

[291] Y. Li, T. Zhang, J. Ma, X. Deng, J. Gu, F. Yang, M. Ouyang, Study the effect of lye flow rate, temperature, system pressure and different current density on energy consumption in catalyst test and 500W commercial alkaline water electrolysis, Mater. Today Phys. 22 (2022) 100606. https://doi.org/10.1016/j.mtphys.2022.100606.

[292] A. Caprì, A. Martínez-Lázaro, J. Béjar, I. Gatto, L. Álvarez-Contreras, M.P. Gurrola, J. Ledesma-García, V. Baglio, L.G. Arriaga, Three-dimensionally ordered macroporous trimetallic spinel for anion exchange membrane water electrolysis, Electrochim. Acta 463 (2023) 1–9. https://doi.org/10.1016/j.electacta.2023.142851.

[293] A. Martinez-Lazaro, A. Caprì, I. Gatto, J. Ledesma-García, N. Rey-Raap, A. Arenillas, F.I. Espinosa-Lagunes, V. Baglio, L.G. Arriaga, NiFe2O4 hierarchical nanoparticles as electrocatalyst for anion exchange membrane water electrolysis, J. Power Sources 556 (2023) 232417. https://doi.org/10.1016/j.jpowsour.2022.232417.

[294] C. Simari, A. Caprì, M.H. Ur Rehman, A. Enotiadis, I. Gatto, V. Baglio, I. Nicotera, Composite anion exchange membranes based on polysulfone and silica nanoscale ionic materials for water electrolyzers, Electrochim. Acta 462 (2023) 142788. https://doi.org/10.1016/j.electacta.2023.142788.

[295] N. Carboni, L. Mazzapioda, A. Caprì, I. Gatto, A. Carbone, V. Baglio, M.A. Navarra, Composite anion exchange membranes based on graphene oxide for water electrolyzer applications, Electrochim. Acta 486 (2024) 144090. https://doi.org/10.1016/j.electacta.2024.144090.

[296] M. Montalto, W. da S. Freitas, E. Mastronardo, V.C.A. Ficca, E. Placidi, V. Baglio, E. Mosca, C. Lo Vecchio, I. Gatto, B. Mecheri, A. D'Epifanio, Spinel-type high-entropy oxides for enhanced oxygen evolution reaction activity in anion exchange membrane water electrolyzers, Chem. Eng. J. 507 (2025) 160641. https://doi.org/10.1016/j.cej.2025.160641.

[297] K.W. Ahmed, S. Habibpour, Z. Chen, M. Fowler, Investigation of NiCoOx catalysts for anion exchange membrane water electrolysis: Performance, durability, and efficiency analysis, J. Energy Storage 79 (2024) 110149. https://doi.org/10.1016/j.est.2023.110149.

[298] M. Ranz, B. Grabner, B. Schweighofer, H. Wegleiter, A. Trattner, Dynamics of anion exchange membrane electrolysis: Unravelling loss mechanisms with electrochemical impedance spectroscopy, reference electrodes and distribution of relaxation times, J. Power Sources 605 (2024) 234455. https://doi.org/10.1016/j.jpowsour.2024.234455.
[299] J.E. Park, M.J. Kim, M.S. Lim, S.Y. Kang, J.K. Kim, S.H. Oh, M. Her, Y.H. Cho, Y.E. Sung, Graphitic carbon nitride-carbon nanofiber as oxygen catalyst in anion-exchange membrane water electrolyzer and rechargeable metal–air cells, Appl. Catal. B Environ. 237 (2018) 140–148. https://doi.org/10.1016/j.apcatb.2018.05.073.
[300] T. Caielli, A.R. Ferrari, S. Bonizzoni, E. Sediva, A. Caprì, M. Santoro, I. Gatto, V. Baglio, P. Mustarelli, Synthesis, characterization and water electrolyzer cell tests of poly(biphenyl piperidinium) Anion exchange membranes, J. Power Sources 557 (2023) 232532. https://doi.org/10.1016/j.jpowsour.2022.232532.
[301] S. Li, T. Liu, W. Zhang, M. Wang, H. Zhang, C. Qin, L. Zhang, Y. Chen, S. Jiang, D. Liu, X. Liu, H. Wang, Q. Luo, T. Ding, T. Yao, Highly efficient anion exchange membrane water electrolyzers via chromium-doped amorphous electrocatalysts, Nat. Commun. 15 (2024) 1–11. https://doi.org/10.1038/s41467-024-47736-0.
[302] L.B. Liu, C. Yi, H.C. Mi, S.L. Zhang, X.Z. Fu, J.L. Luo, S. Liu, Perovskite Oxides Toward Oxygen Evolution Reaction: Intellectual Design Strategies, Properties and Perspectives, Springer Nature Singapore, 2024. https://doi.org/10.1007/s41918-023-00209-2.
[303] I.C. Man, H.Y. Su, F. Calle-Vallejo, H.A. Hansen, J.I. Martínez, N.G. Inoglu, J. Kitchin, T.F. Jaramillo, J.K. Nørskov, J. Rossmeisl, Universality in Oxygen Evolution Electrocatalysis on Oxide Surfaces, ChemCatChem 3 (2011) 1159–1165. https://doi.org/10.1002/cctc.201000397.
[304] S. Yagi, I. Yamada, H. Tsukasaki, A. Seno, M. Murakami, H. Fujii, H. Chen, N. Umezawa, H. Abe, N. Nishiyama, S. Mori, Covalency-reinforced oxygen evolution reaction catalyst, Nat. Commun. 6 (2015) 1–6. https://doi.org/10.1038/ncomms9249.
[305] N. Tsvetkov, Q. Lu, L. Sun, E.J. Crumlin, B. Yildiz, Improved chemical and electrochemical stability of perovskite oxides with less reducible cations at the surface, Nat. Mater. 15 (2016) 1010–1016. https://doi.org/10.1038/nmat4659.
[306] J.E. ten Elshof, Chemical solution deposition of oxide thin films, Elsevier Ltd, 2022. https://doi.org/10.1016/B978-0-08-102945-9.00012-5.
[307] Z. Chen, P. He, D. Wu, C. Chen, M. Mujahid, Y. Li, Y. Duan, Processing and Preparation Method for High-Quality Opto-Electronic Perovskite Film, Front. Mater. 8 (2021) 1–13. https://doi.org/10.3389/fmats.2021.723169.
[308] H. Wang, M. Zhou, P. Choudhury, H. Luo, Perovskite oxides as bifunctional oxygen electrocatalysts for oxygen evolution/reduction reactions – A mini review, Appl. Mater. Today 16 (2019) 56–71. https://doi.org/10.1016/j.apmt.2019.05.004.
[309] J. Sun, G. Li, Z. Li, L. You, J. Lin, Crystal growth and structure determination of oxygen-deficient Sr 6Co5O15, Inorg. Chem. 45 (2006) 8394–8402. https://doi.org/10.1021/ic060862m.
[310] W.L. Roth, The magnetic structure of Co3O4, J. Phys. Chem. Solids 25 (1964) 1–10. https://doi.org/10.1016/0022-3697(64)90156-8.
[311] H. Van Doveren, J.A.T.H. Verhoeven, XPS spectra of Ca, Sr, Ba and their

oxides, J. Electron Spectros. Relat. Phenomena 21 (1980) 265–273. https://doi.org/10.1016/0368-2048(80)85055-9.
[312] A. Cavallaro, G.E. Wilson, G. Kerherve, E. Cali, C.A.M. van den Bosch, P. Boldrin, D. Payne, S.J. Skinner, A. Aguadero, Analysis of H2O-induced surface degradation in SrCoO3-derivatives and its impact on redox kinetics, J. Mater. Chem. A 9 (2021) 24528–24538. https://doi.org/10.1039/d1ta04174f.
[313] T.J. Chuang, C.R. Brundle, D.W. Rice, Interpretation of the x-ray photoemission spectra of cobalt oxides and cobalt oxide surfaces, Surf. Sci. 59 (1976) 413–429. https://doi.org/10.1016/0039-6028(76)90026-1.
[314] M. Oku, K. Hirokawa, X-ray photoelectron spectroscopy of Co3O4, Fe3O4, Mn3O4, and related compounds, J. Electron Spectros. Relat. Phenomena 8 (1976) 475–481. https://doi.org/10.1016/0368-2048(76)80034-5.
[315] K.P. Reddy, R. Jain, M.K. Ghosalya, C.S. Gopinath, Metallic cobalt to spinel Co3O4-electronic structure evolution by near-ambient pressure photoelectron spectroscopy, J. Phys. Chem. C 121 (2017) 21472–21481. https://doi.org/10.1021/acs.jpcc.7b06661.
[316] M.G. Ahmed, Y.F. Tay, M. Zhang, S.Y. Chiam, L.H. Wong, Tailoring Surface Electronic Structure of Spinel Co3O4 Oxide via Fe and Cu Substitution for Enhanced Oxygen Evolution Reaction, ACS Mater. Lett. 6 (2024) 4756–4764. https://doi.org/10.1021/acsmaterialslett.4c00857.
[317] G.F. Liu, P.P. Ma, Y. Qiao, R.H. Xu, D.M. Huang, R.Y. Hu, L.Y. Liu, G.H. Jiang, M. Demir, Perovskite SrCo1-xTixO3-δ as anion-intercalated electrode materials for supercapacitors, J. Energy Storage 52 (2022) 104942. https://doi.org/10.1016/j.est.2022.104942.
[318] A.P. Dementjev, O.P. Ivanova, L.A. Vasilyev, A. V. Naumkin, D.M. Nemirovsky, D.Y. Shalaev, Altered layer as sensitive initial chemical state indicator*, J. Vac. Sci. Technol. A Vacuum, Surfaces, Film. 12 (1994) 423–427. https://doi.org/10.1116/1.579258.
[319] H. Sun, B. Hu, D. Guan, Z. Hu, L. Fei, M. Li, V.K. Peterson, H.J. Lin, C. Te Chen, R. Ran, W. Zhou, Z. Shao, Bulk and Surface Properties Regulation of Single/Double Perovskites to Realize Enhanced Oxygen Evolution Reactivity, ChemSusChem 13 (2020) 3045–3052. https://doi.org/10.1002/cssc.202000704.
[320] B.J. Kim, E. Fabbri, M. Borlaf, D.F. Abbott, I.E. Castelli, M. Nachtegaal, T. Graule, T.J. Schmidt, Oxygen evolution reaction activity and underlying mechanism of perovskite electrocatalysts at different pH, Mater. Adv. 2 (2021) 345–355. https://doi.org/10.1039/d0ma00661k.
[321] L. Lu, M. Sun, T. Wu, Q. Lu, B. Chen, C. Hei Chan, H. Ho Wong, Z. Li, B. Huang, Perovskite Oxides for Electrocatalytic Hydrogen/Oxygen Evolution Reaction, ChemElectroChem 12 (2025). https://doi.org/10.1002/celc.202400648.
[322] J. Song, C. Wei, Z.F. Huang, C. Liu, L. Zeng, X. Wang, Z.J. Xu, A review on fundamentals for designing oxygen evolution electrocatalysts, Chem. Soc. Rev. 49 (2020) 2196–2214. https://doi.org/10.1039/c9cs00607a.
[323] C. Su, W. Wang, Y. Chen, G. Yang, X. Xu, M.O. Tadé, Z. Shao, SrCo 0.9 Ti 0.1 O 3−δ As a New Electrocatalyst for the Oxygen Evolution Reaction in Alkaline Electrolyte with Stable Performance, ACS Appl. Mater. Interfaces 7 (2015) 17663–17670. https://doi.org/10.1021/acsami.5b02810.
[324] H.A. Tahini, X. Tan, U. Schwingenschlögl, S.C. Smith, Formation and Migration of Oxygen Vacancies in SrCoO3 and Their Effect on Oxygen

Evolution Reactions, ACS Catal. 6 (2016) 5565–5570. https://doi.org/10.1021/acscatal.6b00937.
[325] X. Sun, Y. Yuan, S. Liu, H. Zhao, S. Yao, Y. Sun, M. Zhang, Y. Liu, Z. Lin, Recent Advances in Perovskite Oxides for Oxygen Evolution Reaction: Structures, Mechanisms, and Strategies for Performance Enhancement, Adv. Funct. Mater. 35 (2025) 1–27. https://doi.org/10.1002/adfm.202416705.
[326] L. Lu, M. Sun, T. Wu, Q. Lu, B. Chen, C. Hei Chan, H. Ho Wong, Z. Li, B. Huang, Perovskite Oxides for Electrocatalytic Hydrogen/Oxygen Evolution Reaction, ChemElectroChem 202400648 (2025). https://doi.org/10.1002/celc.202400648.
[327] R. Khan, M.T. Mehran, S.R. Naqvi, A.H. Khoja, K. Mahmood, F. Shahzad, S. Hussain, Role of perovskites as a bi-functional catalyst for electrochemical water splitting: A review, Int. J. Energy Res. 44 (2020) 9714–9747. https://doi.org/10.1002/er.5635.
[328] Y. Pan, X. Xu, Y. Zhong, L. Ge, Y. Chen, J.P.M. Veder, D. Guan, R. O'Hayre, M. Li, G. Wang, H. Wang, W. Zhou, Z. Shao, Direct evidence of boosted oxygen evolution over perovskite by enhanced lattice oxygen participation, Nat. Commun. 11 (2020) 1–10. https://doi.org/10.1038/s41467-020-15873-x.